BOTTOM TRACKING ISSUES AND RECOGNITION THEREOF USING SHOALS-3000 GREEN LASER BEAM IN DENSE FIELDS OF ZOSTERA MARINA AND LAMINARIA SP.

by

Pim Kuus

Bachelor of Maritime Operations, 'Maritiem Instituut Willem Barentsz', Terschelling, the Netherlands, 2005

A Thesis Submitted in Partial Fulfillment of the Requirements for the Degree of

Master of Science in Engineering

In the Graduate Academic Unit of Geodesy and Geomatics Engineering

Supervisor: J. E. Hughes Clarke, Ph.D., Geodesy & Geomatics Engineering

Examining Board: D. E. Wells, Ph.D., Geodesy & Geomatics Engineering

External Examiner: S. Pe'eri, Ph.D., Geophysics & Remote Sensing (Centre for Coastal and Ocean Mapping, University of New Hampshire)

This thesis is accepted by the Dean of Graduate Studies

THE UNIVERSITY OF NEW BRUNSWICK

April, 2008

© P. Kuus, 2008

Abstract

This thesis assesses the ability of the SHOALS-3000 bathymetric lidar to correctly track the bottom in areas of dense aquatic vegetation, and explores a method to recognize improper bottom tracking, as a result of the vegetation, without ground truthing data. To perform the analysis, SHOALS-3000 and overlapping ship-based acoustic data were collected near the shores of Bonaventure and Paspébiac on the Bay de Chaleur, Quebec, in June 2006.

EM3002 multibeam bathymetry and water column data, and Knudsen 200 kHz singlebeam water column backscatter were utilized for the SHOALS-3000 bottom tracking assessment. To assure a high level of vertical accuracy and exclude the necessity for real time, or predicted tide values post-processed kinematic (PPK) antenna solutions were allocated to the multibeam transducer face, by which multibeam solutions were matched with ellipsoid-referenced lidar solutions.

An algorithm was developed that characterizes green laser waveforms, but excludes those that returned from land, or too shallow or too deep water. The algorithm includes three techniques to adapt as thoroughly as possible to obscure waveform bottom returns from vegetation soundings. A by-product of the characterization method is a term that describes the water clarity.

The relative assessment revealed that the SHOALS-3000, compared to the EM3002, could achieve the manufacturer's and IHO Order 1 accuracy specifications in unvegetated areas. Once aquatic vegetation is present, the bottom tracking of the

SHOALS-3000 degrades: manufacturer's and IHO Order 1 accuracy specifications could not be met. The green laser beam tracks the vegetation, or fails to return a sounding. This last observation is most concerning, implying that lidar datagaps, aside from reducing the effective coverage, are not necessarily due to lidar extinction depths, but potentially due to marine life covered navigational hazards.

Waveforms from vegetation soundings have a small bottom return height, when compared to typical unvegetated seabeds, and as no sediment was found with similar reflectance, vegetated seabeds could therefore easily be discriminated from unvegetated seabeds. Vegetation identified with ground truthing data showed good agreement with small bottom return height values once the characterized waveforms were spatially plotted. A ratio describing typical bottom return height values of vegetated and unvegetated seabeds, confirmed the unambiguous reflectance of the laser, despite some day-to-day differences. This unambiguous behavior was incorporated with lidar bathymetry slopes to validate lidar soundings and identify fields of aquatic vegetation. Finally, overlapping keel mounted side scan sonar backscatter provides a potential to identify habitat based vegetation such as Laminaria sp. and Zostera Marina species.

Acknowledgements

This thesis included several large datasets, which I could never have obtained alone. I therefore owe gratitude to Captain Serge LeMay for his skilled piloting of the Heron during long and repetitive surveys. I am also thankful I could rely on Steve Brucker's proficiency on an array of Heron related matters and his comments on PPK-processing. My thanks also go to Marketa Pokorná for her assistance during the Heron surveys and members of the FUDOTERAM project group who collected under water photography and sediment grabs. Extra thanks to Antoinne Cottin who acted as a link between FUDOTERAM and the OMG and with whom I shared some informative discussions about the lidar data. I would also like to acknowledge the US Navy for providing the SHOALS-3000, Dynamic Aviation for the airborne survey, Optech Inc for SHOALS processing, Paul LaRoque for providing me additional information about the waveform data, and the Canadian Network of Centres of Excellence GEOIDE and sponsors of the Chair in Ocean Mapping at UNB for financial support.

I am grateful I could work with members of the Ocean Mapping Group especially my supervisor Dr. John Hughes Clarke from whom I have gained knowledge that will aid me in my future career. I am indebted to Dr. Hughes Clarke for his constructive help during this research and essential software modifications for SHOALS data. I also would like to acknowledge his contagious passion to map and learn from the ocean floors. My thanks also go to Dr. Dave Wells for his suggestions to this thesis, and Dr. Shachak Pe'eri for examining this thesis.

This thesis would not be in the current state without help from Rodger Wilkie. I

have greatly appreciated his help in polishing the English and reminding me of grammatical rules that were tucked away in my memory.

Finally, although their contributions to this thesis are not directly related, I owe gratitude to my parents, sister, and grandfather for their continuing support, and special thanks to Pili; gracias por tu interminable paciencia y apoyo, yo estoy inmensamente agradecido contigo.

Table of Contents

List of Tables

List of Figures

List of Abbreviations, Nomenclature, and Symbols

ABS: Acoustical Backscatter

ALB: Airborne Lidar Bathymetry

CRCS98: Canadian Spatial Reference System 1998

DTM: Digital Terrain Model

FOV: Field of View

FUDOTERAM: Fusion des Données Terrestres, Aéroportées et Marines

HD: High Definition

GAPD: Geiger mode Avalanche Photodiode

(d)GPS: (differential) Global Positioning System

IHO: International Hydrographic Organization

IR: Infrared

LADS: Laser Airborne Depth Sounder

LASER: Light Amplification by Stimulated Emission of Radiation

LIDAR: Light Detection and Ranging

MODIS: Moderate Resolution Imaging Spectroradiometer

NAD83: North American Datum 1983

NRCan: Natural Resources Canada

PMT: Photomultiplier Tube

PPK: Post Processed Kinematic

OBS: Optical Backscatter

OMG: Ocean Mapping Group

SHOALS: Scanning Hydrographic Operational Airborne Lidar System

TWTT: Two Way Travel Time

VDOP: Vertical Dilution Of Precision

Feature Detection: "*The ability of a system to detect features of a defined size.*" Adopted from IHO [2008].

Full sea floor search: "*A systematic method of exploring the sea floor undertaken to detect most of the features; utilising adequate detection systems, procedures and trained personnel.*" Adopted from IHO [2008].

Sub-tidal: Below mean low tide

Coastal zone: The geographic area where landward limits that penetrate the marine environment (e.g. headlands, cliffs, estuaries) and water masses are strongly influenced by each other in terms of ecology, oceanography, geomorphology, and human activity.

Inter tidal: The part of the coastal zone that falls between the low and high tide breaker line.

Waveform: Time series of the returned laser beam intensities.

A: surface spot size in m^2

E: energy in J

F_p: FOV loss factor, unit less

H: aircraft altitude in m

I: laser return intensity in digital numbers, DN

L: radiance in $W \cdot m^{-2} \cdot sr^{-1}$

N: loss factor due to tx/rx optical combination

O: offsets in x,y or z direction in m

P: power in W

R: slant range between receiver and water surface in m, or bottom reflectance in same units as P

W: weight, unit less

a: absorption coefficient in m^{-1}

a_v: vertical acceleration in m/s^2

b: scattering coefficient in m^{-1}

c: beam attenuation coefficient in m^{-1}, light speed in m/s

d: depth in m

h: wave height or height with respect to the ellipsoid in m

k_d: diffuse attenuation coefficient in m^{-1}

k_s: system attenuation coefficient in DN/m

r: laser pulse repetition rate in Hz

v: aircraft cruise speed in m/s, or normalized bottom amplitude, unit less

Λ: water suppression on signal

Δt: travel time in s

θ: laser beam off nadir angle in °, or roll in °

λ, λ_{c0}: Butterworth filter parameters, unit less, or wavelength

ϕ: air-water interface refracted laser beam off nadir angle in °, or pitch in °

ρ: data density in $\#/m^2$

φ : scanning azimuth range in °

ω_0 : single scattering albedo, unit less

CHAPTER 1 Introduction

This thesis will address bottom tracking issues, and the recognition thereof, from the SHOALS-3000 green laser beam airborne bathymetric mapping system operated above dense populated fields of Zostera marina and Laminaria sp.

Zostera marina is a seagrass that is commonly known as eelgrass, Laminaria sp. is species of the kelp family. Both types of vegetation grow in the Bay de Chaleur near the shores of Bonaventure and Paspébiac, Quebec, Canada. These shores have been mapped off- and onshore with a bathymetric lidar system, and offshore with a range of acoustic sounders. The collected data were used for this study. Zostera marina or Laminaria sp., herein after referred to as (aquatic) vegetation, can be detrimental to the lidar bottom tracking if the green laser beam reflects from mid-water vegetation, or when lidar datagaps result. Both cases will degrade the quality of the terrain model due to an unreliable estimate of the seafloor, and a decrease in and inconsistency of the sounding coverage. An uncertainty is also introduced since an incorrect sounding event remains known without aiding measurements (e.g. acoustical sounders). For survey areas such as the Bay de Chaleur, where extensive areas covered in aquatic vegetation exist, we thus need to assess the bottom tracking ability of the lidar system in aquatic vegetated regions. In addition, we need to develop a method to identify improper bottom tracking due to aquatic vegetation from the lidar data.

1.1 Problem Statement

The coastal zone is where many important seabed mapping operations take place.

Human activity such as ship traffic, fishing, and underwater construction is common near the coast. In addition, natural offshore disasters, hurricanes, storm surges, and tsunamis for instance, leave their traces behind mainly where water meets the land. For all these coastal zone issues there is a need to map both the shape and substrate of the seabed in the near shore zone. Survey areas are usually elongated along the coast and, maps need to be vertically seamless at the land/water boundaries. To fulfill these requirements, lidar is a favoured method for collection of bathymetric and topographic data (Guenther [2001]). Unlike acoustic swath bathymetry, it maintains a constant sounding density and coverage rate, irrespective of the water depth (to its limit of optical penetration) and can map sub-tidal zones, which would be unreachable with ship based surveys.

The coastal zone may be populated with (sub-tidal) vegetation growing near the seabed, but particularly floating up into the water column. This biological growth can introduce a challenge for the lidar system to correctly determine the water depth. Vegetation can act as a mask for the laser signal, either preventing it from producing a bottom return or producing a return from the vegetation (canopy). When the signal does not properly track the bottom, identifying an underwater feature from a digital terrain model (DTM) becomes unreliable. Aquatic vegetation thus introduces an uncertainty in lidar bathymetry, a phenomenon which has been recognized before by Guenther [1985], Steinvall and Koppari [1996], and Guenther et al. [2001], but assessment of the lidar bottom tracking ability in the presence of vegetation remains untouched in the literature.

Topography changes in the DTM can be recognized as vegetation with the use of

an aiding dataset: acoustic bathymetry, sediment samples, and photo or video ground truthing for example. However, it is unlikely these datasets will be available for each lidar survey. Recent applications include passive digital imagery and/or photography simultaneously collected during the lidar survey. Vegetation in digital photos may be identified either by visual inspection or with texture analysis, but only above shallow and very clear waters, where the sunlight could penetrate. Passive imagery of course requires an extra sensor and processing. Thus ideally, we would want to recognize vegetation presence with only the use of the lidar system. This work proposes a method to assess the limitations of the lidar system in terms of bottom tracking in the presence of aquatic vegetation, and to recognize these circumstances without aiding measurements.

1.2 Research Objectives

The main research objective for this work is stated as,

Bottom tracking issues and recognition thereof using the SHOALS-3000 green laser beam in dense populated fields of Zostera marina and Laminaria sp.

This objective is decomposed into two sub-objectives:

1) Bottom tracking assessment of the green laser beam in vegetated regions

2) Identification of improper bottom tracking due to aquatic vegetation presence

The first sub-objective examines the influence of aquatic vegetation on the bathymetry primarily. The influence will be investigated with ground truthing data (e.g. acoustic, underwater and aerial photography). Acoustical sounders for example will be used to track the true sediment-water surface, and that data will in turn be used as a base to assess the green laser beam bottom tracking. The result of the first sub-objective will thus

demonstrate the limitations and the relative accuracy of the lidar system in vegetated regions.

An assessment of the bottom tracking, however, is not enough. Once we have quantified the bottom tracking performance, we need to know when incorrect bottom tracking occurs. From lidar bathymetry alone it is not possible to unambiguously recognize occurrences of improper bottom tracking that resulted from the presence of vegetation. To overcome this problem a ground truthing measurement or repetitive survey would be necessary, but neither of these options are feasible. The desired product should, therefore, link improper bottom tracking with vegetation presence from lidar data only. The second sub-objective will address the use of lidar waveform data for vegetation identification.

1.3 Methodology

1.3.1 Bottom Tracking

This research involves a SHOALS-3000 bathymetric lidar manufactured by Optech, hereinafter referred to as lidar. It operates with two laser beams, an infrared and green beam, both produced coherently by the same infrared laser (using frequency doubling for the green beam) (e.g. Guenther [2001]). These two beams are reflected from a two-axis scanning mirror that distributes the laser beams as an arc shaped scan on the water surface. Due to the optical properties of the water at the infrared wavelength (1064 nm), water will act as an opaque surface. The receiver will therefore only record returned intensity of the infrared laser beam backscatter on the water surface. The green laser

beam (532 nm) can propagate through the water column as far as the optical water properties will allow. It, too, will produce a reflection on the water surface, but a portion of the emitted signal will also give a return from the bottom, or its first opaque medium. Differencing between (near vertical) travel times of the infrared laser beam surface detection and green laser beam bottom detection leads to the depth (Guenther [1985]). However, when vegetation grows in the water column, the bottom return in the green laser beam waveform may represent the canopy of the biomass and not necessarily from the bottom.

To assess the bottom tracking of the green laser beam, or more specifically, to determine whether it tracks the vegetation rather than the true bottom, we need a reference to compare it against. This reference is provided by the acoustic bathymetry, collected in the same region, though not completely overlapping all the lidar coverage. To assure a high level of vertical accuracy and to exclude the necessity for real time, or predicted, tide values, this study also includes allocating post processed kinematic (PPK) antenna solutions to the multibeam transducer face, by which we can match multibeam solutions with ellipsoid-referenced lidar solutions. Vegetation presence needs to be identified with acoustics or photo ground-truthing, but also the correct bottom needs to be determined. A comparison between these datasets explains the green laser beam bottom tracking ability.

In addition to acoustic bathymetry that is used for the assessment of correct bottom tracking; acoustic seabed and water column backscatter is used to evaluate locations where the green laser beam looses track, thus failing to return a sounding.

1.3.2 Vegetation Identification

Preliminary studies have shown that the shape and magnitude of the green laser bottom return changes due to several influencing factors (Guenther [1985], Steinvall and Koppari [1996], Tulldahl et al [2000], Wang and Philpot [2002], Dijkstra and Elston [2004]), one of which is the seabed type. We can thus characterize the waveform based on its shape or magnitude and examine a correlation with the vegetated seabed.

The waveform first needs to be classified with descriptors. Then, the influence of factors on the waveform (e.g. source level, altitude, surface waves, seabed slope, water clarity, depth) needs to be examined before we can analysis the characterized waveform in terms of seabed type. Finally, characterizing elements of each waveform will be extracted and analyzed spatially, in a plan view and through vertical sections.

The signature that aquatic vegetation leaves behind on the (characterized) green laser waveform is examined for correlations with vegetation presence, that were identified mainly with acoustical data.

1.3.3 Survey

Airborne lidar bathymetry (ALB) and ship-based acoustic data were collected in Bay de Chaleur between June 21 and July 3, 2006. The Bay de Chaleur lies between the New Brunswick northern coast and the Gaspé, a peninsula of Quebec, Figure 1.1. Survey operations took place at locations near the towns of Bonaventure and Paspébiac in very shallow waters. Water depths ranged between 1.5 and 40 metres, although the majority of the survey area had an average depth of 6 metres, and towards the coast the survey launch

(hereinafter referred to as the Heron) operated occasionally close to its navigable limits (~1.5m). The Heron was equipped with a EM3002 multibeam sonar (hereinafter referred to as multibeam), Knudsen 3.5 and 200 kHz singlebeam sonar and Knudsen 200 kHz keel mounted side scan sonar. Ship-based data were acquired with moderate speeds of 4-7 knots during a 10 day deployment. As far as the water depths allowed, 100% multibeam coverage was attempted. Mapping with such dense spacing was inefficient at extremely shallow depths (<8 m). In those cases, efforts were made to have at least full bottom sidescan coverage, i.e. lines adjoining swaths (line spacing ~80 m). An area was defined as the high density zone, referring to dense soundings of both acoustic and lidar bathymetry (Figure 1.1, box). In this area 100% multibeam coverage was achieved, and it covers five smaller scale areas, which were populated by vegetation. These designated areas were mapped with 200% multibeam coverage and mainly intended for vegetation/bottom tracking analysis. Multibeam sounding density is a function of depth, pingrate, vessel speed, swath, and number of beams. The typical inter-ping spacing is (0.17 m at 21 *Hz* pingrate and 3.5 $^{m}/_{s}$) almost equivalent to the beam footprint (0.16 m at 6 m depth with 1.5° beamwidth). The ship-based survey preceded the lidar over-flights by 1 to 12 days.

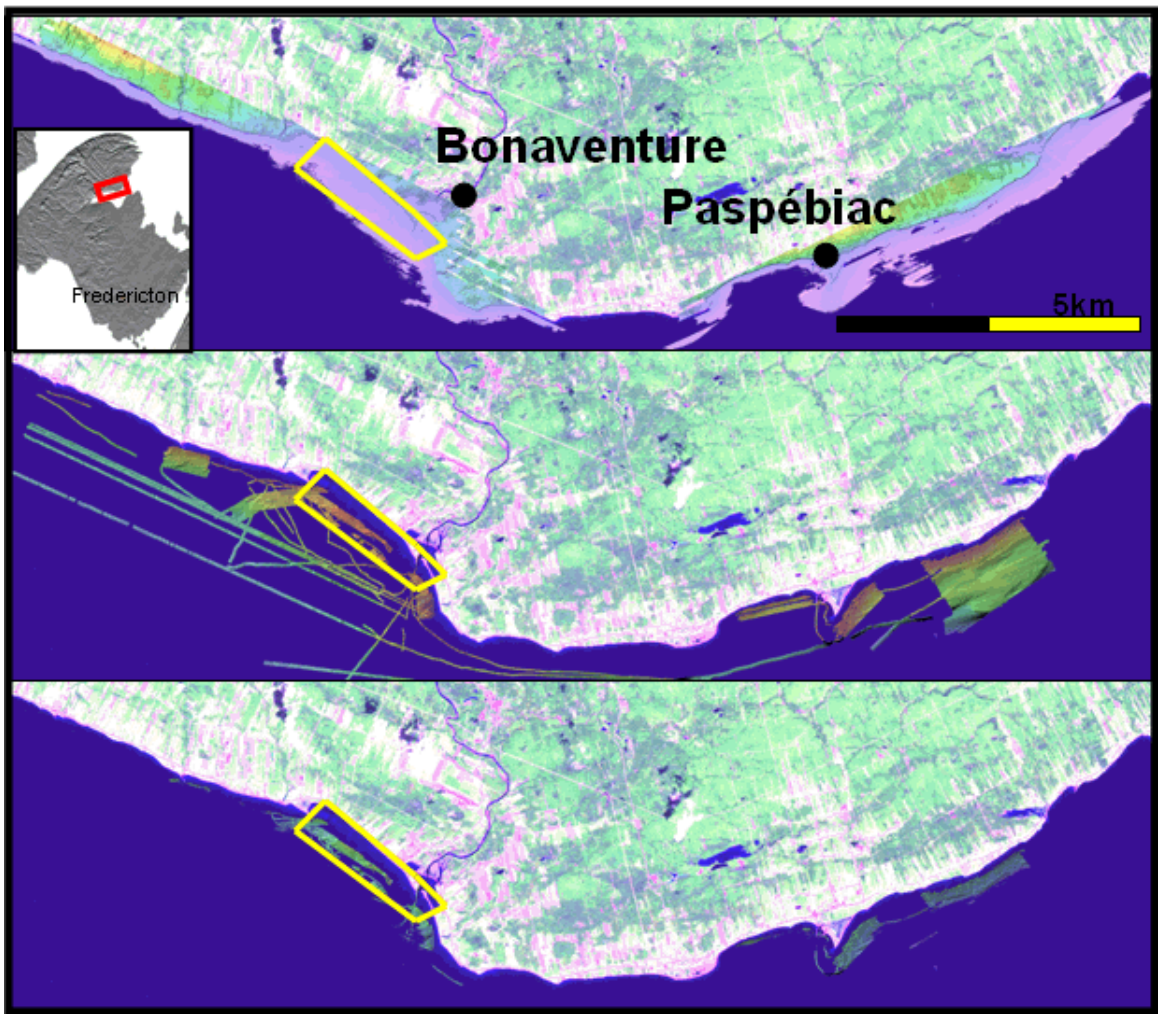

Figure 1.1 Landsat overview image of the survey area with lidar coverage (top), multibeam coverage (middle), and overlapping coverage (bottom). Bonaventure is located west where the Bonaventure river flows into the bay. The town of Paspébiac lies on the sharp elongation found easterly. The box in the upper image defines the high density zone.

The lidar coverage was largely focused on the shallow, near coastal, and land parts of the survey area. Lines with an approximate scan width of 150 m were flown above high density locations at Bonaventure and Paspébiac using ~125 m line spacing (2x2 m spot spacing) and thus overlapping 20% of the outer edges of adjacent scans. The remaining areas were mapped with a much larger scan width (275-300 m, 4x4 m spot spacing) and accordingly larger lines spacing (200 m), resulting in a near 50% overlap.

The swaths above the high density locations consisted of 85 shots along the arc, which is less than the 100 shots usually applied at other locations (Figure 1.2).

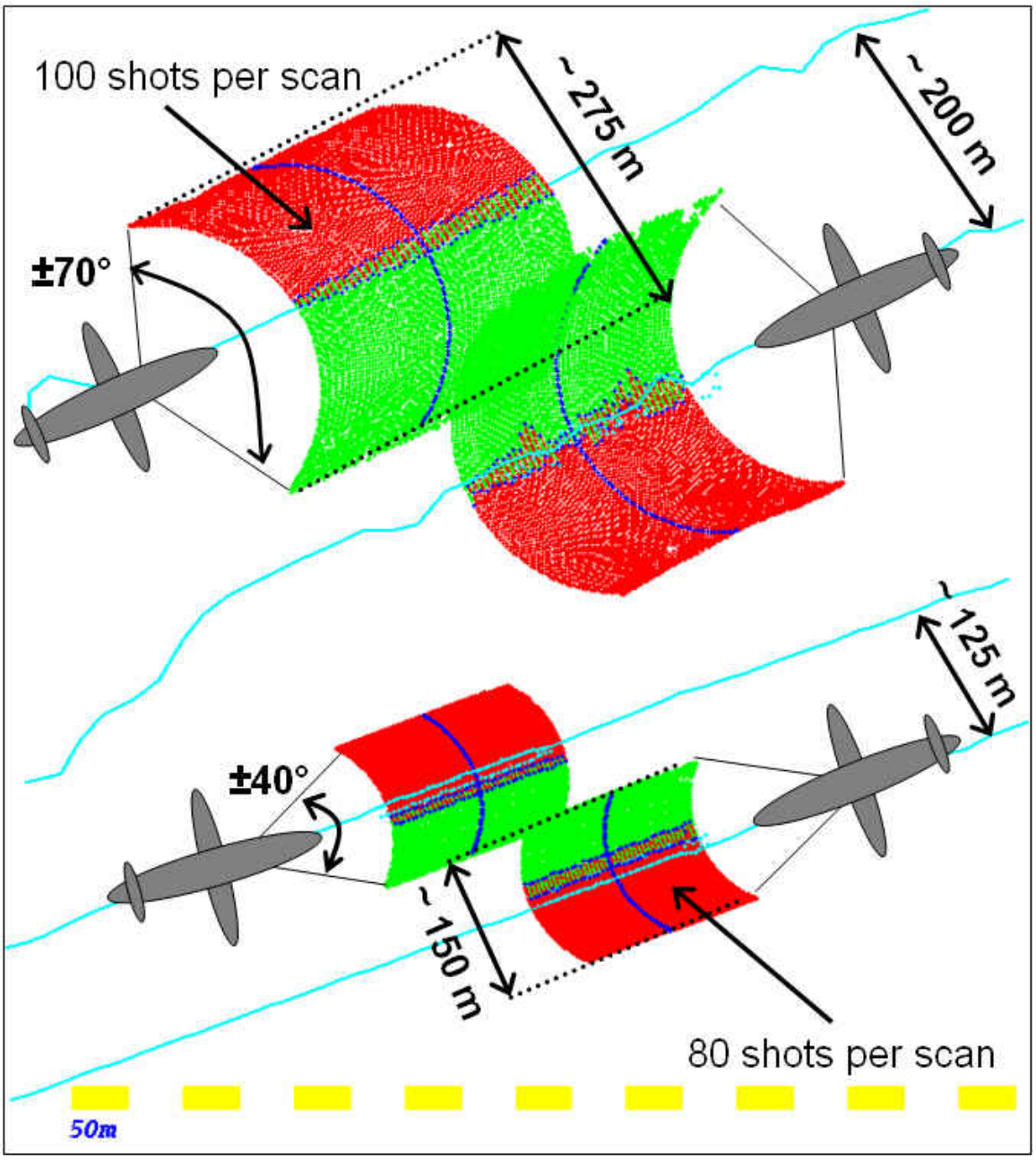

Figure 1.2 Schematic presentation of the sounding distribution when the lidar is operated with the normal (top), and high density (bottom) data collection settings. Typical aircraft altitude between 300 and 400 m, irrespective of shot distribution.

Secchi disk measurements and Optech's Ocean Scientific prediction software estimated the green laser beam maximum depth penetration between 8 and 12 metres (Feygels, [2006]). This proved to be a valid proxy. Regrettably, the boundaries of the Bonaventure high density zone were re-defined subsequent to the acoustic surveys and moved at the last minute towards the extremely shallow coast. Consequently, the multibeam and lidar coverage does not completely overlap. Multibeam and side scan coverage overlaps a small portion of these flight lines.

1.4 Contributions

This study allowed us to work with the latest version of the SHOALS bathymetric lidar and the recent EM3002 multibeam with it's novel water column imaging application: an assessment of the SHOALS-3000 bathymetric performance, or more specifically, an assessment of the bottom tracking of a bathymetric lidar system in vegetated areas, has not been published to date; neither has the bottom tracking performance of the EM3002 in vegetated areas been documented; nor the aiding water column logging application to resolve bottom tracking issues above dense vegetated seabeds. Finally, the allocation of post processed kinematic (PPK) antenna solutions to the transducer face has been done before, but for our case it required the modification of existing, and development of new, in-house software.

Wang and Philpot (2002) have generated reflectance maps from green laser waveforms, and linked regions with low reflectance to seagrass beds. The present study has similar findings although a different method for characterization is used. This method, for example, includes the derivation of water clarity from the green laser

waveforms. Water clarity values have been mapped and spatial patterns are correlated with (sub) surface infrared laser beam intensity and aerial photography.

Also, as this study included acoustic and lidar overlapping regions, the characterized waveforms are compared to acoustical backscatter mosaics. This comparison revealed that the absence of a signal return was linked to seabed substrate, inherently the presence of bottom attached vegetation, rather than depth. This is a concerning correlation as usually a non-bottom track is assumed to be below optical penetration. In this case shoal vegetated rocks could show up as gaps.

1.5 Thesis Structure

The 2nd and 3rd chapters provide the necessary theoretical background to understand the mechanisms and performance of bathymetric lidar and the involved acoustics. Chapter 2 evaluates fundamentals of lidar bathymetry, and reviews previous studies that relate to bottom tracking assessments and waveform characterization. Chapter 3 addresses the acoustics used for the ship-based survey. The acquisition and processing techniques of the acoustics are discussed, with special attention to the allocation of PPK solutions and side scan sonar processing.

Chapter 4 elaborates the algorithm to determine the waveform parameters and the derivation of the water clarity. This chapter also examines the environmental effects to the green laser waveform.

Chapter 5 discusses the results from the bottom tracking performance of both the lidar, and the multibeam. Chapter 5 will also present results from the water clarity extraction, which, although merely a by-product of the characterization process, appeared

an interesting feature to examine. Finally, chapter 5 will discuss results from the waveform characterization, with specific interest paid to regions of dense biological growth and acoustical backscatter overlap.

Chapter 6 lists the conclusions found in this work and recommendations for future work.

CHAPTER 2 Lidar Technology

This chapter serves to familiarize the reader with the bathymetric lidar principle and a few key features associated with it. The concepts discussed are addressed to the SHOALS lidar system (e.g. Guenther [1985], Guenther [2000], and Guenther [2001]). Although this work involved a SHOALS-3000, no distinction is made between older versions of SHOALS. Unless specified, the reader may assume similar techniques involved with other bathymetric lidar systems available.

Basic components of the lidar are introduced in Section **2.1**. Section **2.2** will follow with a description of the SHOALS waveforms, with most attention directed towards the green laser waveform. The geometry of the depth measurement and related issues are discussed in Section **2.3**. Water clarity introduces significant weight in the performance of any optical sensor, and for that reason a few definitions that express water clarity are reviewed in Section **2.4**. This chapter will finish by highlighting work from other researchers in this field and allied topics, Section **2.5**.

2.1 Introduction

The technique behind bathymetric lidar involves a infrared Nd:YAG (neodymium-doped yttrium aluminium garnet; Nd:$Y_3Al_5O_{12}$) laser beam. When the infrared laser beam (1064 nm) is frequency doubled; it will produce an additional laser beam with half the initial wavelength (532 nm). This new laser wavelength falls within the blue-green portion of the spectrum, but is referred to as the green laser. Both infrared and green laser beam are emitted simultaneously from the aircraft towards the sea surface. The infrared

laser beam will return on the surface, whilst the green laser beam propagates through the water column as far as the optical properties allow it to, until it either attenuates completely, or hits its first reflector, in most cases the seabed. Differencing between the elapsed time of the infrared laser beam surface return and the green laser beam bottom return laser leads to a depth approximation. The SHOALS laser scanner consists of a rotating mirror, which redirects the green and infrared lasers under a constant angle away from nadir (~ 20°), producing arc shaped swaths (Figure 2.1). Other ALB systems differ in their scanning strategies; the LADS operates with a rectilinear transverse scanning pattern and the Larsen 500 utilizes a rotary scanning strategy (Wells [1997]). The derived travel time (Δt) of the green laser beam through the water column is the measure for the depth (d) before the wave height correction:

$$d = \tfrac{1}{2} c \Delta t \cos \phi \qquad (2.1),$$

where ϕ is the refracted beam (~15°) following Snell's law, and c the speed of light through water; a value which is hardly influenced by the water properties, in contrast to the sound speed. The refraction index c(vacuum) / c(water) is about 1.34, increasing by 0.02% per ‰ of salinity, by 0.00015% per metre of depth, and by between 0.0005% and 0.0012% per °C of temperature (Wells [1997]).

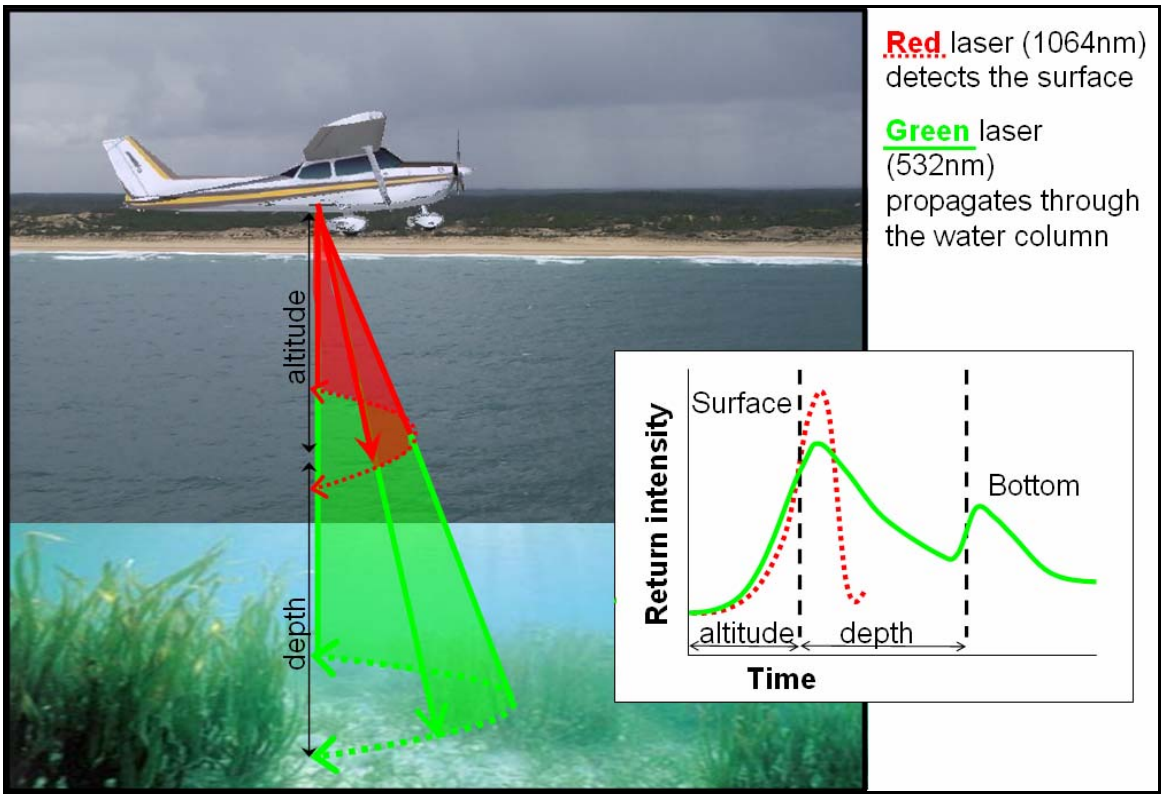

Figure 2.1 The principle of a bathymetric lidar system. It utilizes a near-infrared laser beam to determine the sea surface and a green laser beam to detect a reflector, ideally the seabed. A rotating mirror re-directs the laser, producing arc shaped swaths. The time series of a green laser beam typically shows a high peak identifying the sea surface return, and a second, usually smaller, peak as the bottom return. The returned signal decays as the range through the water column increases.

The SHOALS-3000 system emits the laser with a rate (r) of 3000 pulses per second ($\frac{\#\,scans}{s}\cdot\frac{\#\,pulses}{scan}=\frac{\#\,pulses}{s}$, Figure 2.2), which, at typical flight altitudes of 300 m and cruise speed (v) of 135 knots, is able to distribute soundings at 2x2 m spacing. The swath width depends on the altitude (H), scanning azimuth range (φ) and beam nadir angle (θ). The ultimate data density (ρ in $\#/m^2$) for a unit of time relates as

$$\rho=\frac{r}{2v\left(\sin\tfrac{1}{2}\varphi\left(\tan\theta\cdot H\right)\right)} \qquad (2.2).$$

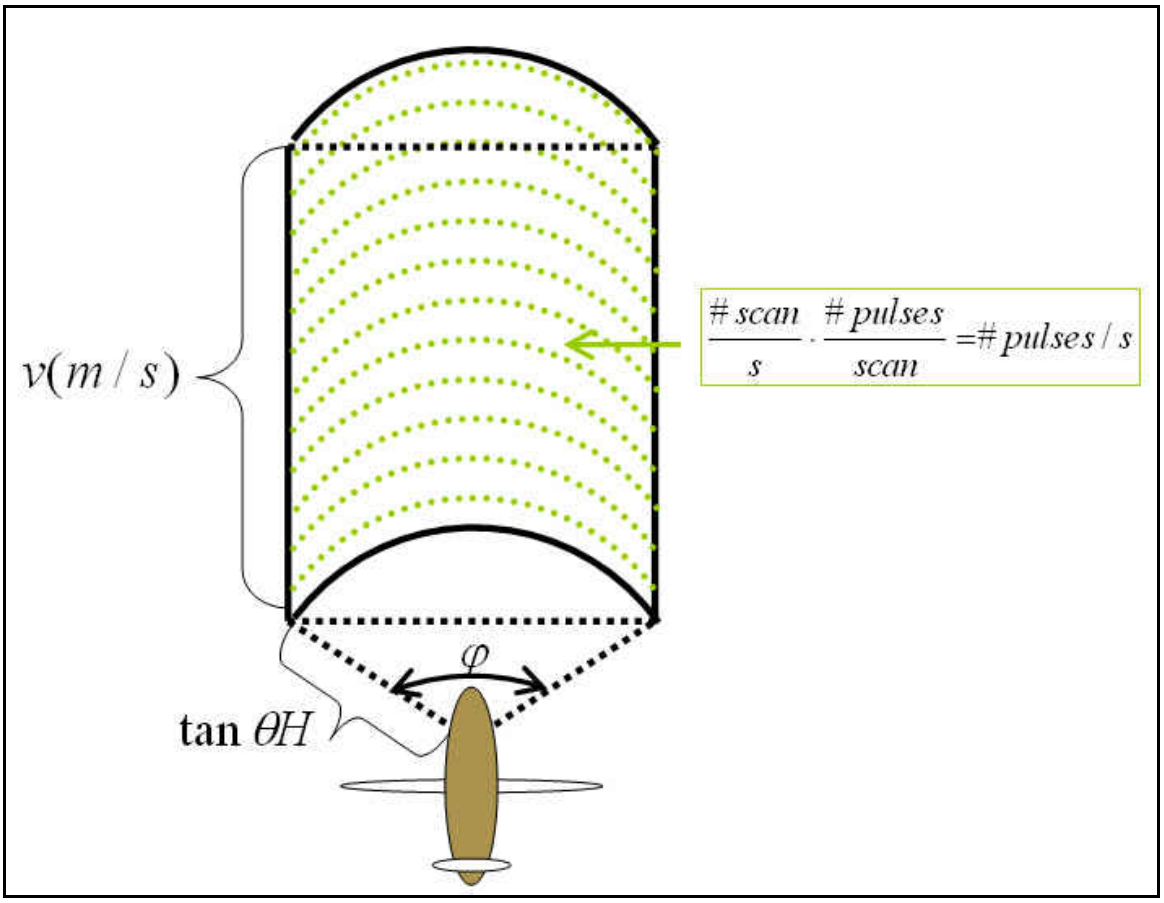

Figure 2.2 The data density for one unit of time is a function of cruise speed, altitude, beam nadir angle, scan range, and pulse rate. These variables are only limited by the system electronics, not the two way travel time. Scan rate ~38 Hz (~80 pulse per scan).

Note that the $(\sin \frac{1}{2}\varphi(\tan\theta \cdot H))$ term describes the swath width. As none of the variables of Equation 2.2 change throughout a flight line or survey since they are limited by the hardware rather than two way travel time, the survey coverage remains constant, unlike acoustics, in which the depth is the dominating factor for swath coverage and density. If the lidar footprint size remains larger than the inter-scan and inter-beam spacing, due to water clarity related reasons explained in 2.3.2, then the bottom will be fully illuminated, although with a much lower data density (expressed in soundings per area) than multibeam acoustics can achieve. However, it is emphasised that lidar and

multibeam are complementary, rather than competing systems. The systems should therefore be chosen according to the survey project. Lidar, for example, cannot meet the same data density as multibeam (from a single overpass) and full bottom search (a feature that will be demonstrated in 5.1.2), while multibeam cannot meet lidar coverage rates. For that last reason, bathymetric lidar may be preferred for shallow coastal water mapping operations.

Another reason to favour lidar above multibeam is that lidar can map the land water boundary. Although the lidar experiences difficulties in extremely shallow depths (<2 m) (Pe'eri and Philpot [2007], Yang et al. [2007]) as explained below in 2.2.1, it can provide a nearly seamless dataset. Such datasets are utilized for nautical charting, coastal modeling processes, hurricane and storm assessments, and military rapid environmental assessment surveys to name a few (Pope et al. [2002]).

2.2 SHOALS Lidar Waveforms

The SHOALS system records the waveforms of the received infrared and green laser beam returns in four channels: the infrared channel, two channels for the green laser beam at different fields of view (FOV) namely, the PMT (Photomultiplier Tubes) and GAPD (Geiger mode Avalanche Photodiode) channel, and the green excited Raman channel. The returned signal amplitudes are originally measured in linear values. These are logarithmically compressed into unsigned 8-bit digital numbers (0 - 255) to cope with the enormous dynamic range in the signal. The green laser bottom return, for example, is six to seven orders of magnitude less than the air/water interface return (Guenther [1985], Guenther et al. [2000]). The signal is digitized at 1ns intervals, this translates to a range

sampling interval of 0.115 m.

For the purpose of this work, most attention is placed on the green laser waveforms recorded with the narrowest FOV, the GAPD channel. The effect of the FOV on the waveforms is described in Section 2.3.3.

2.2.1 Green Laser Beam Waveform

The green laser beam waveform can be decomposed in three components: the surface or interface return, a volume return, and the bottom return (Figure 2.3). The leading edge of the surface return is where the signal reaches the water. Almost simultaneously, the volume return will start to rise, though with a longer rise time. The volume return rise time depends on the incident pulse shape, incident angle to the water surface, pulse width, and of course water clarity. Murky water, with an increased amount of scattering particles for example, will lead to a stronger rise time. The return signal strength of the volume backscatter decays as the travel time of the optical beam increases. This decay, or attenuation, is due to the absorption and scattering of the laser signal. Absorption reduces the energy, while scattering redirects it. The final peak in the waveform represents the bottom return, and it is this component of the waveform that will be studied explicitly in this work.

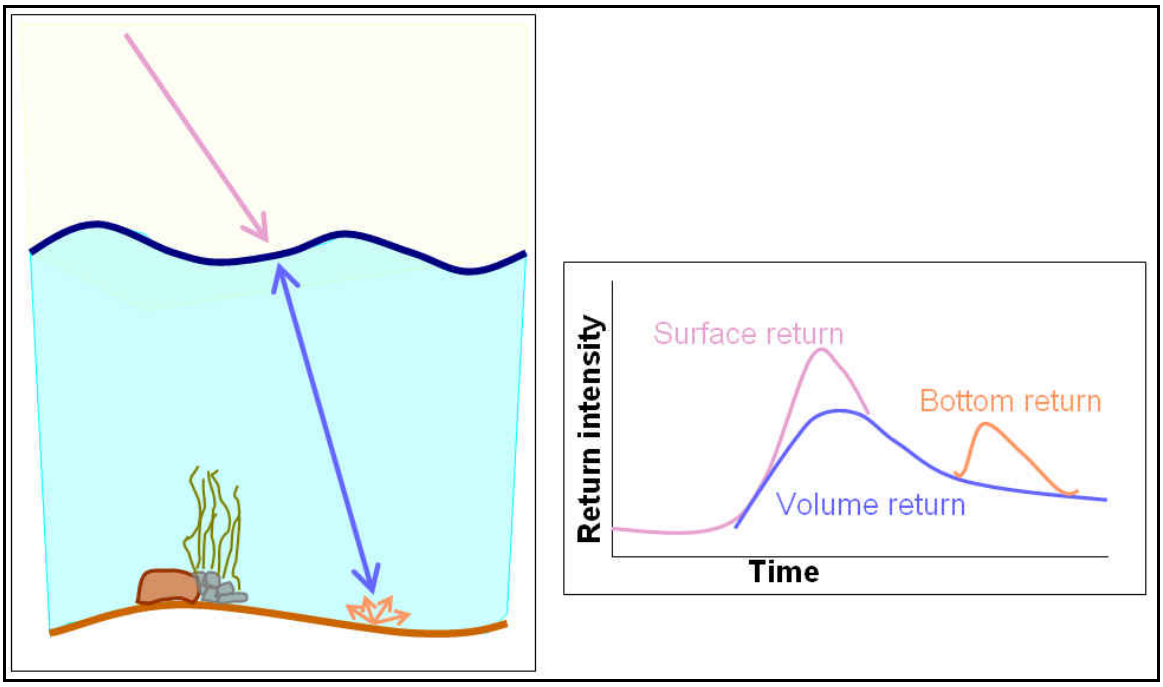

Figure 2.3 The green laser beam waveform consists of a surface, volume, and bottom return.

As the air/water interface and bottom return are distinguishable from the green laser waveform, one could argue that it is sufficient for a depth determination. Although a theoretical method with only a green laser beam does exist, lidar systems require an additional laser beam to discriminate the surface return (Guenther et al [2000]). The green laser beam is not feasible for surface detection with the SHOALS-system for several reasons explained below (Guenther et al [2000]).

In shallow water, the surface return can get swamped by a strong bottom return because the green pulse width is too long to properly separate the two from each other. In such an occurrence the waveform does not exhibit the characteristic display as depicted in Figure 2.1 (the phenomenon of bottom return swamping is also seen in our dataset). As the depth increases, this swamping would not be a problem, however, the so-called "surface uncertainty" problem exists. The surface scattering due to the beam nadir angle,

wind speed, and wave slopes varies considerably from pulse to pulse, while the volume scattering of the interface (just below the water surface) depends on water clarity and can be considered more constant from pulse to pulse. Therefore, the volume return, due to a large scattering component, may be stronger than the surface return. In other words, the volume return contributes more to the first peak in the waveform than the interface return. So the first green laser return consists of either the interface return or the volume return, but more likely somewhere in between, and for this reason introduces the surface uncertainty.

In addition to the previously mentioned surface uncertainty problem, another reason to exclude the green laser beam for the surface detection, is simply the absence of the surface return (Guenther et al. [1994]). The success of the surface return depends on sea surface topography and pulse incidence angle. Capillary waves, for example, promote a surface return, while the green laser beam through a flat trough will only produce a volume return. Thus, the volume return, which has a much longer rise time, will be mistaken for the interface return. This misinterpretation, which in fact yields a timing error, will lead to an unacceptable depth error of approximately 30 – 40 cm (Guenther et al. [1994]).

2.2.2 Infrared Laser Beam Waveform

The Jerlov curves presented in Figure 2.4 illustrate the attenuation of light at different wavelengths through changing water types (Jerlov [1976]), and they explain why infrared and green light are used for surface and water column detection, respectively. Ocean waters are more clear than coastal waters, and the curves show that

light is subject to less attenuation in these waters (Jerlov [1976]). Unfortunately, from a lidar range performance point of view, most survey work is concentrated near the coast, where wave processes suspend scattering particles in the water column. Infrared light is fully attenuated when it meets water, so a volume return, if present at all, is extremely weak (Guenther et al. [1994]). This unambiguous characteristic makes the infrared laser beam a good surface detector. However, in very clear waters and calm seastate, the infrared laser beam surface return becomes undetectably weak. Also, land water boundaries and flats flooded with a thin layer of water introduce ambiguity in the surface/water discrimination. In addition, spray from surface waves, low flying birds or mist will falsely be detected as the water surface. Under these conditions, the Raman channel incorporated in the SHOALS system provides a solution (Guenther et al. [1994], Geunther et al., [2000]).

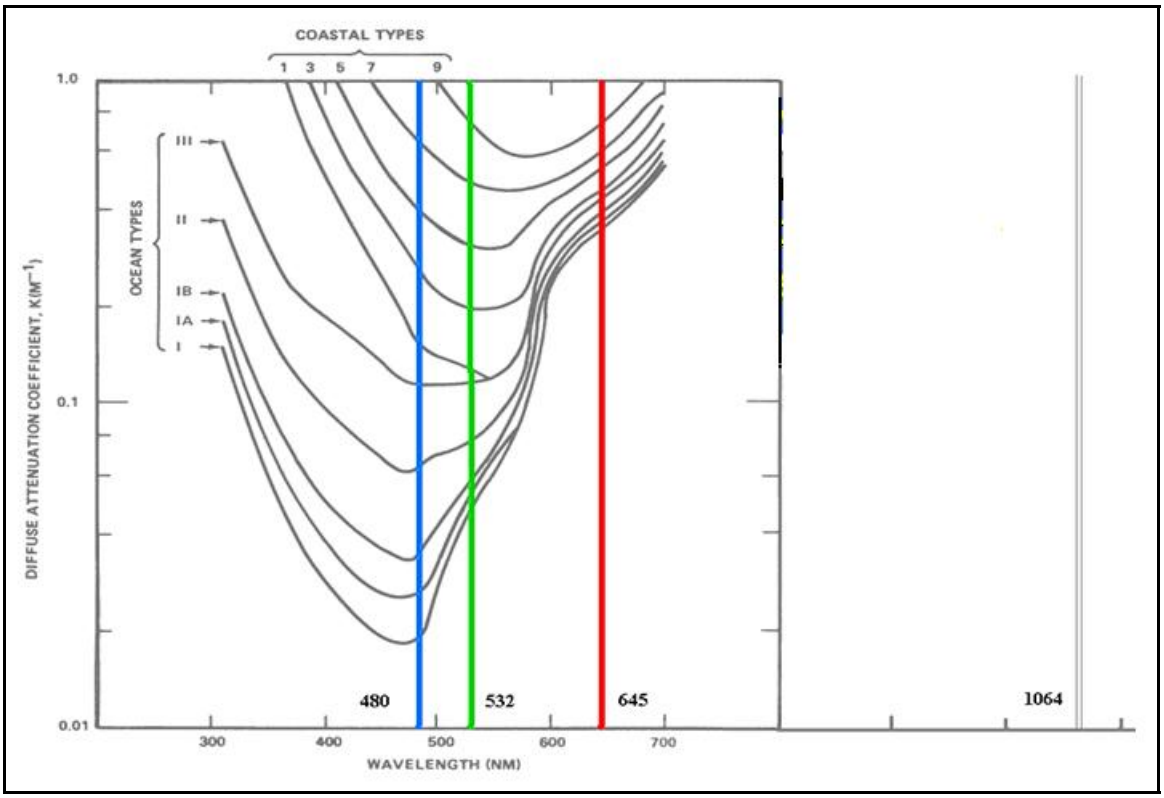

Figure 2.4 Penetration of light depends on the attenuation of its associated wavelength(s). Water near coastal locations contains more dissolved or suspended organic and inorganic material due to numerous coastal processes. As a result, coastal water types are less clear than ocean water types leading to more attenuation of light. The Jerlov curves (Jerlov [1976]) in the plot illustrate light in the blue – green spectrum (480 – 532 nm) is less attenuated than infrared (1064nm); thus, green light is more suitable to propagate through a water column. Green excited Raman (645 nm) has a high attenuation too, though it will only produce a volume return due to water or fluorescence from vegetation. In extremely shallow depths it may reflect on the seabed too. From, Jerlov [1976].

2.2.3 Raman Channel Waveform

The Raman channel records green laser energy that is re-emitted into a weak pulse of red light at 647 nm when green laser energy hits either water or vegetation. If it contacts with the O-H stretch of water molecules, a small portion of the green laser energy is re-emitted at a different wavelength, the Raman wavelength (647 nm, Guenther [1994]). A similar process happens when the green laser reacts with phytoplankton (Pe'eri and Philpot [2007]). Raman returns will only be produced when the green laser

meets a high density of water molecules; thus, it ignores haze, fog or mist unlike the infrared laser, and as the Raman return is strictly a volume return it is an unambiguous method to determine water presence. For that reason, the Raman return offers additional information when determining the land/water boundary, i.e., when the Raman return is absent, so is the water. However, without an interface return, a correction is required to shift the Raman waveform back in time and approximate the surface incidence. This correction is determined through a model, and on-the-fly calibrations with the infrared laser beam (Guenther et al. [1994]).

Not only is the infrared laser beam necessary for the Raman timing corrector, but it is also used to estimate the surface wave height. The wave height is required to correct all calculated depths with respect to mean sea level. The choice of a surface detector is based upon a logic, using, for example, the Raman channel as main surface detector, failing that, the infrared beam, and lastly the green laser beam.

In extremely shallow waters, it is possible to identify a bottom return in the Raman channel, and this will improve the minimum depth limit of the lidar system. This event was mentioned by Guenther et al. [1994], and recent work from Pe'eri and Philpot [2007] has presented such events. Also, the data collected for this work show examples of a bottom return in the Raman channel (Figure 2.5).

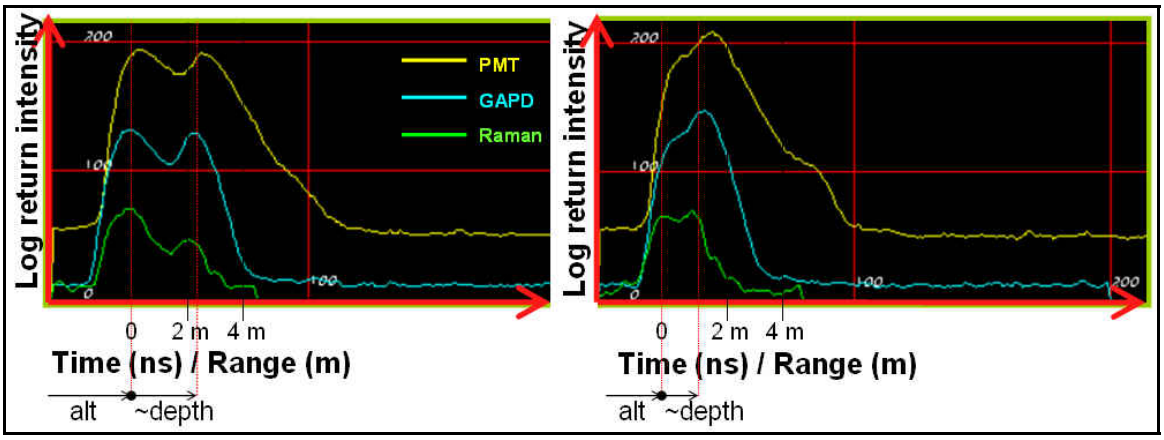

Figure 2.5 Two examples of a bottom return in the Raman waveform. The range scale is given in time and distance. It is clear that in the right image the bottom return merged together with the volume. In contrast, the Raman waveform displays a separated volume and bottom return.

2.3 Geometry

Once the surface and bottom return are located in the waveforms, the derived slant range is corrected for nadir angle, thus yielding the depth. A wave height correction is necessary to reference the depth to mean sea level. The infrared laser beam returns are saved in a buffer for the wave height correction, which is derived through a least squares estimation process (explained below in 2.3.1). When tides in the vicinity are measured (or predicted), the mean sea level depths are coupled to a local chart datum (CD). However, when the depths are referenced to the ellipsoid, for example with kinematic GPS, the need for tidal heights is bypassed. Ellipsoidal heights may then be coupled with chart datum through a local benchmark known in both vertical references. Nevertheless, the necessity for a correct air/water determination and wave height still serves a purpose: the air/water boundary is required since a portion of the green laser's beam path is through the water column; thus, a different light speed is necessary for that portion of the path. The wave height correction procedure also remains a requirement because it aids in

estimating the air/water boundary when surface returns are not detectable.

The water clarity, as mention earlier, is a dominant factor for bathymetric lidar measurements. The propagation of light through water is very different from that of acoustics. Water clarity introduces complex ray paths, which in return, introduce depth and position uncertainties. FOV considerations are also related to water clarity, but there are trade offs concerning range resolution and range performance.

The laser at both wavelengths is fired approximately 20 degrees from nadir, the vertical of the local reference frame. Rotation of the axes of the body fixed coordinate frame (roll, yaw, and pitch) is observed by the motion sensor and accounted for by the programmable rotating scanning mirror, to maintain straight swaths along the flight line.

2.3.1 Wave Height

One of the largest contributors to depth measurement biases is surface waves. Surface waves will introduce three uncertainties: 1) local height change of the water column, 2) beam steering effects, and 3) pulse stretching (Guenther [1985]). The former is the most significant. It requires a determination of the wave height, and will be discussed here. Tuldall et al. [2000] demonstrated a method to correct position errors as a result of beam steering deviation from surface slopes. Pulse stretching effects can be modeled with Monte Carlo simulations, described by Guenther [1985].

The wave height with respect to mean sea level is determined with consecutive ranges from the aircraft to the sea surface with the infrared laser beam. A SHOALS-3000 lidar can produce an approximate surface spot size of 2 m; thus, smaller wavelengths will be averaged out. Larger, wind driven waves for example, and swell, will be recognized

by the wave correction procedure, described below. Following Figure 2.6, the wave height (h) will result from,

$$R = (H - h)\sec\theta \qquad (2.3),$$

where R is the slant range between receiver and sea surface, H the carrier height with respect to mean sea level, and θ the off nadir scanning angle, corrected for roll, pitch, and yaw (Thomas and Guenther [1990]). R and θ are known for each pulse, at each shot, while H can be averaged from each scan. This method would be a valid, if the aircraft altitude would remain constant, and surface wave lengths would not exceed the swath width. Of course, in practice, this situation is not the case; the aircraft's heave motion will alter the H component, thus the heave is also captured in the h term. In addition, the mean sea level cannot truthfully be determined if a full surface wavelength does not fit over the entire number of shots on the swath.

The aircraft's heave motion (double integrated vertical acceleration, a_v, over time from t_0 to t_1 with time variables u and v) recorded by the inertial motion sensor should contribute to the H component, and a new value for H at the following occurrence (t_1) is linearly interpolated, so the corrected height between receiver and sea surface follows,

$$H_1 = H_0 + (t_1 - t_0)\dot{H}_0 + \int\int a_v\,du\,dv \qquad (2.4),$$

where $\dot{H}_0$ indicates the linear slope of H over time. Equations 2.3 and 2.4 can now be combine and rewritten as,

$$R\cos\theta - \int\int a_v\,du\,dv = H_0 + (t_1 - t_0)\dot{H}_0 - h \qquad (2.5)$$

The left argument now presents the knowns of the Equation. When this argument is

plotted against time, it will show a point cloud through which a linear line may be fitted. The slope of that line ($\dot{H}_0$) and residuals (h) are derived through a least squares fit (Thomas and Guenther [1990]). This procedure requires an amount of data to be stored in a buffer for each calculation. The buffer size is driven by aircraft speed and desired surface wavelengths.

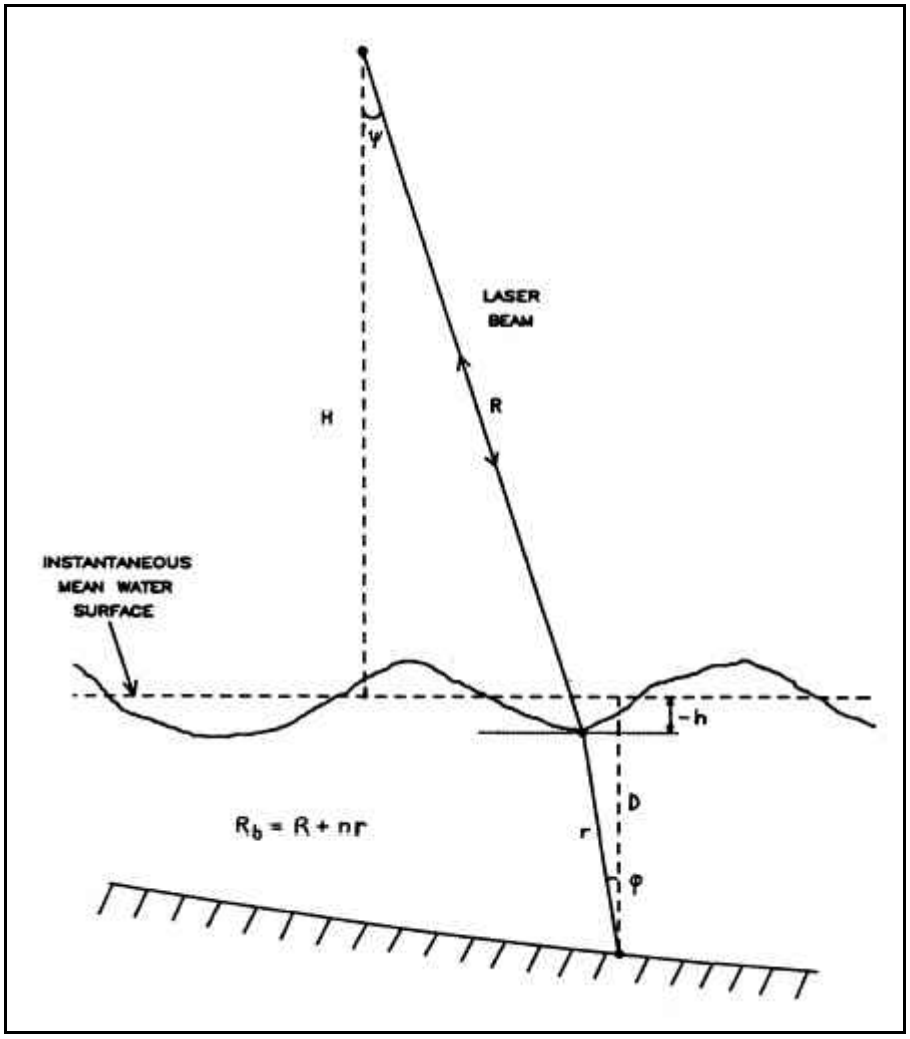

Figure 2.6 Geometry belonging to the wave height correction. From Thomas and Guenther [1990].

2.3.2 Green Laser Beam Propagation

When the green laser beam hits the water surface, it has a spot size of roughly 2 m diameter. The lidar system forces such a large spot size to ensure eye safety (Guenther et al. [2001]. Once it propagates through the water column, it will refract from 20° off nadir in air, to approximately 15° off nadir due to light speed changes, following Snell's law. The cartoon in Figure 2.7 illustrates the green laser beam propagation. The beam follows a scattered path through the water column until it reaches a reflector or the extinction depth, the so-called optical depth. If the present depth exceeds the optical depth, a bottom return will sink in the background noise and will not be detectable. The water clarity is the controlling factor for the depth range performance, of which the scattering component contributes the most to beam spreading. Beam spreading causes the light to diverge from unscattered region. The light will, similar to acoustics, radiate in all directions and thus, in theory illuminate an infinite area. The illuminated footprint is therefore, again likewise to acoustics, defined as the half power widths, or -3dB points of the laser beam (Geunther [1985], Guenther [2001]). The green laser beam footprint is of course a function of depth or range, and seabed slope, but primarily controlled by water clarity. As a rule of thumb, the footprint diameter approximates half the depth (Guenther [1985], Guenther [2001]).

Only a portion of the green laser energy (4-15%, Guenther [1985]) will be reflected upwards again with the same cone shape spreading since the water properties have not changed. Of course, this spreading does not suggest the scattered path lengths are equal too. Once the beam passes through the interface a second time, it refracts again. The surface spot size at the second passing relates to roughly $\sqrt{2}$ of the bottom diameter (Guenther [1985]). All the energy that returns to the receiver falling within the FOV will

be recorded in one of the two designated green channels (PMT and GAPD).

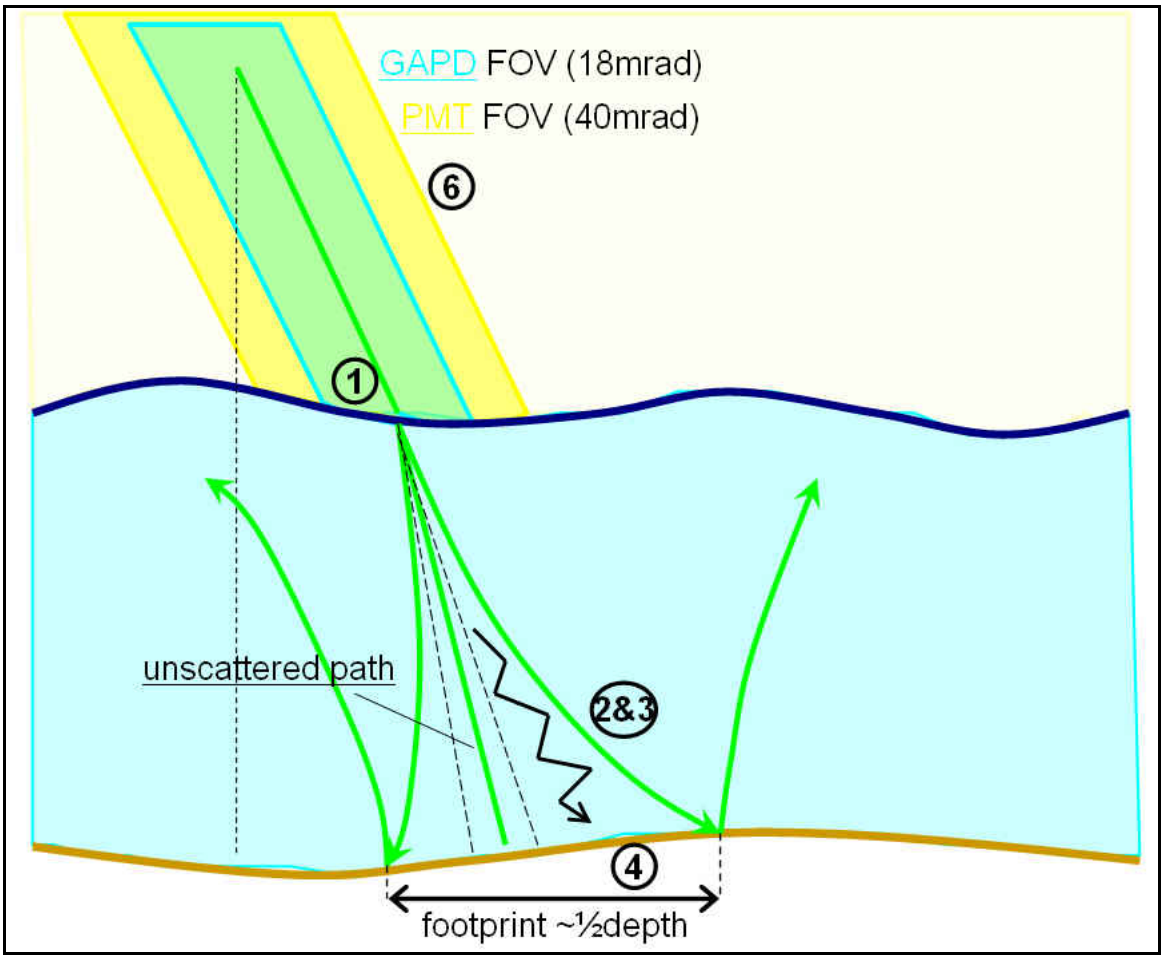

Figure 2.7 Propagation of the green laser beam through the water column. A series of processes takes place: 1) refraction of the beam at the interface, 2) beam spreading downwards due to scattering components in the water column, 3) rays follow a scattered path, 4) illumination of the seabed, 5) repetition of 3, 2, and 1 while beam travels upwards, 6) returned light falling within the FOV is recorded. Redrawn from Guenther [1985].

The shortest path of the light is not through the centre of the beam (Guenther [1985], Gunether et al. [1996a]); it lies, due to the constant 20° off nadir angle, closer to the vertical. As a result, the first arrival may be reflected from this region, and since the path is less attenuated, it will contribute to the highest portion of the bottom return. However, it can, depending on the water clarity, be subject to multiple scattering, and the

path will thus increase, in contrast to the unscattered, though longer path at the centre of the beam. Hence, an uncertainty arises as to where the leading edge of the bottom return originated from. This bias is modeled through Monte Carlo simulations and is discussed in detail by Guenther [1985]. The bottom return typically has a sharp rise, which is the result from either a shorter scattered path, located close to the vertical, or the unscattered reference path at the beam's centre. The seabed reflection is usually identified on the waveform as the 50% up the leading edge of the bottom return (Guenther [1985]).

Mid water features can be identified as the first of two consecutive bottom returns in a waveform, and subsequently the feature height above the seabed can be derived. Such a double return is only possible if the remainder of the signal can propagate towards the seabed and back (e.g. Figure 2.8). The dataset used for this work did not include any occurrences of a double return. Section 5.1 will further discuss the performance of the green laser beam above fields of aquatic vegetated.

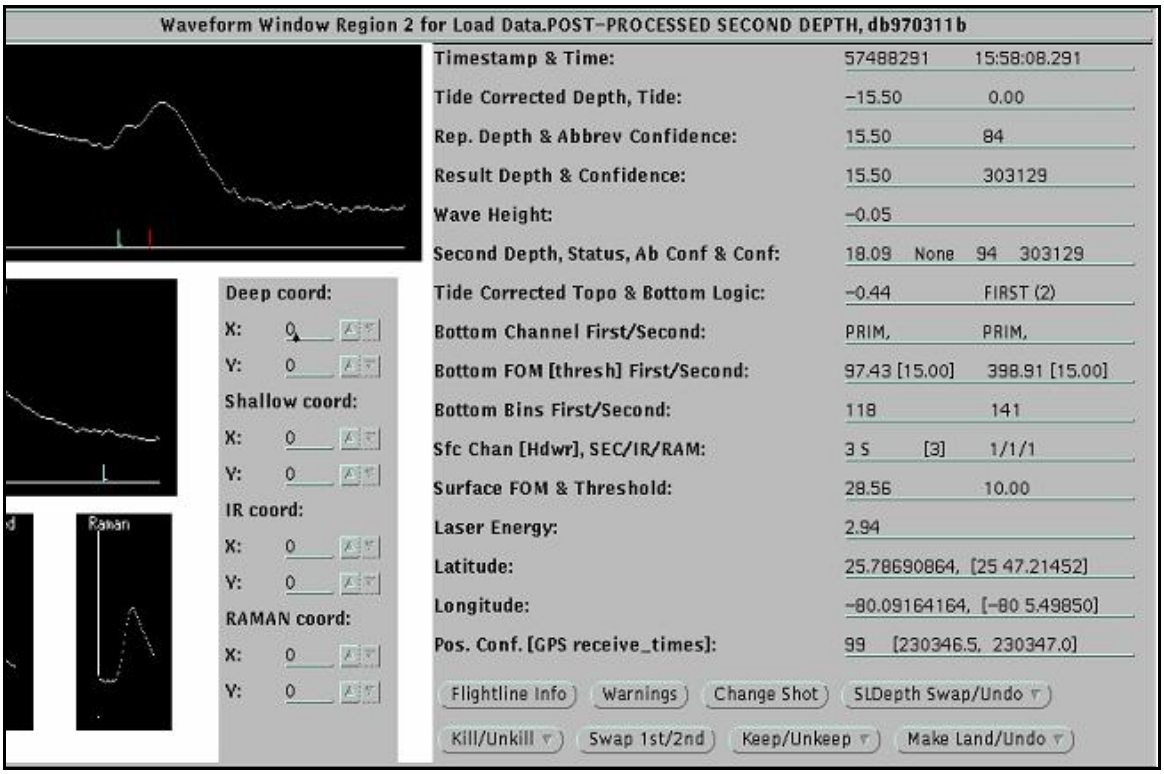

Figure 2.8 The double bottom return of the PMT channel is displayed top left. The first return was found at 15.50 metres, while the second returned was located at 18.09 metres. From Brooks et al. [1998].

2.3.3 Field Of View

The FOV can be described as the aperture angle of the receiver. It defines the area at the sea surface of incoming light that is recorded by one of the channels at the receiver. A narrower FOV allows less returned energy, and for that reason it minimizes ambient sun glint, volume, and interface scattering. Consequently, the surface and bottom return will be sharper (less stretched) which lead to an improved range resolution. In the advantage of a narrow FOV, minimizing the background noise, lies also the trade-off; a narrow FOV will show a stronger decay of the laser signal through the water column, thus limiting the range performance (Feygels et al. [2003]). The optimal FOV to use is a function of depth, water clarity, altitude, and background sunlight (Feygels and

Kopilevich [1996]). The nadir pointing angle also contributes, but since the SHOALS system operates with a constant nadir angle, this influence is of no concern for the SHOALS system.

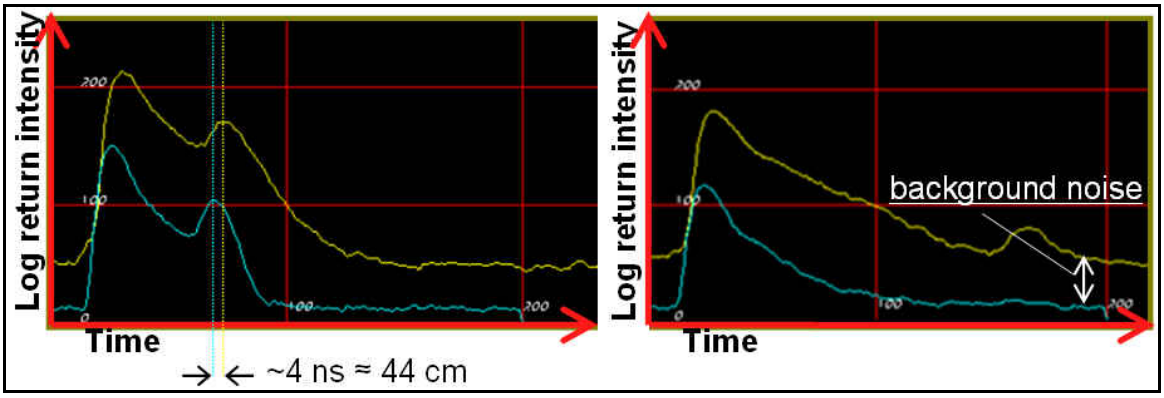

Figure 2.9 Two examples of FOV effects on the green laser waveforms: Left, peak locations misalign about 4 ns, which would lead to 44 cm range bias if the larger FOV (PMT) were used. Right, deep returns (>13 m) are not recorded in the GAPD channel. Note the larger background noise in the PMT channel, and higher return intensities.

2.3.4 Scanning Angle

The SHOALS system operates, as mentioned earlier, with a constant 20 degree angle directed away from nadir towards the aircraft's line of travel. The typical SHOALS scanning strategy distributes laser shots over an arc on the sea surface for each complete scan. At the tip of each scan, when the scanning azimuth alters direction, laser shots may pile up. The SHOALS scanning angle relates with many system variables and the performance in a complex manner. Parameters that are influenced by the scanning angle include swath width, depth biases, target detection, and dynamic range (Guenther [1985], Guenther et al. [1996a], Guenther et al. [2000]). One of the effects that need to be considered is an increased beam steering effect with increasing nadir angle (Guenther [1985]). Another variable that constrains the scanning angle are propagation-induced

depth biases occurring either near or away from nadir (Guenther [1985], Guenther et al. [2000]). Monte Carlo simulations have proven the optimal nadir angle to fall between 15 and 25 degrees.

To limit the dynamic range of interface return amplitudes (which is strongly grazing angle dependent), a scanning angle away from nadir is favourable. Moreover, strong interface reflections returning from nadir may damage the hardware. A stronger interface reflection becomes mainly a problem with a large FOV PMT receiver (Guenther et al. [2000]).

A final process to mention is small target detection (Guenther et al. [1996a]). Small targets (~1 – 1.5 m above the seabed) are best detected in the undercutting region (e.g. Figure 2.7) where path lengths are shortest and thus the range difference of receiver – target and receiver – background is optimal; i.e. large enough to discriminate target and background from each other in the waveform. For near nadir scanning angles, small target detection becomes more challenging because path lengths of receiver – background and receiver – target are nearly equal. A return away from the beams centre can result in a depth bias (i.e., measuring too deep), although it is more likely the target and background return will merge (Guenther et al. [1996a]). A strong bottom return complicates the target detection even more. Naturally, the pulse length, digitizer time bin and detector response influence target detection, as well.

2.4 Water Clarity

Previous sections have already highlighted the fundamental effect of water clarity on lidar measurements several times; a few important and potentially confusing

definitions on water clarity are therefore discussed here.

The decay of light through the watercolumn is expressed with the term *diffuse attenuation coefficient* (k_d). Light energy will decay exponentially with increasing range, this relationship is also known as the Beer-Lambert law. The water clarity signature left behind on the waveforms, however, is not the diffuse attenuation coefficient, but the *system attenuation coefficient* (k_s). The slope of the volume backscatter in the green laser waveform represents the system diffuse attenuation; thus a proxy for the attenuation of returning green laser light that travels through the water column and falls within the receiver's FOV at a certain altitude. The system attenuation coefficient, expressed in m^{-1}, holds the same exponential relationship with signal return (E_d) and traveled distance (depth or range) as the diffuse attenuation coefficient. The general form (with any attention coefficient) is:

$$E_d = E_0 e^{-2kd} \qquad (2.6).$$

From Equation 2.6, it is clear that only e^{-2} (13%) of the initial energy (E_0) remains after a depth or range equal to $\frac{1}{k}$, the so called attenuation length. It will also be clear that the penetration of the green laser beam increases with decreasing k, denoting clearer water. E_d is asymptotic to infinite depths. In reality the maximum depth is approximated with the diffuse attenuation coefficient: $d_{\max} = \frac{n}{K}$. Here n depends on solar background and sun glint. Typical daytime values lie between 3 and 4.

It is important to understand that the waveforms are logarithmically compressed. Therefore, the exponential decay described with Equation 2.6 is a linear trend in

logarithmic space. Linearization of Equation 2.6 yields

$$\ln E_d = \ln E_0 - 2kd \qquad (2.7).$$

Thus a linear regression to the attenuation curve in logarithmic space yields k_s. While the waveform intensities are expressed with signed 8-bit digital numbers (DN), the attenuation coefficients is presented in DN/m. Chapter 4.3 will continue on the derivation of the system attenuation coefficient from the waveforms and resulting water clarity maps.

The ***diffuse*** or ***system*** attenuation coefficient should not be confused with the ***beam*** attenuation coefficient (c), which is the sum of the absorption (a) and scattering coefficients (b). Beam, diffuse, and system attenuation coefficient describe the water clarity and hold interrelationships as explained by various researchers (e.g. Duntley [1962], Gordon [1982], Guenther [1985], Mobley [1994]). The beam, diffuse and system attenuation coefficients are all "spectral" descriptors of water clarity; meaning that they describe the water clarity as a function of wavelength. They differ in the optical class they belong to; the beam attenuation coefficient is an inherent optical property of water (IOP), while the system and diffuse attenuation coefficient are an apparent optical property of water (AOP).

IOP's depend on the medium the light travels through, but are independent of the light within that medium, absorption and scattering coefficients for example. AOP's depend upon the medium and on the direction of traveled light, reflectance for example (Mobley [1994]). The attenuation of the *directed* green laser beam as a function of *range* is thus an apparent optical property.

Two other descriptions of water clarity are Secchi disk measurements and albedo

(IOP) (Mobley [1994]). The former involves a disk (~30 cm diameter) partitioned in four black or white painted sectors. The disk is lowered into the water to a depth at which black and white quarters cannot be discriminated from each other; it has then reached the so called "Secchi depth". It is clear that due to wave motion, sun light, and the observers' judgment, Secchi disk measurements are very disputable, but they may serve as a rough approximation for water clarity. A common proxy for lidar penetration lies between 2 and 3 times the Secchi depth. Prior to, and during the lidar flights, Secchi disk measurements were collected. These were included, among other water clarity terms such as k_s, for a water clarity comparison (Section 5.2).

The albedo coefficient (ω_0) describes the scattering influence on the water clarity. It is the ratio between beam attenuation coefficient and its scattering component:

$$\omega_0 = \frac{b}{c} \qquad (2.8).$$

Recall c being described earlier as the sum of a and b, thus, as ω_0 approaches 1.0 the scattering contribution increases.

2.5 Previous Work

This section reviews experiences and findings from lidar users and researchers done prior to this study. The section addresses according to the two main parts of the research: bottom tracking associated references, and characterization related references. The former is discussed in section 2.5.1, the later in section 2.5.2.

2.5.1 Lidar Ground Truth

A comparison between bathymetric lidar and acoustic surveys, which is one of the by-products of this work, is not new: previous work from Hare [1994], Riley [1995], Guenther et al. [1996b], LaRocque et al. [2004], Optech Inc. [2004], and Lockhart et al. [2005] for example, investigated or discussed the accuracy discrepancies of both sounding systems. Most likely, more such evaluations have been carried out periodically, to validate the sounding performance or calibrate the lidar system, but were not made publicly available. However, this section briefly reviews the previously mentioned work to establish a benchmark for typical, acoustic versus optical, error margins. The general consensus among all the assessments was that acoustics achieve a finer horizontal and vertical resolution, mainly due to their much smaller beam footprints. For that reason, the acoustics act as a reference. Thus once again it is recognized that lidar bathymetry cannot replace acoustics in terms of resolution, but can be efficient to utilize as complement to acoustic surveys.

Bathymetric lidar surveys are commonly aimed to achieve IHO Order 1 specifications. Table 2.1 lists IHO Order 1 specifications of the 4th edition (IHO [1998]). Recently (February 2008) and updated version of IHO specifications for hydrographic surveying has become official. The updated IHO Order 1 specifications (5th edition) are divided into Order "1a where a full sea floor search is required and 1b where it is not required" (IHO, [2008]). Order 1b includes a special requirement for bathymetric lidar spot spacing (5 x 5 m) and has no requirements for "Feature Detection" (an explicit definition replacing the term Target Detection from the 4th edition). The Depth and Horizontal accuracies (or uncertainties as referred to in the 5th edition) remained the

same, Table 2.2

Table 2.1 IHO Order 1 specifications 4th edtion. Depth and Horizontal accuracy in m at 95 % confidence level. After: IHO [1998]

Depth accuracy (95%)	$\pm\sqrt{0.5^2 + 0.013d^2}$
Horizontal accuracy (95%)	5m + 5% depth
Target detection	2x2x2 m

Table 2.2 IHO Order 1 specifications 5th edition. Depth and Horizontal accuracy in m at 95 % confidence level. After: IHO [2008]

Depth accuracy (95%)	$\pm\sqrt{0.5^2 + 0.013d^2}$
Horizontal accuracy (95%)	5m + 5% depth
Feature detection	Not Apllicable
Spot spacing	5 x 5 m

Lockhart et al. (2005) describes an acceptance test including a SHOALS1000T and Reson8101 multibeam. The assessment involved a lidar dataset processed with kinematic GPS or dGPS plus observed tides. In addition, the evaluation involved datasets collected at different spot spacing (2x2 m to 4x4 m). The depth discrepancies observed were smallest for dGPS and observed tides and at the finest grid size: mean depth difference 0.070 m with 0.189 m standard deviation. However, these values increased dramatically when a wreck was included in the dataset: mean depth difference 0.352 m, 1.486 m standard deviation. A target detection assessment was also included; the lidar was not able to accurately resolve sharp objects on the seabed. In other cases, the lidar tended to measure shallower than the multibeam.

The assessment by LaRocque et al. (2004) and Optech (2004) involved SHOALS1000T, and EM1002 and EM3000 multibeam, and side scan sonar data. Mean depth differences varied, ranging from 1.24 cm with 20.87 cm standard deviation to 22.71 cm with 15.81 cm standard deviation. There was no trend between accuracy and

increasing depth. Horizontal and depth accuracies were met with IHO order 1, and 2 m cubic features, planted prior to the survey on the seabed, were resolved.

Riley (1995) and Guenther et al. (1996b) discuss the comparison between SHOALS-200 and singlebeam (Raytheon 100 kHz) and side scan sonar surveys. Their results revealed a mean depth difference of 0.07 m with 0.20 m standard deviation.

Results from Hare (1994) include a LARSEN-500, which operates at a 35 m spot spacing (Banic et al. [1986]), and singlebeam. Average depth differences (acoustic-lidar) are much greater than mentioned above: between -0.72 m with 0.51 m standard deviation, and +0.18 m with 0.24 m standard deviation.

It may seem attractive to compare the results of all these separate assessments with each other to judge different bathymetric lidar systems, however, as they involve different systems and or configurations, and were operated with different environmentally conditions (e.g. water clarity, depth, topography, seabed type) doing so is not justifiable. Table 2.3 summarizes the depth accuracy achievements.

Table 2.3 Mean depth differences ($\Delta\bar{d}$) and standard deviation ($\sigma_{\Delta d}$) of acoustic and lidar depth comparisons. Derived from Lockhart et al. [2005], LaRocque et al. [2004], Optech Inc. [2004], Riley [1995], Guenther et al. [1996b], and Hare [1994].

	$\Delta\bar{d}$ (cm)	$\sigma_{\Delta d}$ (cm)	Acoustic reference
SHOALS1000T	7.0	18.90	Multibeam; Reson8101
SHOALS1000T	1.24 – 22.71	20.87 – 15.81	Multibeam; EM1003, EM3000
SHOALS200	7.0	20.0	Singlebeam; Raytheon 100kHz
LARSEN500	-72.0 – +18.0	51.0 – 24.0	Singlebeam; unspecified

An assessment of the SHOALS-3000 is not published yet, although the achievable depth accuracy should lie within 50.0 cm 2σ (Optech Inc. [2006]). Research on lidar accuracy has had specific attention on the detection of small navigation hazards (~2 – 1 m), and improvements to limit object detection failure (Guenther. [2001], Guenther et al [1996a], Steinvall [1996]). The detection of aquatic vegetation, inherently failure of the bottom tracking, and a practical assessment thereof has not been commented upon. However, Wang [2005] studied the induced bias from sea grass on the waveforms, revealed through Monte Carlo simulations. These simulations predicted sea grass presence not to "significantly alter the lidar determination of bottom depth" (Wang [2005], page 68). Depth biases depended mainly on sea grass density and leaves, or water current angle. With extreme values of these variables, the resulting bias was not greater than 11.25 cm.

2.5.2 Waveform Characterization

Several researchers have demonstrated that the shape and magnitude of the bottom return changes due to a list of factors (e.g. Guenther [1985], Steinvall et al. [1996], Wang and Philpot [2002], Dijkstra et al. [2004]). We can categorize these factors as system dependent, or as environmental dependant. The former may be assumed constant through each survey line, and maybe even for each independent lidar system. Examples of system factors that influence the bottom return include beam nadir angle, source pulse, and FOV. Environmental factors are spatially and temporally variable. Known environmental factors are surface waves, water clarity, depth, seabed slope, and

bottom type.

It will be clear that when possible to correct the waveform for the majority of the (variable) environmental factors other than bottom type, any significant change in bottom return, could indicate a different bottom composition. Several promising results in this direction have been published (Wang and Philpot [2002], Lee and Tuell [2003], Dijkstra and Elston. [2004], Wang [2005]). However, one will always need to couple the characterized data with ground truthing data (e.g. acoustics, aerial or submerged photo mosaics, sample cores, or grabs) to actually classify the bottom material. Characterization is thus not equivalent to classification.

The bottom return power (P_{Rx}) is described as

$$P_{Rx} = \frac{P_{Tx} N R F_p A \cos^2 \theta}{\pi (n_w H + d)^2} e^{-2\Lambda K d \sec \phi} \tag{2.9}$$

(Guenther [1985]), where P_{Tx} is the transmitted power, N losses due to transmission/reception optical combination, R bottom reflectance, F_p FOV loss factor, A surface spot size, θ off nadir angle, n_w air/water refraction index, H altitude above air/water interface, d depth, Λ water suppression on signal due to temporal dispersion, K attenuation coefficient, and ϕ the refracted green laser beam nadir angle. Wang and Philpot [2002] simplified Equation 2.9 by combining all the environmental variables into a single term (W) ,

$$P_{Rx} = W P_{Tx} \widetilde{R} \cdot e^{-2Kd} \tag{2.10}.$$

Note that the contribution of d in the denominator of Equation 2.9 is negligible, since

H is always much greater. Inversion of Equation 2.9 yields an estimate for the reflectance or pseudo-reflectance ($\widetilde{R}$). Although the work assumed homogenous water clarity, and ignored incident laser angle, seabed slope effects, and surface waves, their pseudo-reflectance maps showed correlation with aerial photography and sea grass maps.

In addition, Wang's [2005] work focused on the Raman channel, introducing a ratio that describes the contrast between pseudo-reflectance and fluorescence coefficient. The index should discriminate between living (e.g. sea grass) and non-living material (sand or mud).

Work from Lee and Tuell [2003] followed a similar strategy; again Equation 2.9 was simplified,

$$v = \widetilde{\mathrm{R}}\mathrm{e}^{-2Kd} \qquad (2.11),$$

while v now presents the "normalized bottom amplitude", derived from P_{Rx} and P_{Tx}. First K was solved iteratively through least squares and then used to solve the pseudo-reflectance. Also, this study was based on the assumption of homogenous water properties.

The pseudo-reflectance found its way into sensor fusion projects with hyperspectral data. Tuell et al. [e.g. 2004, 2005a, 2005b] use the depths and pseudo-reflectance from the SHOALS, along with surface radiance ($L_\lambda^{surface}$), measured by a CASI-2 spectrometer, to estimate the bottom (L_λ^{bottom}) and water column radiance (L_λ^{water}), and upwelling diffuse attenuation coefficient. First, pseudo-reflectance images are used to locate homogenous reflectance areas. Then, data from these locations (depth and surface radiance) are used to solve Equation 2.12 with a least squares process, resulting in

estimates of bottom and water column radiance, and upwelling diffuse attenuation coefficient (k_λ) for each of the selected areas. A final interpolation yields bottom and water column radiance and diffuse attenuation coefficient images or contour maps.

$$L_\lambda^{surface} = L_\lambda^{bottom} e^{-k_\lambda d} + L_\lambda^{water} \quad (2.12)$$

Segmentation and characterization of green waveforms have been done with success by Elston and Dijkstra (Elston and Dijkstra [2004], Dijkstra and Elston [2004]). Elston and Dijkstra [2004] presented a procedure that extracts the bottom return amplitude and width directly from a waveform and uses these to constrain a curve fitting approach based on a gamma-distribution function. Dijkstra and Elston [2004] continued by adjusting for a PMT/GAPD misalignment and resolved detrended peak power estimates to correct for different water masses. Although their results did not account for seabed slope, or incorporate ground truthing data, regions with different reflectance values were recognized.

The pseudo-reflectance in our work includes the seabed optical backscatter and all other terms that were assumed constant, including the transmitted energy (P_{Tx}) and terms mentioned by Wang and Philpot [2002]. The original lidar equation is then simplified to

$$P_{Rx} = \widetilde{\mathrm{R}}\mathrm{e}^{-2Kd} \quad (2.13).$$

With the waveform data being logarithmically compressed, the water clarity related term becomes merely an additive. The pseudo-reflectance, or bottom return height as referred to in this work, will then follow from linearization of Equation 2.13 to

$$\ln \widetilde{R} = \ln P_{Rx} - 2k_s d \quad (2.14),$$

where k_s is the slope of the attenuation curve on the waveform expressed in positive units (Figure 2.10). In logarithmic space, the bottom return height is clearly an additive to the extrapolated attenuation curve. By measuring the excess over the attenuation curve, our pseudo-reflectance is instantly corrected for water clarity and the gross depth effect. As indicated above, the depth component with respect to the flight altitude is negligible, especially at the small depth ranges found in our survey. Therefore, depth changes will not contribute significantly to spherical spreading or the delimiting behaviour of the FOV at increasing depths. Figure 2.11 depicts waveforms from overlapping locations waveforms (same depth and seabed) from two datasets that were collected approximately a day apart. At both waveform sets the height of the bottom return with respect to the attenuation curve runs nearly parallel, illustrating hardly any depth contribution (Figure 2.11 top). Although both series were collected at different water masses (note the different surface returns and attenuation slopes), once detrended, the bottom return heights are the same. A slight bottom return height decrease is seen at depths beyond 7 m, which was for the most part noticeable in the GAPD channel. Possibly at these depths, the PMT channel is preferred by the bottom detection algorithm for depth measurements.

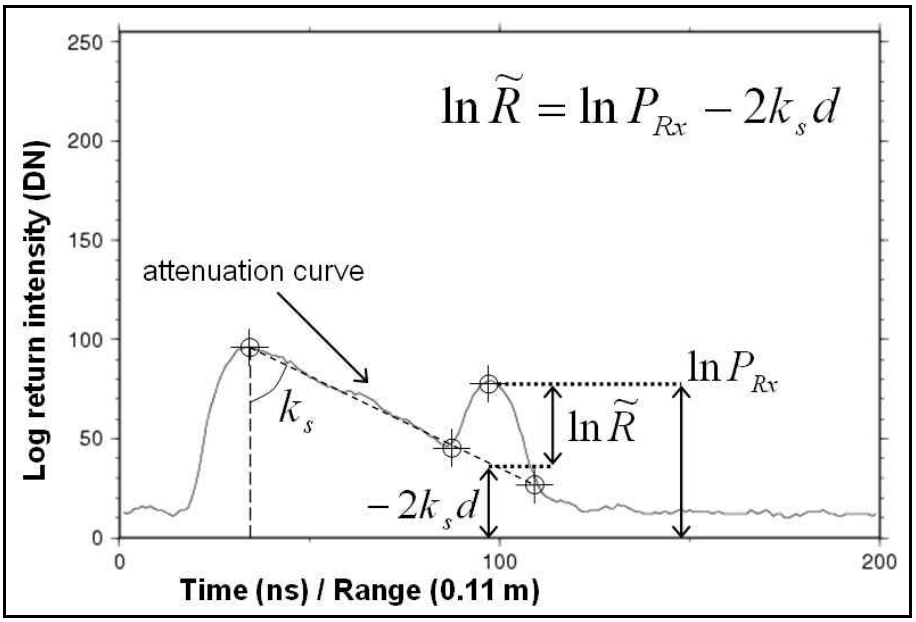

Figure 2.10 By measuring the reflectance, or bottom return height, relative to the extrapolated attenuation curve, water clarity and depth terms are bypassed. Note that the depth term is actually expressed as a time range. A 1 ns range translates to approximately 0.11 m.

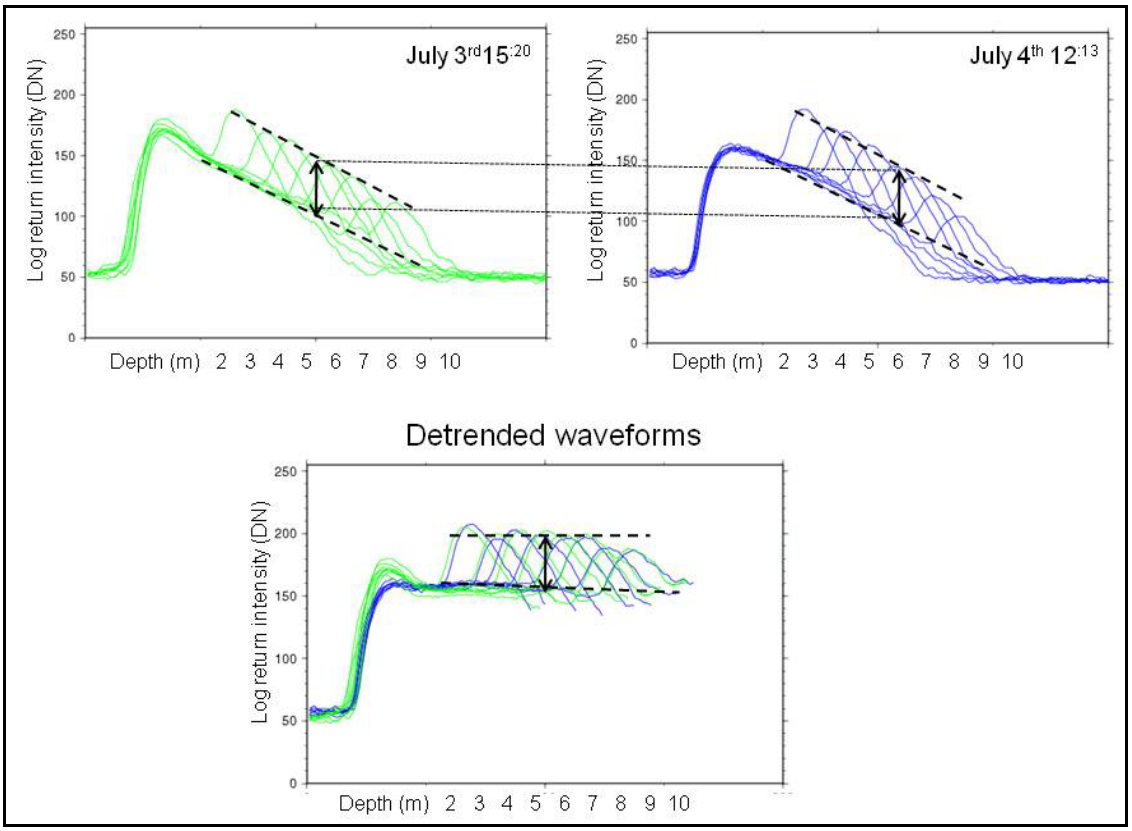

Figure 2.11 PMT waveforms at consecutive depths from overlapping locations. The bottom return height w.r.t. the attenuation curve nearly changes with increasing depth or between different water masses. Waveforms are detrended with the linear slope of the volume return in logarithmic space.

CHAPTER 3 Acoustic Technology

Ship-based surveys were executed with the 11 m survey launch the Heron. She was equipped with acoustic systems operated at various frequencies, and with aiding equipment such as a motion sensor, positioning system, and a sound speed sensor. Swath bathymetry was collected with a hull mounted Simrad EM3002 multibeam. In addition, it measured seabed acoustical backscatter and watercolumn acoustic imaging. Singlebeam data were collected with two Knudsen singlebeam sounders, and keel-mounted Knudsen sidescan staves were utilized for bottom backscatter data. The Knudsen recoding channel was shared between the 200 kHz singlebeam sounders and one of the sidescans; therefore, both instruments could not operate simultaneously. Figure 3.1 depicts the vessel's hull with transducer configuration.

Multibeam features and processing will be discussed in Section **3.1**. Section **3.2** covers all Knudsen instruments.

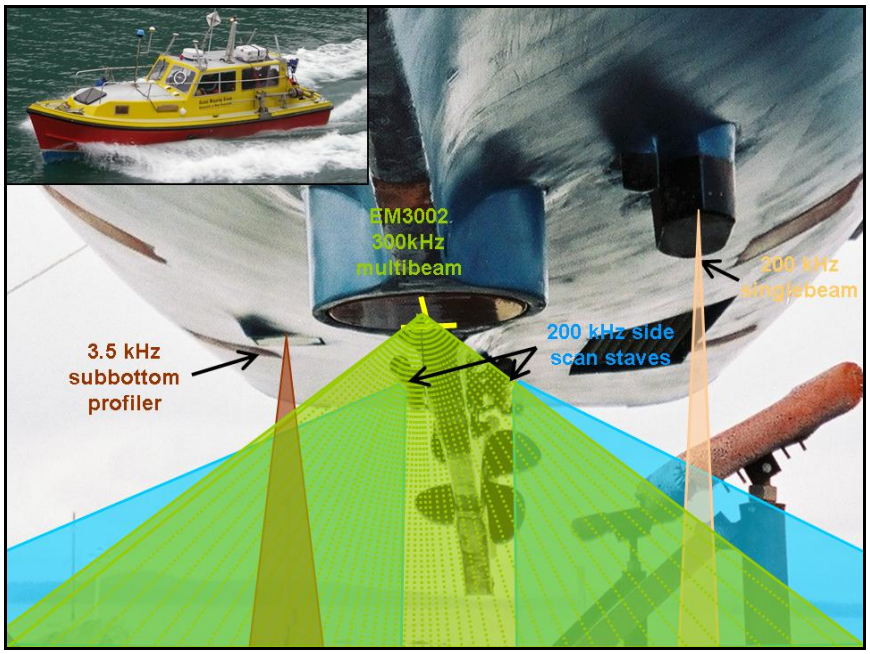

Figure 3.1 Hull of the CSL Heron with the transducer configuration.

3.1 Multibeam

3.1.1 Acquisition and Processing

The EM3002 on the Heron, is an upgraded version of the previously mounted EM3000 and operates at 300 kHz. It is single sector type multibeam; thus, it cannot actively stabilize for yaw motion. However, it does electronically correct for roll and pitch motion, ensuring unperturbed swaths in along and across track directions.

Receive beams are pointed obliquely to ±65°, creating a swath on which the multibeam projects 164 physical beams. Through the so called High Definition mode, several returns from a physical beam (upon which phase detection is applied) are used, enhancing the number of solutions to 256. The physical beams near nadir, where amplitude detections are used, are spaced equi-angularly apart, resulting in 0.8° spacing. However, within the outer beams, thus usually in the phase detection region, multiple solutions are obtained, resulting in an equidistant spacing of depth estimates. The product of transmit and receive beams near nadir have a width of 1.5°, across and along track, but grow as the across track beams are pointed obliquely. The swaths are fired at a typical rate of 21 Hz (at depths <11 m). The acoustic pulse length is 0.15 ms.

The Mills cross type array geometry is configured in a tablet shaped housing. As a result of the small array length, though high frequency, the nearfield lies within 3 m, which exceeds the minimum depths found in the survey area. Dynamic focusing prevents the relatively large nearfield from introducing range errors.

Multibeam data were acquired and controlled through Simrad software (SIS). The

acquisition software also interfaced dGPS positioning (CNAV) and attitude sensing from an Octopus F-180 motion senor that includes a pair of kinematic GPS receivers, and three gyros and accelerometers. Sound speed profiles were measured with a free falling probe (MVP30), trailed behind the vessel. Due to the extremely shallow depths and presence of lobster pots, the probe was not operated continuously. Dips were made at strategic points in time and space, and these proved the water column to be stratified, i.e.; the top layer of the water column was significantly warmed up by solar heating. As a result, the sound speed profile was temperature dominated.

The sound velocity profiles were applied during the processing based on their location and/or measurement time in order to simulate the local sound speed as well as possible. In addition, empirical sound speed profiles were derived when the bathymetric data showed refraction issues.

All data were processed with OMG swathed software. For bathymetric data, this processing mainly includes reformatting the Simrad files into an OMG-file format, applying time delays, applying either real time, interpolated, or empirically derived sound speed profiles, applying Post Processed Kinematic (PPK) antenna heights, manual bathymetric data cleaning, and generating DTM's. Since the use of PPK is a relatively novel feature to the OMG and the author, the processing steps will be discussed in the following section. Section 5.1.2 describes the creation of multibeam and lidar DTM's.

3.1.2 PPK Processing

The PPK processing involved base stations at Caplan and Bonaventure, and rover data (Heron CNav dGPS antenna positions). GPS base station data at Caplan

(M02K1000) were collected and maintained by the Quebec authorities. A temporary base station was set up during the survey at Bonaventure. Stations were positioned 14 km apart; surveys in the Paspébiac vicinity were furthest from any base station (Figure 3.2).

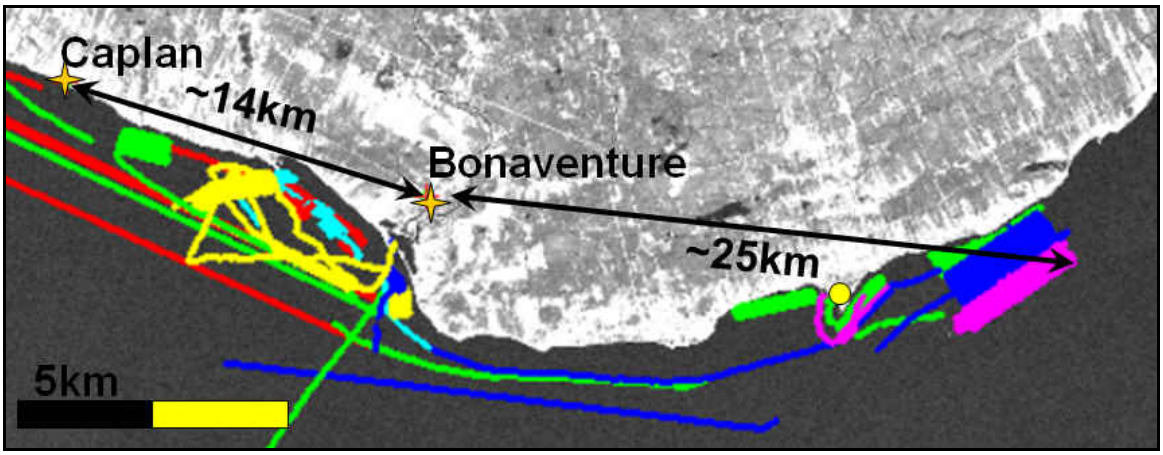

Figure 3.2 Data from a permanent base station, located at Caplan, and a temporal base station at Bonaventure were used for the PPK processing. Heron navigation tracks are color coded per survey day. Predicted tide time series were derived for the Paspebiac harbour, in the figure marked with the yellow dot.

All data files were converted into the generic Rinex format and processed using Trimble Geomatics Office (TGO v1.63) software. Comparisons between heights processed with only the Caplan or Bonaventure base station data revealed alarming differences (Figure 3.3). A nearly systematic shift, which varied per day, was noticed (Table 3.1). The Caplan processed data proved to be consistent, and the heights (w.r.t. the waterline) matched with the predicted tides at Paspebiac, derived with the tide predicting software xtide. Discrepancies in Figure 3.4 are probably due to daily variabilities such as wind and pressure.

Due to battery failure, the GPS data logged, by the receiver at the Bonaventure, does not completely cover the rover survey time. Given this lack of overlap, and the

unknown source(s) of the vertical shifts seen in the Bonaventure data, the PPK processing was continued without the Bonaventure base station data.

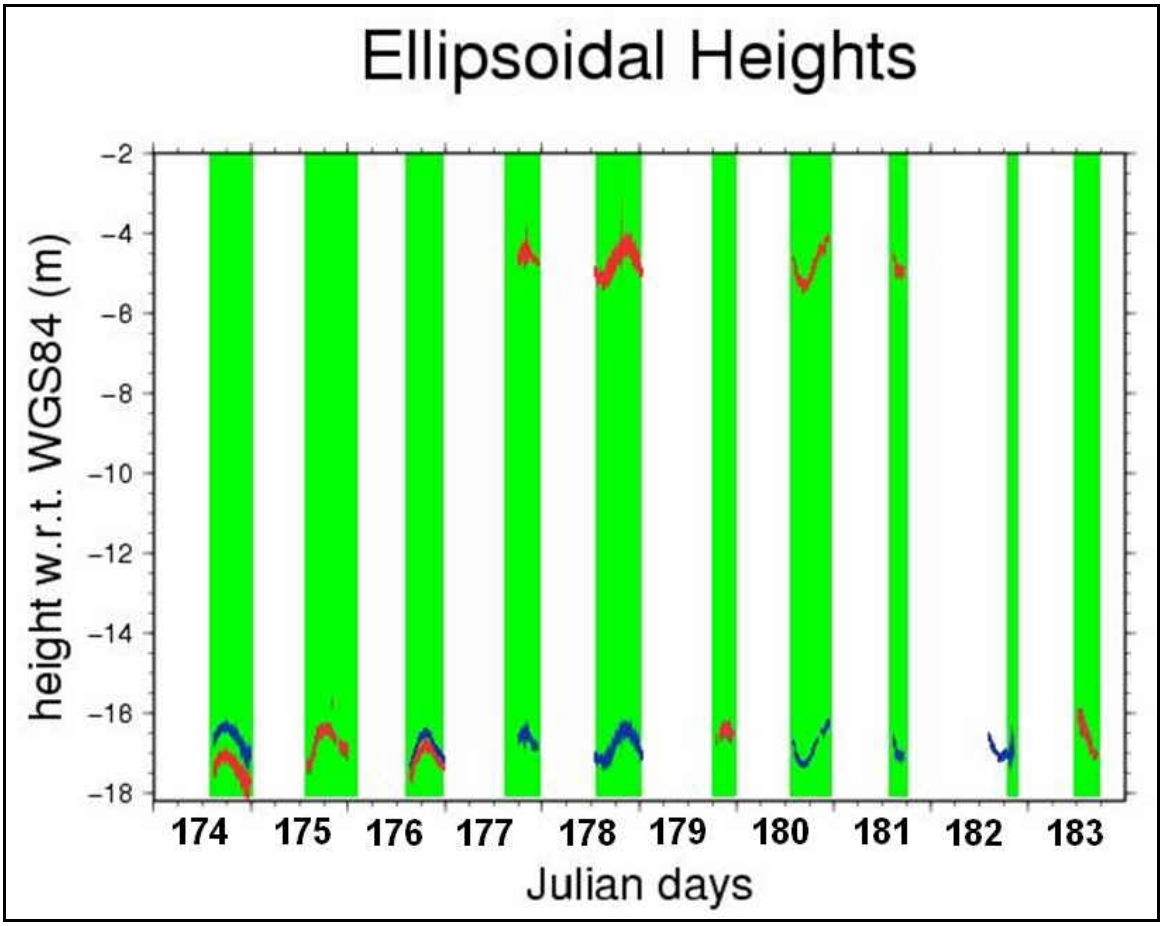

Figure 3.3 Heron ellipsoidal antenna heights processed with Caplan base station data (blue) and Bonaventure base station data (red). Green bars indicate Heron survey time.

Table 3.1 Height differences of data processed by Bonaventure and Caplan base stations.

Julian day	Mean difference (m)	Standard deviation (m)
174	0.742	0.046
176	0.276	0.571
177	12.091	0.081
178	12.086	0.177
180	12.039	0.070
181	12.121	0.042

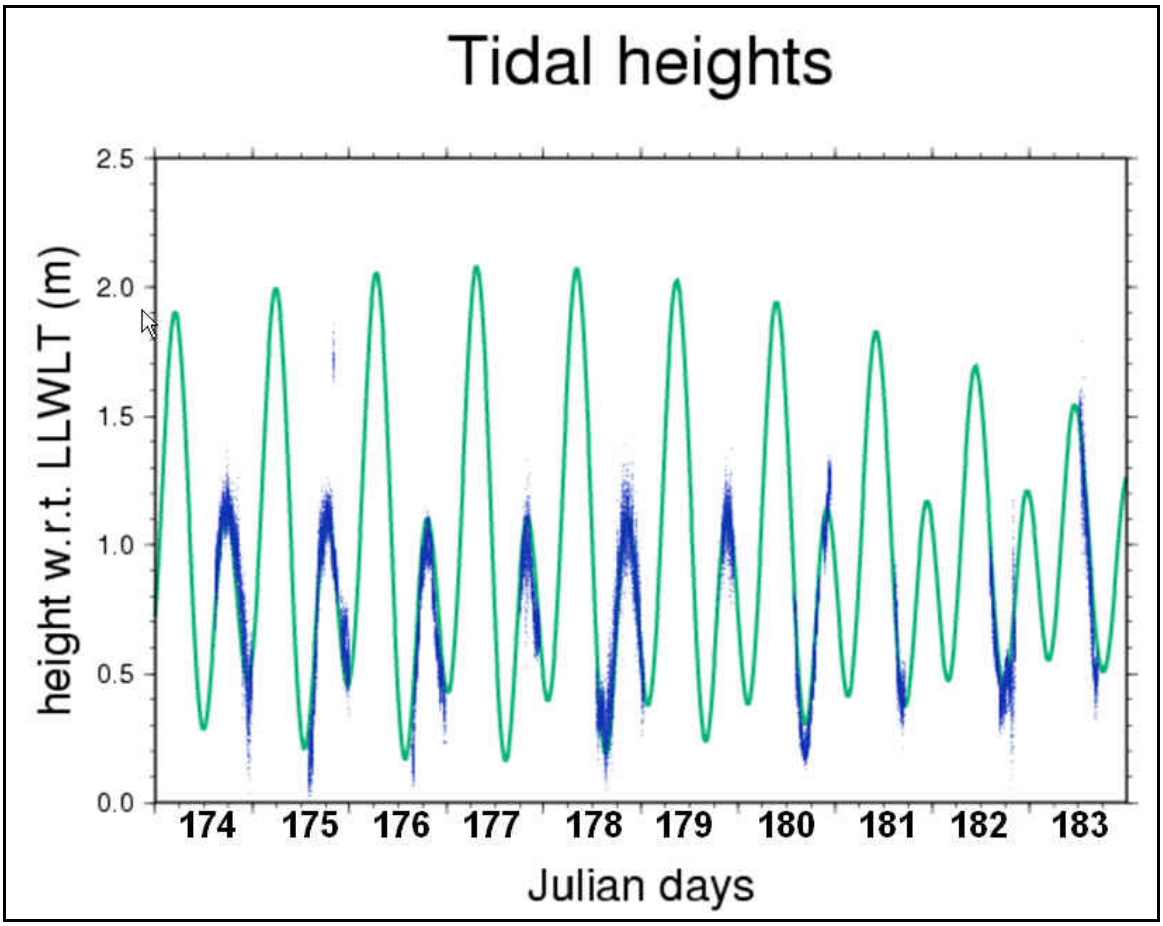

Figure 3.4 Predicted tides of Paspebiac (green), acquired by xtide. The tidal signature on the PPK heights (amplitude and phase), presented in blue in the figure, matches the predicted time series.

Once processed, the exported antenna heights with respect to the NAD83 ellipsoid (h_{ant}) could be applied to the multibeam data. The height of the transducer (h_{tx}) will then follow as,

$$h_{tx} = h_{ant} - Z_{ant\_tx} \qquad (3.1),$$

where Z_{ant_tx} is the vertical offset between antenna and transducer. Due to the vessel's motion (roll, pitch) Z_{ant_tx} will change constantly. Accounting for this change requires a rotation of the static offset between antenna and transducer (O_x, O_y, O_z) around the x-

(roll, θ) and y-axes (pitch, ϕ) :

$$Z_{ant} = -\sin\phi \cdot O_x + \sin\theta\cos\phi \cdot O_y + \cos\theta\cos\phi \cdot O_z \quad (3.2).$$

Note that vertical changes such as tides, heave, squat and (dynamic) draft are captured in the h_{ant} variable. The Z_{ant_tx} term accounts for roll and pitch rotations. A low pass filter (tapered cosine squared moving box filter allowing periods of only more than 10 seconds) was applied to the PPK heights to eliminate short period wave motion, though preserving the tidal signature and other long period events such as squat and swell. The same analogy was adopted to achieve high pass filtered heave, thus only allowing surface wave motion of periods less than 10 seconds. The ellipsoidal depth (d_e) following from Equation 3.3 will then not apply height changes (e.g. heave, swell) measured by both dGPS and heave sensor twice.

$$d_e = d_{obs} + f_{lpf}\left(H_{tx}\right) + f_{hpf}\left(heave\right) \quad 3.3$$

The control station at Caplan was updated every five seconds; as a result, all processed data exhibit the same data interval, even though the rover data were originally collected at a rate of 1 Hz. This interval inconsistency introduces a problem because the multibeam pings at 21 Hz at a typical survey speed of 3.5 m/s, implying an updated PPK height every 105 swaths, or 17.5 metres of travel. Therefore, for each multibeam ping in between, the PPK heights were (linearly) interpolated before the low pass filter was applied. Figure 3.5 shows results of the filtering process. As a result of the large sampling rate of the PPK heights, the short term components of the heave are less pronounced (Figure 3.5 top), though occasionally still apparent. These heave components disappear after the low pass filtering. Note the static roll and pitch offset of the vessel, due to trim and listing caused by the engine and generator mounted on portside of the vessel.

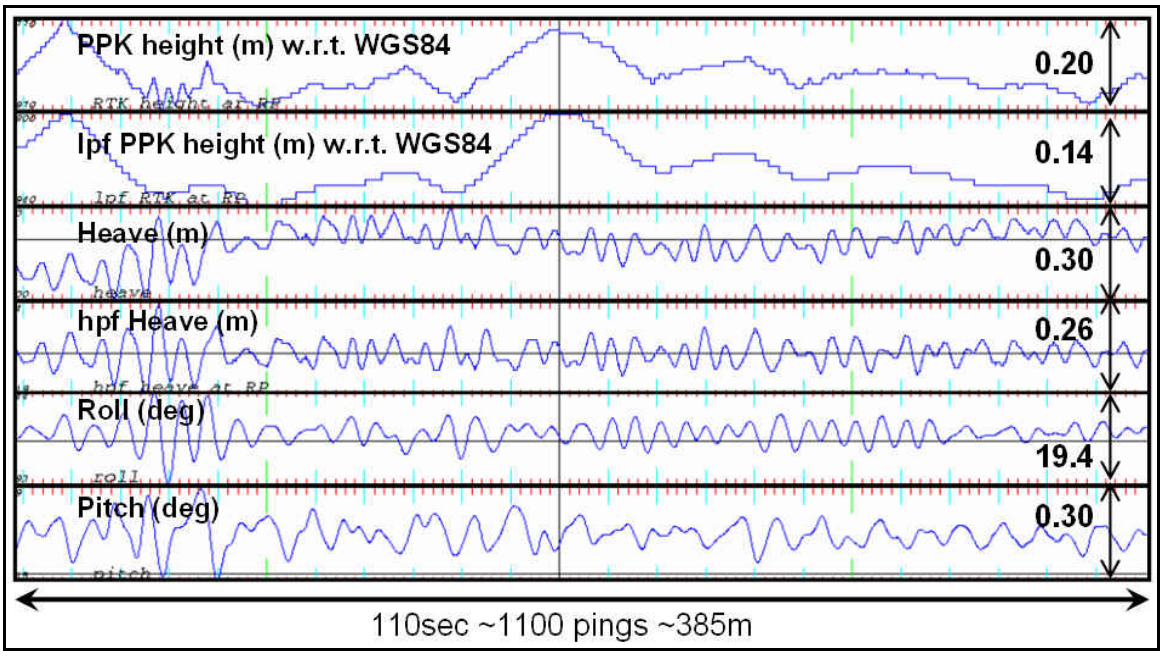

Figure 3.5 An excerpt of the motion data (line 0009_20060630_163236), pingrate 21 Hz, vessel speed 3.5 m/s. Green ticks mark every 30 seconds, red every second.

Figure 3.6 depicts a close-up from a DTM in the Paspebiac area with PPK heights at the transducer and Vertical Dilution Of Precision (VDOP) values. The abrupt vertical downward shift draws attention. The line first starts with a positive bias, the height then re-establishes approximately six minutes (~1500m) after the start of the line (SOL), and finally settles to the proper value. This sudden systematic bias was not related to any vessel related motion events, but to the poor satellite geometry at that time of day. The figure also includes the predicted VDOP values. Extreme high VDOP correlates with the vertical shifts. Fortunately this event occurred offshore, out of range of the lidar coverage; thus, it will not contribute a problem during the DTM comparisons. Other features or concerns were not seen through the data.

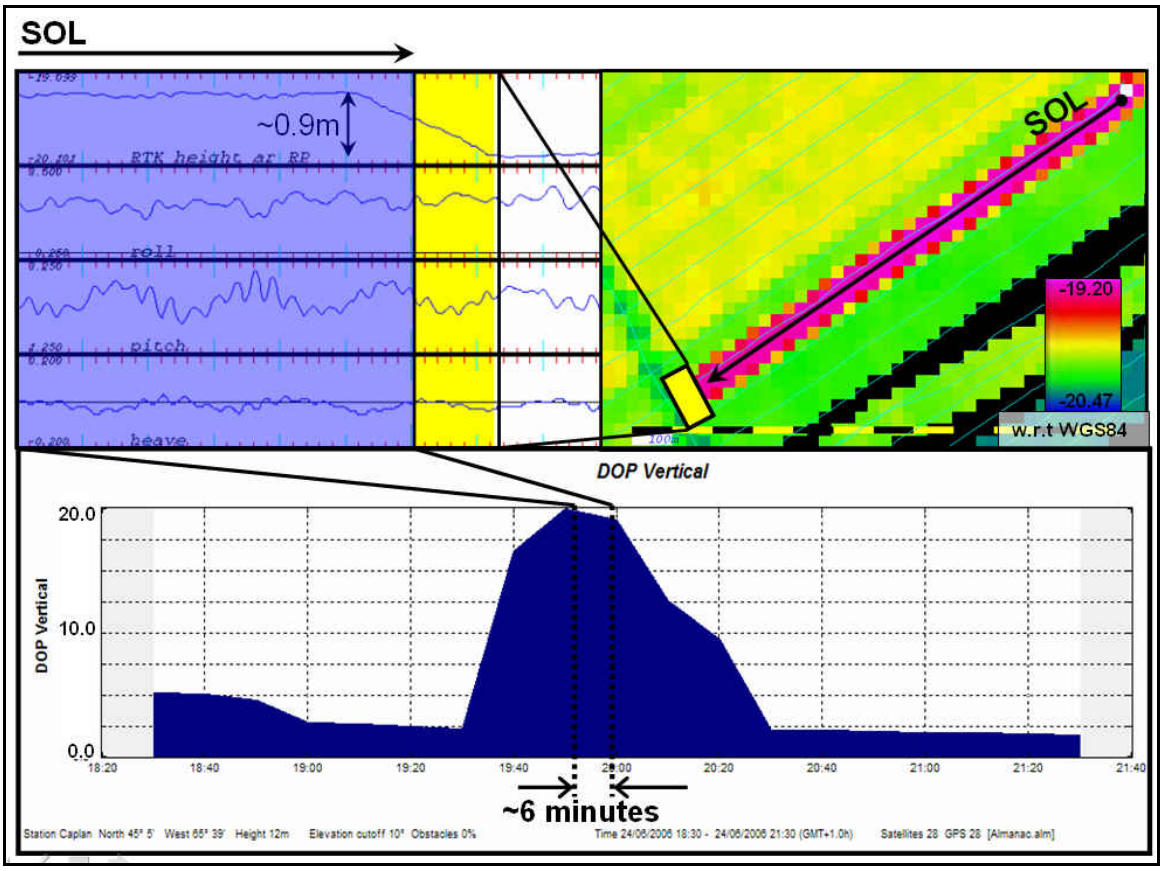

Figure 3.6 Transducer PPK height DTM in the Paspebiac area, with the associated motion time series (line 0053_20060624_195358). The height was re-established after approximately 6 minutes of travel from the start of line (SOL) due to an improved VDOP. Other variations seen in the DTM above are due to tides or heave.

The qualitative bottom tracking analysis is done with lidar and multibeam datasets referenced to the ellipsoid. However, we can reduce the ellipsoidal heights to chart datum (Lower Low Water Large Tides) with an ellipsoid – geoid and geoid – chart datum separation model. The ellipsoid – geoid separation model used was the GPS-H v2.01 (NRCan, 2004), developed by the Geodetic Survey Division, Natural Resources Canada. This model converts NAD83 (CSRS98) ellipsoidal heights to CGVD28 orthometric heights (heights above mean sea level). Figure 3.7 presents the model in the area of survey, the model slopes in SWW direction (indicated by the arrows in Figure 3.7)

leading to a maximal difference in the order of ~0.8 metres from east to west. The geiod – chart datum separation (Z_0) can be derived with nearby tide stations. At the Paspébiac tide station (controlled by the CHS) the geiod – chart datum separation is 0.978 m. Other tide stations in the vicinity but beyond the survey area are Black Cape (50 km WNW, Z_0 = 1.188 m), Port-Daniel (29 km NE, Z_0 = 0.840 m), and Caraquet (27 km SSE, Z_0 = 0.737m). The geiod – chart datum separation values indicate a surface sloping down towards the New Brunswick coast and sloping up towards the interior of the bay. While Z_0 -values of neighbouring tide stations do not change dramatically within the survey area (e.g. +42 cm/km WNW, indicating +5.7 cm change at the outer limits of the Bonaventure survey area), the geiod – chart datum separation at Paspébiac is used as a static offset throughout the complete survey area. It is emphasised that the bottom tracking assessment is done with ellipsoidal heights only; reduction to chart datum is only done in order to obtain meaningful depths.

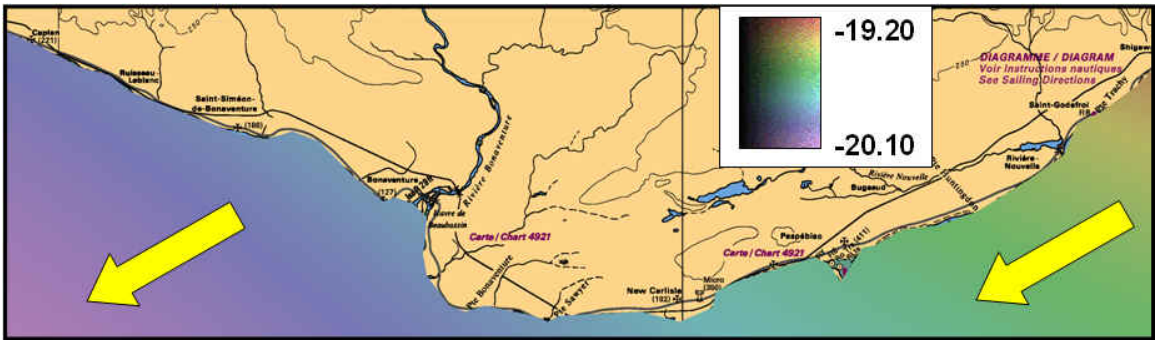

Figure 3.7 Ellipsoid – geoid separation model; GPSH in the survey area. Arrows indicate the SWW oriented slope.

3.1.3 Backscatter

The multibeam backscatter strength, the ratio of returned energy from the seabed and transmitted energy at the transducer, is commonly used to interpret the seabed type. Indeed, scattering depends largely on the seabed material and shape, but other factors contribute too. These are mostly accounted for internally by the Simrad system. They include acoustic spherical spreading, ensonified area, and an approximate correction for water column absorption and angular response. Research done within the department describes the internal Simrad and OMG multibeam backscatter processing in more detail (Llewellyn [2005], Oliveira [2007]). The processing in this study applied to the Simrad first-order corrected backscatter involved an empirical beam pattern correction to account for acoustic intensity fluctuations and imperfect angular response modeling of the Simrad system. The beam pattern correction reduces the effect of strong (near) nadir backscatter due to rapid changes of the Simrad angular response model near nadir, and sediment changes. The correction also removes beam pattern residuals seen along track.

While multibeam and side scan sonar systems are both capable of producing seabed backscatter images, they are complimentary, rather than competing methods (Hughes Clarke [2004b]). For example, multibeam bathymetric data can aid by associating heights to targets identified by shadows on the side scan mosaic. In return, towed side scan mosaics provide better aspect ratio, promoting the detection of targets on the seafloor, mainly those that could not be resolved with the multibeam's resolution or around which shadows are not cast at the higher aspect ratio of the multibeam. Although for this work the side scan sonar was at the same altitude as the multibeam, the side scan sonar could still achieve a significantly lower aspect ratio in shallow water due to its

larger slant range (set to 50 m). For that reason, the mosaics of the keel-mounted side scan sonar were preferred over multibeam mosaics (Figure 3.8). One exception to this preference occurs at dense vegetation inspection areas. During surveys at those locations the recording channels of the side scan sonar were in use with the Knudsen 200 kHz downward looking singlebeam sounder. Moreover, vegetation inspection areas were not always covered by the adjacent side scan sonar lines; thus, only multibeam backscatter was available.

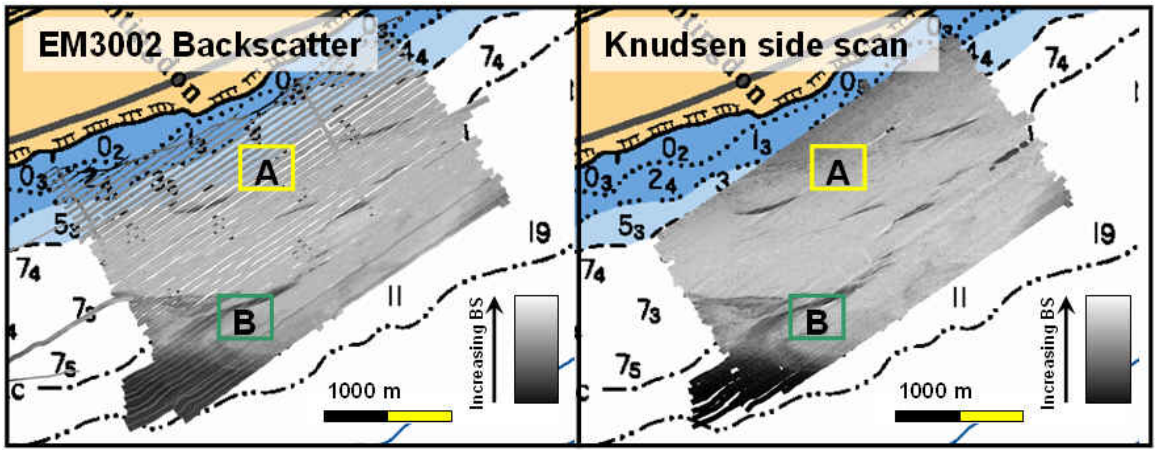

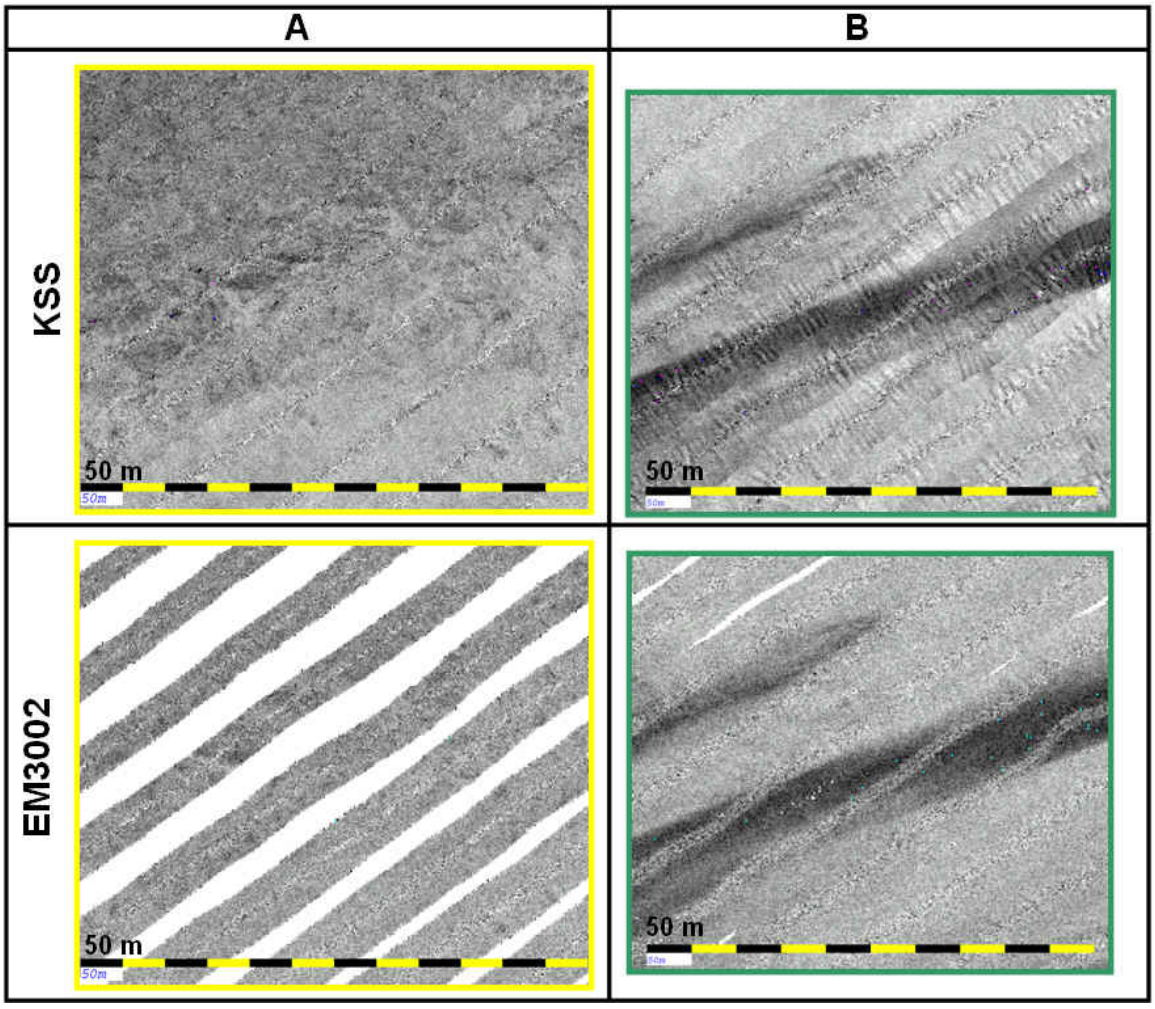

Figure 3.8 Backscatter mosaics from the EM3002 (top left) and keel-mounted Knudsen side scan (top right). The enlarged images (middle and bottom) illustrate the value of the keel-mounted side scan at shallow depths; swath widths are almost irrespective of depth. The qualities of both mosaics are equivalent, although the keel-mounted side scan mosaic shows some roll artifacts.

3.1.4 Water Column

Water column imaging is a novel application that introduces a valuable qualitative tool to hydrographic surveyors. It can be utilized by the hydrographer to monitor the bottom tracking, detect hazardous targets, and identify oceanographic features. A review of multibeam water column applications and detailed description of the imaging geometry can be found in Hughes Clarke (2006a, 2006b).

Whereas bathymetry and backscatter concentrate on the seabed, water column imaging displays the scattering of the emitted signal from transducer face, through the water and on the seabed. This functionality is not uncommon; the fishing industry is familiar with such multibeams as they use this approach to identify schools of fish. Though the major difference is in the broad beam width of those so-called fish finders (12°), the EM3002 uses beam dimensions of 1.5°x1.5°. As with the bathymetric data, in which narrow beams increase resolution of the sampled seabed, narrow beams also increase the resolution of the water column image.

Figure 3.9 shows an example of a multibeam water column swath profile. The backscatter intensities of each received physical beam (164 in total, HD mode is not used for water column) are mapped according to their depression angle. The logarithmic intensities are greyscale coded. Due to the logarithmic compression, weaker echoes from the water column or sidelobes are promoted, rather than peak intensities from the main lobe. The upper plot in the figure, illustrating the signal intensities along the oblique line, show high return intensities near the top of the vegetation and the seabed. Fortunately the seabed return was stronger than the vegetation return through which the bottom detection was not mistaken. Signal intensities with a range common to the algal canopy (yellow arc) are shown in the lower plot. The strongest return on the displayed arc appears to originate from vegetation. Section 5.1.1 will discuss the performance of the multibeam tracking during vegetation presence in more detail.

Since the EM3002 is a single sector type multibeam, only data within the minimum slant range is useful for water column interpretation. Data falling outside the minimum slant range are contaminated with echoes of inboard sidelobes. In addition, the angular

response of the seabed can promote the contribution of sidelobe echoes, and the off-track topography introduces an increased uncertainty. The effects of all these features and engine or propeller noise, third party sonar's and oceanic features are described in detail by Hughes Clarke (2006a). Multisector multibeams such as the EM710 limit side lobe contamination, and have an increased selection of data suitable for water column interpretation.

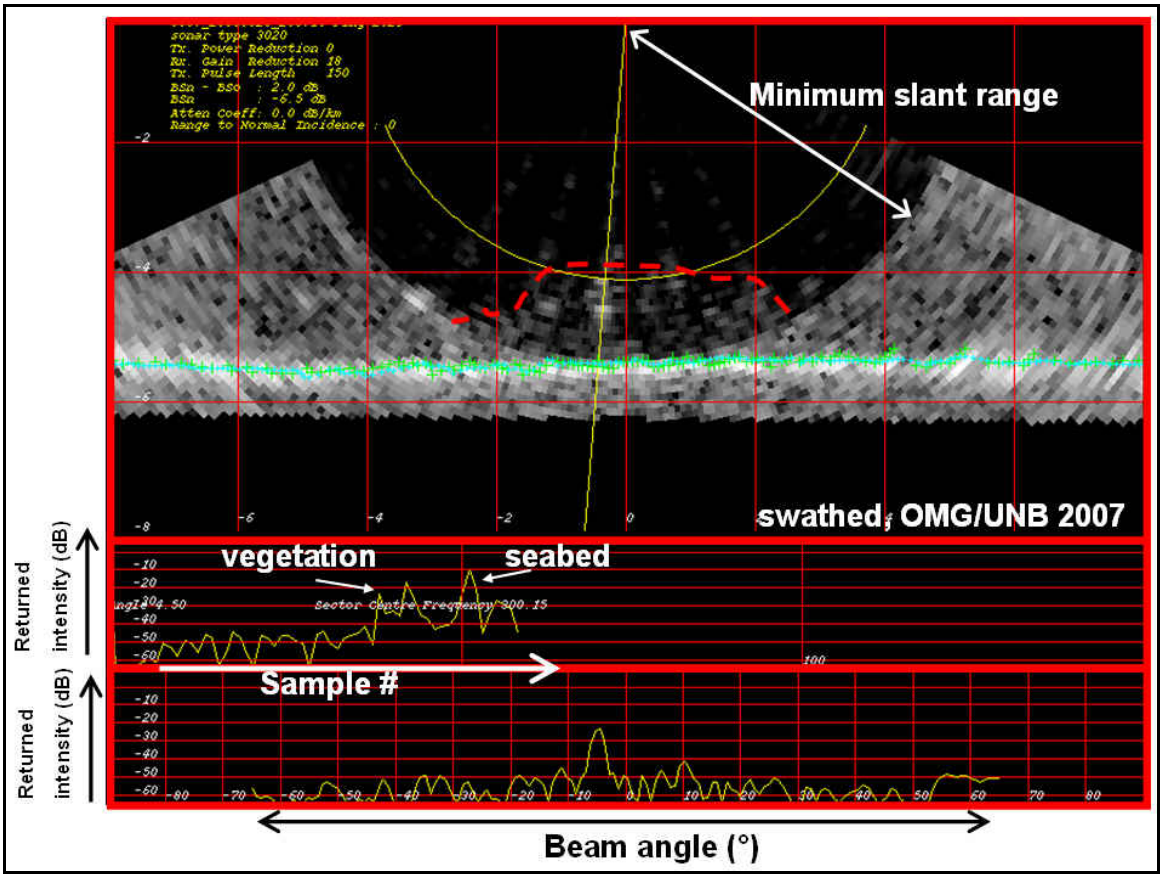

Figure 3.9 An example of an EM3002 water column swath profile. The blue dots represent the bottom determined by the HD beams. Aquatic vegetation is seen in the water column, circumscribed by a dashed red line. The plots show the returned intensities along the oblique line (upper plot) and the arc (lower plot).

3.2 Knudsen Acoustics

The CSL Heron is outfitted with a range of Knudsen 320 transducers that are operated at varying frequencies; three echosounder transducers (3.5, 28, 200 kHz) and a pair of Airmar side scan staves (200 kHz). The 28 kHz sounder was not operational at the time of the survey. The 3.5 kHz sounder data appeared to be contaminated with much reverberation, and occasionally tracked the algal canopy, although the sounder is commonly used to map the sub-bottom layers. An imperfect gain setting was most likely the cause to the degraded data quality. The 3.5 kHz sounder, therefore, did not play a role in the analysis in vegetated area's, but it was used to assess the absolute bottom tracking of the multibeam (Chapter 5.1). The 200 kHz sounder and side scan have been valuable for this work. A summary of these instruments and processing will follow in the remainder of this chapter.

3.2.1 200 kHz Echosounder

High frequency sounders are commonly used to reveal mid-water features such as zooplankton, turbulence, suspended sediment, or density interfaces (Delpeche [2007]). The reasons for an increased amount of backscatter from a high frequency acoustic signal are twofold: 1) The high frequency signal promotes backscatter since the acoustic wavelength and pulse length are often much smaller than the scattering target(s) (e.g. 200 kHz, $\lambda \approx 7.5$mm, $\tau \approx 0.1$ ms, range resolution ≈ 0.08 m). 2) The high frequency will, along with an increased array length, produce a narrower beam (6° for this particular transducer), thus improved angular resolution. With more energy focused on a smaller

patch on the seabed, scatterers within the ensonified volume can contribute more strongly to the backscattering.

For the visualization of mid-water vegetation, the Knudsen 200 kHz sounder proved to be of great value. The large surface of algal leaves, and air bubbles captured in them, promote backscatter from high acoustic frequencies (Figure 3.10). Equations for the backscattering strength of spherical targets such as the air bubbles seen in Figure 3.10 are given in Urick (1983). The sounder was operated with the highest gain settings, which increase the volume scattering, but also, ambient noise. One limitation is the dynamic range of the returned signal which is recorded as an unsigned 15-bit linear value. In order to reasonably view the weak vegetation scatterers, the much stronger echoes from the seabed are clipped; i.e., return signal intensities will not exceed the 15-bit value, as illustrated in Figure 3.11. We can therefore not estimate the relative scattering strength between vegetation and seabed. Fortunately, this is not the case with the multibeam. Multibeam water column data are logarithmically compressed, excluding the need to clip the data. Section 5.1 continues with a relative comparison of mid-water vegetation and seabed scatterers.

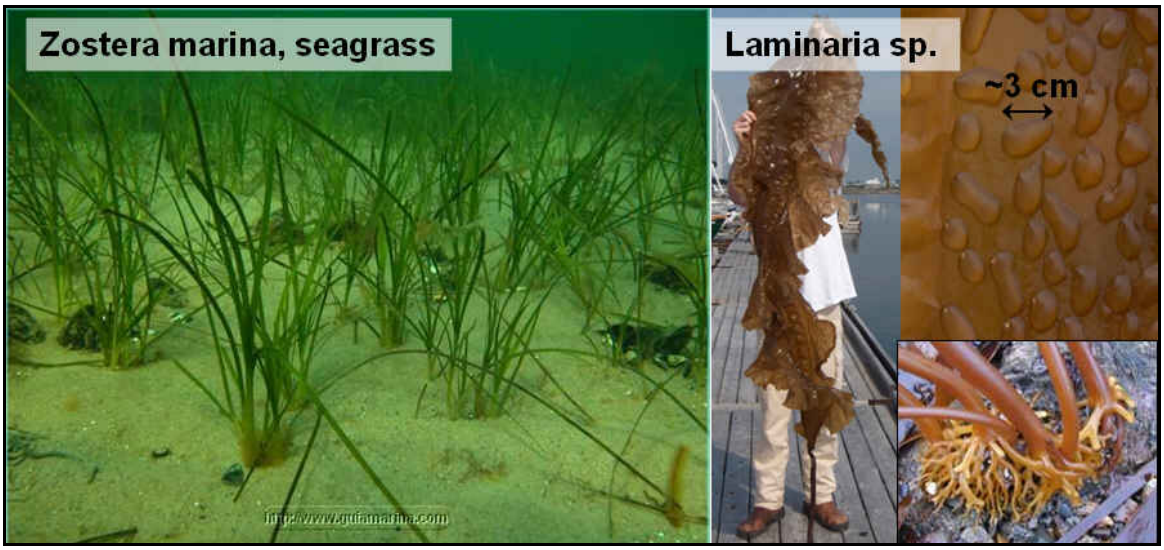

Figure 3.10 Two commonly found species in the survey area are Zostera marina (seagrass), and Laminaria sp. In particular the latter contains large air bubbles, which create a considerable impedance contrast. Laminaria sp. populate rocks, whereas seagrass grows in sand. Underwater photograph of Zostera marina from: www.guiamarina.com

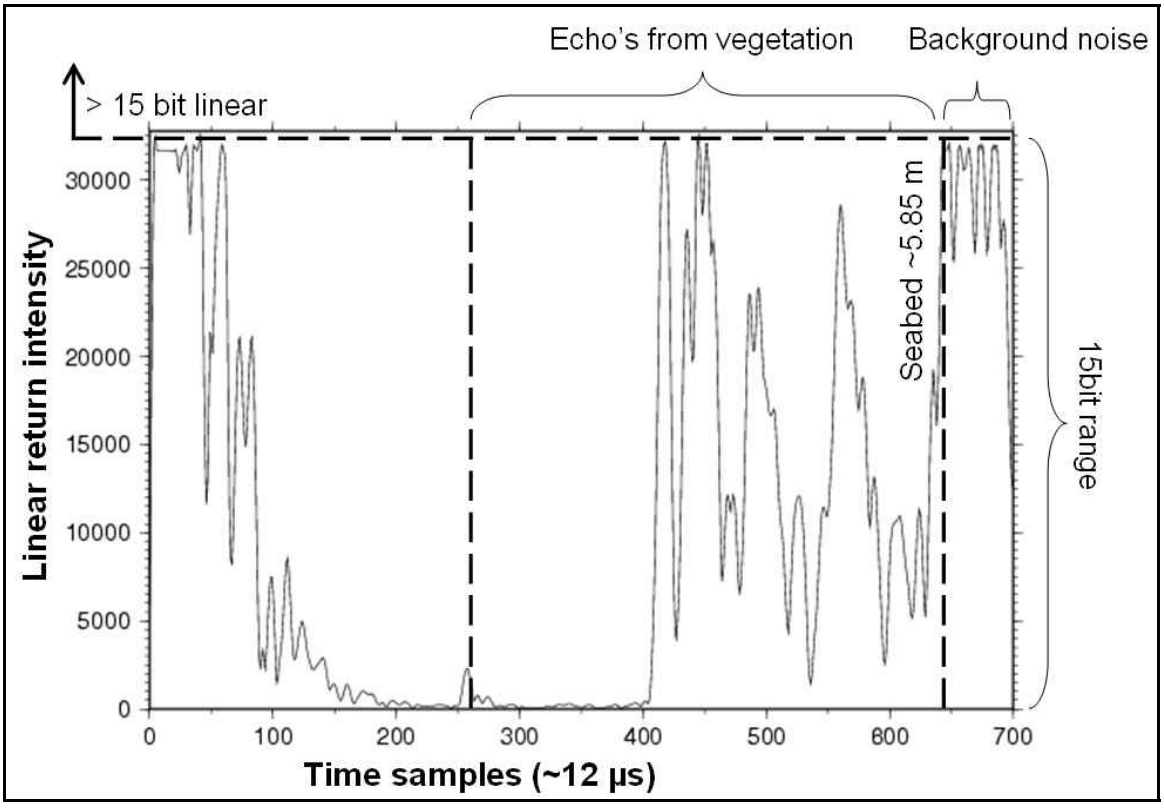

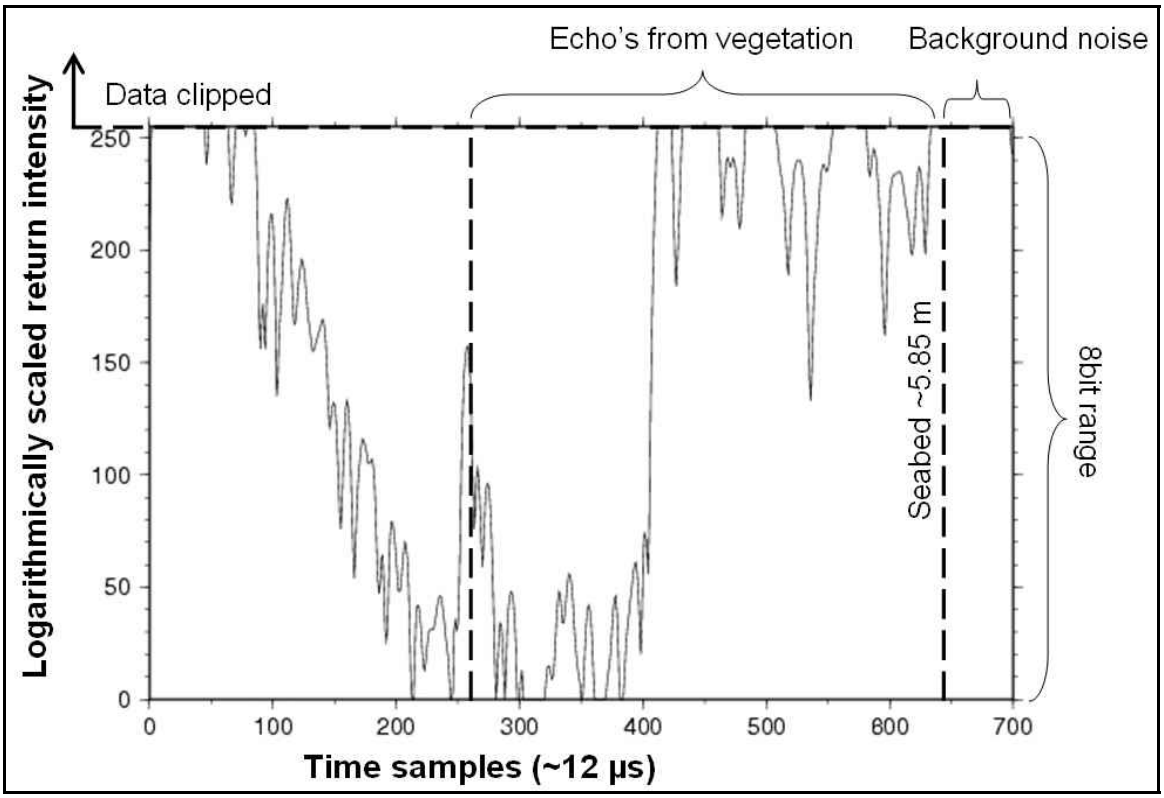

Figure 3.11 An example of a linear (top) and logarithmically scaled (bottom) echo trace including mid-water vegetation scatterers and the seabed. The original linear 15-bit trace data is compressed to 8-bit. Due to the linear logging, strong returns from the seabed are clipped above the 15-bit number (or 8-bit number after the logarithmic compression). Note that only a portion of the echo trace is displayed: the complete echo trace is sampled in 1600 bins. Each time bin translates approximately to 12 µs.

The binary Knudsen engineering (keb) files are converted into the OMG file structure format. With in-house software the data were converted from linear 16bit data (but actually 15-bit data) to logarithmically compressed 8-bit data. A correction for spherical spreading (40logR) is applied in the recorder. The longitudinal transects over dense vegetated areas are purely of qualitative value for the analysis since the high frequency, in combination with an increased gain, greatly degrades the bottom tracking of the sounder at vegetation presence. All the profiles in this work use a linear backscatter grayscale. The data distributed along track are a function of ping rate and survey speed,

but typical 2 or 3 soundings per metre. The sounder shares the recording channels with one of the two side scan staves; thus, both could not be recorded simultaneously. At vegetation inspection sites, it was decided to use the 200 kHz sounder only.

3.2.2 Keel-Mounted Side Scan

3.2.2.1 Acquisition

Two side scan staves (200 kHz, 0.5° along track, 50° across track) are fitted to both sides of the keel with a 30° tilt angle, approximately 0.80 m below the waterline. In contrast to most side scan sonars, which are commonly towed behind the vessel, the keel-mounted side scan sonar ensures a more accurate position. The positioning of a towed side scan sonar is determined with less confidence (e.g. with USBL-positioning or an approximate position based upon the layback, vessel's azimuth and position). Alternatively the keel-mounted side scan sonar suffers from the vessel motions, mainly roll and yaw. Unlike multibeam systems, it is not possible to actively compensate for motion through beam steering; thus, motion artifacts remain in the mosaics. An empirical beam pattern correction may reduce artifacts to some extent, but this enhancement is not guaranteed (Hughes Clarke [2004a]).

Keel-mounted side scan sonars have proved to be a useful instrument in extremely shallow waters (Hughes Clarke [2004a]), mainly from an operational point of view. Where towed side scan versions risk the chance of hitting the seabed or underwater objects, a keel-mounted side scan sonar is, navigation-wise, only limited by the vessel's draft and, in addition, the vessel is much more maneuverable without a trailing cable with

side scan fish. The low side scan's altitude in shallow depths and the 30° tilt angle result in a lower aspect ratio, i.e., higher than achievable with a multibeam. For that reason, the keel-mounted side scan is favored above multibeam backscatter, as was highlighted in the previous section.

The side scan data was collected with a 50 m range. This allowed us to survey with ~80 m line spacing and provided full bottom backscatter coverage. A 0.1 ms CW pulse was used. The resulting range resolution is ~0.08 m. The horizontal resolution improves as the across track distance increases, and is also a function of pulse length. An along track ping to ping separation of 0.7 m is achieved with a typical pingrate of 5 Hz and vessel speed over ground of 3.5 m/s. The along track ensonified area will grow with increasing across track distance, the smallest ensonfied along track separation is approximately 0.25m at the maximum across track range (Figure 3.12). The received signal is amplified by a 40logR ramp to account for losses due to spherical spreading.

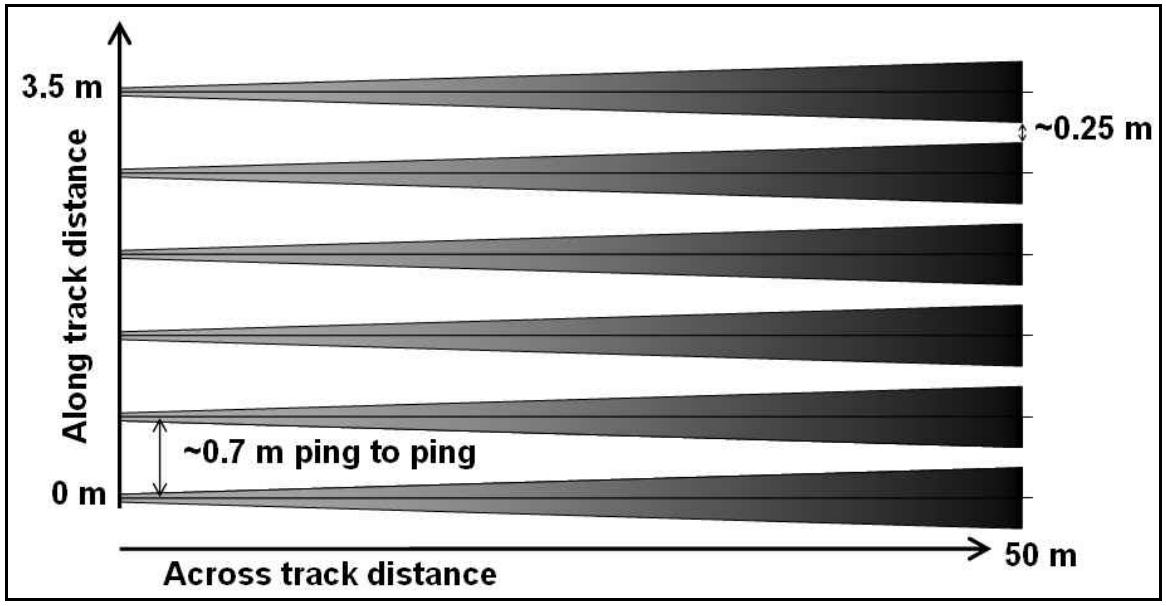

Figure 3.12 Example of the along track separation, displaying here only starboard swaths (grayscale shaded for increasing along track distance). For one unit of time the sonar fires five pings spaced

approximately 0.7 m apart. The along track separation reduces away from nadir.

3.2.2.2 Processing

The raw keb-files are, likewise to Knudsen 200 kHz singlebeam data, converted into the OMG file structure and format. The conversion includes a logarithmic compression of the data from originally 15-bit to 8-bit. The software corrects the backscatter for attenuation loss (50 dB/km) and ensonified area (based upon the pulse length, slant range, incidence angle, and beam widths). The two way travel times are converted into across track distance through the slant range correction. This correction, assuming a flat seabed, derives the across track distance with Pythagoras from the altitude and the slant range. The altitude, in fact, the first return, is sensitive for noise in the water column. It is replaced by the nadir depth measured by the multibeam. Also, attitude data from the multibeam are passed on. Synchronization errors between side scan and multibeam PC clocks are accounted for, although these tend to wander off during the day. The across and along track backscatter data are georeferenced with the heading (from multibeam orientation data) and dGPS position levered from the receiver to the transducers.

A final, cosmetic, correction is the beam pattern correction. The product of transmit and receive beam patterns can be seen on a mosaic as along track regions with a coherent backscatter. At a null, between an inboard side lobe and main lobe, a weak backscatter stripe will appear. Where the main lobe intersects the seabed, a stronger backscatter stripe appears. The beam pattern signature remains in the mosaic when an improper angular response is applied. The beam pattern correction radiometrically

corrects the backscatter at each pixel across track, relative to the average backscatter at that pixel over the survey line or period of pings. The average backscatter is found by stacking along track backscatter for each angular bin. The derived empirical beam pattern will, as it is a product of both transmit and receive beam patterns and the angular response, differ above varying seabed material. A summary of the side scan processing chain and the beam pattern correction is illustrated in Figure 3.13.

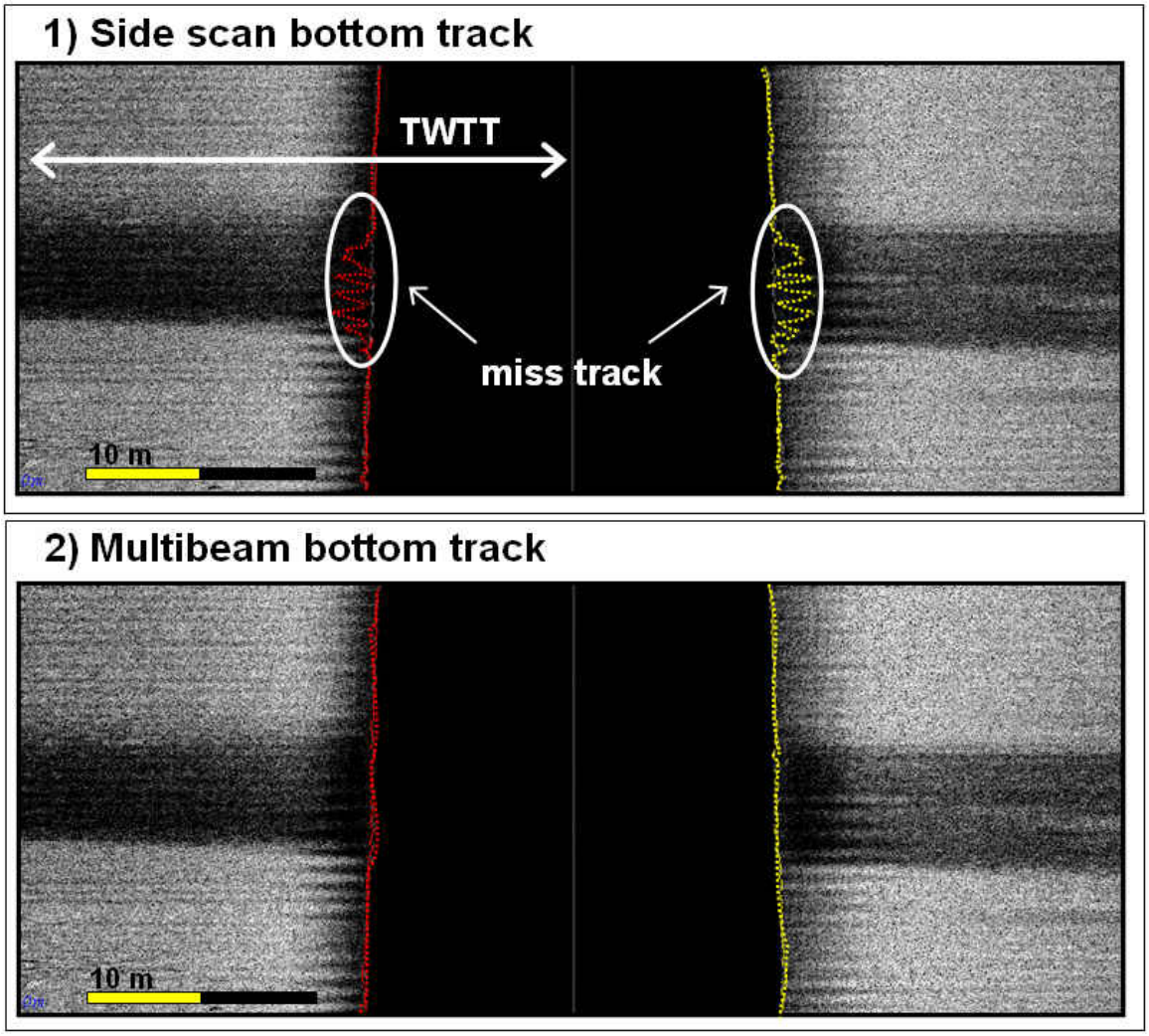

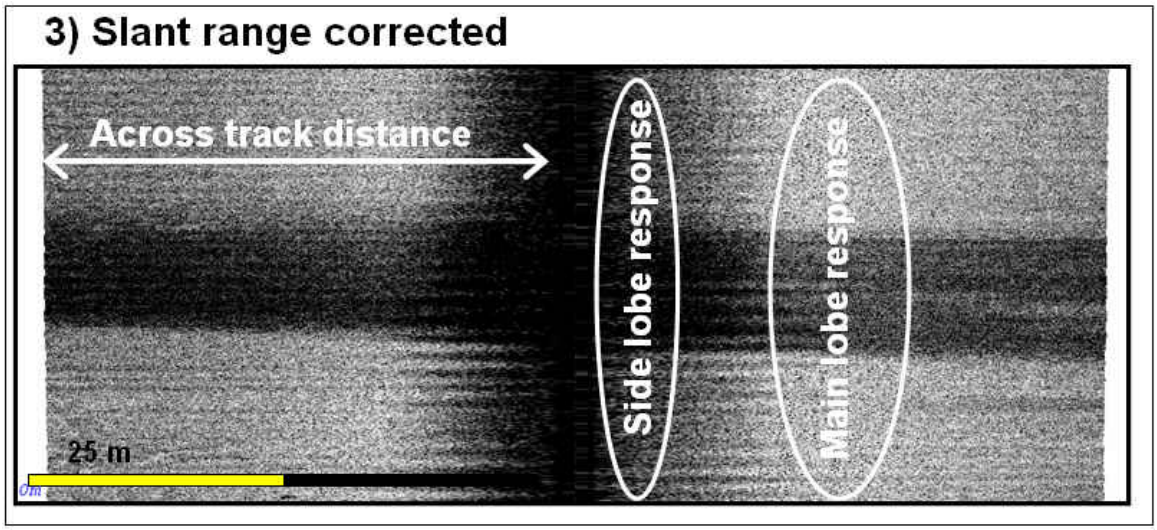
3) Slant range corrected
Across track distance
Side lobe response
Main lobe response
25 m

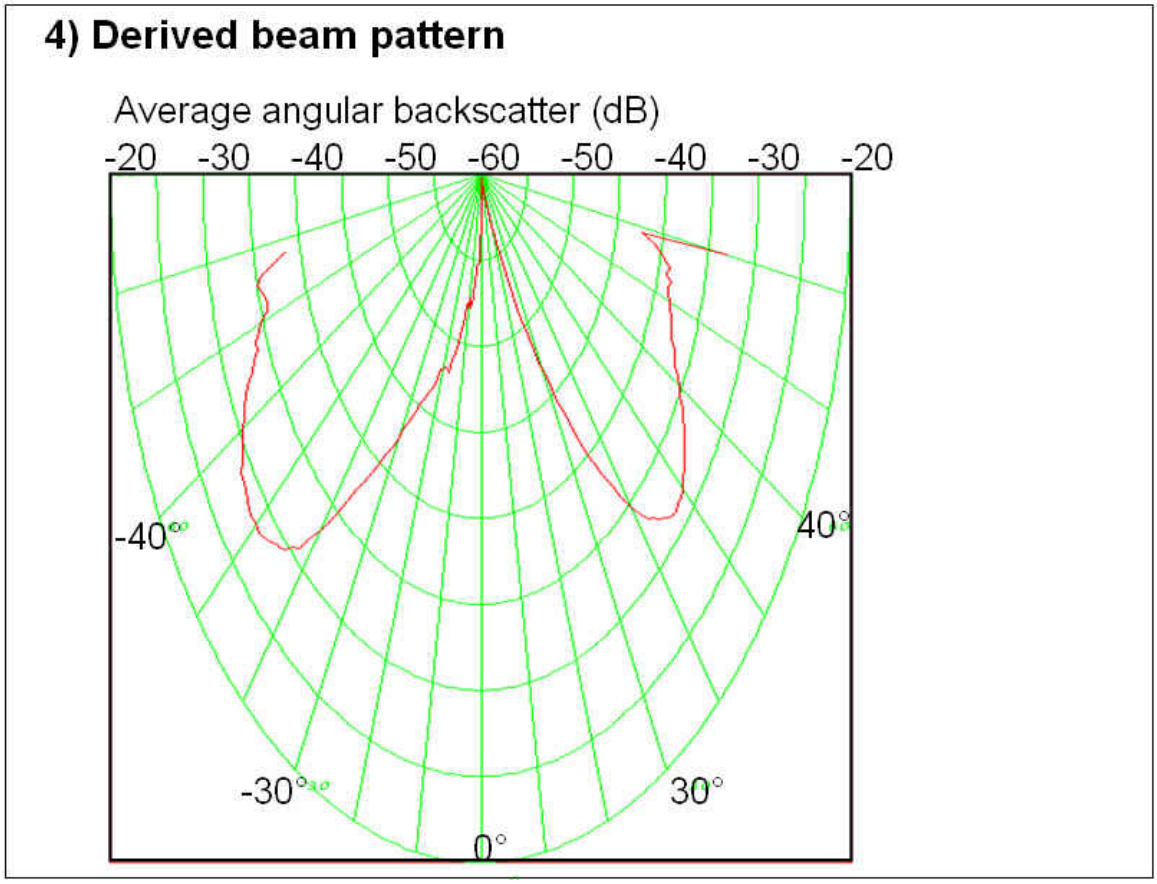
4) Derived beam pattern
Average angular backscatter (dB)
-20 -30 -40 -50 -60 -50 -40 -30 -20
-40°
40°
-30°
30°
0°

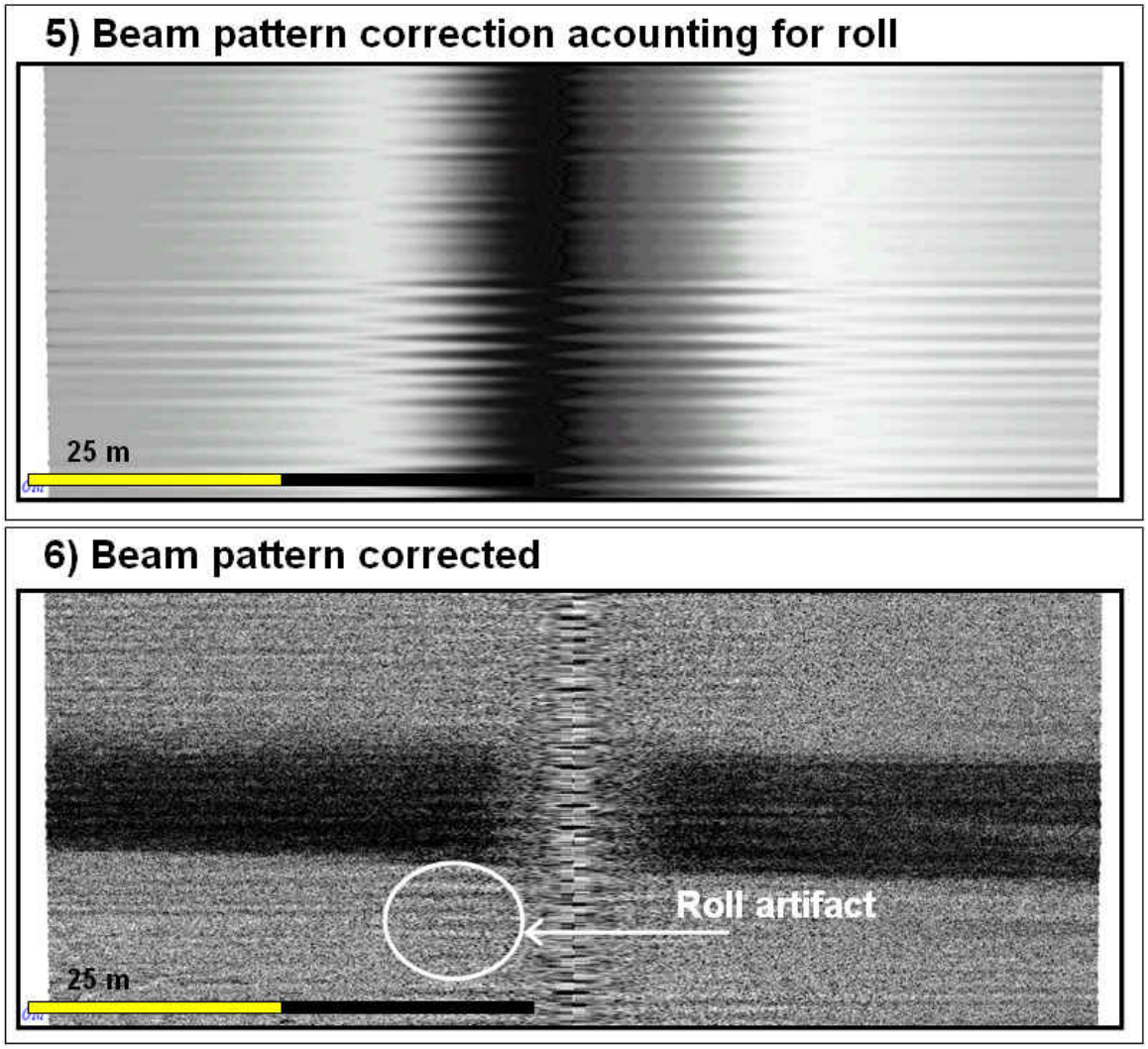

Figure 3.13 The side scan processing summarized in six steps: 1) The bottom tracking of the side scan is disturbed when it passes over a mud region. 2) Once the bottom tracking of the much more stable multibeam is used, the data are again corrected for the attenuation and ensonfied area. 3) Each ping is georeferenced; this georeferencing includes a slant range correction. The TWTT's are now converted into an across track range. 4) An empirical beam pattern fixed in the sonar reference frame, i.e., rolling with the vessel, is derived from the average backscatter in along track direction for each angular bin. 5) The beam pattern correction will radiometrically correct the backscatter. 6) The beam pattern signature is significantly reduced. The correction removes some roll artifacts although large artifacts remain (line 0019_2006_178_2224_018).

CHAPTER 4 Waveform Extraction and Environmental Dependence

Since the existing UNB Ocean Mapping Group hydrographic software tools are predominantly developed for multibeam echo sounders, the analysis of SHOALS lidar data requires modifying present software and developing novel applications. Section **4.1** describes the software development in the support of SHOALS bathymetric and waveform data.

The waveform characterization is based upon the shape or magnitude of the bottom return peak. Locating designated points on the waveform from which waveform parameters are extracted is thus the basis of the characterization process. The success of the routine that extracts the necessary points holds a pivotal role in the complete characterization process; waveforms on which the routine fails will be disregarded for the characterization. The waveform parameter extraction is discussed in Section **4.2**.

The water clarity parameter is extracted based upon the points located by the routine. The extracted water clarity parameter of each waveform describes the whole water column and these values are presented geographically. Section **4.3** continues on the water clarity parameter extraction.

Before we can interpret characterized waveforms in order to investigate a correlation with the vegetated seabed, we must consider environmental effects to the waveform. These effects are discussed in Section **4.4**. In order to confidentially use the characterized waveform to distinguish vegetation, the environmental effects on the waveforms need to be investigated.

4.1 Software development

For the analysis of the SHOALS bathymetry, waveforms, and aerial photography, existing in-house hydrographic software has been modified. These modifications include 1) reformatting of the original data files into an OMG file structure, 2) development of a waveform viewer, and 3) analysis tool kit. In addition, several programs that support SHOALS data have been developed.

SHOALS bathymetric data are delivered in binary las-files. These contain, besides sounding position (latitude, longitude, ellipsoidal height), wave heights at each shot, pseudo-reflectance (if recorded), scanning azimuth, and time reference. Data from the las-files are reformatted into OMG "merged" files. Bathymetric data in the OMG file structure are always referenced to the survey platform. However, the las-file does not contain the aircraft's position at each shot or scan. To overcome this problem, a least squares regression of each scan yielded the aircraft's heading, while the average sounding coordinates provided a guessed aircraft position. With the pseudo craft's position, the soundings were transformed to a body fixed coordinate system. The described methodology implies that incomplete scans, due to optical depth for example, distort the aircraft's pseudo position (Figure 4.1b). Nevertheless, the sounding's positions are not harmed.

Waveform data, for all four channels, are reformatted from the original binary SHOALS inw-files, into OMG "waveform" files. Soundings from the merged files are then linked with their associated waveforms via the timestamps. Once the reformatting is complete, the SHOALS data can be viewed in "swathed," OMG's main hydrographic tool.

Swathed is originally used to handle and process multibeam data; it allows the user to view and edit acoustic data. Editing of SHOALS data in swathed did not involve bathymetric cleaning, but was focused on the waveforms primarily. The data are displayed in blocks of 80 scans. Bathymetry may be inspected using a plan view, scan view, or profile view, and the data can be viewed in a geographical mode (Figure 4.1a&b). In support of the analysis, a waveform tool kit was developed. It displays the waveforms for each channel, individually, and per scan (Figure 4.1c). Results from waveform parameter and water clarity extraction, and correlation plots of waveform parameters can be called upon in the waveform tool kit.

A program is developed to display waveforms in a vertical profile. The profiles depict waveforms of consecutive scans with color or grayscale coded return intensities. The volume return in the profile is detrended according to the derived system attenuation coefficient, allowing a larger color range for the bottom return. The program can output data of a specific beam, and data within a specified scan range. Figure 4.2 presents an example of a vertical waveform intensity profile.

SHOALS aerial photographs are delivered as jpg-image files with associated georeferencing coordinates. The image-files are converted into PPM-format and then into an 8-bit in-house image file format. These georeferenced 8-bit images are mosaiced to provide ground truthing of the water clarity and surface intensity analysis (Section 5.2). During the mosaicing no motion or sun light corrections have been applied.

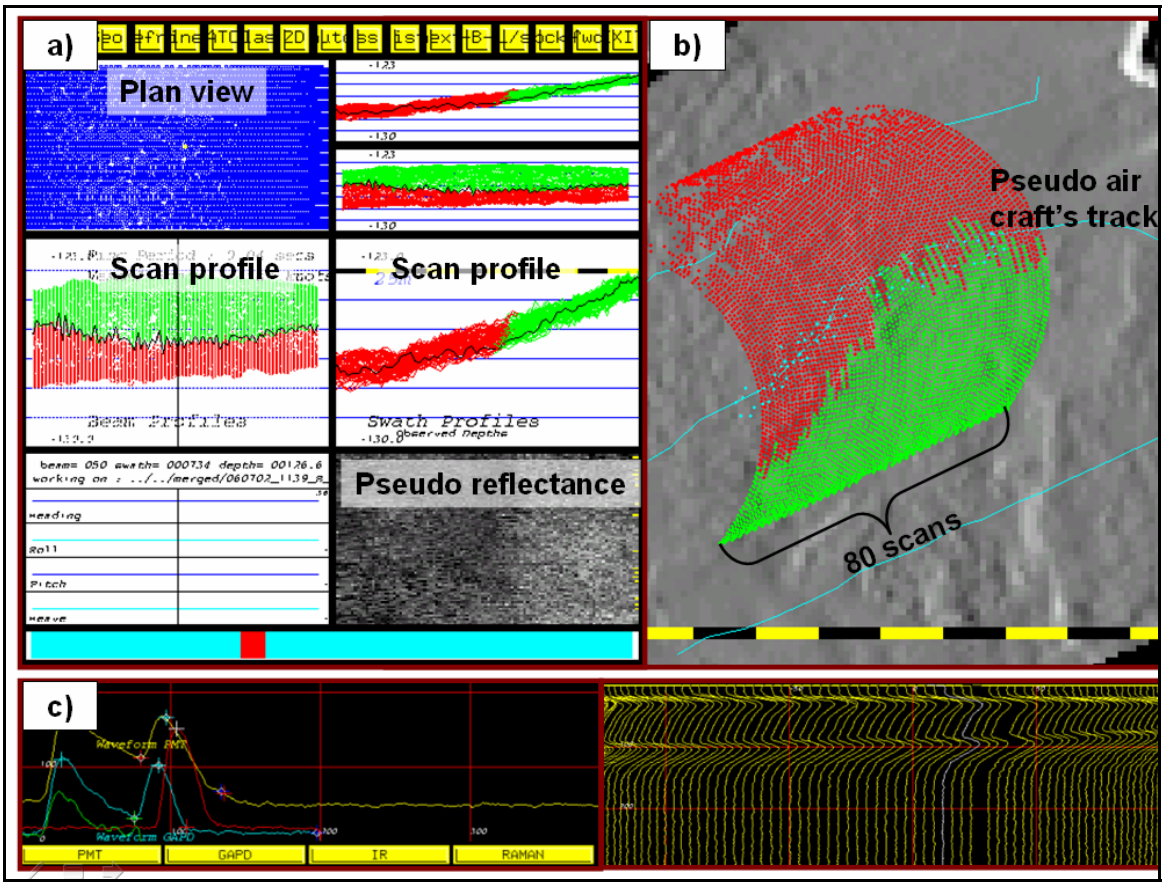

Figure 4.1 A overview of the swathed setup: a) the main window with the bathymetric and pseudo reflectance data, b) a block of data (80scans) displayed geographically w.r.t. a terrain model (either from the SHOALS or from multibeam or another image such as side scan sonar mosaic, laser intensity map or aerial photography), c) display of waveforms (PMT, GAPD, infrared, Raman) individually or per scan.

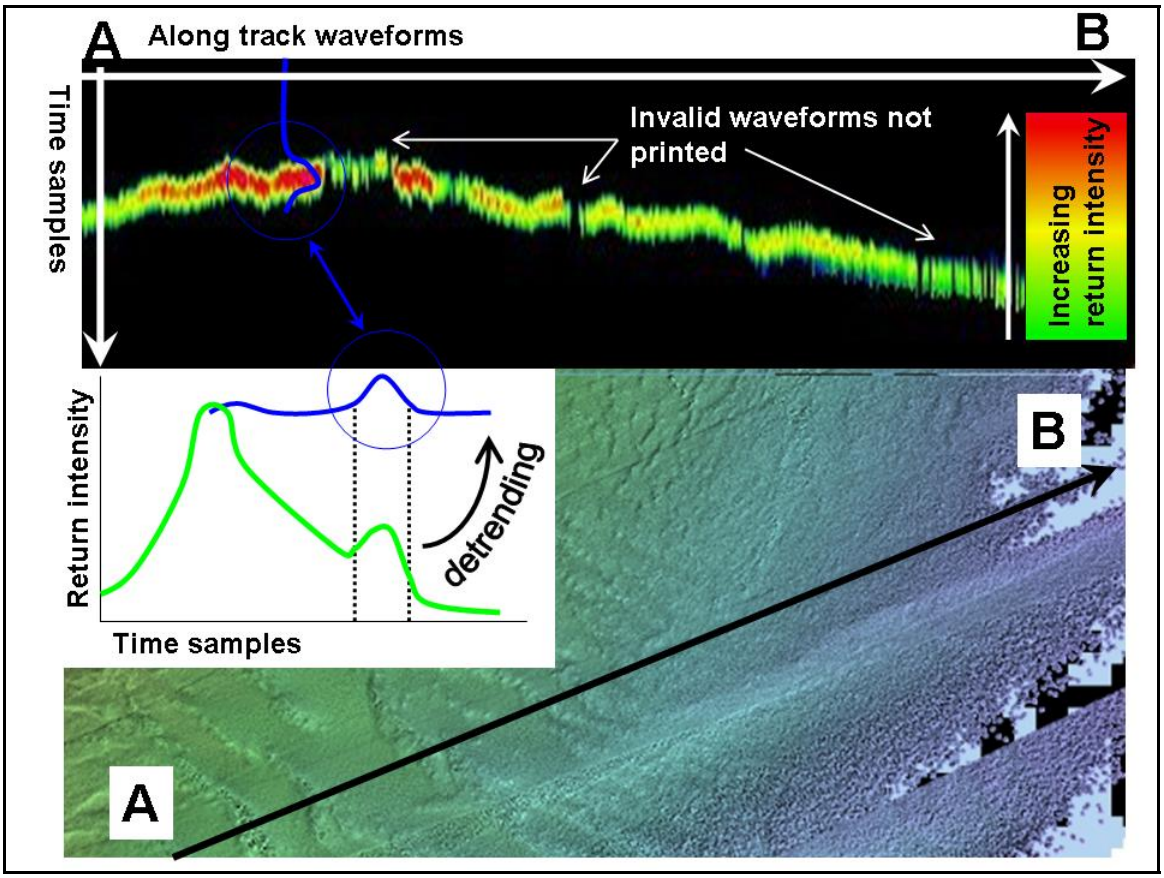

Figure 4.2 An example from a vertical waveform profile. Waveforms between 'A' and 'B' are detrended and vertically plotted. Invalid flagged waveforms, which, for example, occur in the deep section near 'B', are not plotted. From the profile it can be seen that the bottom return intensity in the troughs appear weaker. Distance A-B ~800m

4.2 Waveform parameter extraction

The first step in the waveform characterization process is to locate specific points on the waveform from which certain characterizing parameters and the water clarity descriptor are determined. The waveform parameters describe the dimension and shape of the bottom return from the green laser GAPD and PMT waveforms. These bottom return parameters include 1) the height, defined as the top of the bottom return to the extended attenuation curve, 2) width, located between the points where the waveform leaves and

rejoins the attenuation curve, 3) rise and fall slopes, and finally, 4) area of the bottom return, again bounded by the attenuation curve (Figure 4.3). Maps of the extracted bottom return height showed the best contrast and correlation with seabed material; thus, this waveform parameter was chosen to use as a descriptor for the characterization.

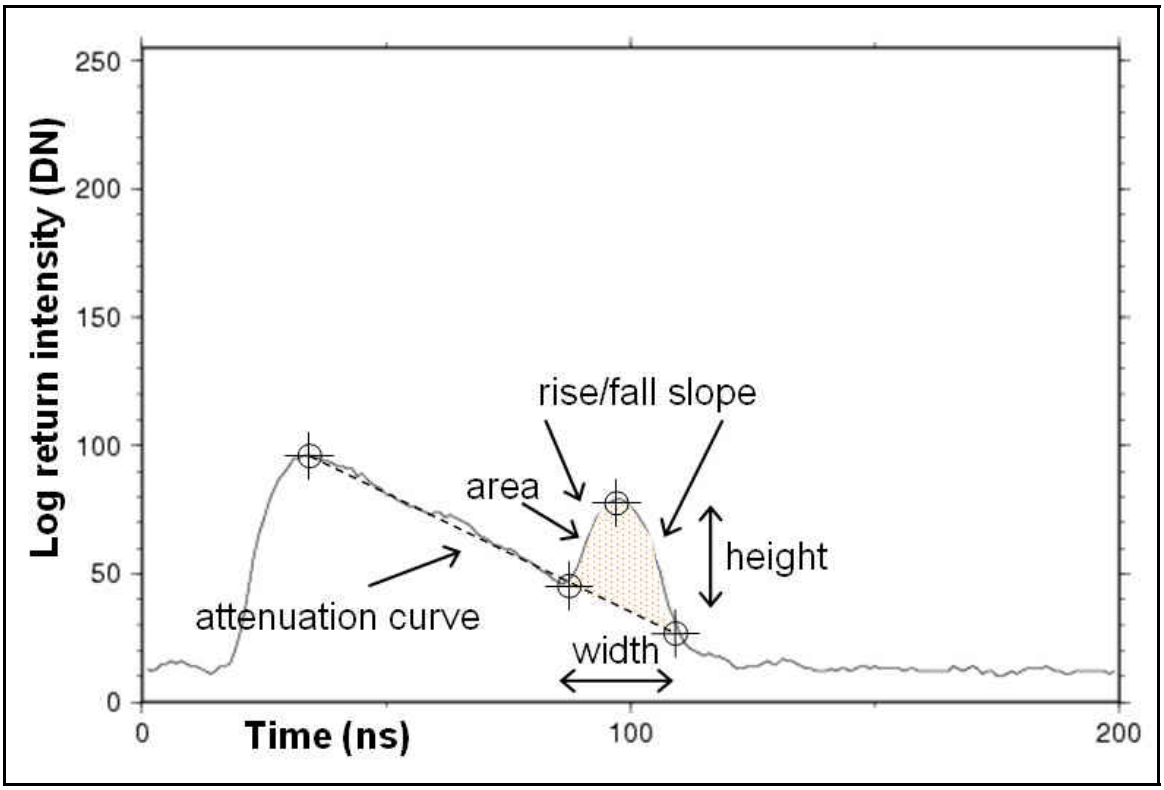

Figure 4.3 From four points on the waveform (surface return, start of bottom return, top of bottom return, and end of bottom return) presented by the markers, the waveform parameters (height, width, rise and fall slopes, and area) were determined.

Before the waveform parameters are determined, the water returns are separated from land returns. Due to the unambiguous detection of a water surface with the Raman channel, waveforms from this channel are used as separators: only green laser waveforms with an associated Raman return that exceeds a predefined threshold are considered. A routine named get_bot_char is used to locate the surface return, the start and end of the

bottom return, and the top of the bottom return. The routine is a chain of operations, which are schematically presented in Figure 4.6. First, the waveform is smoothed with a, 10-sample moving box averaging filter. Then, the surface return is located. To prevent a strong bottom return being identified as surface return, instead of choosing the highest intensity on the waveform, the maxima and minima of the first derivative from the first section of the waveform is located. Between these points, the surface return is then easily located as the highest peak. This approach works better than searching for the first zero crossing of the first derivative because, although smoothed, the surface return proceeds with some noisy samples. The start of the bottom return is identified as the maxima of the first derivative after the surface return. The following intensity peak is then the bottom return. The end of the bottom return is found as the point on the waveform that crosses with the extended attenuation curve. The method for extracting the water clarity or attenuation curve will be discussed in section 4.3.

Figure 4.4a demonstrates a PMT and GAPD waveform with the above described procedure successfully performed. Waveforms of vegetation hits do not show the characteristic second peak, instead a slight undulation in the decaying waveform represents the bottom, or vegetation, return (Figure 4.4b). In these situations, the derivative approach fails. In addition, the derivative approach is, although applied to the smoothed waveform only, very sensitive to noise and therefore this approach does not always return satisfying results. The get_bot_char routine assesses the results from the derivative approach, when the waveform does not pass the checks, it is flagged as invalid, and a second approach is attempted. This second attempt is rigorous but successful, many invalid vegetation returns, for example, pass the assessment the second time. The point

when the waveform sinks into the noise level is located. Between this point and the surface return, a straight line is drawn (dashed white line in Figure 4.4b). The top of the bottom return is then considered to be at the maximum residual between waveform and the straight line. The improved start of the bottom return is then easily found as the lowest value between surface and bottom return. When the re-determined waveform parameters fail the second assessment, they are flagged as invalid and are ignored for the remainder of the characterization routine. Valid flagged waveforms are passed on to the water clarity parameter extraction function. This function is called twice in the characterization routine: first, to get an estimate of the signal decay, which is used to detrend and relocate the bottom return parameters; and second, for the final water clarity parameter, which will improve with the improved bottom return parameters, as well.

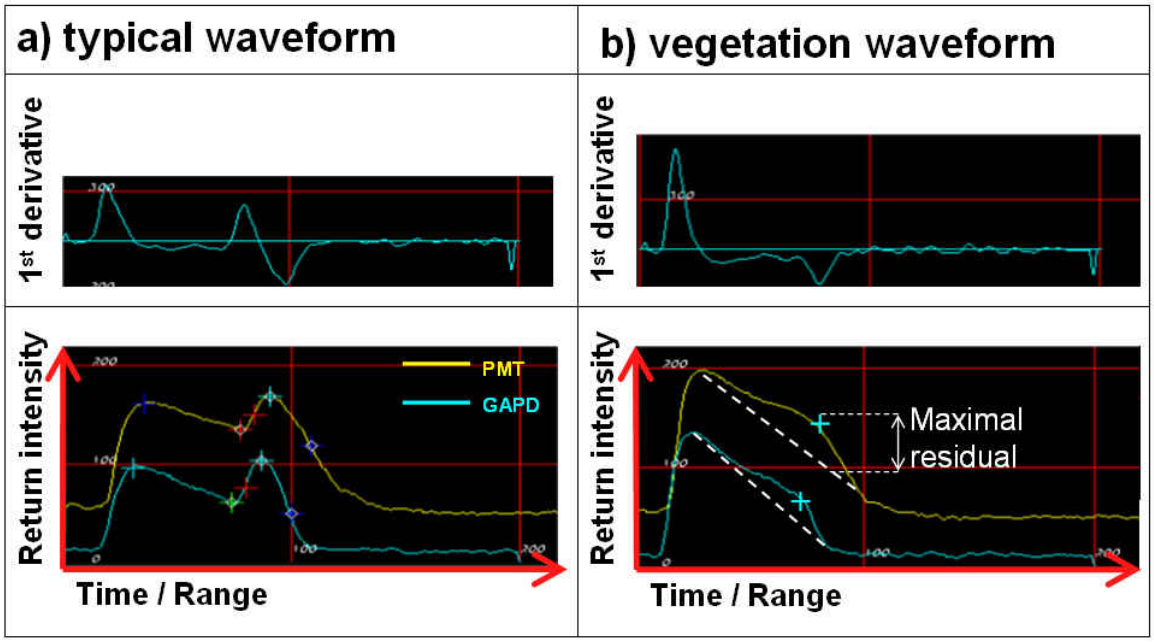

Figure 4.4 Results from the get_bot_char routine using a) the derivative approach, and b) an approach that anticipates the reduced returns from vegetation hits. The markers indicate the surface return, start of bottom return, 50% of the leading edge, top of bottom return, and end of bottom return. The maximal residual between the waveform and the white dashed line in b) presents the top

of the bottom return. Note, only the derivatives of the GAPD waveform is presented here.

The maximum residual approach gives a fair estimate of the top of the bottom return, but the start of the bottom return may be located directly against the top of the bottom return. A neighboring start and top of bottom return is frequently seen at waveforms from vegetation, from which a significant return is difficult to discriminate (Figure 4.4b). These situations bias the water clarity extraction, as will be discussed in Section 4.3. Once a waveform successfully passes the derivative or maximum residual approach the slope of the attdecay of the signal (the attenuation curve in Figure 4.3) is determined. With the estimation of signal decay, the end of the bottom return is relocated at the intersection of the waveform signal and extrapolation of the decay. The signal decay is also used to detrend the waveform. The waveform is detrended until the location of the end of the bottom return, by which the top of the bottom return is now easily found as the highest value on that detrended waveform. The start of the bottom return is located when the detrended waveform exceeds the baseline (Figure 4.5).

The detrending approach mainly improves the start of the bottom return, and subsequently improves the signal decay (water clarity parameter) when it is determined for the second time. Hereafter, the signal decay is again used to locate the end of the bottom return but most importantly, the height of the bottom return, which is chosen as *the* characterizing element of the waveform.

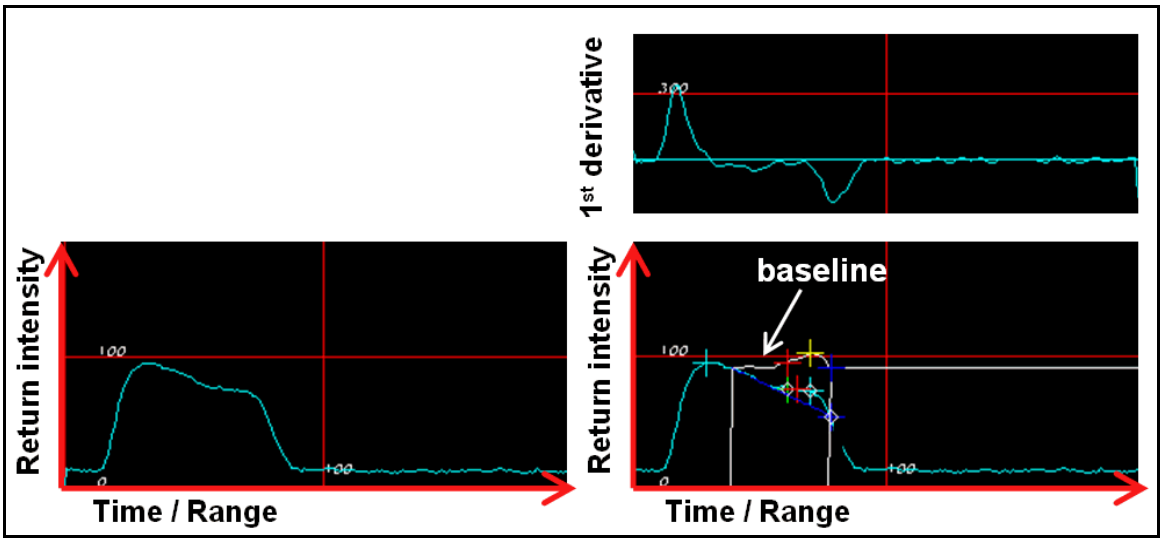

Figure 4.5 An example of detrending the waveform to locate the bottom return parameters. Note that the derivatives do not show a zero-crossing at the bottom return.

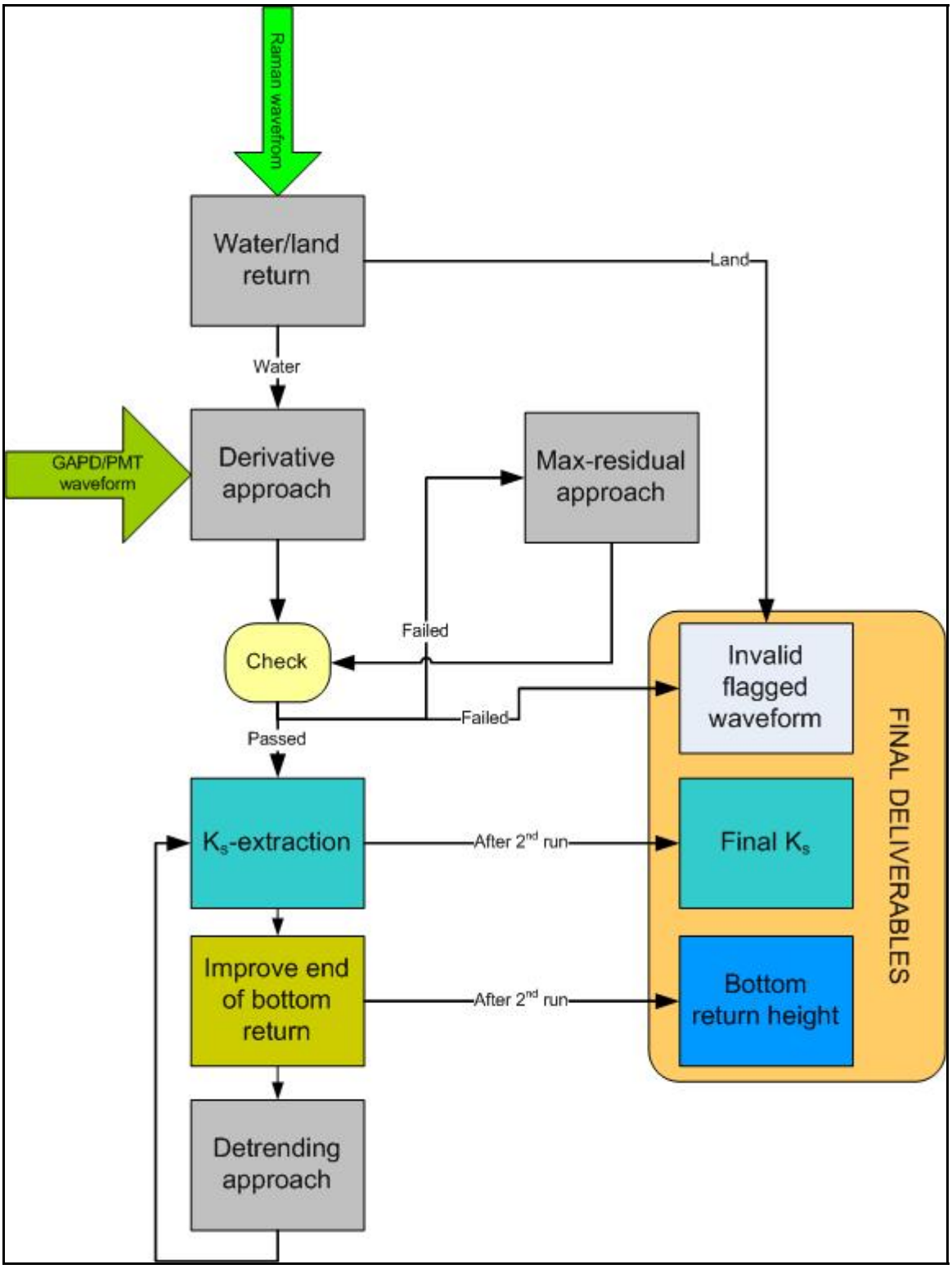

Figure 4.6 Schematic representation of the get_bot_char routine.

4.3 Water clarity extraction

The signature of the water clarity is seen on the green laser waveforms by examining the slope of the decaying signal. This decay, which is of exponential nature in linear space (Equation 2.6), becomes stronger in more dirty waters. Indeed, if the water is extremely clear, a minimal amount of energy will be attenuated and the slope of the decaying signal approaches zero. Thus, the slope may be used as a descriptive term of the water clarity at the designated wavelength. Also, as hinted in section 2.4, as the slope of the decaying signal is influenced by the FOV, water clarity values from a GAPD or PMT waveform will differ. However, their spatial variability corresponds; i.e. they describe the same water clarity changes (Figure 4.9). Due to the much larger FOV, the PMT waveform will have a smaller slope, indicating less loss. As the extracted water clarity parameter is influenced by wavelength and FOV, the parameter will therefore be referred to as the system attenuation coefficient k_s at either a GAPD or PMT waveform.

The section of the waveform from which k_s is extracted should cover the complete water column return (Figure 4.7). The volume return is assumed to lie between the surface return plus a 10 ns offset (~1.15 m) to exclude late surface reflections, and the start of the bottom return. Invalid flagged waveforms and waveforms from depths less than 2.2 m are rejected for the water clarity extraction process. As we are dealing with logarithmically compressed values, the exponential decay in originally linear space is presented in the waveform as the linear slope of the volume return in logarithmic space. The intensities (I) on the volume return are then linearly described at each time bin (t) with

$$I_n = I_0 - k_s 0.115 \cdot (t_n - t_0) \qquad (4.1),$$

where the constant 0.115 represents the two way travel time in each time bin (1ns wide), and k_s is expressed in DN/m. Note that, although k_s represents a decaying trend, the negative sign is omitted but incorporated in Equation 4.1. Therefore, all k_s-values presented in this work are positive: increasing k_s reflects an increased decay; thus, more turbid water.

Two arrays are filled with intensity and range ($\Delta t \cdot 0.115$) values found on the volume return. These two arrays are used for a least squares fit, which returns a best approximation of the volume return slope, or water clarity, k_s.

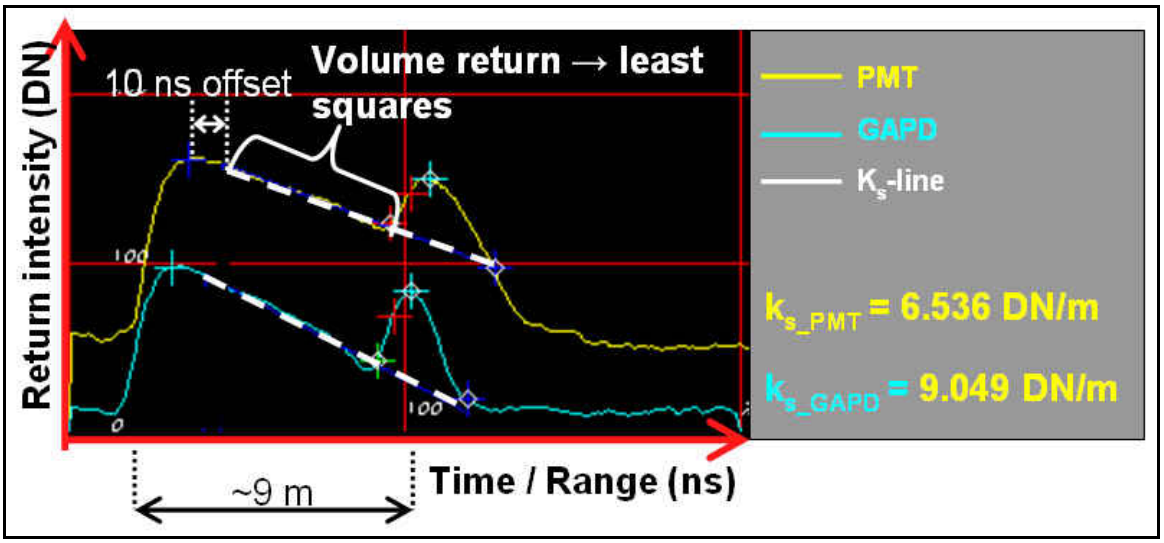

Figure 4.7 Example of the derivation of k_s from a green laser waveform.

It is difficult to determine the start of the bottom return when the waveform does not have a distinct bottom return. This, for example, is the case if the green laser beam reflects on vegetation. In these circumstances the start of the bottom return will lay higher, resulting in a less steep slope. The water clarity will appear to improve above the vegetation. This bias is minimized by applying a negative time offset to the start of the

bottom return. Of course, applying the offset reduces the portion of the waveform on which the least squares is performed, thus excluding some waveforms that do not fit the criteria for k_s-extraction anymore. The examples in Figure 4.8 illustrate what has been explained: due to the poor bottom return peak from vegetation reflections, the extracted k_s is higher than surrounding waveforms.

Section 5.2 discusses the analysis and results of the water clarity maps.

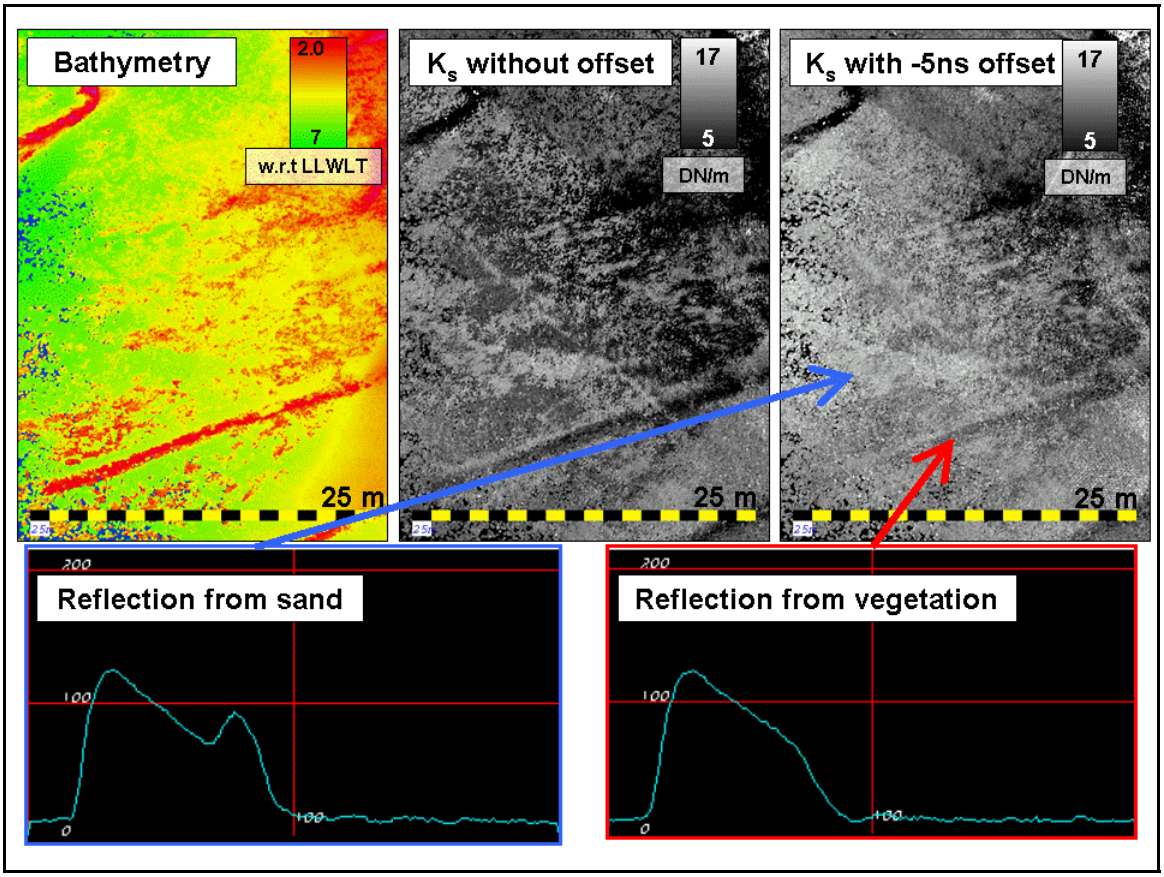

Figure 4.8 When the laser reflects on vegetation, the transition from volume return to bottom return in the waveform, which is assumed to be at the start of the bottom return, is much less significant. As a result, the extracted k_s is lower (clearer water) than surrounding waveforms. The contamination of vegetation to k_s is reduced when an -5 ns offset is applied, although shallow soundings from the vegetation remain that correspond with lower k_s values. Note the slight line-to-line variation in the top right of the k_s-images.

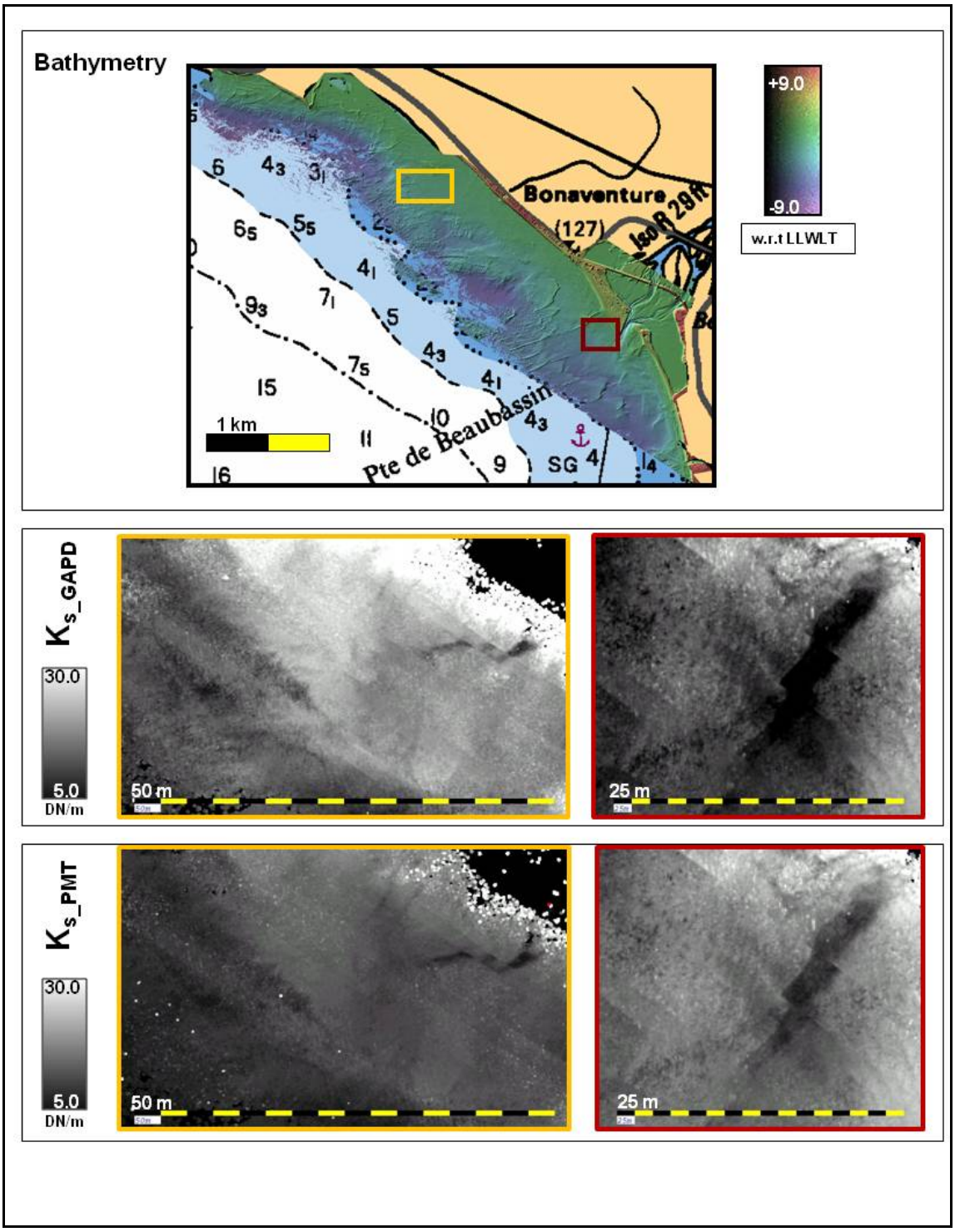

Figure 4.9 An example demonstrating the consistency between the system attenuation coefficient derived from GAPD and PMT waveforms. Vegetation hits have a blunted bottom return which complicates the k_s extraction, leading to noisy results. The features seen in the water clarity maps are not present in the bathymetry. Note the misalignment of a clear water mass between consecutive swaths in both examples. The left water mass migrated approximately 75 m in 6 minutes (20 m/s) south easterly; the right water mass migrated 17 m in more than 5 minutes (0.05 m/s) south easterly. Section 5.2 discusses the results of the water clarity maps.

4.4 Waveform effects

We would like to characterize the green laser waveform, based, for example, on its bottom return height, to identify seabed material changes. Before we can confidentially do so, we need to investigate the influence other variables have on the waveform, and specifically, the bottom return. These variables, as mentioned in Section 2.5, include depth, water clarity, surface waves, and seabed slope.

4.4.1 Seabed slope

When considering the seabed slope, we are examining the depth changes within the beam footprint, in fact, the slope of the illuminated area. It is this intra beam seabed slope that can influence the bottom return height, as reported by Steinvall and Koppari [1996]. Note that seabed slope effects apply to the effect of depth changes on the waveform within the illuminated area whereas depth effects (discussed in 4.4.5) apply to the effect of depth changes between individual beams. The effect of a bottom slope on the green laser beam is illustrated in Figure 4.10. The left example shows the beam illuminating a flat seabed. Once the seabed is tilted, the illuminated area will change while the amount of energy projected on the area remains the same but is dispersed differently, ultimately affecting the bottom return shape and magnitude. When the seabed is tilted away from the off-nadir beam direction, energy is more dispersed leading to a diminished bottom return (Figure 4.10, middle). The opposite happens when the seabed slopes towards the off-nadir beam direction: energy is now more focused leading to a

sharper bottom return (Figure 4.10, right).

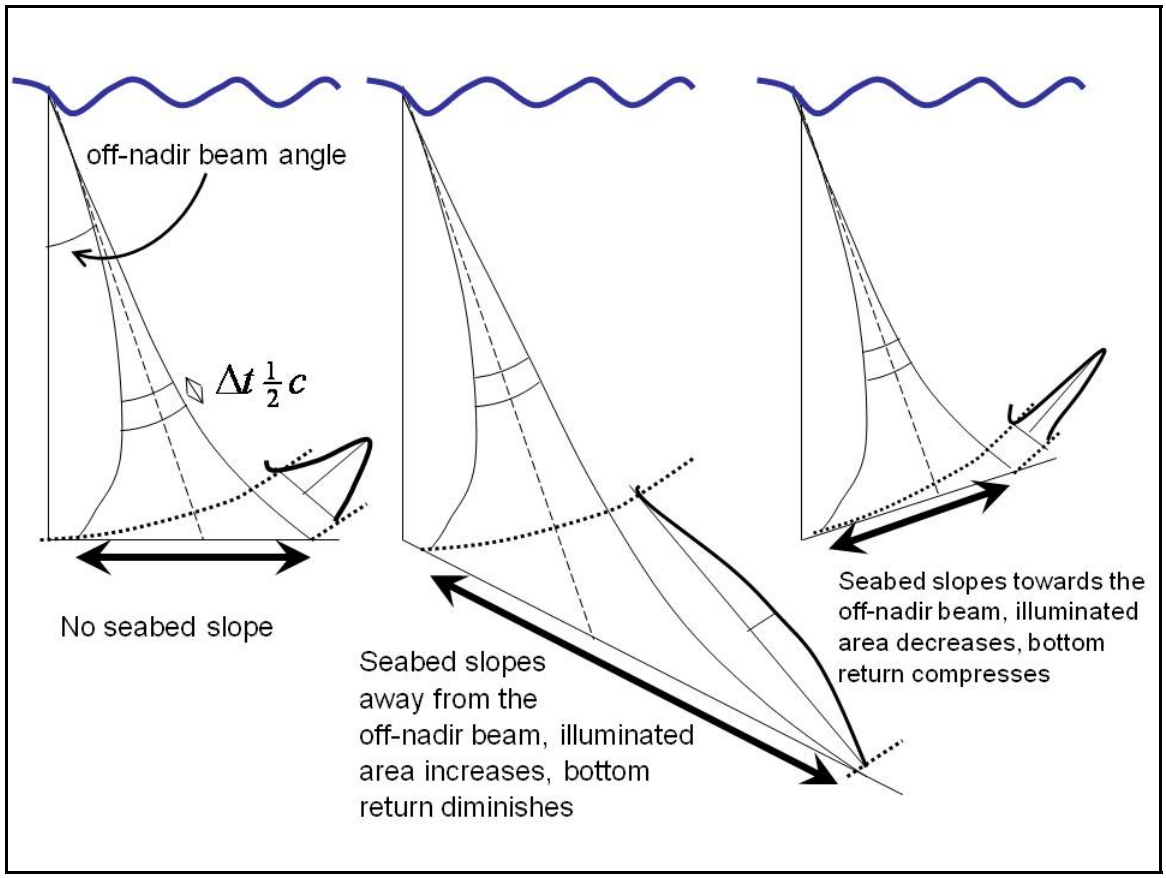

Figure 4.10 The green laser beam when it interacts with the seabed and the resulting bottom return. The effective range resolution is a function of pulse duration, digitizer bin, and detector response.

Due to the nature of the geomorphology, the seabed slope at all the locations in the survey area is less than a degree, suggesting that the intra beam slopes are negligible as well (Figure 4.11). This suggestion is explored with the plots in Figure 4.12. Bottom return heights are extracted from overlapping portions of two lines, which were flown in opposite directions (marked with the dashed arrow in Figure 4.11). If the intra beam slopes significantly affect the bottom returns, their height for the overlapping illuminated areas should differ considerably; indicating a overestimated bottom return height when beams are directed against the slope, and a underestimated bottom return heights when

beams are directed with the slope. The left plot in Figure 4.12 shows minor differences, while the right plot demonstrates that the slope over approximately 10 m in across track direction (negative values indicating sloping towards the shore) is minimal, too. These results imply that an intra beam slope, or the effect thereof, is non-existent and can justifiably be ignored for the waveform characterization correction procedure.

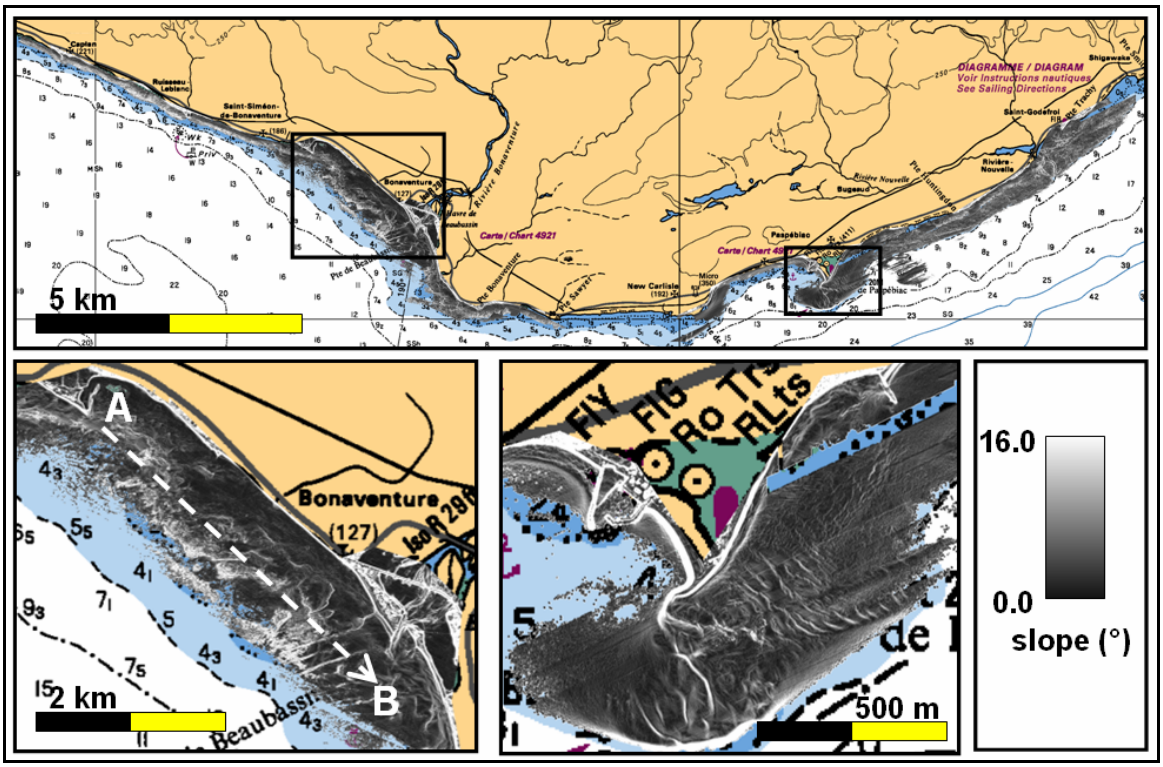

Figure 4.11 Terrain model illustrating of the seabed slopes (degrees). Typical slope angles are less than 1.0. Higher slopes are seen when the laser tracks the weed (bottom left, up to 16°) and at sand waves (bottom middle, up to 6°). The dashed A – B arrow relates to the overlapping swaths used in Figure 4.12.

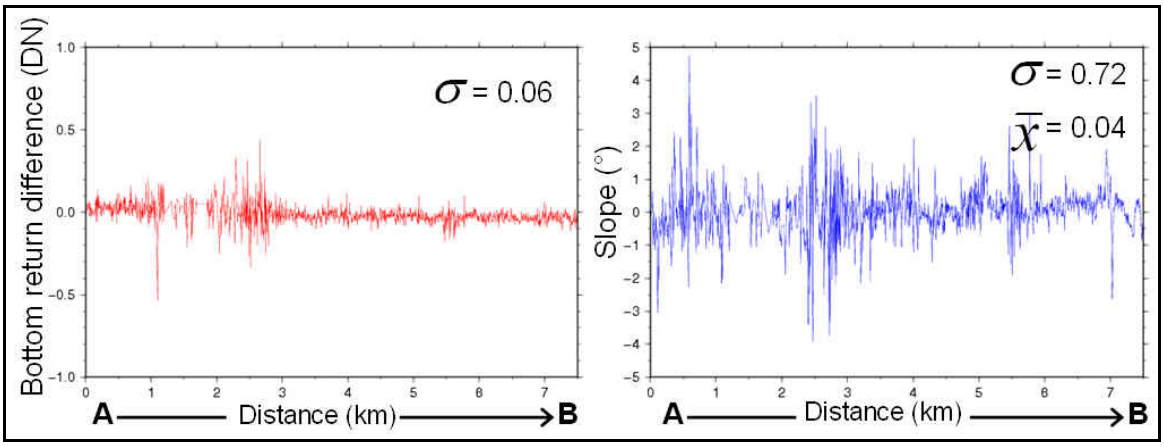

Figure 4.12 The bottom return differences (given in digital numbers) of the bottom return at overlapping footprints have little variance and are minimal. The slope is determined 10 m across track towards the shore from each overlapping beam footprint. Positive slopes indicate the seabed sloping down off shore. Note the matching peaks in the left portion of both plots. In this area many datagaps and false soundings were seen as a result of aquatic vegetation.

4.4.2 Surface topography

Surface waves focus or defocus the beams that pass the air – water boundary, resulting in an unequal amount of energy from shot to shot projected on the seabed. In addition, the light will focus or defocus again when it returns to the receiver. This double focusing effect may lead to a variation of the bottom return height.

The infrared laser beam peak intensity and the wave heights derived from the slant ranges were chosen to represent the surface reflection and topography, respectively. Both datasets were compared against the bottom return height, to investigate whether surface related spatial patterns were overprinted in the bottom return height. The infrared laser beam attenuates almost immediately once it strikes on the water surface, while the surface return of the green laser beam will include increased contribution from the volume return. For that reason, the infrared laser beam has the preference above the green laser beam for this experiment.

Figure 4.13 presents maps of the GAPD bottom return height (top left and middle), infrared laser beam peak intensity (top right and middle), and surface wave heights from north-east oriented- (bottom left) and south-west oriented lines (bottom right). With the associated Raman waveforms, land returns are excluded and invalid flagged waveforms were not included in these datasets. The result of the waveform validation procedure can be seen in the marsh area in the top right of both bottom return height and infrared maps. With inclusion of the Raman waveforms, small channels and pools are discriminated from land. However, due to the shallowness of the marshes, the bottom return of the green waveforms were merged with the surface return, and subsequently the waveforms will not pass the checks.

One may also observe data gaps in the eastern section in both the bottom return height and infrared laser beam peak intensity map. Data gaps from the GAPD data are due to depths at these locations exceeding the extinction depth (~12 m). The infrared data show an extended coverage because the 'deep' PMT channel was more successful. If, during SHOALS processing, a depth cannot be resolved from either the GAPD or PMT channel, none of the waveforms are provided, resulting in data gaps in the infrared and the Raman data as well. Note also the match between the bathymetry contour (in fathoms) from the background chart, and signal loss.

The bottom return height in Figure 4.13 top left faintly decreases off-shore; strongest returns are seen around the sand spit in the southern section, and noise appears near the extinction area. Low bottom return heights are present at the sand wave field. These trends are further discussed in section 4.4.5.

The striping seen in the infrared laser beam peak intensity map is directly related to the

flight altitude. Flight lines collected at approximately 10 m higher altitude resulted in lower infrared laser beam peak intensity (in log space: 10 DN, or 17% less). However, the striping pattern is not present in the bottom return height map. Altitude dependence is discussed in Section 4.4.4.

The infrared laser beam intensity map also shows spatial patterns of high infrared intensities. These patterns suggest some kind of surface related feature such as slick lines. Aerial photography did not reveal any surface features, but water clarity maps showed a strong match. In section 5.2, this correlation is explored in more detail. Spatial patterns such as those presented in Figure 4.13 top left were not seen back in the bottom return height data. One exception, however, is presented in the middle images of Figure 4.13. The close-up from the infrared data (Figure 4.13 middle right) shows line to line shifts, indicating that the feature was moving. On one rare occasion, the peak intensity is overprinted on the bottom return height, resulting in a lower bottom return height (Figure 4.13, middle). This indeed makes sense; when more energy is reflected at the air/water interface, less energy will remain for the bottom interaction while the laser propagates to and from the seabed.

Finally, the bottom images of Figure 4.13 show the wave heights while the aircraft traveled in north-east and south-west. Theses two sets of flight lines are displayed separately to prevent overlapping wave height being interpolated during the weighted gridding process. It will be clear from these examples that the surface waves also do not appear in the bottom return height.

With the exception of the weak correlation seen in Figure 4.13 left middle image, surface related effects (i.e., topography or reflectance related surface effects) appeared to

have no significant influence on the bottom return height and are therefore ignored. Should there be more significant sea surface effects such as tide or vegetation slicks and large swell (neither of which were present), then this decision may have to be reconsidered.

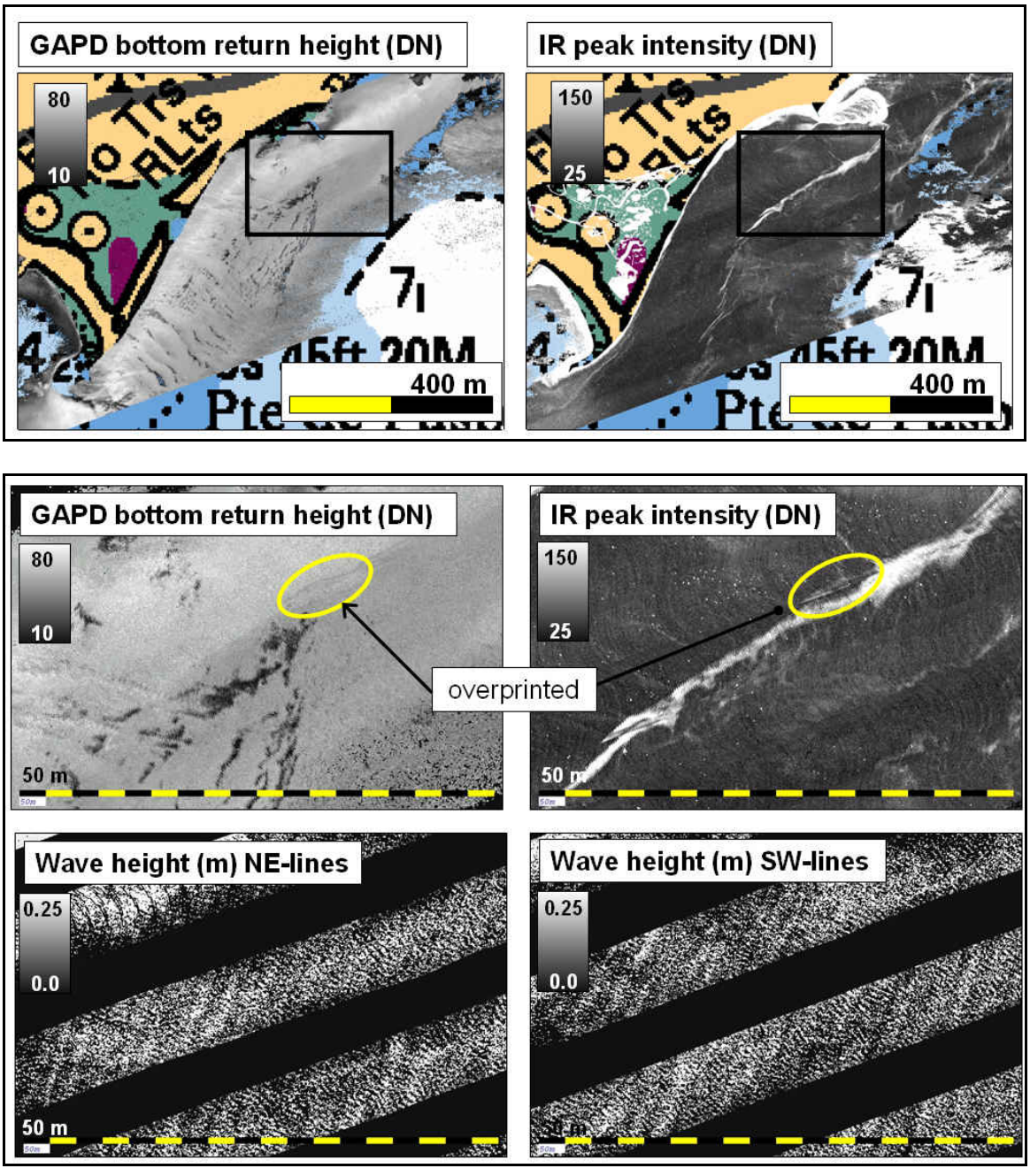

Figure 4.13 Bottom return height and infrared laser beam peak intensity maps above an area with sandwaves (top), and close-ups with wave heights (middle and bottom).

4.4.3 Water clarity

Light through turbid water will undergo an increased amount of absorption and scattering events, which reduce the amount of energy transmitted to and from the seabed. The net result would be a reduction of the bottom return amplitude if measured from zero. This type of amplitude was used by Dijkstra and Elston [2004] who indeed reported different decaying trends within their dataset, and suggested this difference was due to water mass changes (Figure 4.14). As explained in Section 2.5.2, the bottom return height derived with our algorithm is measured in logarithmic space relative to the attenuation curve; therefore instantly avoiding the attenuation effect.

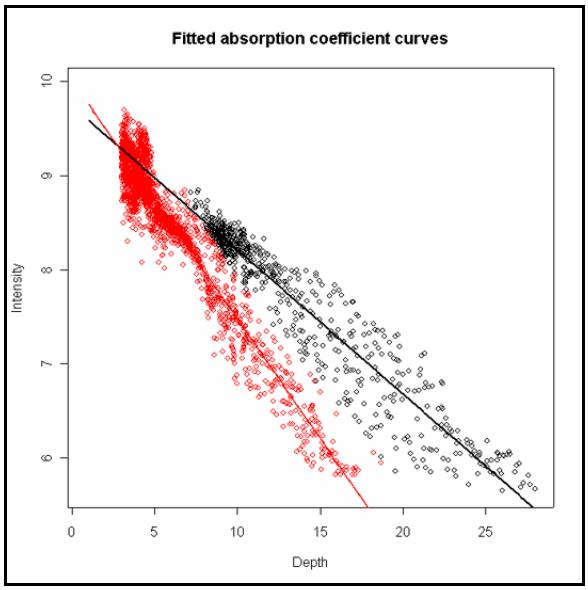

Figure 4.14 Two decaying trends linked to water mass changes. From Dijkstra and Elston [2004].

For this analysis, four datasets from two locations, Bonaventure and Paspébiac,

were used (Table 4.1). Bottom return height, and k_s-maps of these four datasets are presented in Figures 4.15 to 4.22. The data at each location cover approximately the same area, but were collected at different survey times, allowing us to compare the spatial and temporal variability of the water clarity over a period of ~24 hours, but more importantly, examine the water clarity changes in relation to bottom return height.

Table 4.1 GAPD waveform data used for the analysis in this section.

Dataset	Location	Spot spacing (m)	Survey date, time (UTC)
A	Bonaventure	2 x 2	July 3rd, 2006, $19^{26} - 21^{48}$
B	Bonaventure	4 x 4	July 2nd, 2006, $12^{01} - 13^{48}$
C	Paspébiac	2 x 2	July 4th, 2006, $12^{03} - 13^{21}$
D	Paspébiac	4 x 4	July 3rd, 2006, $12^{45} - 16^{01}$

The k_s of dataset A and B show different patterns, but most evident is the different green laser beam range performance. Dataset A, which was collected a day after dataset B, contains returns in the north while the green laser beam in dataset B failed. Not surprisingly, the mean k_s of dataset A is smaller than that of dataset B, indicating less turbid water at dataset A. Note also data gaps near shore; at these locations, the waveform is flagged as invalid for k_s-extraction when the surface and bottom return are merged, or when the volume return is not considered long enough (> 15 ns ~1.7 m). Additionally, the k_s-maps of datasets C and D show spatial and temporal changes: dataset D, for example, is less homogenous than dataset C and shows high k_s-values near shore and above the elongation of the sand spit in the south. Dataset D appears, in general, to be more turbid, as proven by the fact that more deep soundings are present in dataset C. A large water mass with low k_s can be seen in dataset C, and this clear water mass is faintly

represented in the bottom return height map, as well (Figure 4.21 inset). This is the same feature as seen in the infrared laser beam peak intensity map presented in the previous section (Figures 4.13 and 4.17). Figure 4.28 also shows slightly higher bottom return height values as the result of large k_s above the sandspit. An explanation for these contradictions could not be found.

When examining the bottom return height maps of overlapping areas, two interesting processes are detected. Firstly, dataset B appears more successful in extremely shallow locations. In these cases, the data were collected during higher tides, which naturally increased the absolute depth range for the volume return, and led to a waveform without a merged bottom return that successfully passed the validation. The second process is seen in dataset D, where a band of low bottom returns follows the deep water portion of the data. This is a range performance concern (increase of k_s, compared to dataset C, and depth) and is discussed in section 4.4.5.

The weak bottom returns along shore and in sand waves in the Pasbépiac area, and weak returns dispersed over the Bonaventure area, are present in both datasets. Cross plots between overlapping datasets (Figure 4.23 and 4.24) indeed illustrate the correlation, although not compelling. However, the water clarity patterns are not over printed on the bottom return height, which is the main concern. While the cross plots demonstrate that survey-to-survey factors other than water clarity contribute to the bottom return height, apparent water clarity variations do not contaminate the bottom height and, subsequently, the interpretation thereof. Section 5.3.2 explores day-to-day bottom return height variations.

With the exception of the correlation related to the bottom return height derivation

described above, no other correlations between water clarity and bottom return height were discovered. Water clarity effects are suppressed since the bottom return height is measured relative to the attenuation curve in logarithmic space. Based on the SHOALS-3000 dataset used for this work, the water clarity is assumed not to influence the bottom return height.

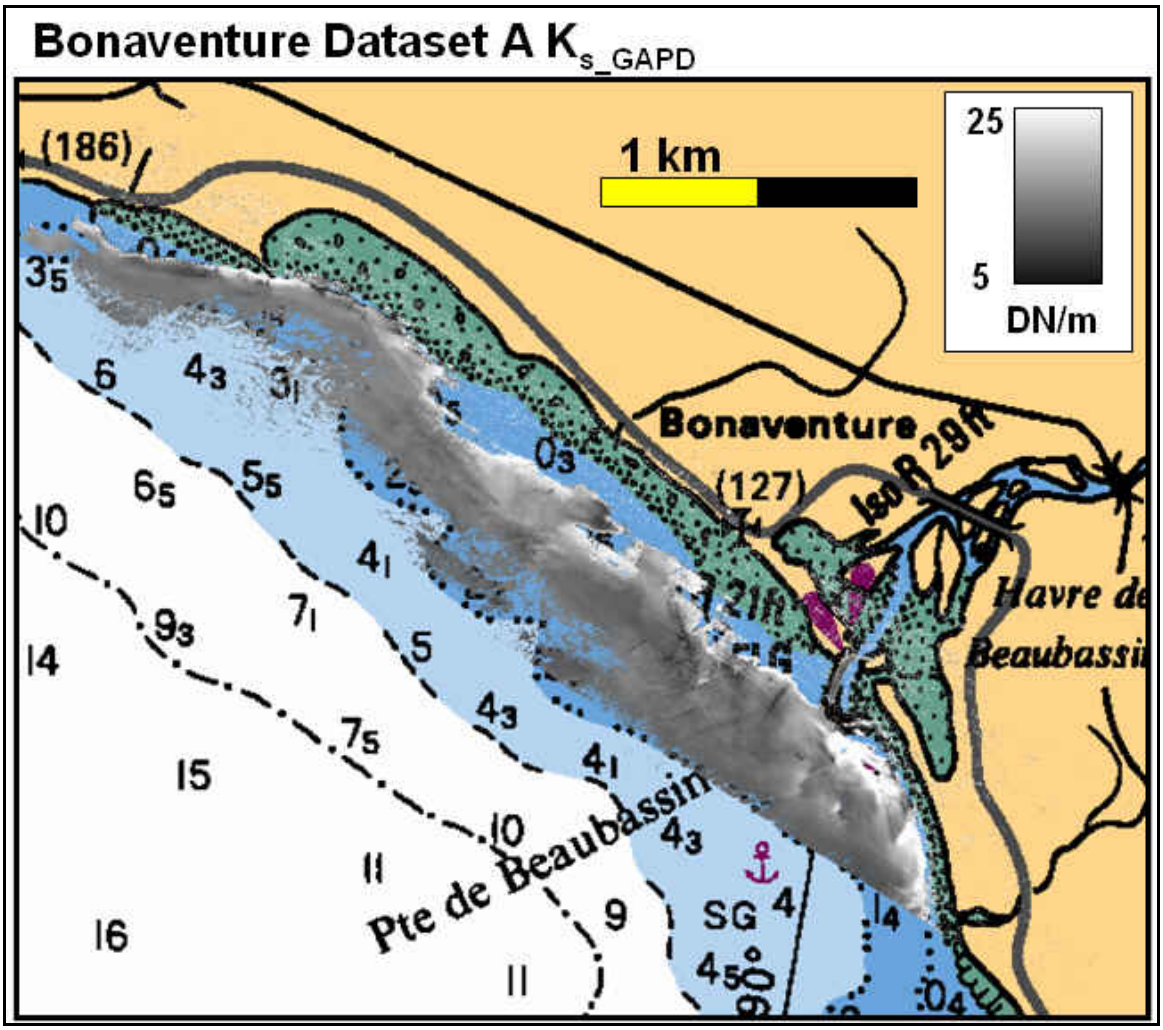

Figure 4.15 k_s **-map from GAPD dataset A, Bonaventure.**

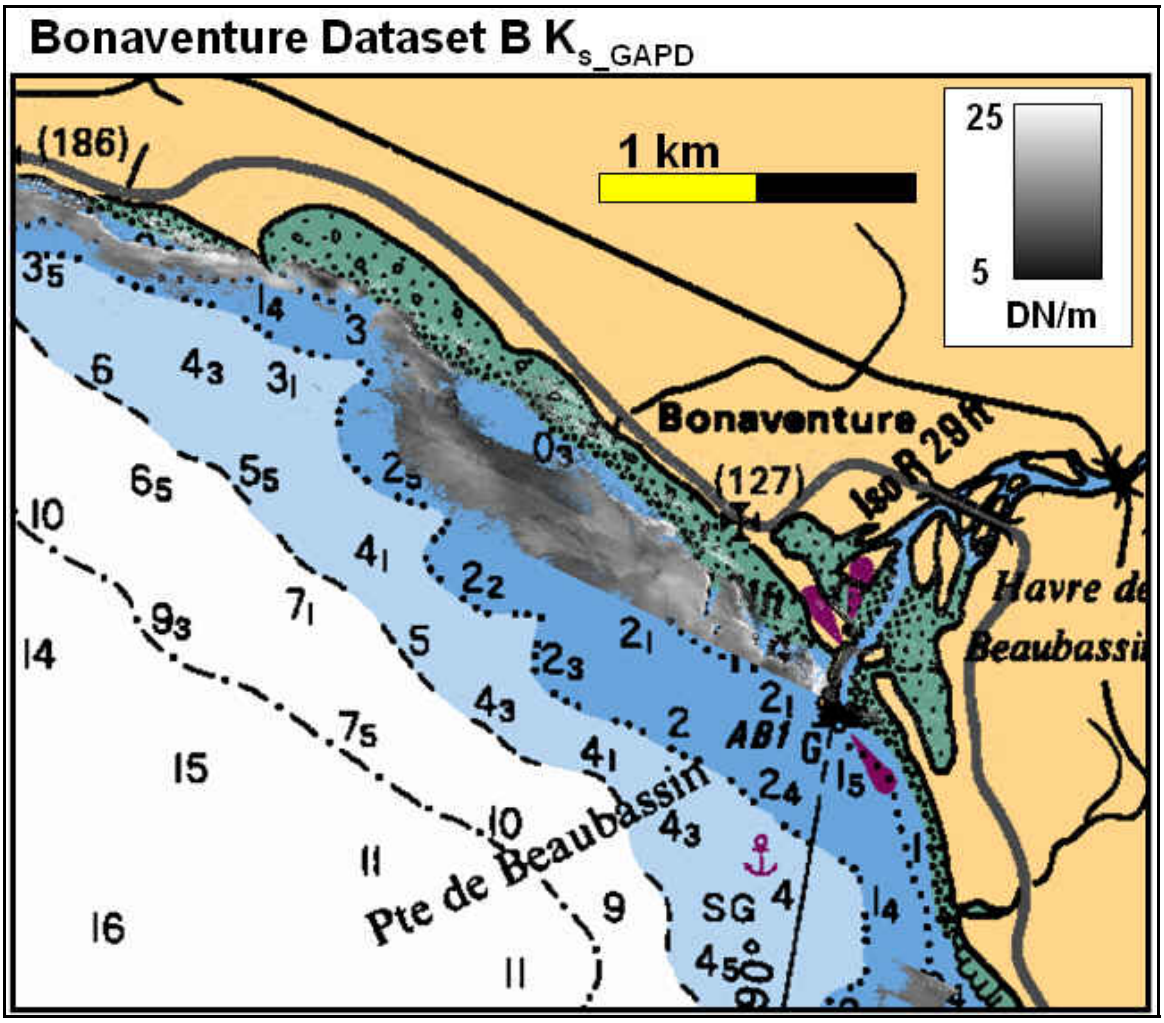

Figure 4.16 k_s **-map from GAPD dataset B, Bonaventure.**

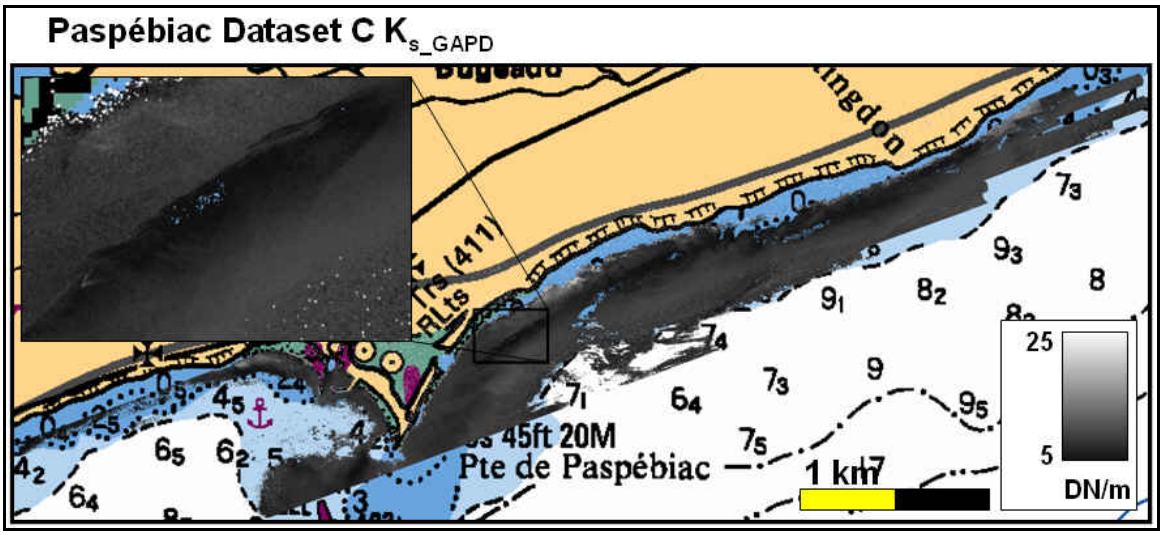

Figure 4.17 k_s **-map from GAPD dataset C, Paspébiac.**

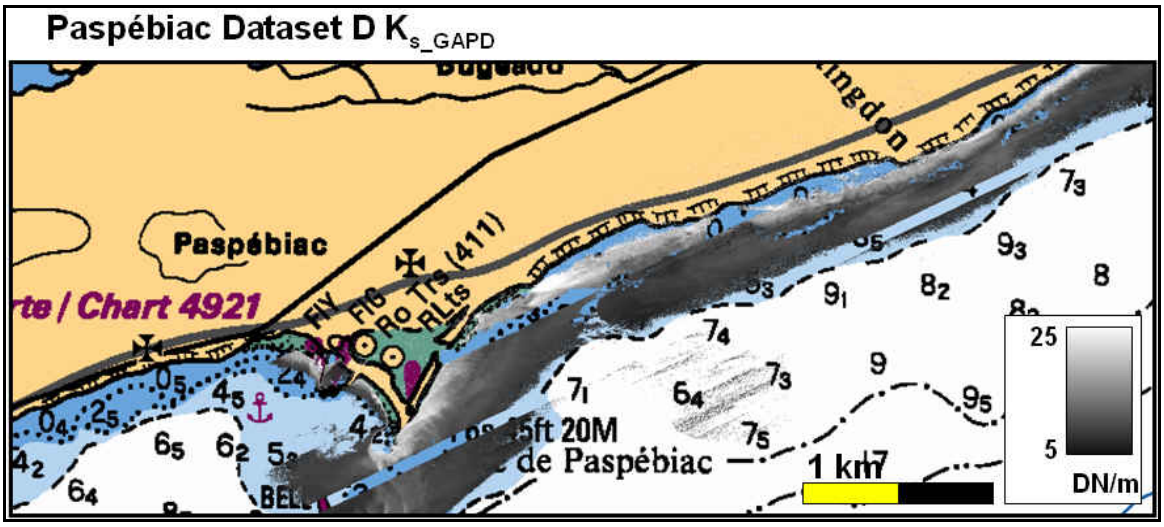

Figure 4.18 k_s **-map from GAPD dataset D, Paspébiac. Waveform data at some flight lines were not provided in the INW-files.**

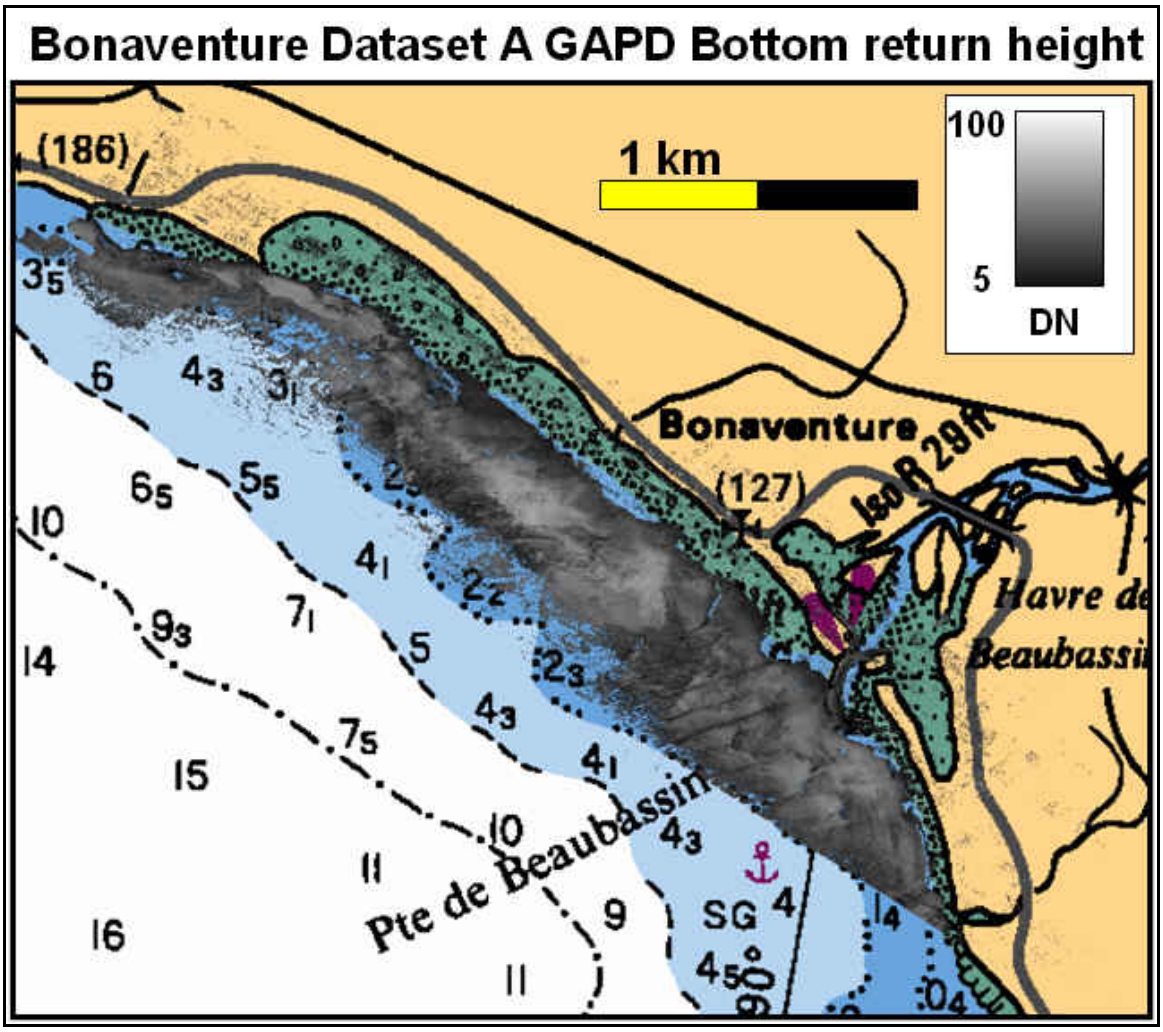

Figure 4.19 GAPD bottom return height map from dataset A, Bonaventure.

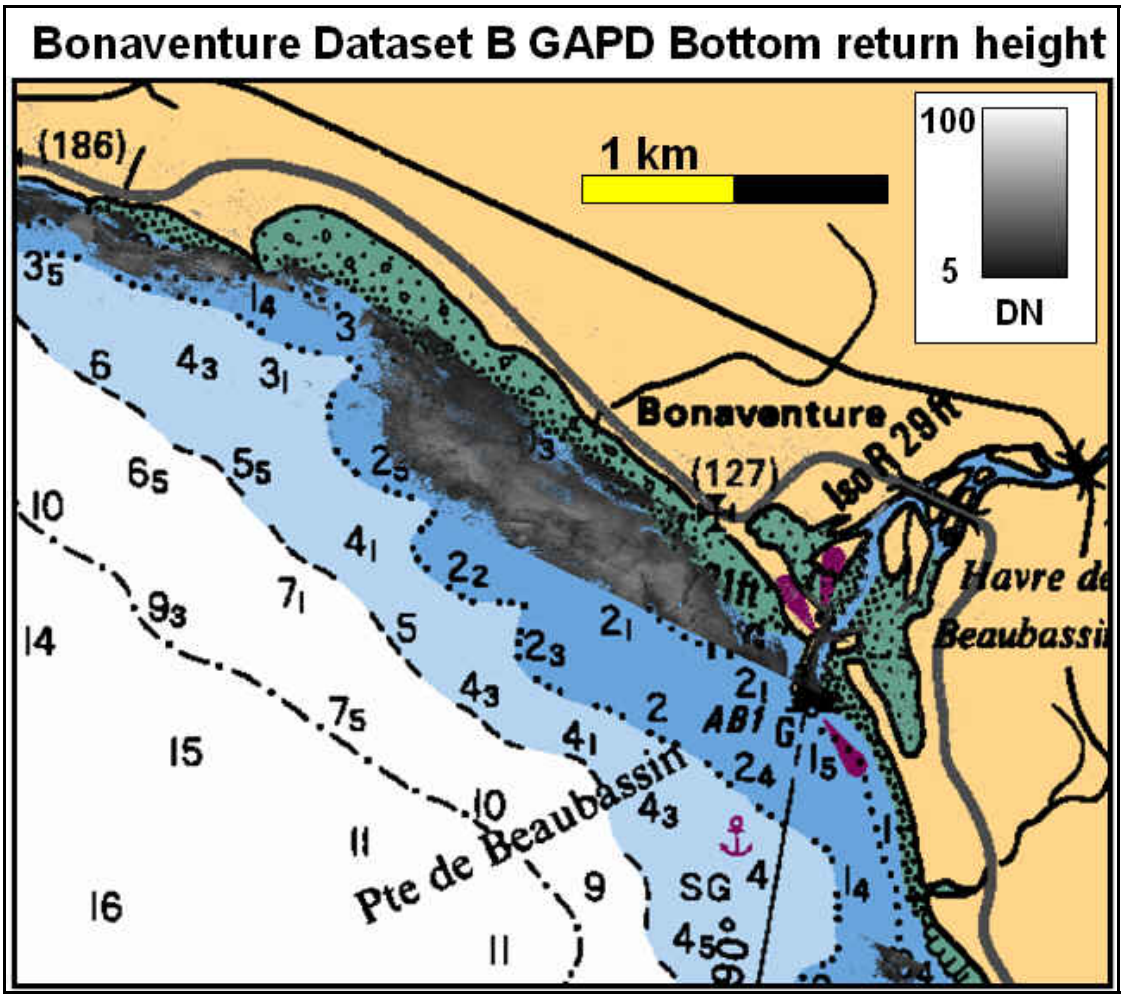

Figure 4.20 GAPD bottom return height map from dataset B, Bonaventure.

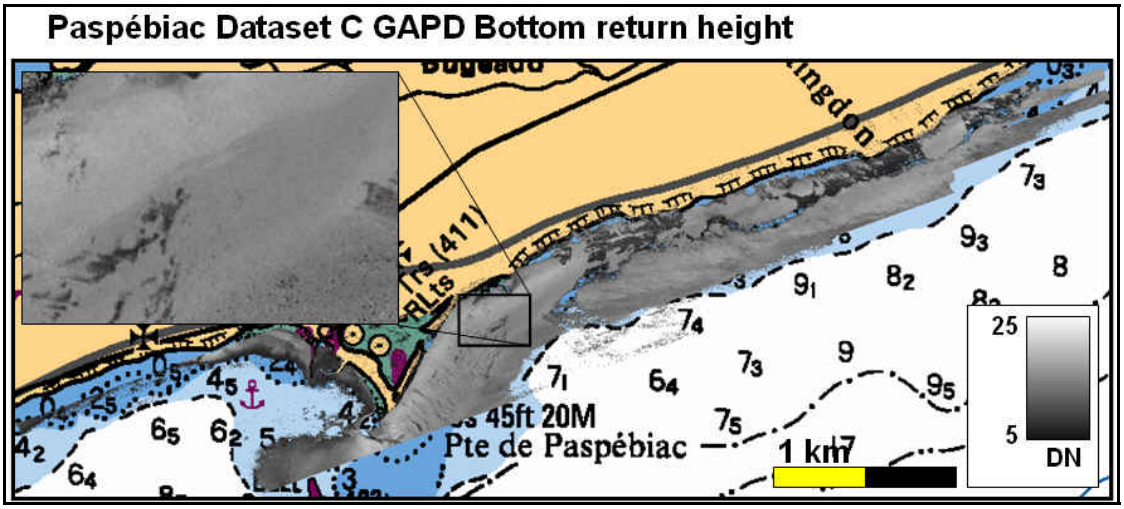

Figure 4.21 GAPD bottom return height map from dataset C, Paspébiac.

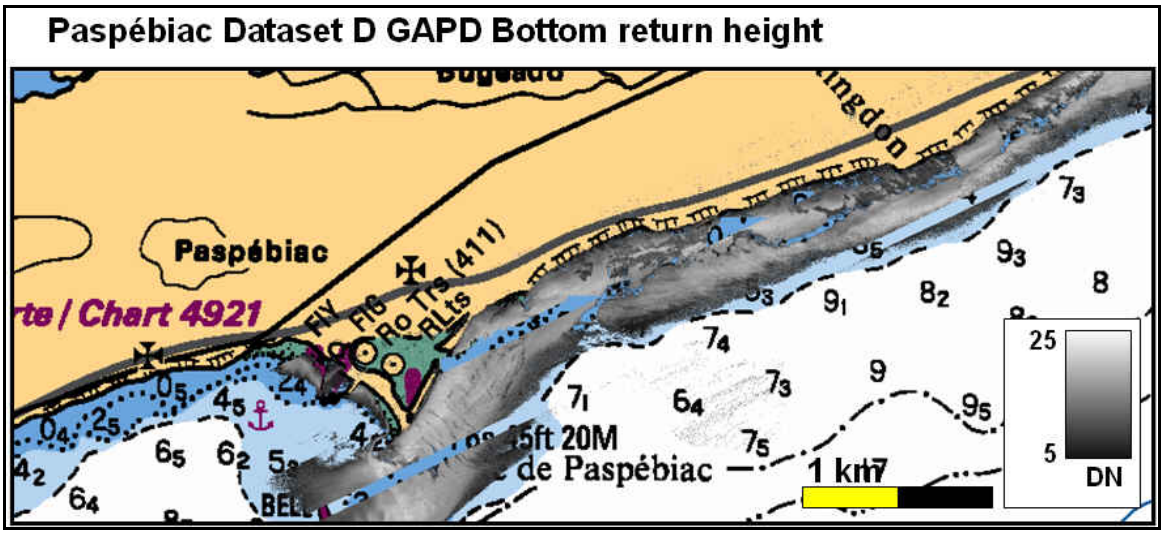

Figure 4.22 GAPD bottom return height map from dataset D, Paspébiac.

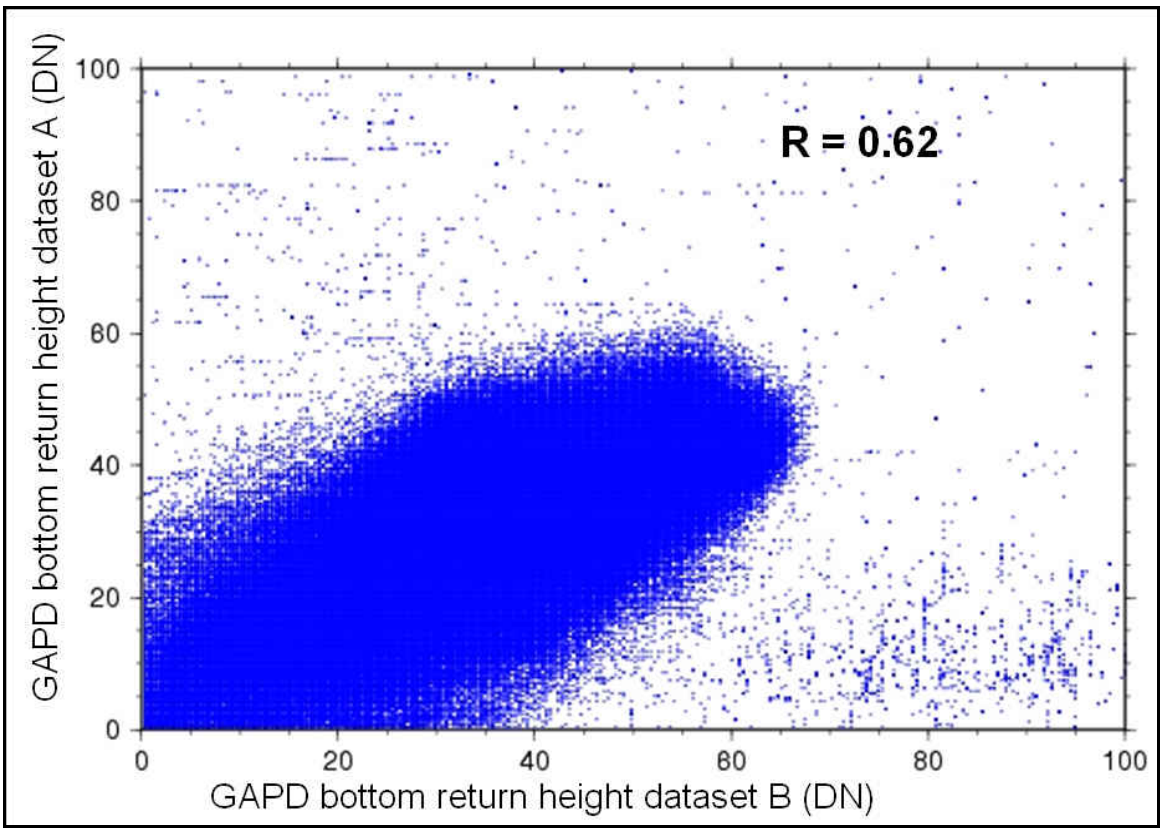

Figure 4.23 Cross plot of GAPD bottom return heights from dataset A and B. Correlation coefficient R = 0.62.

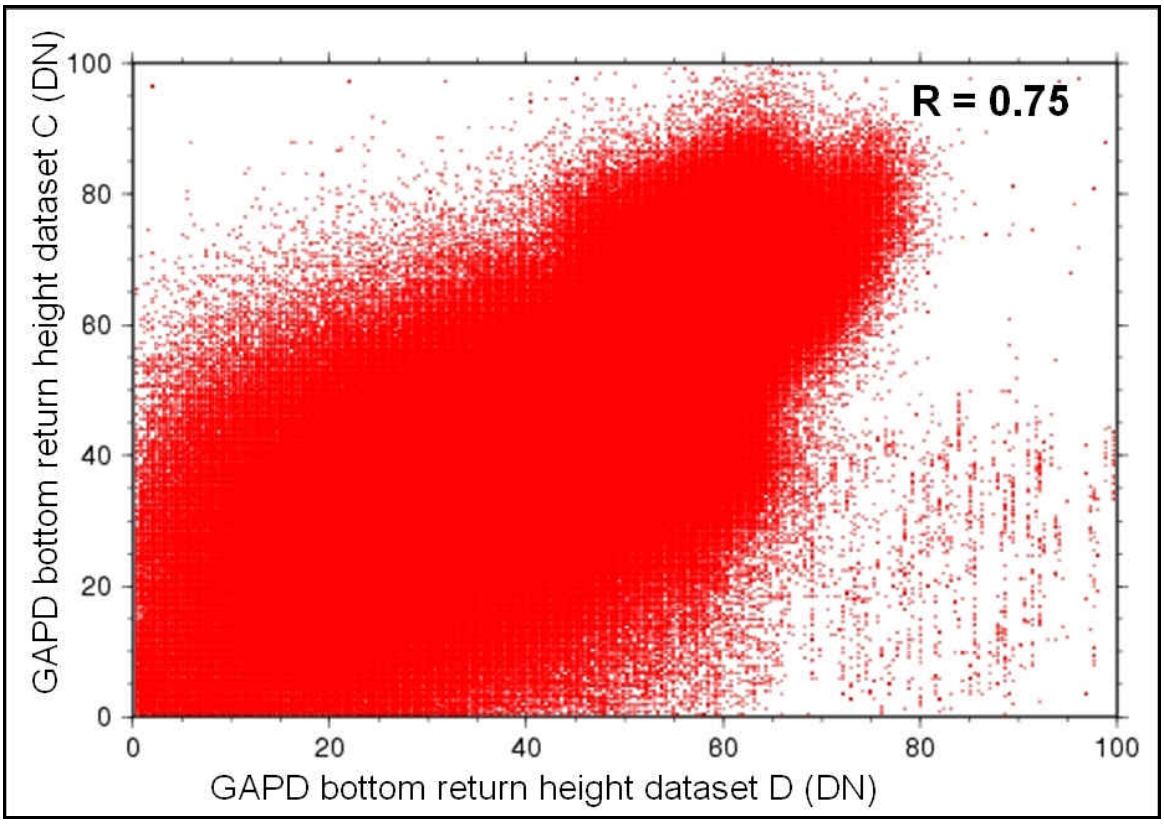

Figure 4.24 Cross plot of GAPD bottom return heights from dataset C and D. Correlation coefficient R = 0.75.

4.4.4 Flight Altitude

The previous sections indicated the anti-correlations between flight altitude and infrared laser beam peak intensity or k_s. A change in altitude, inherently a change of the attenuation path between receiver and water surface, can be directly linked to the variation of energy that passes the air/water interface. Although the altitude is kept fairly constant during each flight line, with only large changes at the turns before or after the start and end of each flight line, line-to-line altitude variations are present. The plot in Figure 4.25, for example, presents the altitudes for a 2½ hour survey (21 lines).

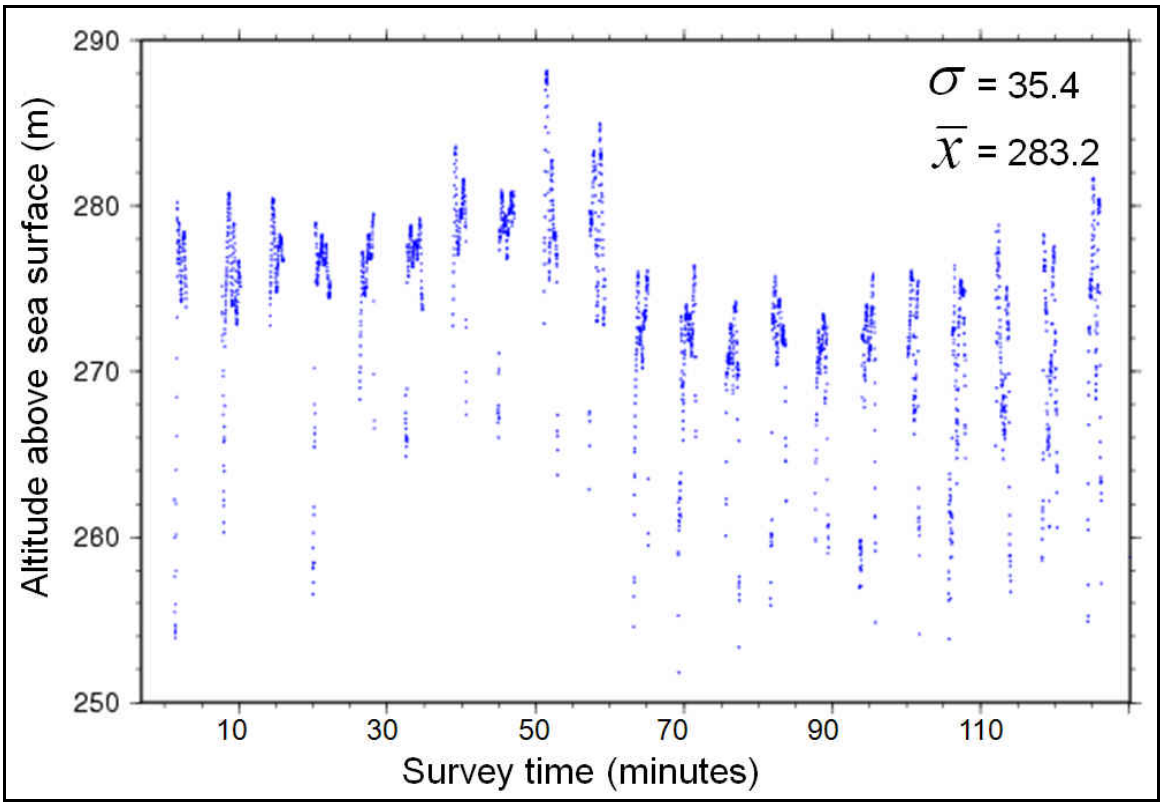

Figure 4.25 Aircraft's altitude above the sea surface for a 2½ hour survey (21 lines). Low altitudes at turns, at the start and end of each line, yield to a somewhat overvalued standard deviation. When the aircraft is "on line," the altitude may be assumed as constant.

Neither the bathymetry data (from LAS-files), nor the waveform data (from INW-files) were associated with the flight attitude. The altitudes presented here were extracted from aerial photography meta-data files. These files contain, for example, the position and attitude of the digital camera at the time a photograph was taken. Although photographs were collected with a lower repetition rate than the scanning laser (photographs at 1 Hz; scans at 33 Hz), the repetition rate of the digital camera suffices for the experiment presented in this section. Each scan is therefore assigned to an altitude from the aerial photography meta-file that is nearest in time.

Figure 4.26 depicts images with the IR peak intensity (top left), k_s (top right),

GAPD bottom return height (bottom left), aircraft altitude w.r.t. sealevel (bottom right), and altitudes superimposed on each image. The examples from Figure 4.26 prove that flight lines with lower altitudes result in a stronger infrared laser beam peak intensity and larger k_s. The anti-correlation between infrared and altitude is straightforward: reducing the attenuation path through air allows for increase of signal return. The anti-correlation between k_s and altitude is less clear. Possibly the surface signature leaks into the upper part of the attenuation curve, allowing for an increased slope, or k_s. However, a more important observation is the bottom return height not being affected by any altitude change.

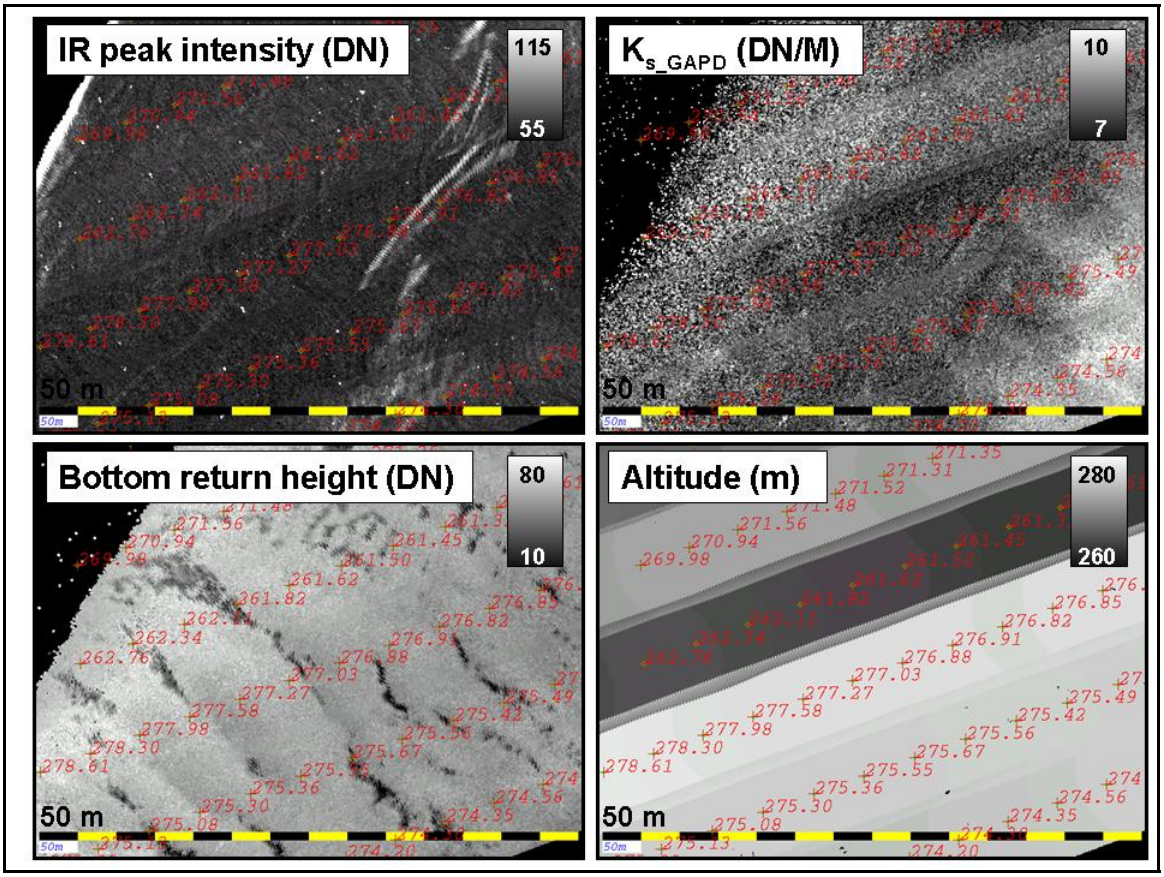

Figure 4.26 Images with the IR peak intensity (top left), k_s (top right), GAPD bottom return height (bottom left), aircraft altitude w.r.t. sealevel (bottom right), and altitudes superimposed on each image. The altitude anti-correlates with infrared laser beam peak intensity and k_s; the bottom return height is not affected by altitude changes, whatsoever.

4.4.5 Depth

A final effect addressed in this section is depth. The range performance of any optical signal is bounded by attenuation and range itself. Section 4.4.3 Water clarity demonstrates that, as a result of the bottom return height measurement relative to the attenuation curve in logarithmic space, the apparent water clarity (k_s) may be disregarded as an accountable effect on the bottom return height. An increased range allows for more scattering (leading to more signal spread) and absorption events, but is unimportant as the depth with respect to the flight altitude is negligible. A decrease of reflected signal strength with increasing depth will then only be observed if the bottom return height would be measured from zero. This trend is examined with data around the Paspébiac sandspit, an area with the greatest extinction depths (~13 m).

Figure 4.27 to Figure 4.29 depict the bathymetry, GAPD bottom return height with bathymetry contours superimposed on it, and keel-mounted side scan backscatter of the Paspébiac sandspit, respectively. The sandwave field, clearly visible in the bathymetry, is also present in the bottom return height map. Waveforms with a smaller bottom return height appear in the troughs of the sandwaves (e.g. Figure 4.30). The bottom return height variation follows the sandwaves, which are mainly oriented in the along shore direction, but do not change with the bathymetry contours, indicating that the low bottom return height in the troughs is linked to sediment change, rather than depth.

Interestingly, the keel mounted backscatter mosaic depicts the same sandwave fields, although the troughs in this case match with high acoustic backscatter. Underwater photography and sediment grabs reveal a sandy seabed over the whole area, with locally (i.e. within 40 – 80 m) varying distributions of granules, pebbles, sand dollars, Laminaria sp. leaves, or an unidentified low growing vegetation species. Moreover, none of the ground truthing data was collected directly in a sandwave trough. Underwater photography did reveal marine life covered pebbles, but these were found beyond lidar coverage (Figure 4.29, inset). These pebbles returned high acoustic backscatter and the marine life could potentially reduce the green laser reflectance. In addition, pebbles are likely to get trapped in the troughs, not being easily washed out as finer sediments would. However, this hypothesized presence of marine life covered pebbles in the troughs can not be supported by any ground truthing data. Acoustical backscatter and green laser reflectance are very different physical phenomena, without denser ground truth, only the presence of spatially coherent and repeatable patterns can be noted. Aquatic vegetation, in contrary, or the substrate on which the vegetation grows, was revealed in acoustic (volume) backscatter and lidar bathymetry. These observations are discussed in Section 5.1 and 5.3.

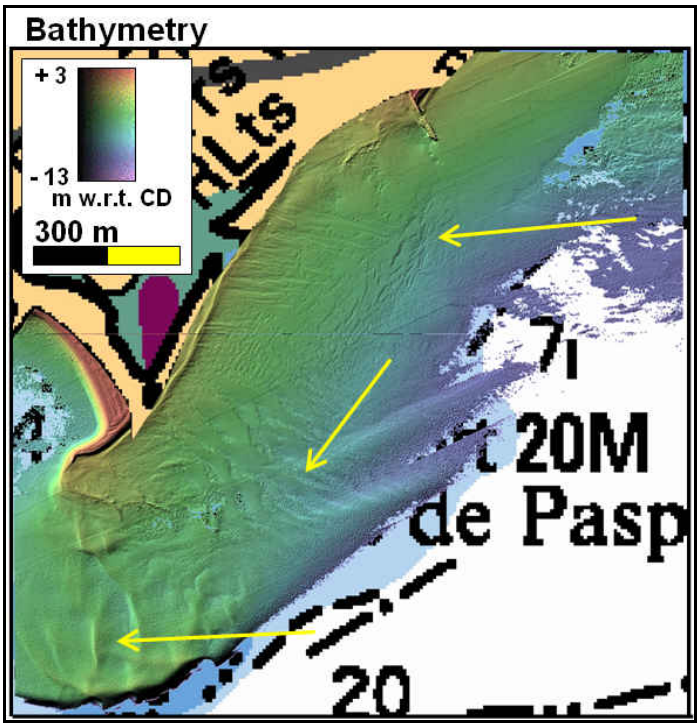

Figure 4.27 SHOALS-3000 bathymetry around the Paspébiac sandspit. An alongshore western current (indicated with arrows) creates sandwaves, first E – W, turning to NE – SW, and finally, E – W again around the elongation. Nautical chart depths are in fathoms.

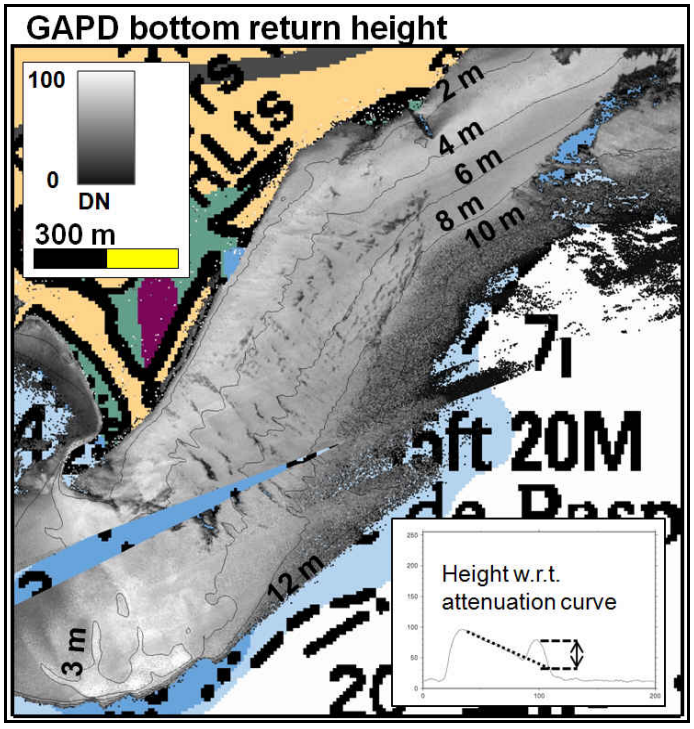

Figure 4.28 GAPD logarithmic compressed bottom return height w.r.t. the attenuation curve and superimposed bathymetry. Waveforms at large datagap were not provided.

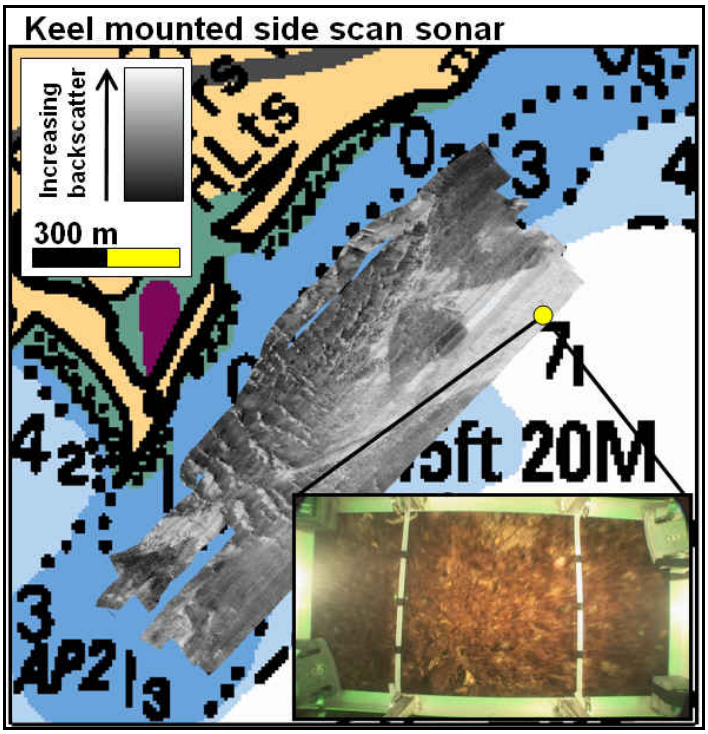

Figure 4.29 Knudsen keel mounted side scan sonar. Inset: underwater photograph of marine life covered pebbles.

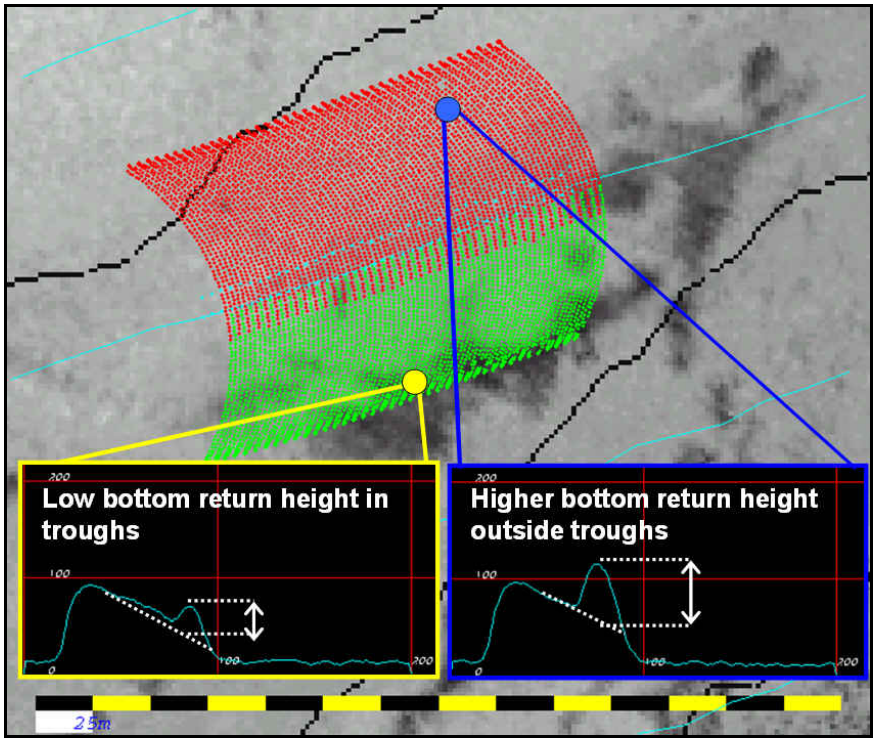

Figure 4.30 Typical waveforms in a sandwave trough (left) and around it (right). 1 m contours.

Once the waveform data reach relatively deeper water, the quality degrades: the bottom return in the waveform is located in the noisy tail of the waveform, or saturated into the noise level. In both cases, the algorithm, which assumes the bottom return located on the k_s-line, will derive a false bottom return height. For that reason, deep water data in GAPD bottom return heights are sparse or untrustworthy. The GAPD bottom return height map presented earlier, for example, (Figure 4.28) shows that the cut-off depth for data quality lies approximately at 8 m. Naturally, waveform data improve with an increase of FOV; therefore, the PMT waveforms, as opposed to GAPD waveforms, were more suitable for bottom return height maps at deep water, as demonstrated in Figure 4.31. This figure shows that the decrease of bottom return height is an FOV related concern, rather than a depth concern.

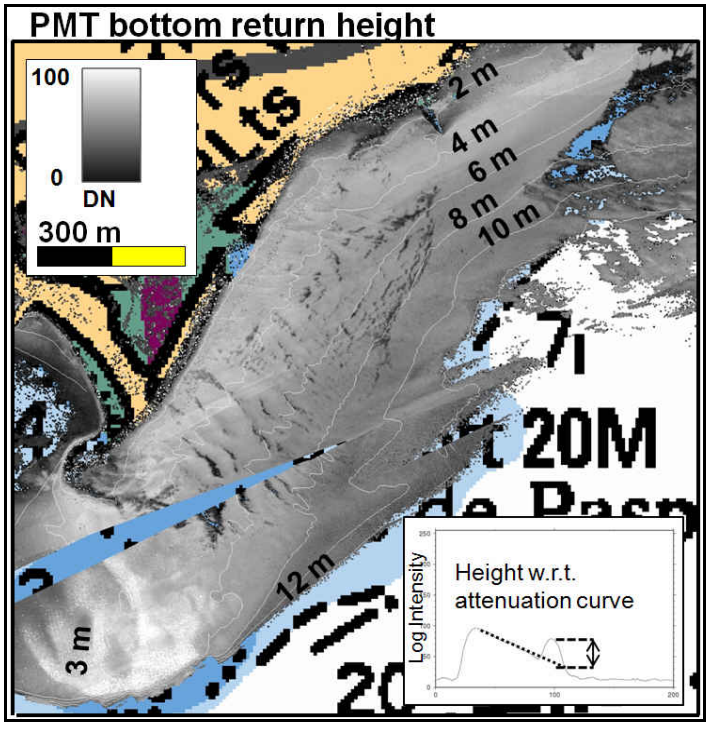

Figure 4.31 PMT logarithmic compressed bottom return height w.r.t. the attenuation curve, and superimposed bathymetry contours.

If the seabed reflectance had been defined as the height of the bottom return measured from zero, then a depth effect would be clearly present, Figure 4.32. By measuring the bottom return height relative to the attenuation curve in logarithmic space, strong shallow water returns are reduced and weak deep water returns are amplified. The logarithmic compression is originally used to reduce the dynamic range for data management concerns and bottom depth algorithms, but also conveniently suppresses the gross depth effect (Figure 4.33).

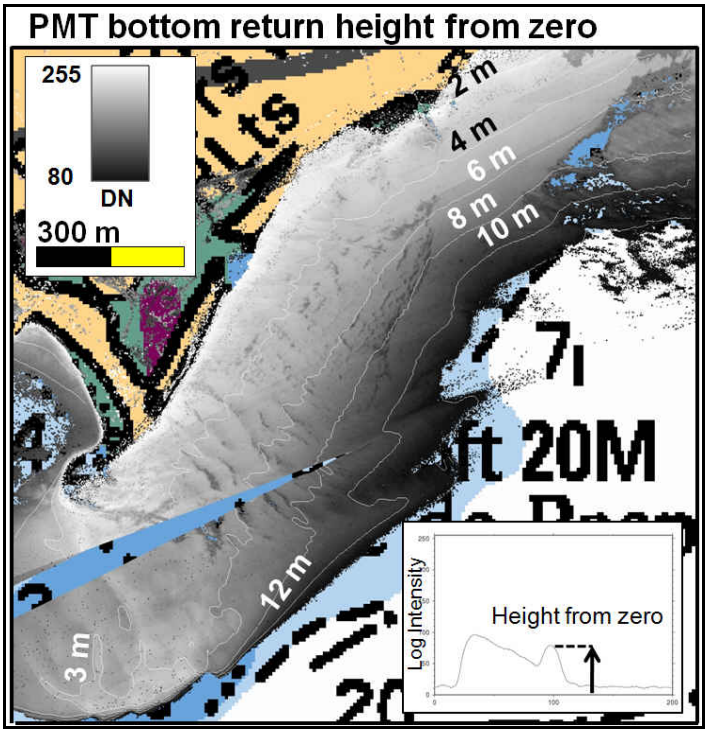

Figure 4.32 PMT logarithmic compressed bottom return height from zero and, superimposed bathymetry contours.

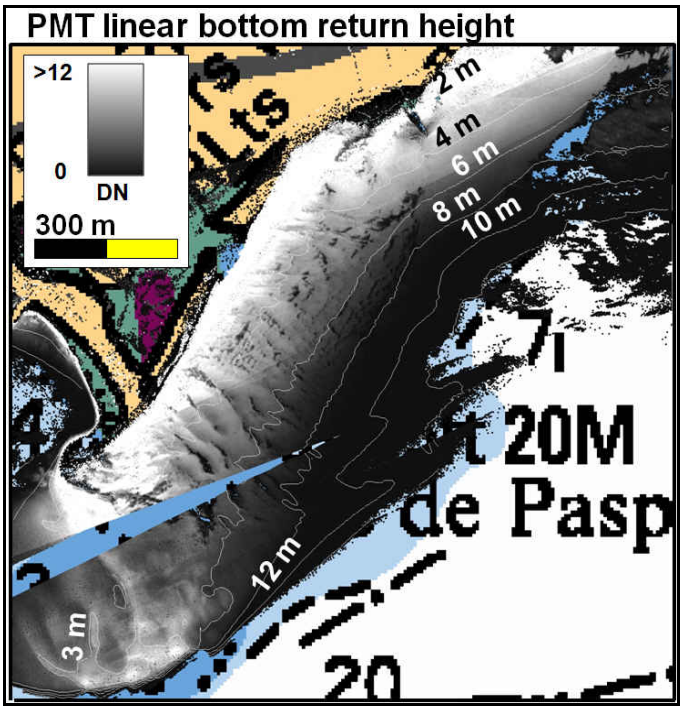

Figure 4.33 PMT linear bottom return height w.r.t. the attenuation curve, and superimposed bathymetry contours.

4.4.6 Conclusion

Environmental effects on the waveforms were investigated, but neither seabed slope, nor surface topography, water clarity, altitude, or depth variation significantly influenced the derived bottom return height. By measuring the bottom return height in logarithmic space relative to the attenuation curve, depth or water clarity effects were bypassed to a first order. Without dense ground truth, only the presence of spatially coherent and repeatable patterns of the acoustical backscatter and green laser reflectance data can be noted. The bottom return height diminishes after a cut-off depth, a depth close to the extinction depth, but this diminishment is an FOV related concern. It was found that, the bottom return height is a suitable parameter for characterization to examine the presence of aquatic vegetation in our dataset. The results of that examination are discussed in Section 5.3.

CHAPTER 5 Results

This thesis studies two main topics: bottom tracking, and waveform characterization at densely vegetated seabeds. The first topic includes acoustic sounders in order to assess the green laser beam bottom tracking ability. The results for this assessment are found in Section **5.1**. A by-product of the waveform characterization is a proxy for the water clarity. Although derivation of water clarity originally did not fall within the scope of this thesis, the study reveals exciting results, which were therefore documented. These results are discussed in Section **5.2**. Once the bottom tracking ability of the green laser beam above dense fields of aquatic vegetation is determined, the opportunity to identify vegetation or the resulting incorrect bottom tracking, without ground truthing data, is explored. The proposed method is based on waveform characterization and is discussed in Section **5.3**.

5.1 Bottom Tracking

The green laser beam bottom tracking assessment is purely a relative comparison with the multibeam bathymetry. The work done in this study does not attempt to determine the absolute accuracy of the SHOALS-3000 system, or the EM3002 multibeam. For such a comparison, control points and an accuracy model for both systems are necessary. Control points, such as a lock or a surveyed submerged structure, were not available in the survey area. A patch test, which assesses the alignment of the multibeam's reference frame with that of the motion sensor and the timing between both instruments (Hughes Clarke [2003]), was executed before arriving at the survey area. This calibration revealed roll and pitch corrections of +0.15°, -0.45°. Accuracy models of

multibeam systems do exist (e.g. Hare et al [1995a] and Hare [1995b]), though such models for bathymetric lidar systems are untouched in the literature. But, as the scope of this work is to assess the bottom tracking at the presence of vegetation, a relative comparison will suffice.

5.1.1 Multibeam Bottom Tracking

Previous experience of the EM3002 bottom tracking performance through thick layers of eelgrass demonstrated the difficulties the system has in correctly determining the seabed. The Ocean Mapping Group in conjunction with the Canadian Hydrographic Service has executed repeat surveys near Sidney, Britsh Columbia, Canada, in areas of dense biological growth at different periods during the year. Where and when eelgrass (Zostera marina) was present the multibeam tracked on top of the eelgrass layer (Figure 5.1). Simultaneous multibeam acoustic water column logging made the vegetated seabed visible. Work from Sabol et al. [2007] demonstrated similar results, though with a different multibeam (Reson8124, 200kHz). That experiment revealed the multibeam tracking dense eelgrass data as well.

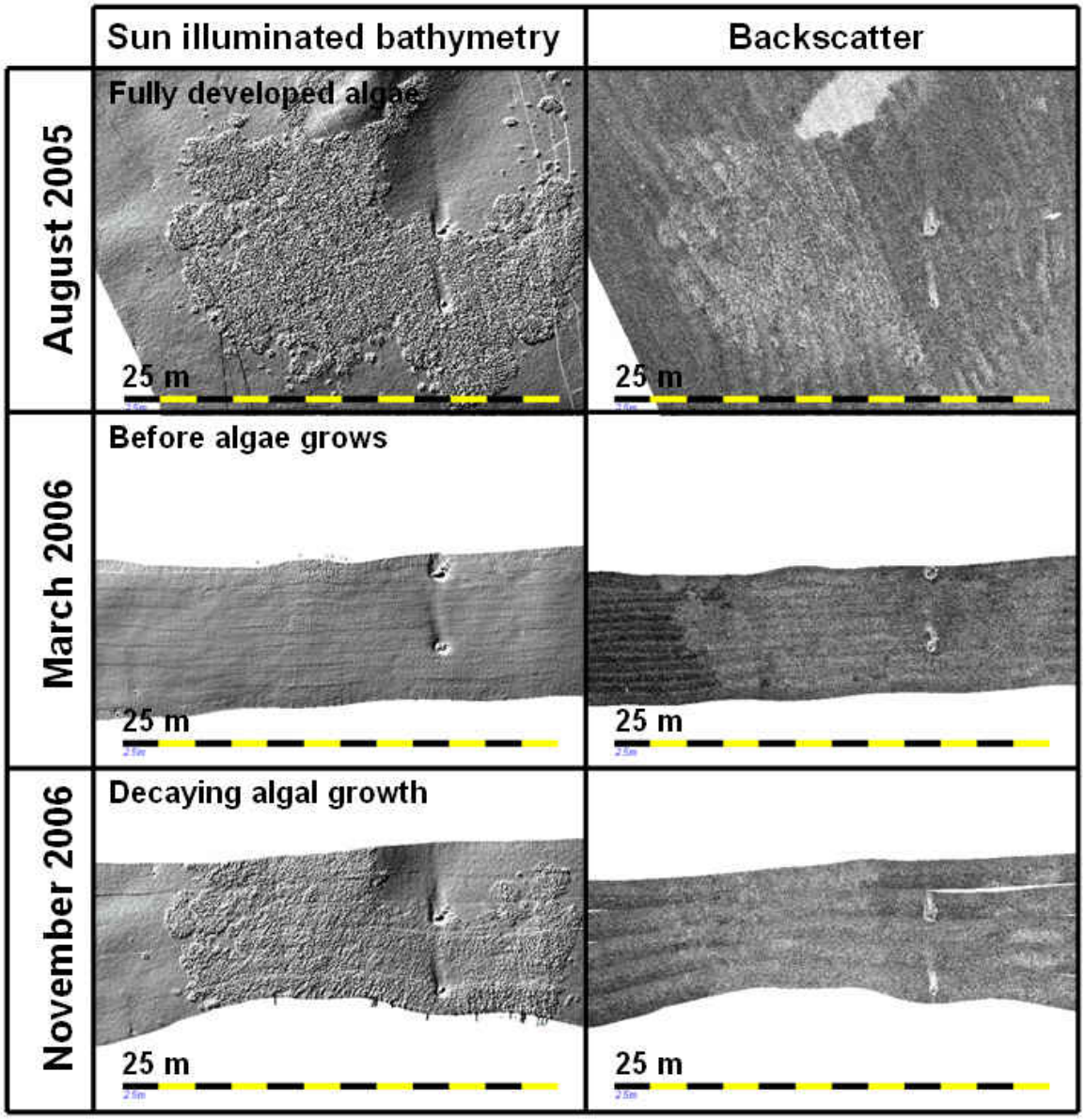

Figure 5.1 Multibeam bathymetry and backscatter collected with a EM3002 from the CCGS Otter Bay near Sidney, British Columbia, Canada. Data were processed with OMG/swathed. Gravel was identified in the backscatter mosaics by the high backscatter (light colored) and is colonized with eelgrass during certain periods of the year. The typical depth was less than 10 m, and eelgrass averaged 1m. Note the sudden backscatter change above the eelgrass in the August 2005 data set (top right). The left portion of the backscatter data is collected before low tide, the right most portion is collected while the tide was rising again. The reversing tidal flow probably changed the orientation of the eelgrass, and with that, the amount of backscatter.

Based on the results depicted in Figure 5.1 the multibeam was expected to have similar difficulties in the Bay de Chaleur, tracking the bottom through aquatic vegetation dispersed over the survey area. However, it performed well above these expectations; i.e.,

where vegetation was present, the multibeam could properly locate the seabed. The Knudsen 200kHz singlebeam and multibeam water column imaging proved to be very useful for identifying the vegetated seabed. The examples shown in Figure 5.2 illustrate that vegetation presence did not hinder the multibeam bottom tracking. Both examples are representative for the complete survey area and multibeam performance. The multibeam was able to discriminate the seabed from the returned time series that were contaminated with background noise and vegetation reflections. Above transition zones, seen in example A of Figure 5.2., where the vegetation suddenly appears, the multibeam did not mis-track, denoting that the range gate filter correctly excluded abrupt depth changes. Note that the Knudsen 200 kHz and multibeam water column profile differentiate from each other in beam width. The multibeam has a across- along track beam width of 1.5° near nadir, whereas the Knudsen 200 kHz uses a ~6° beamwidth. Also, the Knudsen 200 kHz profile only presents data from that broad beam; the multibeam water column profile includes data from beams ±1m from nadir. A final note to take into account is the different logging methodology of the Knudsen and EM3002 sounders. As described in section 3.2.1, the linear logged Knudsen data is overgained and the data is clipped whereas as the multibeam data is logarithmically compressed which accommodates the large dynamic range better. As a result of the Knudsen clipping methodology high scatterers, such as the seabed and (overgained) vegetation, display equal or near equal backscatter while in reality their scattering strength may not lie that close and consequently we cannot determine their relative scattering strength. The Knudsen sounders have the option to automatically control the gain (AGC). This option logs relative to the highest encountered scatterer; thus, in most cases the logging will

adapt to the seabed, which, for our purpose, is of lesser importance than visualization of mid-water vegetation.

The sounding consistency of the multibeam is proven with the Knudsen 200 and 3.5 kHz singlebeams. In Figure 5.3 the multibeam' nadir depths are compared against the Knudsen sounders above the flat, sandy, unvegetated seabed seen in the left portion of Figure 5.2, example A. Although the 200 kHz sounder is much noisier, due to the high gain settings, it shows coherence with the other two sounders. The coherence between all three sounders validates the multibeam bathymetry.

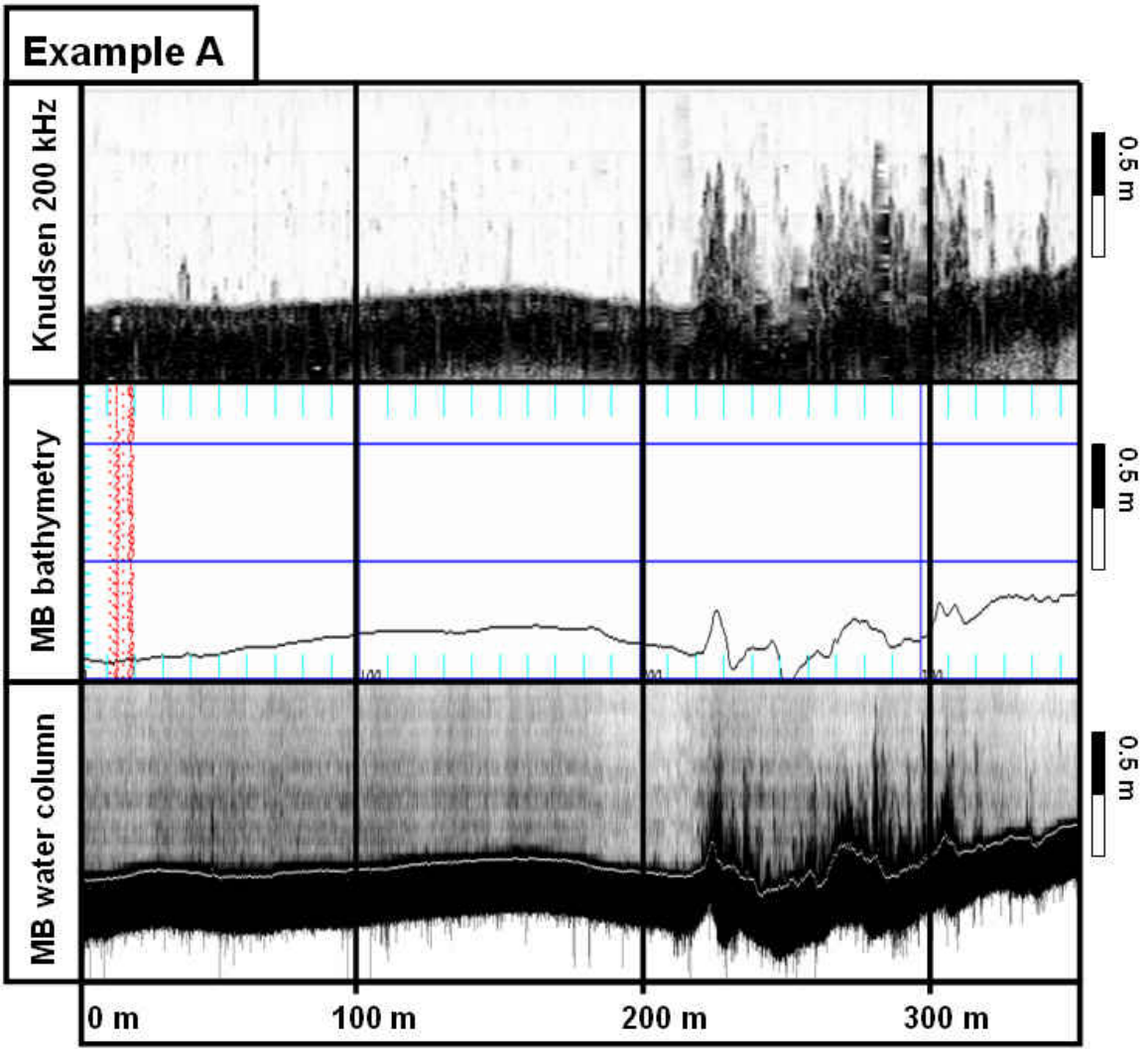

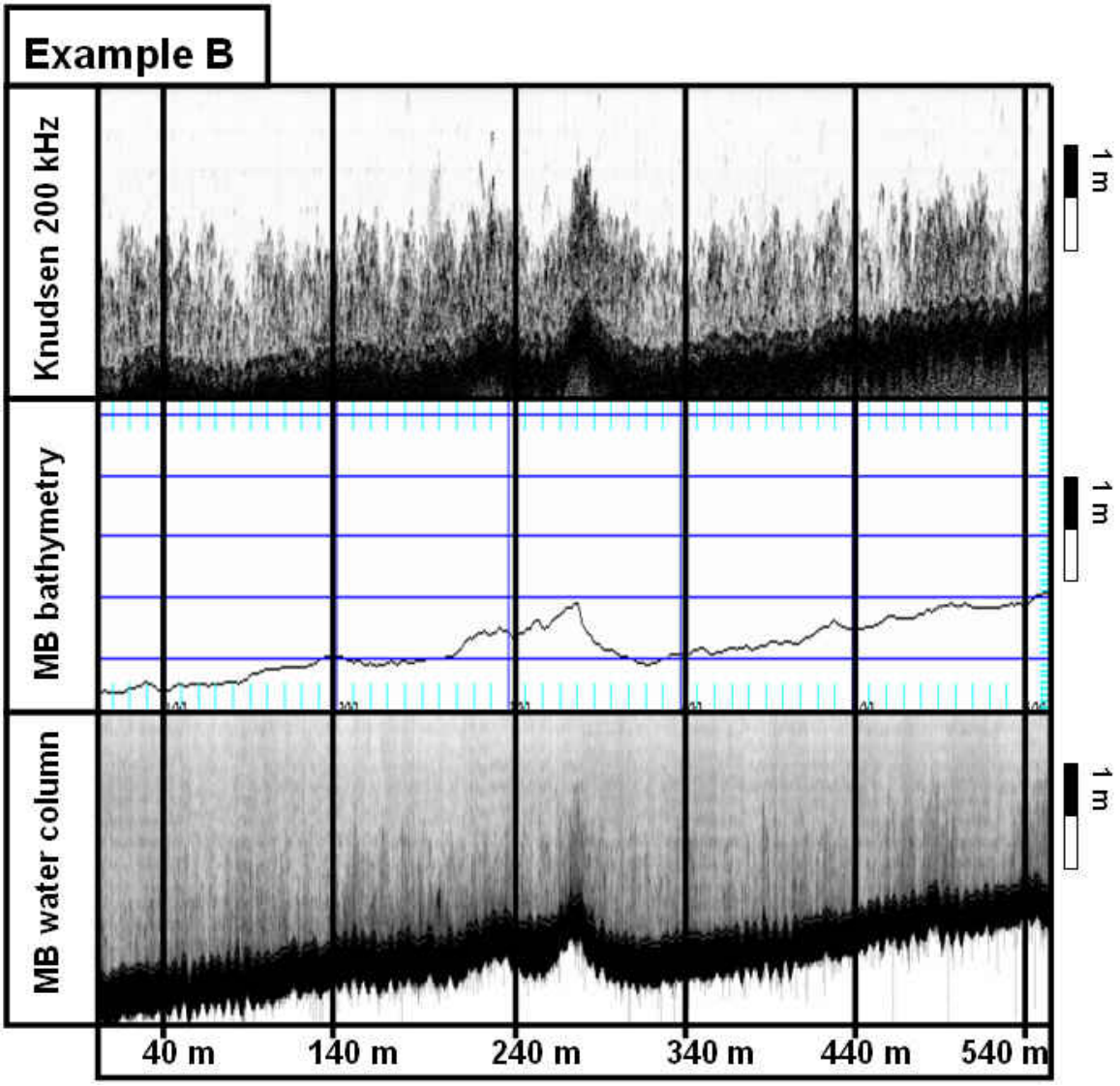

Figure 5.2 Two examples that demonstrate the correct bottom tracking performance of the multibeam. The seabed throughout the survey area had uncovered sand patches or was populated with vegetation (on rock formations); both examples shown here are good representations of the typical seabed found. The Knudsen backscatter and multibeam water column imaging profiles show a similar signature, while the bathymetry clearly follows the seabed. Rough topography is due to the rock formations used by the vegetation as bases to grow on. Note that Knudsen 200 kHz and multibeam water column profiles are not corrected for heave motion. The faint white line in the water column profile presents the (average) multibeam bottom tracking.

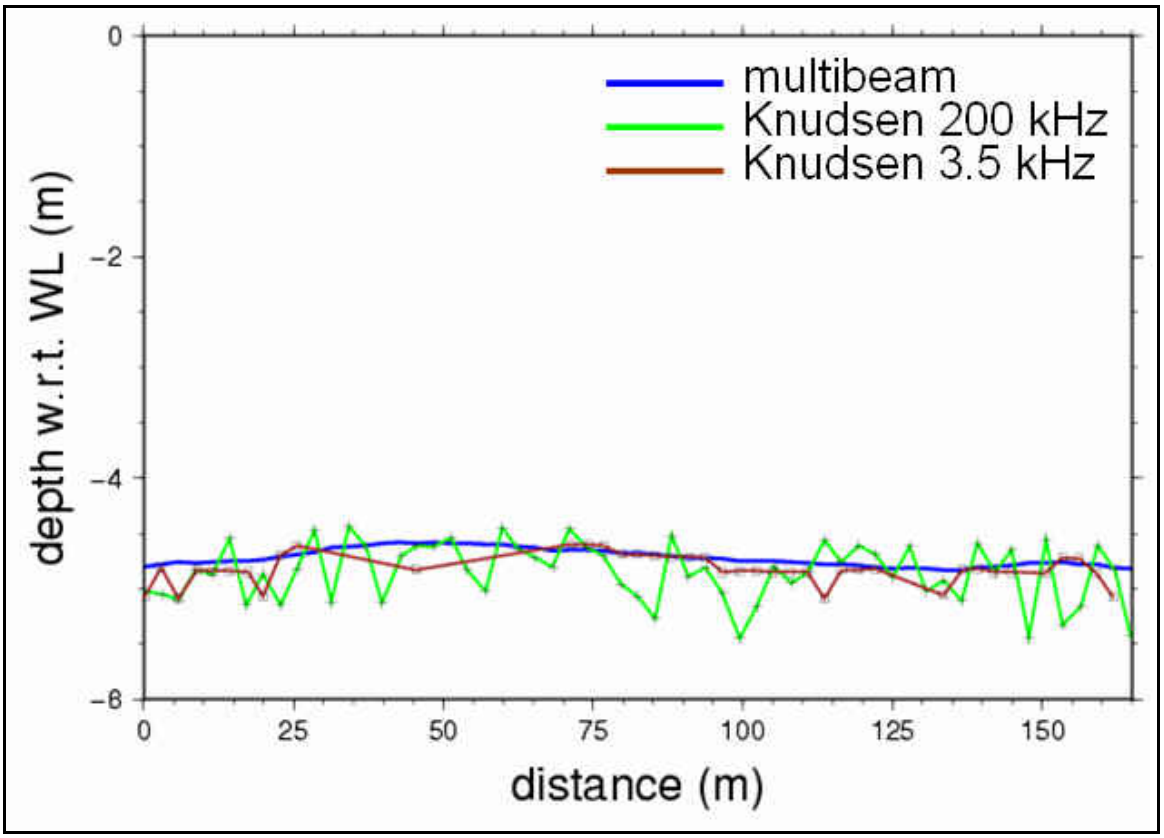

Figure 5.3 Longitudinal depth profiles with respect to the waterline of multibeam nadir beam, Knudsen 200 and 3.5 kHz. The markers on the Knudsen profiles indicate the measured depths. The profile covers the left portion of Figure 5.2, Example A. Note that 200 kHz profile was obtained from deliberately overgained (clipped) data, which are not representative for the usual tracking capability.

Comparisons of the returned 300 kHz signal strength from vegetation hits between the Sidney and Bay de Chaleur dataset show that the Sidney vegetation returns exhibited a much stronger return strength (Figure 5.4). It was particularly noticed that the returned intensity of the vegetation relative to the seabed was much stronger for the Sidney dataset. The bottom detection algorithm of the Sidney case was fooled by the strong returns from the vegetation. As most of the signal returns from vegetation, the remainder may propagate through the algae layer and back, but the seabed echo will not contribute a significant weight in the received signal strength time series. For this work, we were fortunate that the mid-water vegetation thickness did not introduce any bias to

the bottom tracking. Therefore, the multibeam bathymetry is extremely useful to utilize as a reference for the lidar bottom tracking assessment.

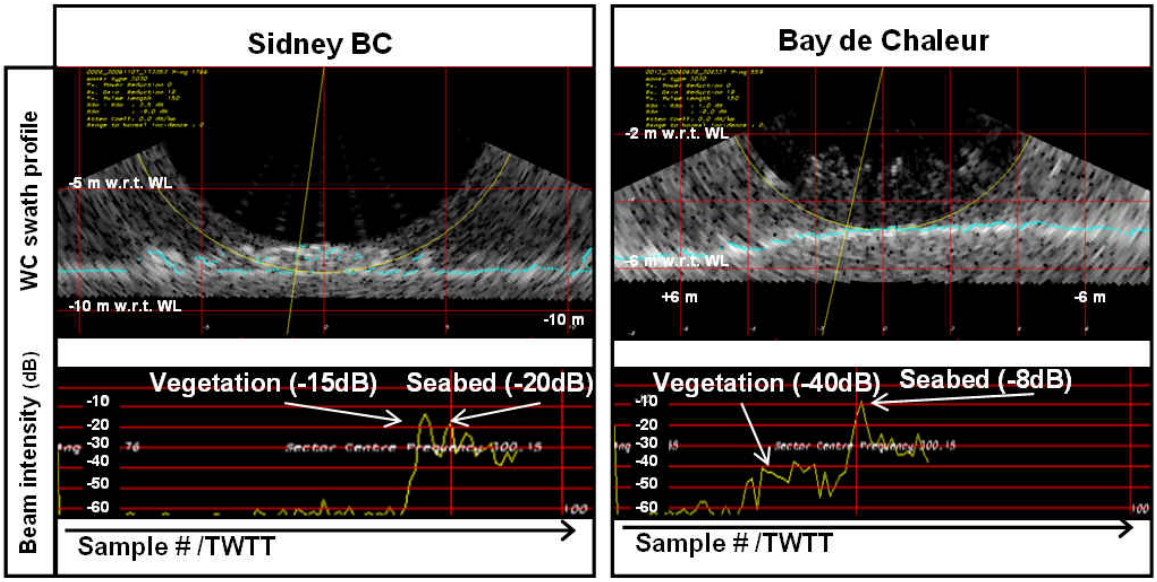

Figure 5.4 Water column data from the Sidney and Bay de Chaleur datasets. The water column swath profile (top) show a vegetated seabed in both cases. The multibeam bottom tracking is superimposed on the swath profile, illustrated with the (cyan) crosses. The beam intensity time series found along the straight (yellow) line in the swath profile are plotted in the bottom graphs.

5.1.2 Data Preparation

The lidar bottom tracking is assessed by differencing the DTM from the multibeam DTM. Assuming the multibeam data is not contaminated with false soundings from the vegetation, lidar data shallower then multibeam data is likely due to the weed tracking. Differencing grids requires them to share equal dimensions and a vertical reference. The latter was achieved during the PPK processing, as described in section 3.1.2; multibeam depths were transferred to ellipsoidal heights (NAD83).

The decision of grid size is primarily based on the data density. Each lidar scan

and the individual shots are distributed homogenously over each flight line, since the data density is mainly a function of flight altitude and scanning rate (see section 2.1 for details). Data used for this exercise were collected with the highest achievable spot spacing, 2x2 m (across x along). The multibeam can distribute soundings at a much higher density over the seafloor (e.g. 0.07x0.35 m at 5m depth, Figure 5.5). Moreover, its sounding density is always greater than that of the lidar, and therefore a grid size was chosen to accommodate the lidar data. A common proxy for the grid size is half the data density (de Moustier [2004], Li et al. [2005]); hence, the grid size is set as 1x1 m.

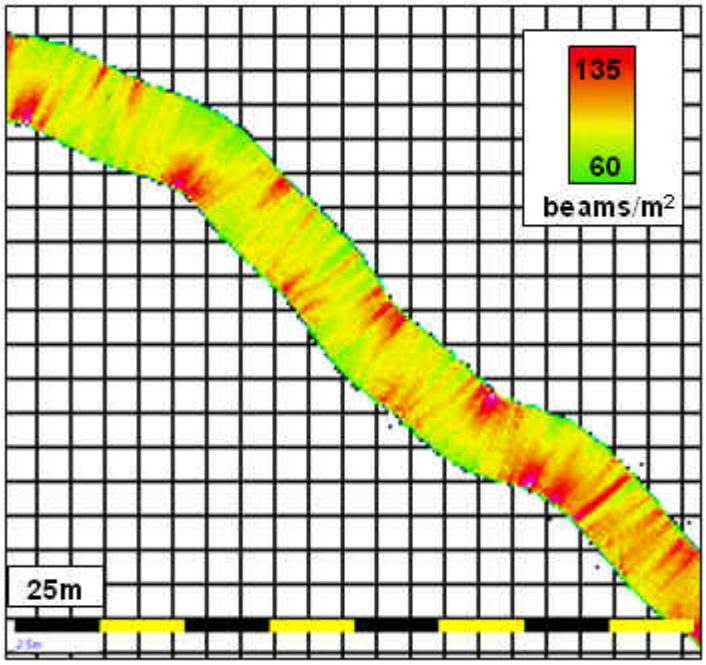

Figure 5.5 This example depicts the multibeam data density in the survey area. It demonstrates the extreme redundancy multibeam achieves in shallow water. Multibeam data density typically depends on depth, swath angle, number of beams, pingrate, and survey speed. Note the effect of ship motion (e.g. turning and pitch) in this example. The lidar produced a homogenous spot spacing, although at the end of each scan, when the rotating mirror changes direction, the data density increases a bit. Despite the highest data collection mode of the lidar (2x2m) utilized above the study site, lidar cannot compete with multibeam in terms of data density.

Weighted grids have been generated with the OMG-software which, incorporates a Butterworth range weighting function (Slootweg [1978]). The weights ($W(r)$) are determined with

$$W(r) = \left(1 + \left(\frac{r}{\lambda}\right)^{2n}\right)^{-1/2} - \left(1 + \left(\frac{\lambda_{co}}{\lambda}\right)^{2n}\right)^{-1/2} \qquad (5.1),$$

where λ_{co} is the cutoff range and n the order of Butterworth filter. All these settings control the maximum interpolation radius that remains constant for each griding process, but the horizontal acoustic data distribution is a function of depth; thus, as depths increase the interpolation may be limited due to the constant search radius. The gridding software takes this limitation into account by scaling $W(r)$ for depth. The scaling also includes the (acoustic) beamwidth and grazing angle, which, driven by depth, determine the acoustic footprint size (Hughes Clarke [2004c]). Although the depth changes in the study site are minimal, the described scaling procedure is executed by default for each multibeam grid.

The Butterworth settings for multibeam grids are controlled by the acoustic beamwidth (1.5°). A different approach is followed for the lidar grids; the maximum search radius should be limited to the illuminated area of the green laser beam; thus, points exceeding this footprint radius will be excluded for weighting and gridding at a certain grid node. As described in Chapter 2, a green laser beam that travels through water is subject to scattering and refraction, forcing the beam to spread in a cone shaped manner. The resulting footprint is thus dictated by the water clarity (of the affected optical wavelength) and depth and seabed slope. Guenther [1985] showed examples of relations between optical depth, albedo, and footprint diameter. For our case, these

relations are not useable as we do not have an estimate for the albedo. Indeed, the water clarity can be extracted from the decaying signal in the waveform, but it does not tell us the contribution of the scattering component relative to the absorption (recall, $\omega_0 = \frac{a}{b}$). However, a common proxy for footprint diameter at the -3dB points (half power) is equal to roughly half the depth (Geunther [1985, 2001]). Acoustic bathymetry showed that the maximum depth in the evaluated areas was approximately 8 metres; thus, the cutoff radius was set to 2 metres. This value also appeared to provide the best compromise to achieve interpolation between consecutive pings, while preserving the data gaps (likely due to water clarity or vegetation presence), (Figure 5.6).

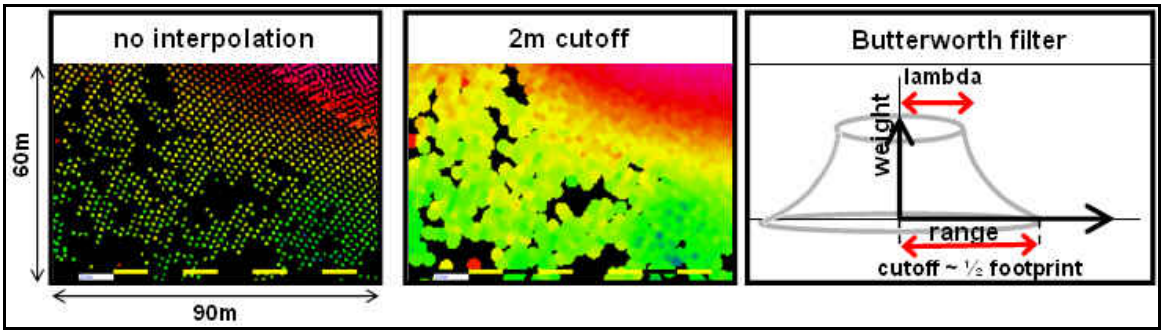

Figure 5.6 The lidar data were gridded with a 2m interpolation radius. This took the maximum possible beam footprint and interping interpolation into account while preserving the most significant datagaps (λ = 0.5m, λ_{co} = 2m, n= 2). The far right figure illustrates the Butterworth concept.

5.1.3 Lidar Bottom Tracking

The lidar bottom tracking assessment consisted of two parts: 1) an evaluation through longitudinal profiles involving singlebeam backscatter data, and 2) a quantitative analysis through DTM differencing.

5.1.3.1 Longitudinal Profiles

To demonstrate the bottom tracking performance of the lidar, one example that is representative for the complete dataset, will be evaluated in this section. The chosen study area contains dispersed vegetation populations, but mainly on, or close to, the vicinity of rock formations. A rock ridge that crosses the study area, for example, is extremely densely colonized with vegetation. The study area was surveyed with 200% multibeam coverage and high frequency volume singlebeam imaging, and showed sufficient overlap with lidar soundings (Figure 5.7).

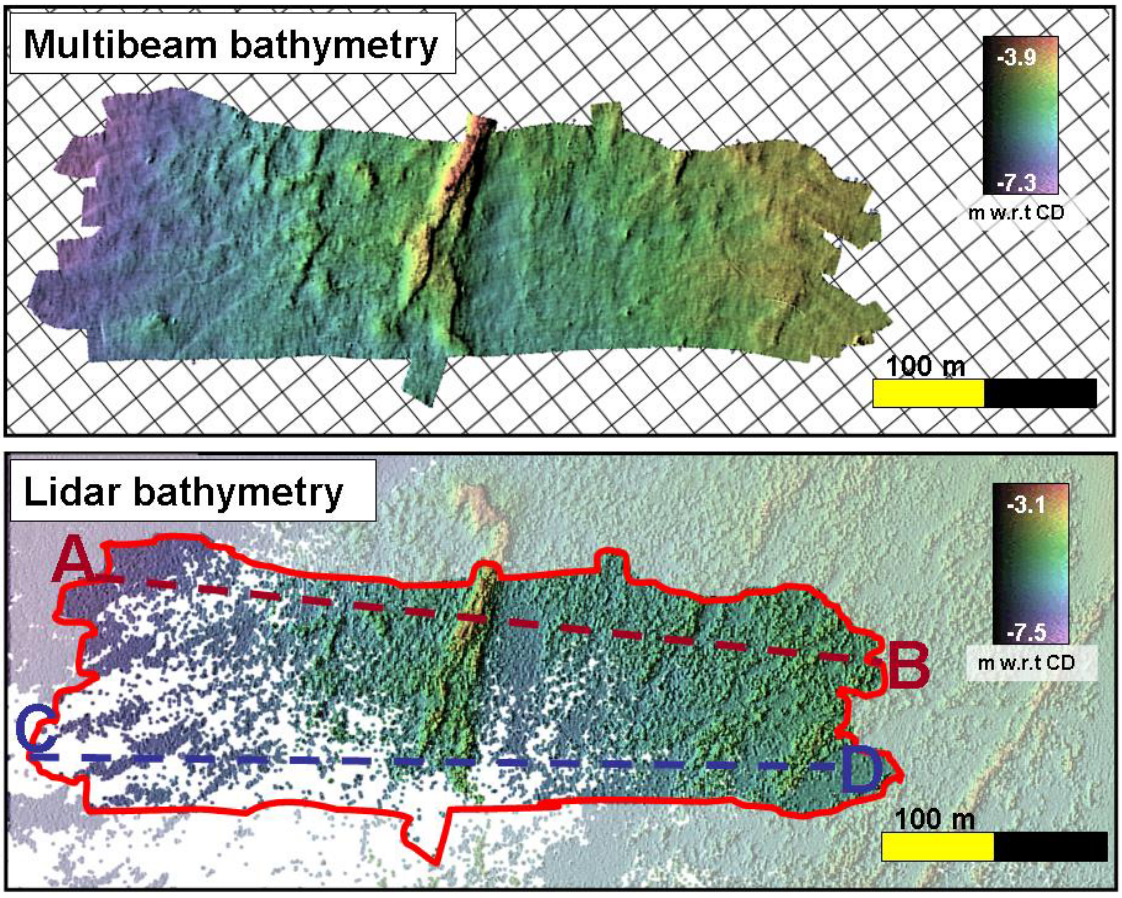

Figure 5.7 Multibeam (top) and lidar (bottom) bathymetry. Overlapping multibeam coverage on the bottom image is displayed unshaded. A rock ridge divides the area in the middle. The vegetation is known to grow on the rocks. Lines A-B and C-D correspond with longitudinal profiles in Figure 5.8. Background grid size is 25 m.

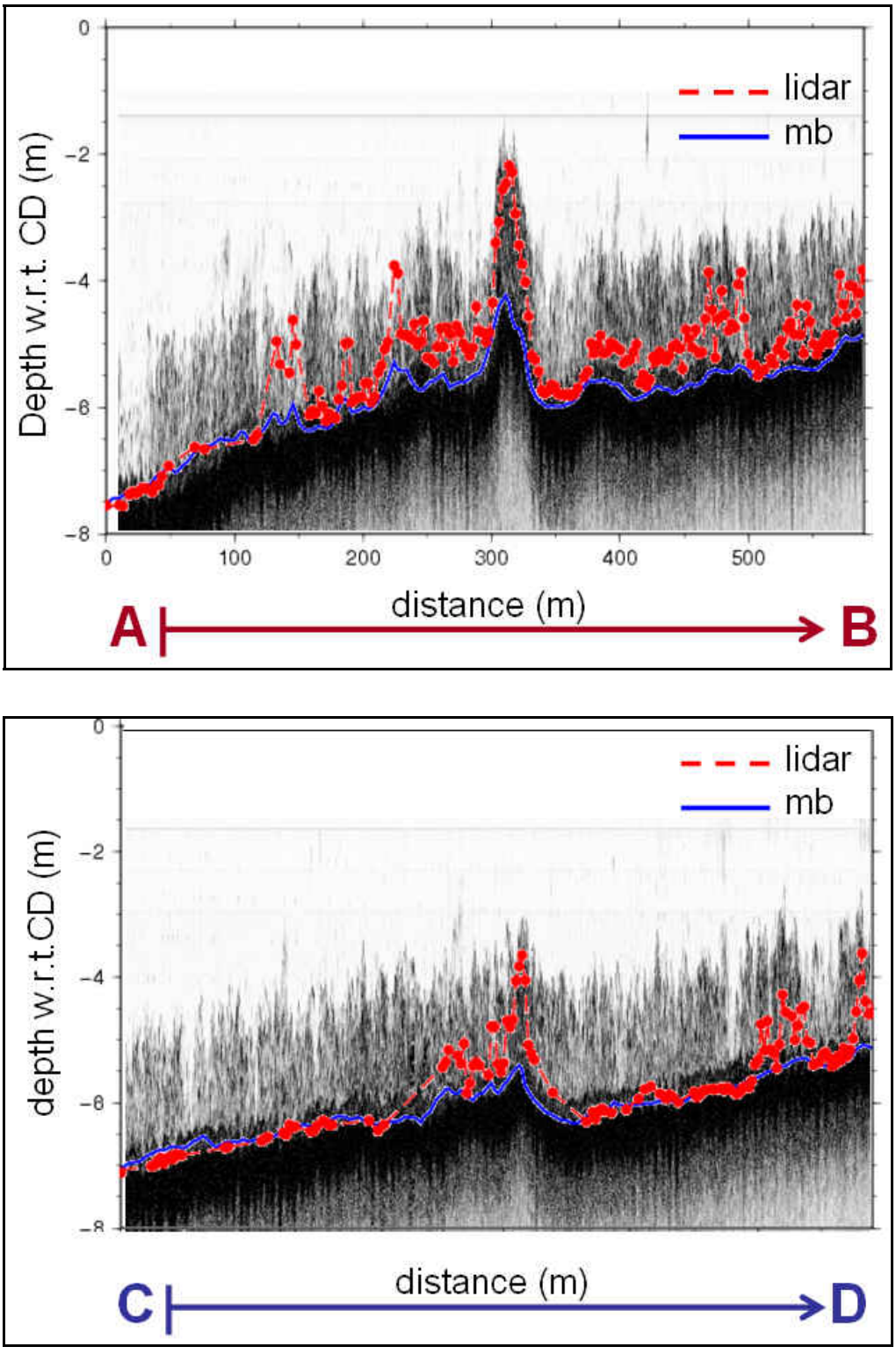

Figure 5.8 Two sets of longitudinal profiles corresponding with the dashed lines in Figure 5.7. Lidar (dashed red) and multibeam (blue) bathymetry is plotted with Knudsen 200 kHz singlebeam backscatter as background. Successful lidar returns are plotted with a dot. Note the slight mismatch of multibeam and Knudsen seafloor in the C-D profile. This is likely due to a bend in the ship track. Knudsen data follows exactly the ship's track, whereas the multibeam profile contains depths extracted from a straight line between C and D.

The longitudinal profiles of the multibeam follow the strongest Knudsen backscatter that indicates the seabed. The rock ridge is clearly recognized in both multibeam profiles. Lidar profiles illustrate two events of bottom tracking failure at the presence of vegetation: 1) tracking of the vegetation, 2) absence of a return:

1) *Tracking of vegetation* – The lidar profiles appear noisier than multibeam, and shallow peaks match with high Knudsen backscatter, especially above the rock ridge where dense vegetation populations are present. In the top example (A-B), the lidar profile above the rock ridge matches vegetation backscatter precisely. The vegetation blocks the green laser light, and the remainder of the signal is absorbed and scattered, decreasing the chance of a successful penetration towards the seabed. The dark color of the vegetation promotes the blocking of the green laser light as well.

2) *Absence of a return* – The lidar profile in the left portion of the lower example (C-D) appears undisturbed, while the Knudsen backscatter clearly reveals the vegetation, thus suggesting that the lidar successfully tracked the seabed at this location. However, this is an invalid interpretation; as the DTM in Figure 5.7 illustrates, the lidar was not able to produce soundings at these locations, so the undisturbed profile is in fact only connecting soundings between successful returns. Depth and/or water clarity are common causes for a datagap to occur. Both factors will reduce the return signal strength and subsequently complicate the lidar bottom detection algorithm in determining a bottom return in the waveform. However, vegetation presence as a cause for data absence, should also been taken into consideration. Figure 5.9 proves this hypothesis. The depicted DTM shows multibeam depths at lidar datagaps. The multibeam data do not show extreme depths, i.e.;

depths exceeding the optical depth, which is proved to be around 13 m at other locations. Moreover, the lidar successfully measured the seabed at deeper depths than seen in this study site. Thus, it is unlikely the depth was the controlling factor for the absence of lidar data. Water clarity, as described in 2.4, limits the depth penetration. A plume of dirty water, for example, can dramatically degrade the depth penetration of the green laser beam. As also described in previous sections, the slope of the decaying signal in the waveform is a descriptor of water clarity. Unfortunately the non-tracking waveforms were not provided, but instead waveforms near data gaps have been evaluated. These waveforms do not show any slope changes; thus, we may confidently assume a homogenous water mass at the study site. Once we can cancel out the role of depth and water clarity, the influence of algal presence surfaces. The vegetation absorbs the signal to that extent, possibly in combination with an increased depth, that no significant bottom return could be resolved by the bottom detection algorithm, which thus fails to produce a depth at all.

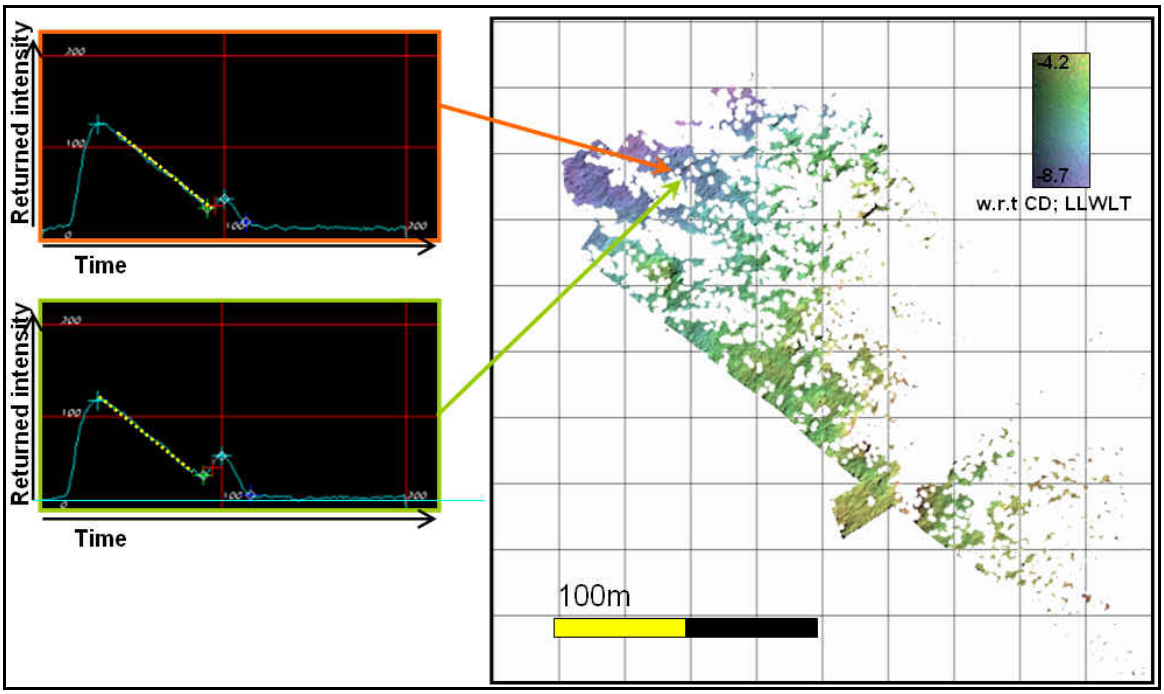

Figure 5.9 The DTM displays multibeam depths (with respect to Chart Datum: Lowest Low Water Large Tides) at locations where the lidar failed to produce a sounding. Two examples of GAPD waveforms are shown near a datagap. The dotted yellow line illustrates no change in slope, thus implying equal water clarity.

5.1.3.2 DTM Analysis

For the DTM analysis two area types were defined: 1) bottom tracking in areas where no vegetation was identified through ground truthing data, typed as "vegetation free" areas; and 2) bottom tracking at algae presence: "vegetation rich" areas. Vegetation free areas provide an indication of the minimum relative accuracies achievable between the acoustic and optical dataset, whereas the vegetation rich areas show a "worst case" solution when vegetation interferes with a correct bottom tracking of the green laser beam.

The evaluated areas differed in size and depth range, and consisted of data collected at different days. Sounding data from the LAS-file were not associated with a GAPD/PMT flag, it is therefore unknown with waveform was used to determine the

bottom detection. The results from the subtraction of lidar from multibeam DTM's are presented in Table 5.1. The mean depth differences and standard deviations found at vegetation free locations are similar to those seen in other assessment studies that included a multibeam as reference (Section 2.5.1). A positive mean depth difference indicates the lidar measuring shallower than the multibeam. This discrepancy is not surprising, as one would expect the lidar to underestimate the seafloor due to the large footprint. The result of the lidar tracking on the vegetation canopy, as seen in the examples of the previous section, is found back in the statistics in Table 5.1; at vegetation rich areas a large *positive* mean and standard deviation results. Also, presented in Table 5.1 are the depths ranges of both systems. The depth range of the lidar soundings compared to the depth range of multibeam soundings in vegetation rich areas indicate two things: (1) shallower lidar soundings due to tracking on the vegetation canopy, which, in fact, confirms with the example profiles from Figure 5.8 and the statistics in the Table 5.1, and (2) limited maximal achievable depth. This second observation is ultimately the result of the absence of a lidar return and usually occurs when the green laser beam reaches its optical depth. The absence of a lidar return is, however, more likely a combination of increasing depth and vegetation presence, as suggested with Figure 5.9 earlier. The far right column in Table 5.1 presents the percentage of empty grid cells in the lidar DTM compared to the multibeam DTM. It is only derived when multibeam and lidar swath or scan coverage overlap, thus; only datagaps, and not un-surveyed areas, are included. As the multibeam DTM is free of any datagaps, the percentage describes data absence in the lidar DTM. In areas without vegetation (and without depths exceeding the optical depth) the failures of lidar returns are insignificant

and the data absence compared to multibeam data is near zero. In the vegetated areas included for the DTM analysis, however, the lidar data absence increased to 11 %.

Table 5.1 Results from differencing between lidar and multibeam DTM's.

	$\Delta\bar{d}$ (m)	$\sigma_{\Delta d}$ (m)	Coverage (m^2)	Lidar depth range (m)	MB depth range (m)	Data absence (%)
Vegetation free	+0.05	0.15	1493468	2 – 11	2 – 11	0
Vegetation rich	+0.44	0.42	218475	1 – 8	2 – 9	11

Once again we use the same area as in the previous section to show the effect of algal presence on the lidar DTM (Figure 5.10). Note that this area is not categorized as purely vegetation rich; the area exhibits varying densities of vegetation populations. Due to this variation, the mean depth difference is less than for a purely vegetation rich area, though still significant, +0.38 m. Also, as the result of the improper bottom tracking the depth differences have a large standard deviation, 0.45 m, indicating a low precision. The bathymetry in the examined area would, due to vegetation presence, greatly exceed IHO Order 1 accuracy norms (±0.99 m (95%) at 7.5 m depth) and the specifications of the SHOALS-3000 system (<0.50 m 2σ): $\Delta\bar{d} + 2\sigma_{\Delta d} = 1.28m$. Moreover, the examined lidar DTM includes many datagaps (20.2 %), mainly in the deeper portion of the area.

A visual inspection of the lidar, multibeam, and histogram DTM in Figure 5.10 show spiky, or disturbed regions in the lidar data corresponding with larger positive (thus shallower) depth differences. The largest discrepancies are seen on the rock ridge, where singlebeam acoustics and multibeam water column imaging identified the majority of the vegetation. In fact, high positive bins (~>1.6 m) on the rock ridge are approximately

equal to the height of the vegetation measured from the Knudsen 200 kHz profiles.

As a comparison, Figure 5.10 also includes the histogram of a vegetation free area ($\Delta\bar{d}$ = +0.11 m, $\sigma_{\Delta d}$ = 0.18 m, area = 0.27 km^2). It can be seen that when vegetation is present, the positive depth difference bins increase in value and number. Notice also the increased number of negative difference bins, these bins represent lidar soundings that are deeper with respect to the multibeam. At the time of writing an explanation for this increase of over estimated lidar soundings is not found. These over estimated deep lidar soundings occur near the northern portion where, occasionally, the lidar did not return a sounding at all (also noticeable in the left most part of the longitudinal profiles from Figure 5.10). At these locations the lidar's performance is more intensely challenged: vegetation densities are still present while the light's travel paths (the depth), and thus the amount of attenuation, increase. Thus the lidar not only tracks the vegetation where large densities are present, leading to shallow biased bathymetry, but the lidar may also fail to return a sounding at all. Although not seen in this area, if there was a heavily colonized rock shoal, the absence of bottom tracking could obscure a navigational hazard.

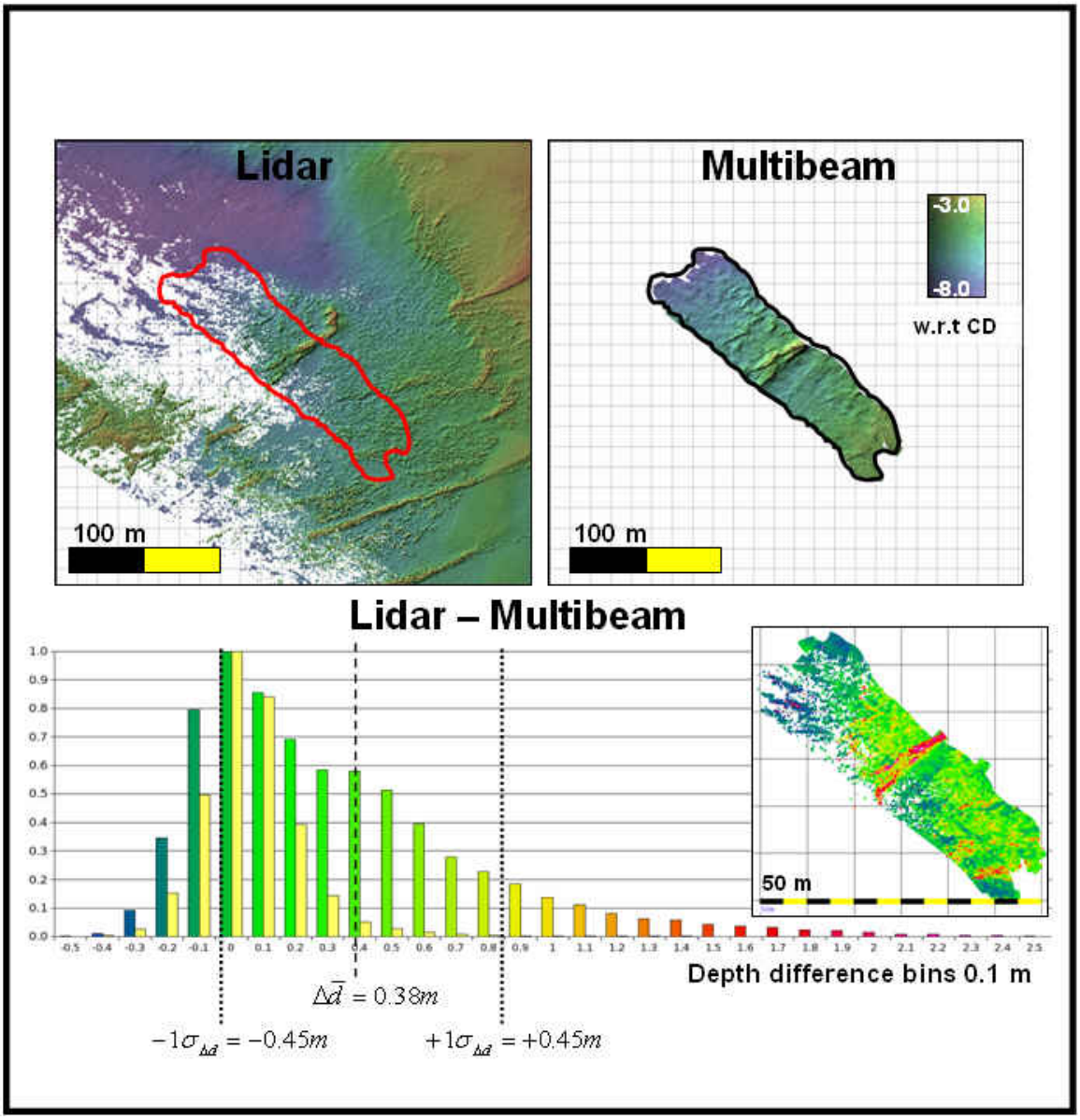

Figure 5.10 Lidar (top left) and multibeam (top right) DTM of a mixed vegetation free and vegetation rich area. The red line in the lidar DTM bounds the multibeam overlap. The normalized histogram shows depth differences of an vegetation free area (yellow bars, $\Delta\bar{d} = 0.11$ m, $\sigma_{\Delta d} = 0.18$ m, area = 0.27 km^2) and of the subtraction of the upper lidar and multibeam DTM's ($\Delta\bar{d} = +0.38$ m, $\sigma_{\Delta d} = 0.45$ m, area = 0.11 km^2, data absence = 20.2 %). The lower right DTM presents the color coded histogram bins.

5.2 Water Clarity Maps

This section discusses the water clarity maps generated from the derived system

attenuation coefficient of each green laser waveform. The possibility to verify or compare the system attenuation with other water clarity terms is investigated. Water clarity terms are valuable information prior to each lidar survey as they can yield an estimate of the extinction depth of the green laser beam. This section will therefore also briefly evaluate the green laser beam performance predictions made from a set of water clarity parameters. Some examples of features found in the water clarity maps are presented in this section and these appeared to have strong correlations with infrared laser beam near-surface intensity maps.

5.2.1 Water Clarity Sources

The system attenuation coefficient, extracted from the green laser waveforms of the GAPD and PMT channels, are spatially plotted to present the water clarity in the survey area. Other sources available that describe the water clarity are,

1) Secchi disk measurements,

2) NASA AQUA MODIS diffuse attenuation coefficient at 490 nm and,

3) lidar performance estimated by Ocean Scientific (OS) software.

The Secchi disk measurements were performed at the time of flight and prior to survey at various locations in the survey area. The first Secchi disk measurements, executed in February 2006, and daily averaged NASA AQUA MODIS data from June and November 2005 were fed into OS-software that predicted two alternative values of the lidar penetration (Feygels [2006]). These estimates yielded a maximum depth penetration between 6 – 11 m in June 2006, and 8 – 14 m in November 2006. The two series Secchi disk measurements are listed in the table in Figure 5.11.

The Moderate Resolution Imaging Spectroradiometer (MODIS) aboard a set of satellites acquires data in 36 spectral bands. Unfortunately, the satellites' swath did not cover the survey area on a daily basis: only weekly averaged data is available for our case. Figure 5.12 presents the diffuse attenuation coefficient for the period July 4, 2006 – July 11, 2006 of the entire Bay de Chaleur; the resolution is 4 x 4 km.

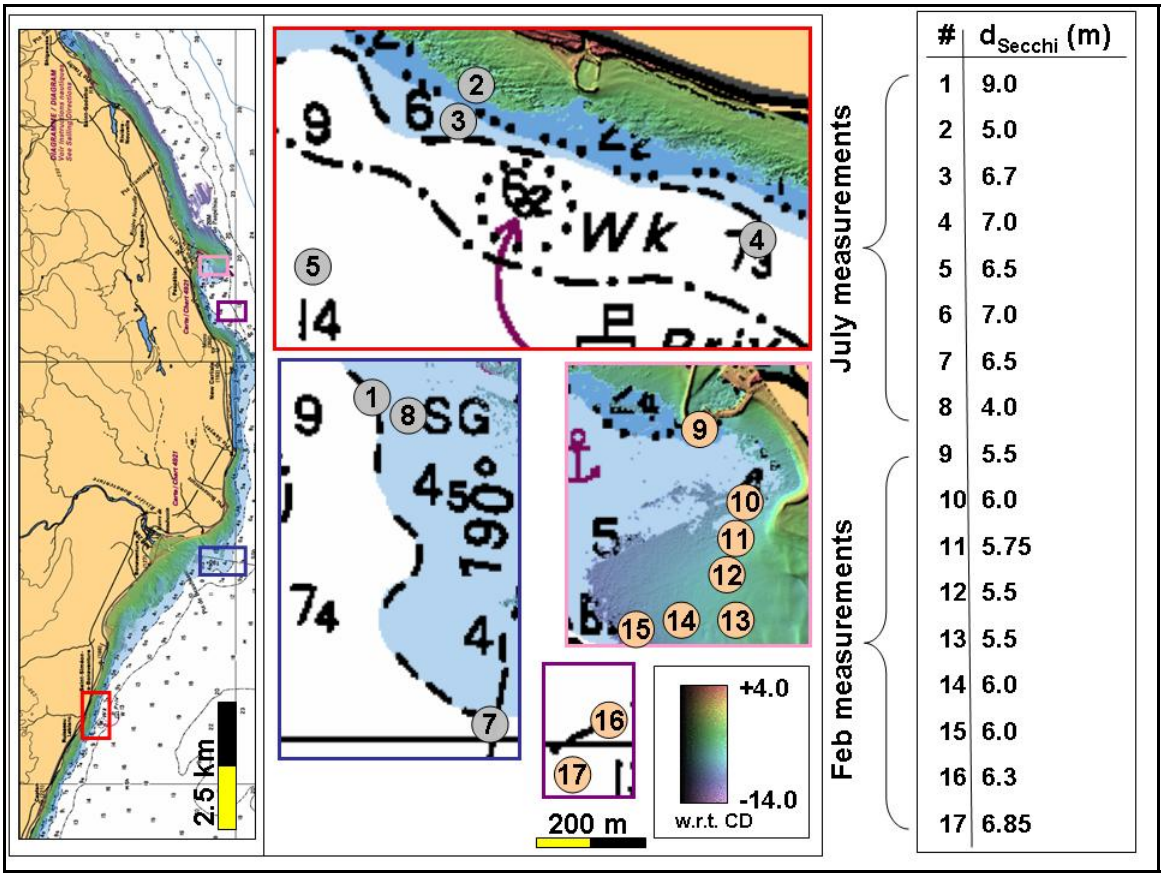

Figure 5.11 Overview of the Secchi disk measurements. Secchi depths 1 to 8 were collected in July 2006, during the lidar flights. Secchi depths 9 to 17 were collected in February 2006. Secchi disk measurement #6 lies south of measurement #5 but falls outside the displayed chart.

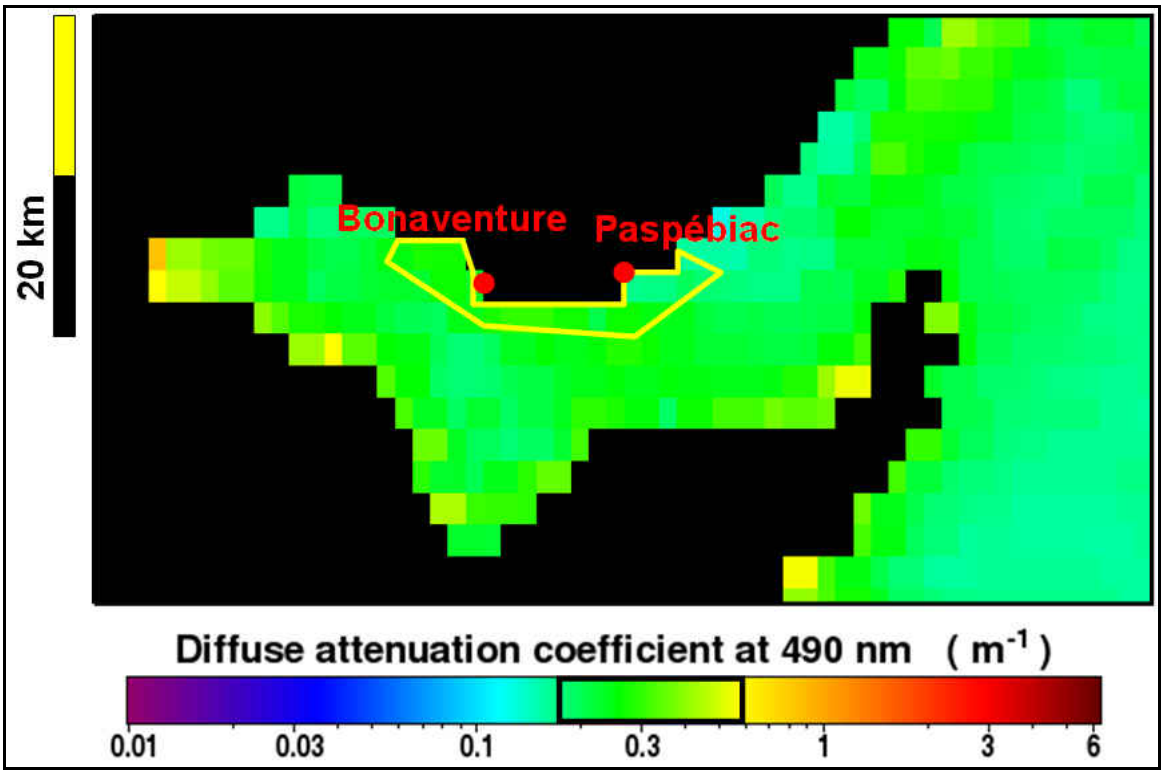

Figure 5.12 Diffuse attenuation coefficient map of the Bay de Chaleur average values from NASA MODIS over passes between July 4, 2006 to July 11, 2006; 4 km resolution. K_d ranges between 0.2 and 0.6 m^{-1}. Survey area is indicated with the line. From: http://oceancolor.gsfc.nasa.gov/

Although the terms presented here all relate to water clarity, absolute or relative comparisons are not entirely possible. The diffuse attenuation coefficient, for example, describes the loss in an uncollimated light field, while the system attenuation coefficient is restricted to all the light that falls within the receiver's FOV. Gordon (1982) describes inter-relationships between the lidar-derived water clarity and diffuse attenuation coefficient, but these are linked with the beam attenuation coefficient or albedo, which can only be found from measuring absorption, scattering and radiance of the spectral light through the water column. Also, both coefficients represent the water clarity at different wavelengths: 490 nm for the diffuse attenuation coefficient against 532 nm for the system attenuation coefficient. Following Jerlov's curves (1976) seen in Figure 2.4, the diffuse

attenuation coefficient in coastal waters, and likely any attenuation coefficient, will be less at 532 nm wavelength, than at 490 nm wavelength. Based on MODIS measurements and the Jerlov curves, the Bay de Chaleur water is classified as Coastal Type 3 or 5. A relative comparison between the diffuse attenuation coefficient from the MODIS measurements and the system attenuation coefficients from the green laser beam waveforms is not feasible either, due to the much poorer resolution of the MODIS dataset.

Although a comparison of the available water clarity parameters appears impractical, we can still utilize some water clarity parameters to estimate the green laser beam penetration performance (ignoring vegetation presence) and investigate the spatial variability of the system attenuation coefficient that demonstrates the relative water clarity changes.

5.2.2 Extinction Depth Comparison

The lidar extinction depth is of great concern at any lidar survey and it is usually controlled by the water clarity, although the previous section showed the influence of aquatic vegetation on the maximum depth penetration, as well. The sand wave field area presented in Figure 5.13 is free of vegetation and it therefore provides a suitable location to compare the extinction depth with the expected maximum depth penetration derived from the water clarity parameters. One must be aware that the prediction of the depth penetration is based upon rough or empirical relationships and should be considered as such.

The estimated depth penetration is listed in Table 5.2. Note that the depth

contours in Figure 5.13 are with respect to chart datum, while the maximum depth penetration values in Table 5.2 describe the complete water column. However, the predicted tidal difference between both datasets included in Figure 5.13 is not larger than 0.35 m. From the depth contours it can be seen that the penetration limits of the laser signal are found between 10 and 15 m CD.

Two rules of thumb exist for the Secchi disk predictions: the multiplication of the Secchi depth with a factor of 2 is used to account for a significant amount of absorption, the factor of 3 is used for scattering-dominated waters (Guenther [2001]). Although this set of Secchi disk measurements was collected four to five months before the actual over flight, the experienced extinction depth falls well within the predicted depth penetration figures. The factor of 2 appeared to approach closest to the true depth penetration.

From the MODIS image, presented in Figure 5.12, a diffuse attenuation coefficient (at 490 nm) of 0.3 m^{-1} is used to present the whole survey area. Factors of 3 and 4 are used according to Guenther [2001]; both correspond with the true depth penetration. Indeed, based upon the n/k_d relation we could scale our k_s values, but the resolution of the diffuse attenuation coefficient is too coarse compared to the spatial variability of our system attenuation coefficient (k_d each 4 x 4 km square, k_s each waveform).

Predicted values from the OS software are the most conservative. These predictions correspond well with the depth penetration experienced over the whole survey operation, but this includes areas with limited penetration due to vegetation presence.

Table 5.2 Predicted depth penetration from Secchi disk measurements, diffuse attenuation coefficient, and OS-software.

	d_{max} (m)	
Secchi disk measurement (d_s, m)	**$2d_s$**	**$3d_s$**
# 9) 5.5	11.0	16.5
# 10) 6.0	12.0	18.0
# 11) 5.75	11.5	17.0
# 12) 5.5	11.0	16.5
# 13) 5.5	11.0	16.5
# 14) 6.0	12.0	18.0
# 15) 6.0	12.0	18.0
k_d (m^{-1})	**$3/k_d$**	**$4/k_d$**
0.3	10.0	13.3
OS-software	6 – 11	

5.2.3 The k_s-map

An area around the sand spit of Paspébiac was chosen for the water clarity comparison (Figure 5.13). This area is dominated by sand wave fields and includes the deepest depths measured by the lidar (~15 w.r.t. CD), which makes the area suitable to test the limit of the green laser beam depth penetration. Acoustic measurements did not reveal any aquatic vegetation in the deep waters, the presence of which may, additionally, limit the depth penetration, as discussed in the previous section (5.1).

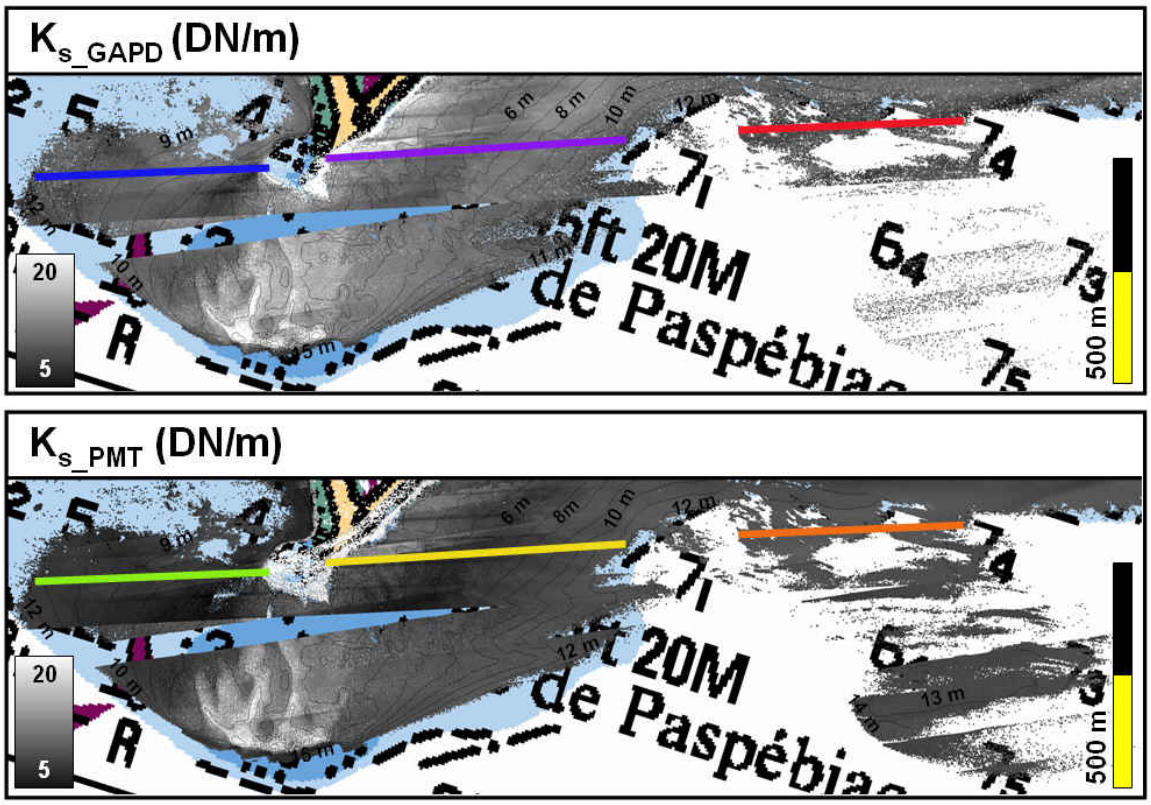

Figure 5.13 GAPD and PMT k_s-maps with superimposed 1 m bathymetry contours. The lines in the figure correspond to Figure 5.14. Note that chart depths are in fathoms. The southern set of lines was flown one day earlier. The (predicted) tide difference between the northern and southern data set is limited to 0.35 m.

Figure 5.13 shows the system attenuation map of the GADP and PMT waveforms with superimposed 1 m bathymetry contours. Note the striping in the k_s-maps mainly visible in the western section. These striping features follow the flight lines exactly and are due to changing water masses between consecutive flight lines. The stripes are thus the result of averaged k_s-values at overlapping flight lines. The thin along-track features seen in the k_s-maps result from line to line variations (~6 minutes apart); broad along-track features result from the overlapping southern set of lines flown one day earlier (~21 hours). Section 5.2.4 continues with an evaluation of migrating water masses seen in the water clarity maps.

From the k_s-maps it can be seen that the water appears clearer as depths increase. This trend corresponds with common near-shore mixing processes (e.g., wind and tide mixing) from which we expect more dirty water near shore. Another reason for low system attenuation coefficients at shallow depths is that when the bottom and surface return contribute (too much) to the volume return and it will bias the k_s extraction.

5.2.4 Sub-Surface Features

The analysis of the water clarity maps revealed a set of interesting features. These features, like the one presented in Figure 4.9 show water masses migrating between consecutive flight lines. In an attempt to understand the source or cause of the migrating water masses, the water clarity maps are compared with infrared laser beam intensity maxima and aerial photography. Examples in Figure 5.14 show the derived water clarity, infrared laser beam maximum intensity return, and aerial photography of flight lines in a chronological order. These are ~5 to 7 minutes between each consecutive flight line. The flight lines in example A are covered in ~8 seconds: flight lines in example B take ~40 seconds. The flight directions are indicated with arrows. Aerial photographs were collected at 1 Hz (~65 m apart) but when mosaicing, half the collection rate sufficed. The aerial photographs were converted from JPG-format to three separate (red-green-blue) 8-bit images, but only one 8-bit band (green) is displayed here. Spatial patterns related to camera geometry, such as the aircraft's shadow and solar radiation, were removed or reduced as best as possible with a line-averaging filter.

Both examples show that, as time progresses, a stream of clear(er) water migrates westerly. The (wind driven) surface waves, seen on the aerial photographs, are directed south east, and these waves appear to provide the momentum of the water clarity features

seen in both examples. A remarkable correlation exists between the water clarity and the infrared laser beam intensities (Example A, Figure 5.14); the clear water stream correlates with the smooth water surface where low infrared laser beam returns are seen and bounded by high infrared laser beam returns on the western side. Note also the flight direction dependence and the surface waves in the infrared maps. A correlation between water clarity and infrared patterns is also apparent in Example B (Figure 5.14). Similar to Example A, an infrared laser beam highlight bounds the (north) western side of the clear water mass. This process suggests a build up of water due to the westerly directed surface waves. The cause of the correlation between water clarity and infrared laser beam intensity suggests, in the first place, a surface feature such as a slick line from colliding water masses. However, the aerial photography does not verify this hypothesis, neither the 8-bit nor the original PCI-image show any kind of surface feature. One explanation may be that the infrared laser beam return contains a (minimal) volume return, suggesting that the feature seen in the water clarity maps is only present in the upper layer of the water column. This explanation is supported by the fact that the surface is not detected at the top of the return but at the 50% threshold (Geunther [1996b]). Besides the volume return, a bottom return, in extremely shallow water and with seabed material with strong optical bottom backscatter strength, could have contributed to the strong infrared laser beam return. The typical depth at the feature is 4 m, a depth to which it is unlikely that the infrared signal can reach; thus, we can confidently speak of a surface or sub-surface feature and ignore any contribution from the seabed.

The feature in example A is ~500 m north of the Bonaventure River estuary. Temperature and salinity transects collected ~1500 m offshore with a moving-vessel

profiler and a day before the flight lines indeed show the discharge of warmer and fresh water from the river. Whether the surface feature indeed originates from the Bonaventure River is difficult to tell with this dataset. A (near) real time series of transects would be needed. Moreover, no significant water clarity changes or infrared laser beam intensities are found at the Bonaventure inlet, and by examining the orientation of the feature it is unlikely that the clear water stream origins from the inlet and is pushed away by the surface waves.

The strong correlation between water clarity and infrared laser beam intensity invites further investigation of their inter-relationships and significance, although these issues lay beyond the scope of this work. Possibly, the features would also be present in passive spectral imagery (e.g., CASI, Compact Airborne Spectrographic Imager). Also, if the derived water clarity can be corrected for the receiver's field of view a more accurate (i.e., closer towards the attenuation coefficient of light at 532 nm) description of the water clarity would be available.

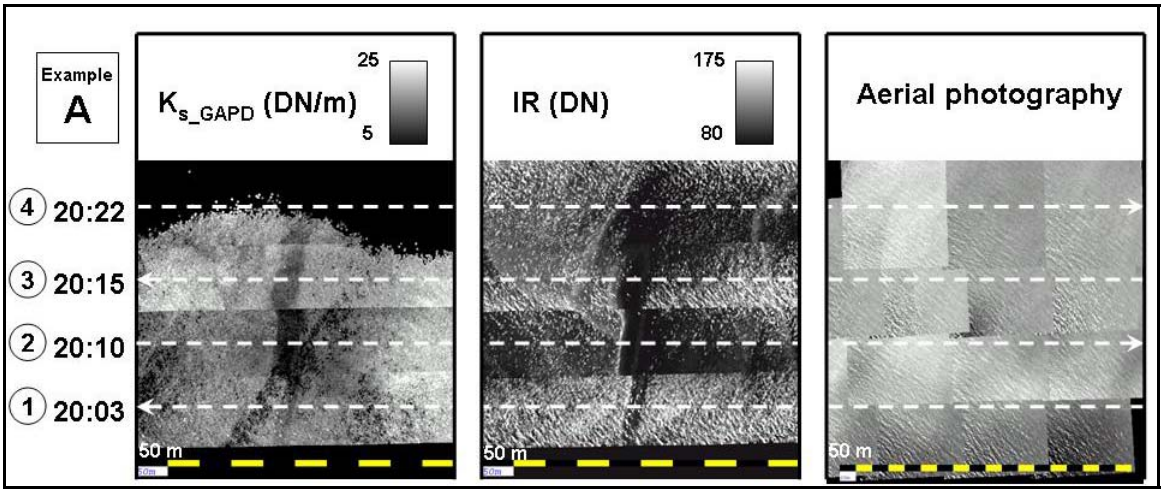

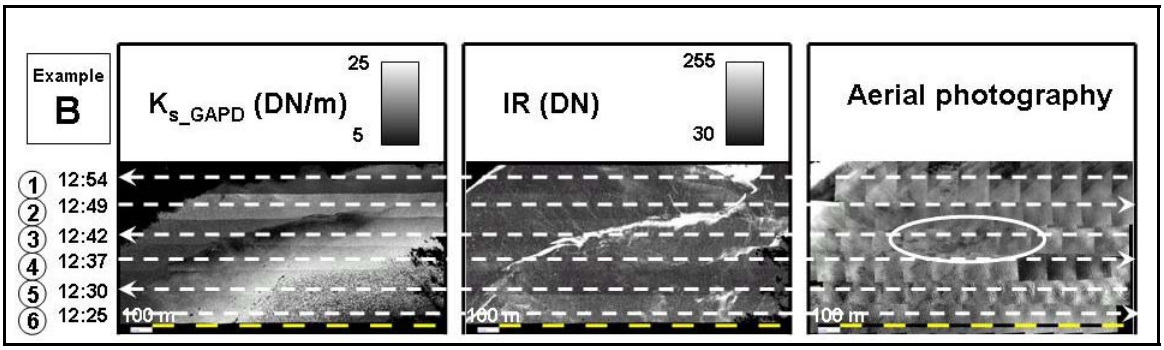

Figure 5.14 Examples of the derived water clarity, infrared laser beam intensity maxima, and aerial photography from consecutive flight lines. The associated time is in UTC. Figure 5.15 displays the location of both examples. The ellipse in the aerial photo mosaic of Example B flight line 6, circum vents aquatic vegetation, but this vegetation is not related to the sub-surface features in the water clarity and infrared laser beam intensity maps.

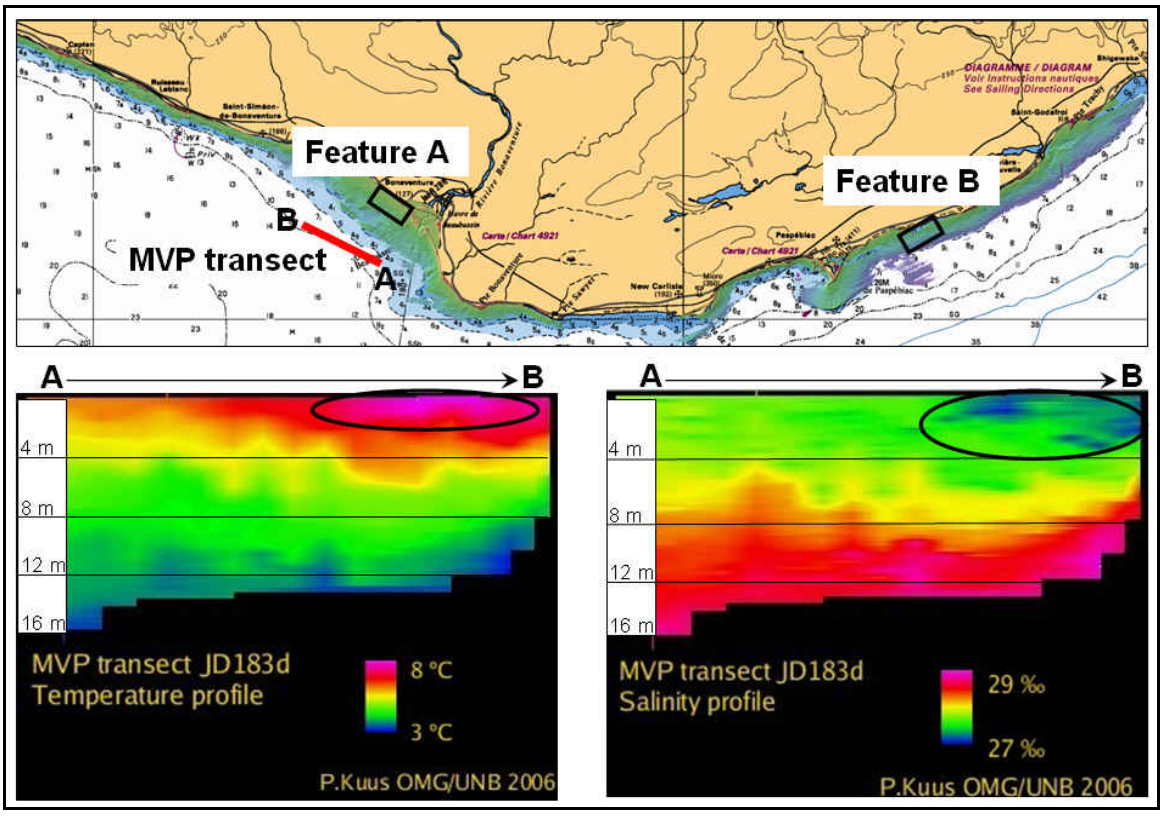

Figure 5.15 Temperature and salinity profiles obtained by the moving vessel profiler one day before the lidar flights at feature A.

5.3 Characterization

The bottom return heights derived with the "get_bot_char" algorithm were plotted to investigate a correlation with seabed vegetation. This section presents the bottom return height maps for both GAPD and PMT waveforms. First, a set of examples are presented that demonstrate correlations between seabed vegetation and bottom return height. These correlations were revealed by incorporating ground truthing data. Then, bottom return height values of the seabed and vegetation are examined in order to establish threshold values. Finally, the possibility of distinguishing vegetation from lidar bathymetry and waveform data is investigated.

5.3.1 Incorporating ground truthing data

This section reviews three examples of strong correlations between waveform characterization and seabed vegetation. Ground truthing data included aerial and underwater photography, sediment grabs, and acoustical backscatter. Each ground truthing dataset utilized for this experiment has weaknesses and benefits, but most are common to the nature of the data type.

Aerial photograph mosaics cover the same area as laser scans (aerial photographs ~ 240 x 320 m), and are therefore extremely useful to identify fields of submerged vegetation. The vegetation is clearly distinguishable from the surrounding sand dominated seabed. However, the value of aerial photo mosaics is controlled by water clarity and sunlight (and ultimately depth); hence, aerial photo mosaics are only useful in shallow regions.

Underwater photography is very unambiguous in terms of vegetation presence, but the value of the photographs depends completely on a coincidental overlap with bottom return height anomalies or patterns.

Sediment grabs are less explicit, since these allow us only to compare the substrate on which the vegetation grows with the green laser beam reflection, and the laser reflection is of course not necessarily from the substrate itself. We are thus never sure whether we are comparing the reflection with the sediment, or the vegetation that grows on the sediment. Underwater photography is therefore favored above sediment grabs. Although we cannot classify the seabed in terms of grain size with underwater photography, we can determine the presence of weed, which is ultimately most important.

The final ground truthing dataset used for this work is acoustic backscatter. The green laser bottom return height can be seen as the optical equivalent of acoustical backscatter since both methods utilize the intensity strength of the reflected signal, which is related to seabed properties (amongst other influencing factors such as geometry and pulse characteristics). Acoustical backscatter, however, differs from the bottom return height since impedance contrast is the most important parameter, and while vegetation and water generally have similar impedance, vegetation is rarely directly seen from the acoustical mosaic. In contrast, optical backscatter is related to color; moreover, the optical signal is blocked by the non-translucent vegetation. As the waveform and backscatter data are both swath-wise collected, they are very useful for spatial comparisons. Unfortunately, the overlap is restricted due to ship-based navigable water depths and lidar extinction depths; moreover, the overlap does not always include

vegetation dominated seabeds.

The first example is presented in Figures 5.16 to 5.18 displaying the GAPD and PMT bottom return height, and a mosaic of aerial photography, respectively. Fields of aquatic vegetation are clearly visible in the aerial photographs and exactly match regions of low bottom return height. Invalid flagged waveforms, found mainly in the shallow near shore zone (~1.5 m CD), are not displayed. The datagaps in the middle portion of aligning flight lines are the result of unsuccessful soundings, and these data were unavailable to us. Aerial photography, however, indicated submerged vegetation at these locations; thus, indicating the success of a lidar sounding is not only dependent on water depth or water clarity. In addition, a series of underwater photographs were coincidentally collected above this area of datagaps. These photographs, depicted in Figure 5.19, show dense populations of vegetation when the lidar cannot track the seabed, and an unpopulated sandy seabed once the lidar achieves proper bottom tracking again. Note also the region south of the vegetation fields where a variation of bottom return height is apparent. Underwater photography revealed rock and pebbles on the seabed covered by marine life such as low growing vegetation, sea stars, and sea urchins. In contrast, underwater photography north of the vegetation fields reveals an empty sandy seabed. Based on the available photo ground truthing, the bottom return height appears to be influenced strongly by seabed life: highest bottom returns result above empty sand dominated seabed, whereas bottom return heights decrease when vegetation or marine life is present. The absolute variation of the bottom return height is discussed in more detail in Section 5.3.2.

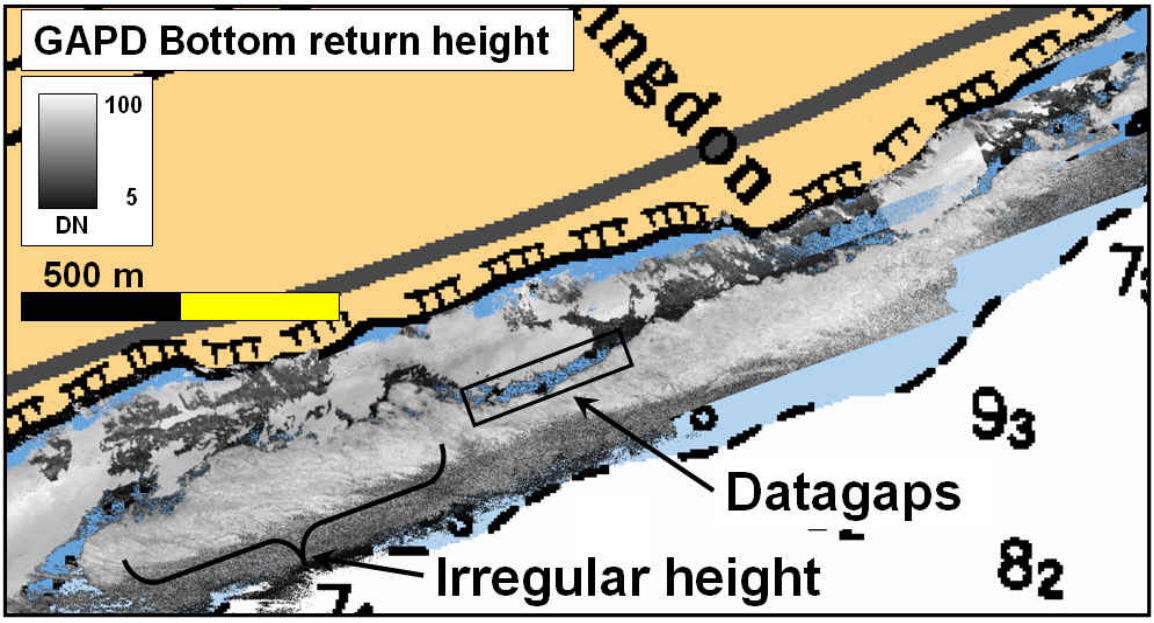

Figure 5.16 GAPD bottom return height map visualizing low bottom returns where weed was identified in the aerial photographs. Note the cut-off depth for data quality at ~ 9m w.r.t CD. Background chart depths in fathoms.

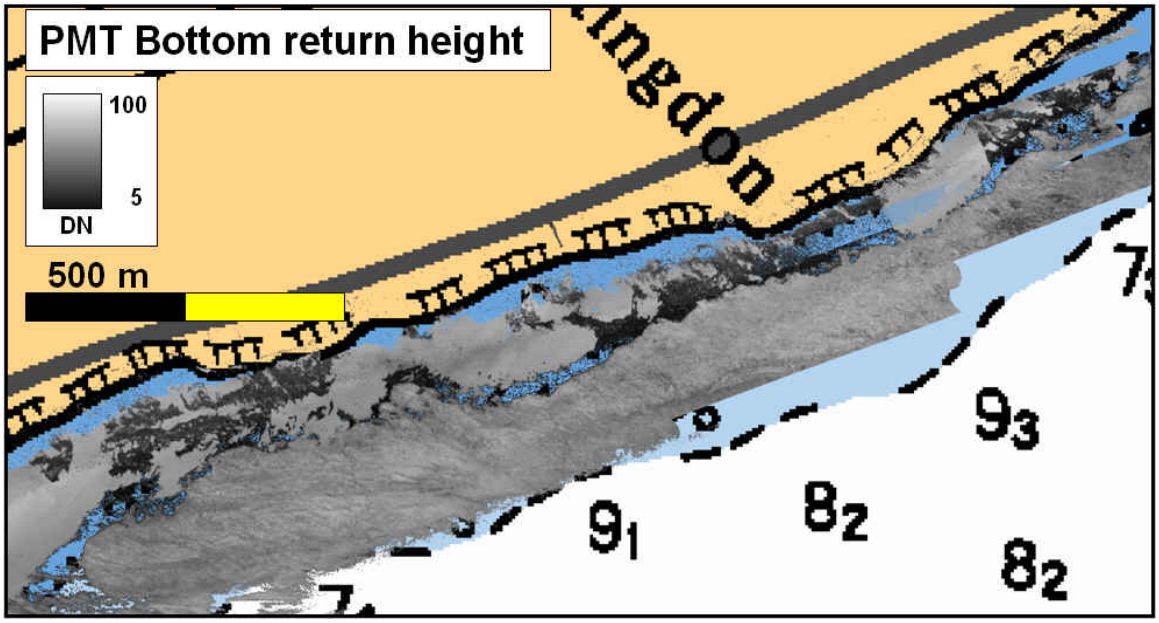

Figure 5.17 PMT bottom return height map visualizing low bottom returns where weed was identified in the aerial photographs. Note the stable data quality compared to GAPD waveforms beyond ~ 9m w.r.t CD. Background chart depths in fathoms.

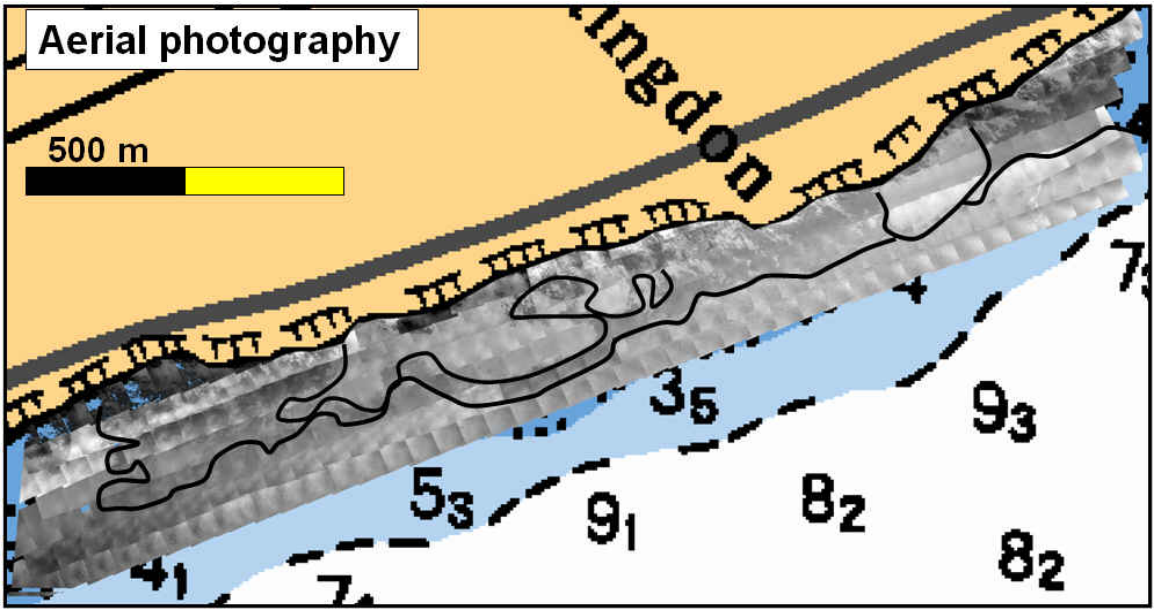

Figure 5.18 Mosaic of aerial photographs collected simultaneously with laser data. The vegetation fields are visible in shallow waters and were seen in the bottom return height maps as well.

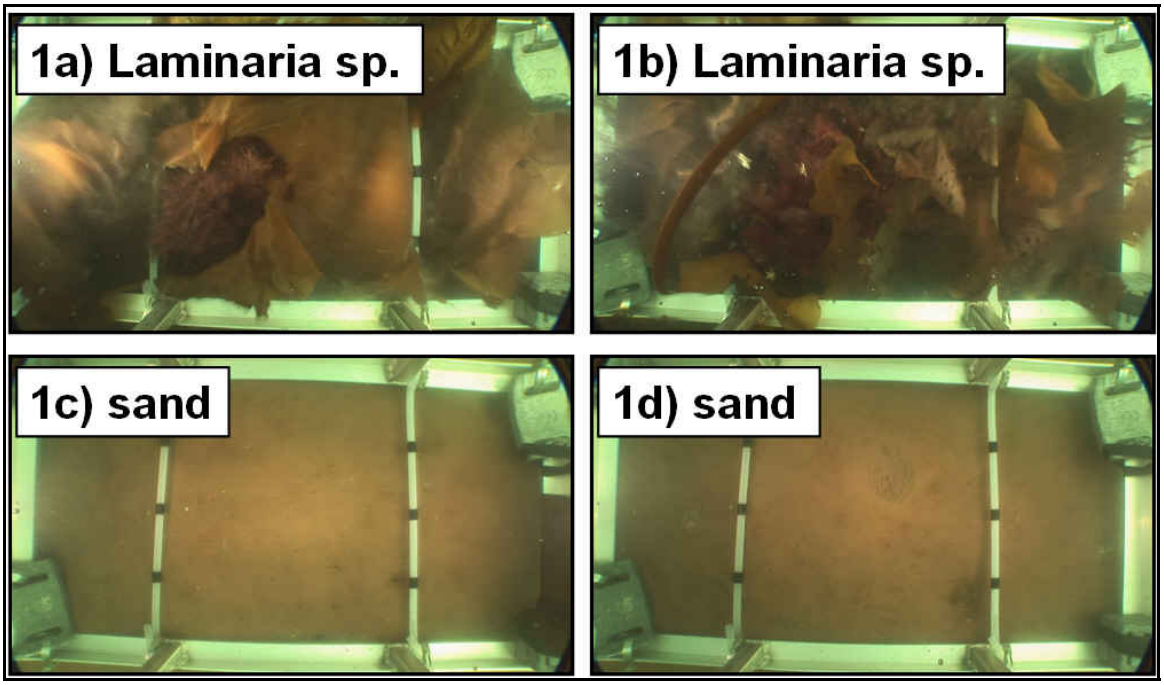

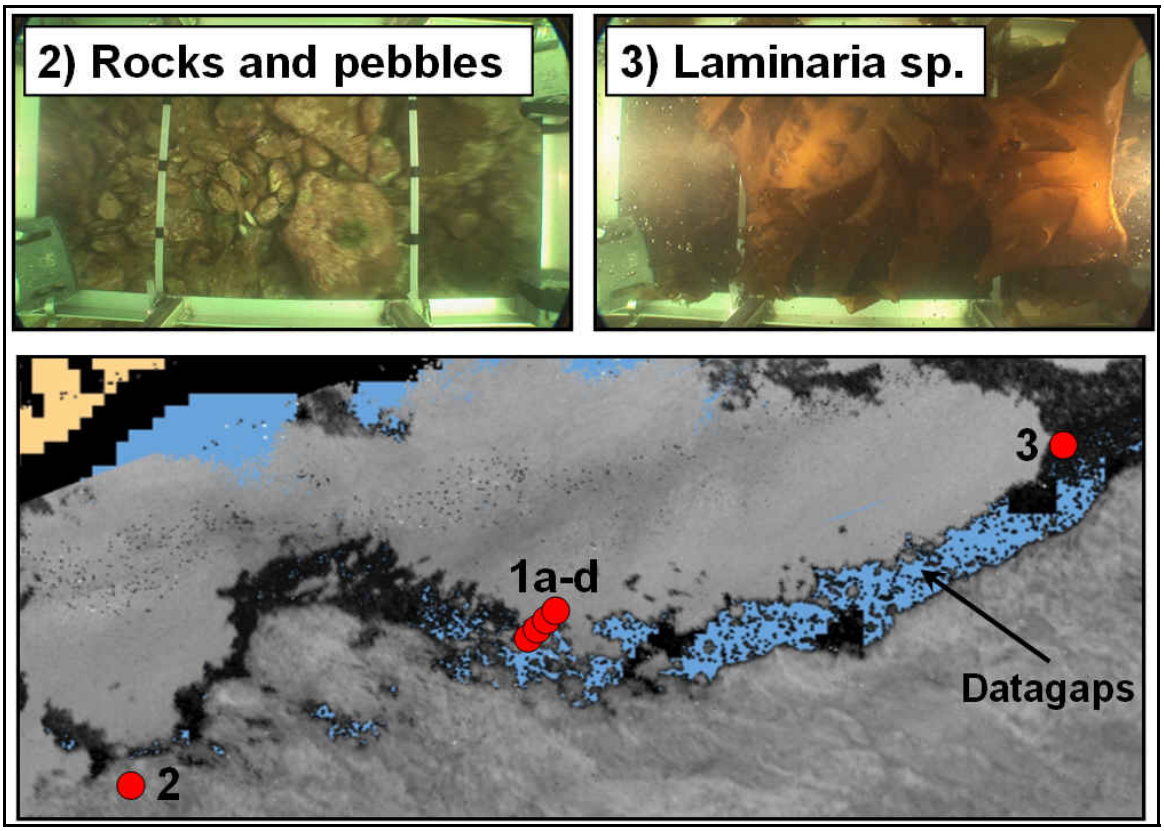

Figure 5.19 Underwater photography. Photos 1a-d were coincidentally collected at a location where the lidar fails to return a sounding. These photographs show that the lidar fails when vegetation is present but succeeds once the seabed is unpopulated, even if deeper. Photos 2 and 3 reveal rocks and pebbles on the seabed, and Laminaria sp. populations, respectively.

The second example discussed in this section involves keel mounted side scan sonar backscatter. As mentioned earlier, few locations showed overlap between lidar and side scan sonar data. The data presented in Figures 5.20 to 5.22 were collected in an area with dense seabed vegetation (Figure 5.25) that resulted in a degradation of the lidar bottom tracking performance, ultimately limiting the lidar coverage. Although apparently only the limits of both lidar and acoustical backscatter coverage overlap, both datasets proved to have value in the analysis.

The bottom return height map in Figure 5.20 reveals many datagaps, especially compared to the bathymetry map. The reasons for these datagaps are twofold. Firstly,

datagaps that are also present in the bathymetric data were the result of failure of the lidar (processing) system to return a sounding. These unsuccessful lidar soundings are mainly present in the southern flight lines. The second reason for datagaps in the GAPD bottom return height map (those datagaps that were not present in the bathymetry) is the validation process in the characterization scheme. Waveforms from shallow water depths with a merged surface and bottom return, or waveforms without a detectable bottom return (waveforms above vegetation) are flagged as invalid and not passed to the bottom return height derivation.

The sparse (valid) waveform data mainly have low bottom return heights, which are better viewed in the close-up images in Figure 5.24 and 5.25. In these images, high acoustical backscatter (bright shaded) can be linked (by underwater photography) to rock or pebble covered seabeds. The contour of high acoustical backscatter is superimposed on the bathymetry and bottom return height maps. It appears that the contours isolate lidar datagaps, suggesting that the occurrence of a datagaps is linked to substrate, or infact, the vegetation that grows on the substrate. This correlation is again confirmed with surrounding underwater photography. Interestingly, the lidar datagaps and high acoustical backscatter correspond to the presence of Laminaria sp., which indeed preferably grows on rock-like material, while low acoustical backscatter and low bottom return heights correspond with the presence of Zostera Marina, as identified with underwater photography. This observation implies that aiding acoustical backscatter data at lidar datagaps yields a potential to distinguish populations of rock- or sand-based vegetation. In summary, based on the data depicted in Figure 5.20 to 5.25, while assuming lidar datagaps are only due to the presence of vegetation, we can conclude that

1) a datagap in combination with strong acoustical backscatter suggests the presence of rock- or pebble-based vegetation such as Laminaria sp.

2) Weak acoustical backscatter in combination with a low bottom return height suggests the presence of sand based vegetation such as Zostera Marina.

3) Since datagaps appear in conjunction with strong acoustical backscatter, rock- or pebble-based vegetation reflects the green laser signal less intensively than sand based vegetation. Therefore, rock- or pebble-based vegetation is more detrimental than sand based vegetation in terms of lidar coverage (although both vegetation types degrade the bottom tracking). Naturally, rock outcrops are more likely to exhibit local shoals and thus we cannot be so confident of maximum clearance in rocky areas swept by lidar.

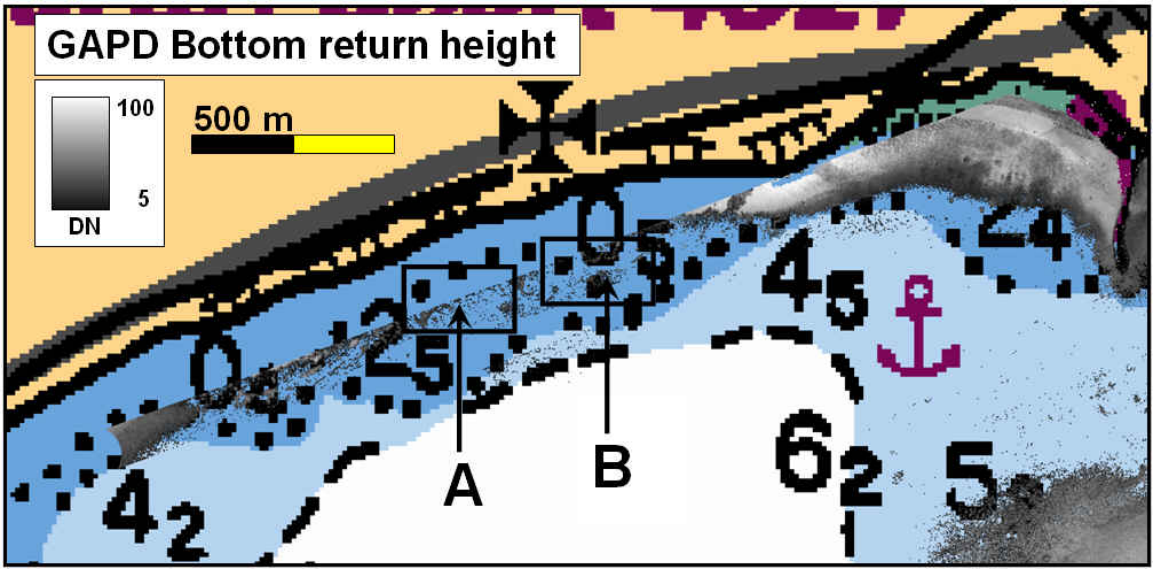

Figure 5.20 GAPD Bottom return height near the shore of Paspébiac. Boxes A and B refer to Figures 5.23 and 5.24 respectively. Extremely shallow waveform data were flagged as invalid and are therefore not depicted on the image.

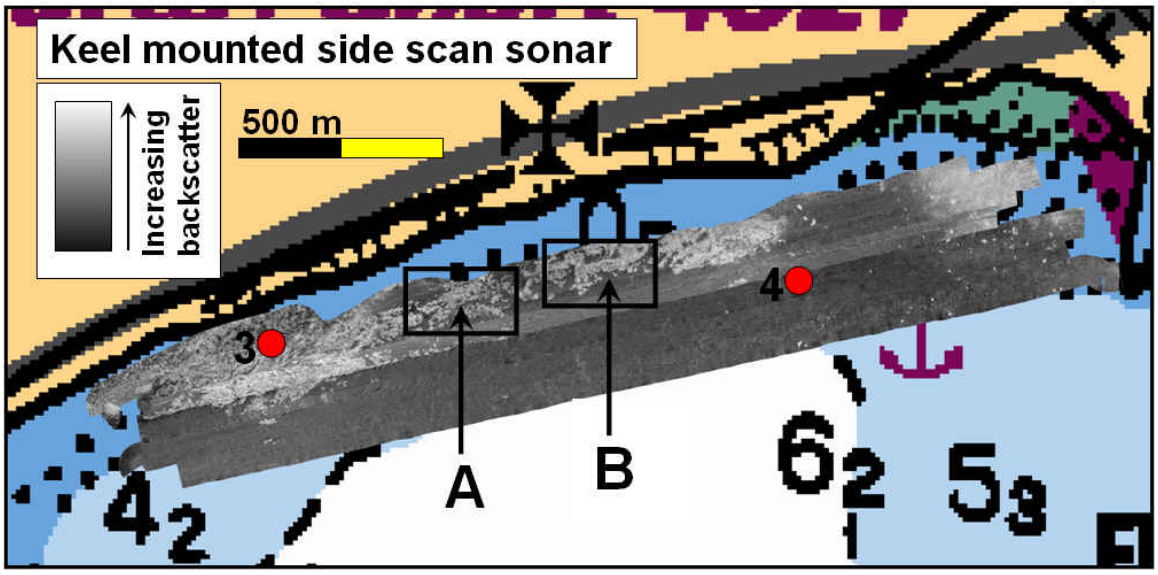

Figure 5.21 Keel mounted side scan sonar backscatter. Brightly shaded backscatter represents rocks or pebbles on the seabed. Markers at '3' and '4' refer to underwater photography in Figure 5.25.

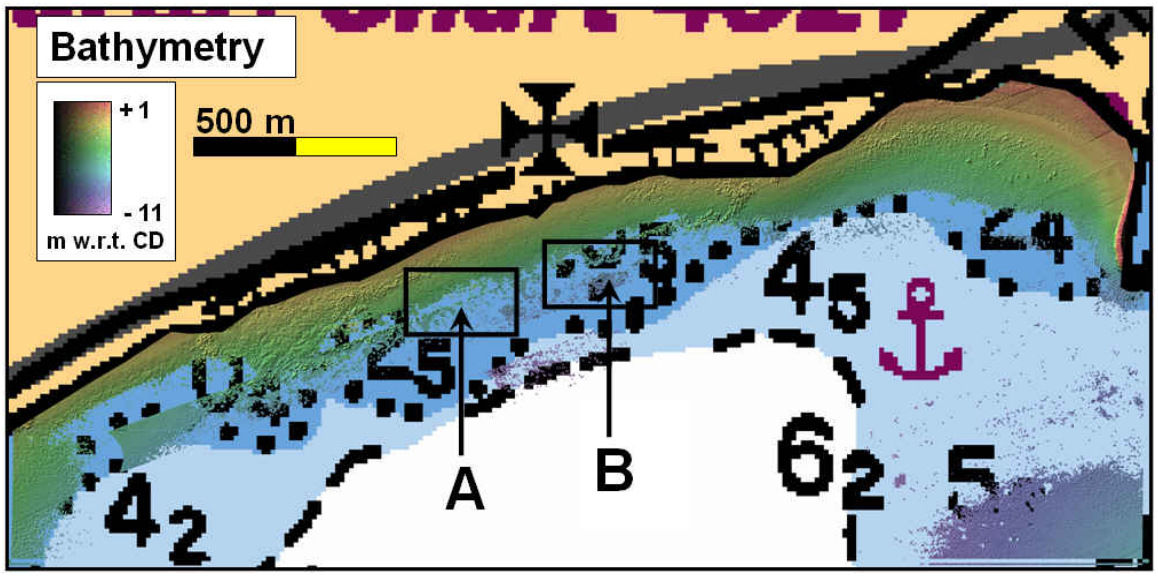

Figure 5.22 SHOALS-3000 bathymetry. Background chart depths in fathoms

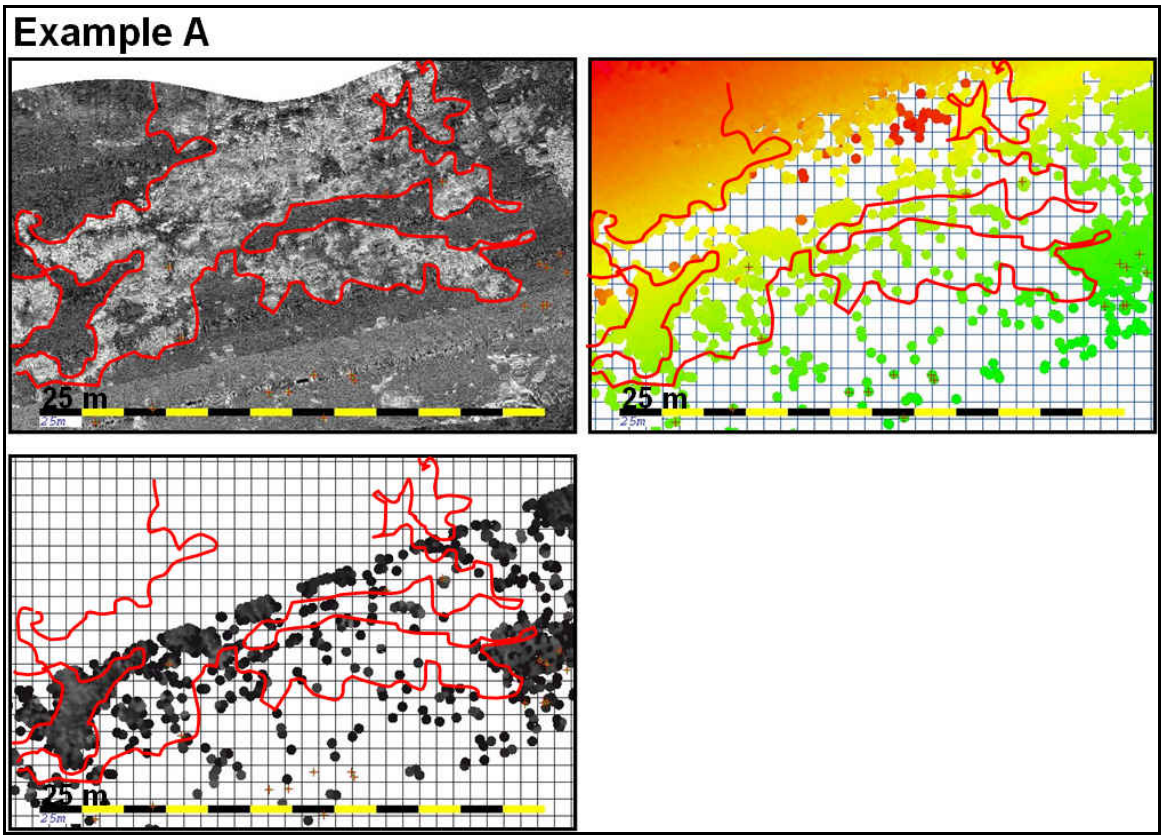

Figure 5.23 A close-up of the left box in Figure 5.22 presenting acoustic backscatter (top left), lidar bathymetry (top right), and GAPD bottom return height (bottom left). High acoustical backscatter is bounded with a contour. The backscatter contour is superimposed on the bathymetry and bottom return height maps.

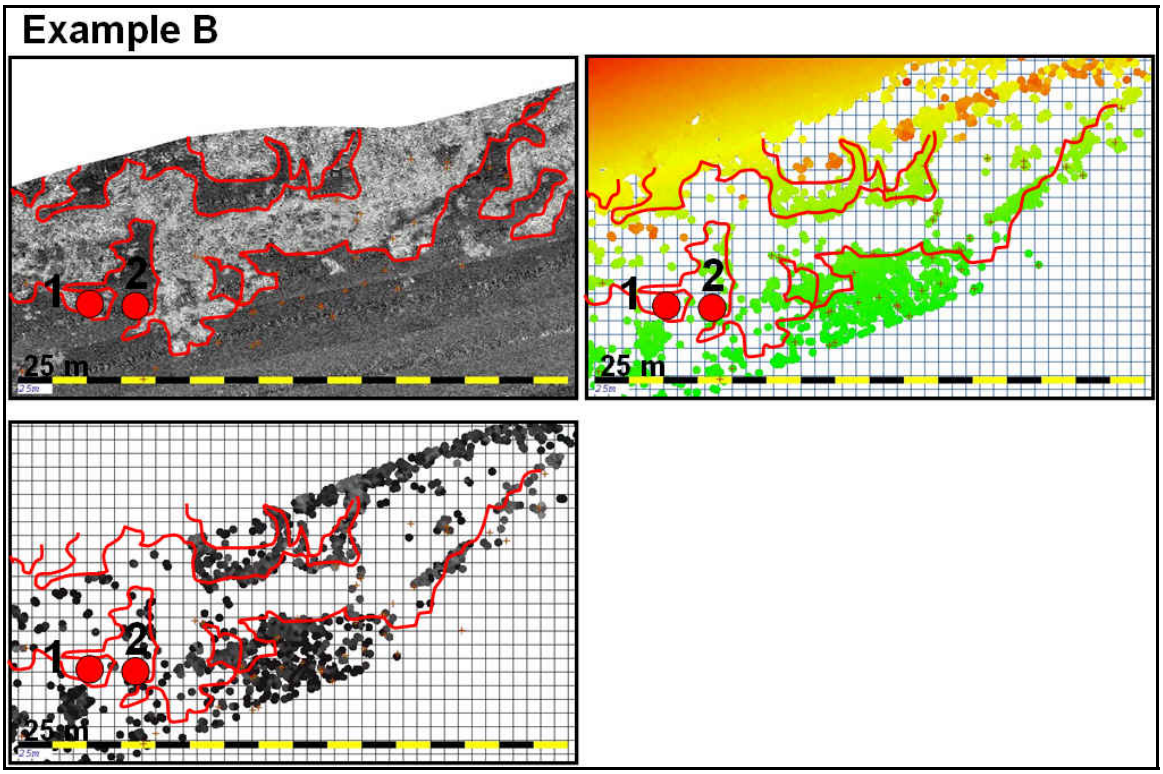

Figure 5.24 A close-up of the right box in Figure 5.22 presenting acoustic backscatter (top left), lidar bathymetry (top right), and GAPD bottom return height (bottom left). High acoustical backscatter is bounded with a contour. The backscatter contour is superimposed on the bathymetry and bottom return height maps. Markers at '1' and '2' refer to underwater photography in Figure 5.25.

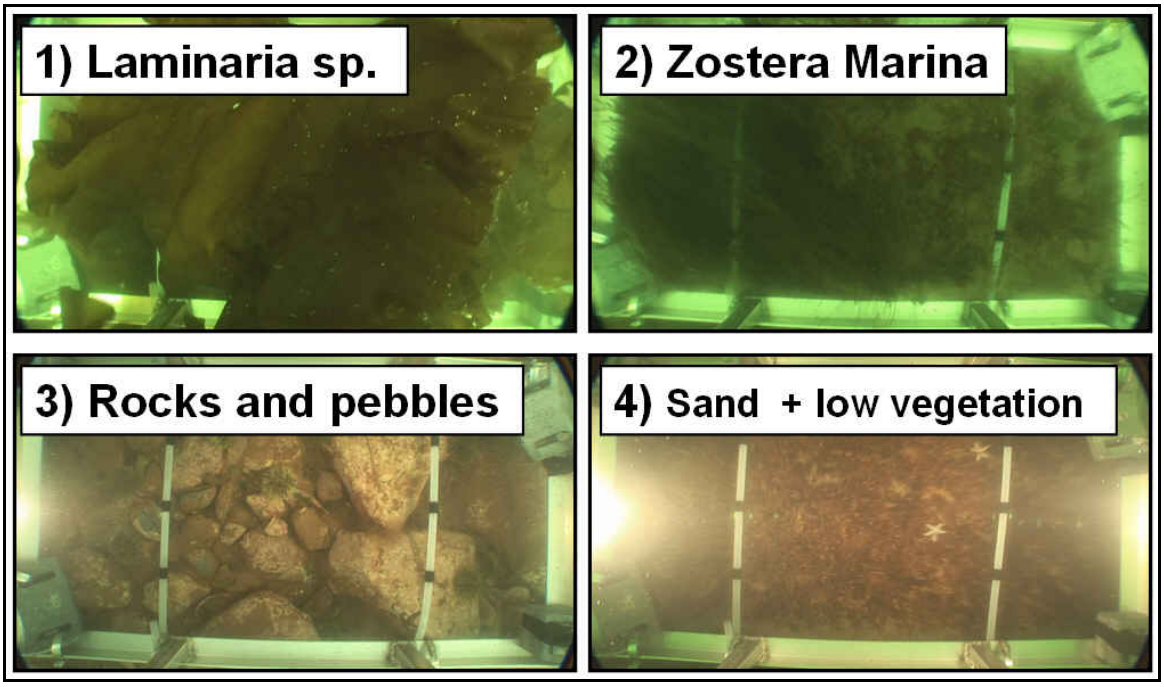

Figure 5.25 Underwater photography corresponding to locations indicated in Figure 5.23 and 5.21.

The next waveform dataset with overlapping acoustical backscatter is less explicit in terms of vegetation presence. The area (Figure 5.26) includes two sets of acoustical backscatter and lidar data. Again, the acoustical backscatter data overlaps beyond the lidar extinction depths (~ 8 m CD), but does not overlap the shallow portion of the lidar data (~ < 1 m CD). The area mainly shows strong acoustical backscatter over the whole area, suggesting rock- or pebble-like sediments, similar to the examples presented earlier in this section, although underwater photography and sediment grabs were not available in the surrounding area to verify this assumption. An interesting contradiction is seen when weak(er) acoustical backscatter is compared to overlapping bottom return height values. A cluster of weak acoustical backscatter seen in the north correlates to high bottom return heights, Figure 5.26 A. In contrast, apparently weak acoustical backscatter in the southern portion correlates to lower bottom return height values, Figure 5.25 B. In this case, the (sandy) seabed must have been populated with vegetation, leading to a weak bottom return.

As mentioned above, the optical signal is influenced by color, while the acoustical signal is insensitive for color. Reflectors with a color similar to the laser signal (532 nm: in the blue-green spectrum) will absorb most of it, thus acting as bad reflectors. The laser signal on marine life will therefore mostly be absorbed, while the laser signal on sand, for example, will reflect because its color lies further from the blue-green portion of the spectrum. With acoustical backscatter we can distinguish different sediment types, and subsequently, if a vegetation species dominantly populates a specific substrate, we can use acoustical backscatter to identify potential habitats of that specific vegetation. A

habitat for Laminaria sp., for example, is identified from acoustical backscatter based on the assumption that it colonizes rocks or pebbles, which return a strong acoustical backscatter. Likewise, habitats for Zostera Marina are identified based on the assumption that it grows on sand, which returns weaker acoustical backscatter (note that groundtruthing data, e.g. sediment grabs or underwater photography, are necessary to link the backscatter with sediment class).

The correlations between acoustical backscatter and bottom return height presented here demonstrate that acoustical backscatter cannot arbitrarily be used to locate the vegetation itself, but only to locate potential habitats of the vegetation. In contrast, the bottom return height can be used to locate the presence of vegetation. By combining these two relations we can identify sand-, or rock- and pebble-based vegetation with the following logic:

- weak acoustical backscatter and low bottom return height suggest the presence of sand based vegetation (e.g. Zostera Marina),
- weak acoustical backscatter and high bottom return height suggest an unvegetated sandy seabed,
- strong acoustical backscatter and low bottom return height suggest the presence of rock- or pebble-based vegetation (e.g. Laminaria sp.) ,
- strong acoustical backscatter and high bottom return height suggest an unvegetated rock-, or pebble-like seabed.

This section demonstrated that, by incorporating ground truthing data, we were able to link acoustical or laser characteristics with seabed material or biological growth.

Moreover, by joining these characteristics, we can formulate a logic that yields the presence of vegetation and the substrate. Section 5.3.3 presents the result of this logic when overlapping acoustical and laser data are automatically compared.

Typical bathymetric lidar surveys, however, do not include acoustical data, or underwater photography. Although aerial photography is indeed simultaneously collected, its value is strongly dependent upon the water clarity and water depth. Ideally, we want to utilize the lidar data without any aiding datasets to link vegetation presence and the resulting improper bottom tracking. This linking can be done with lidar bathymetry and the associated waveforms. Note that, despite the varying associated acoustical backscatter, the low bottom return clusters do share a common correlation; low bottom return height values all match with noise in the bathymetry (Figure 5.26). These disturbances in the bathymetry are caused by improper bottom tracking of the green laser beam when it strikes on vegetation (discussed in section 5.1 Bottom tracking). We can thus link two characteristics to the presence of vegetation: 1) improper bottom tracking, and 2) a low bottom return height. Section 5.3.3 continues with this observation.

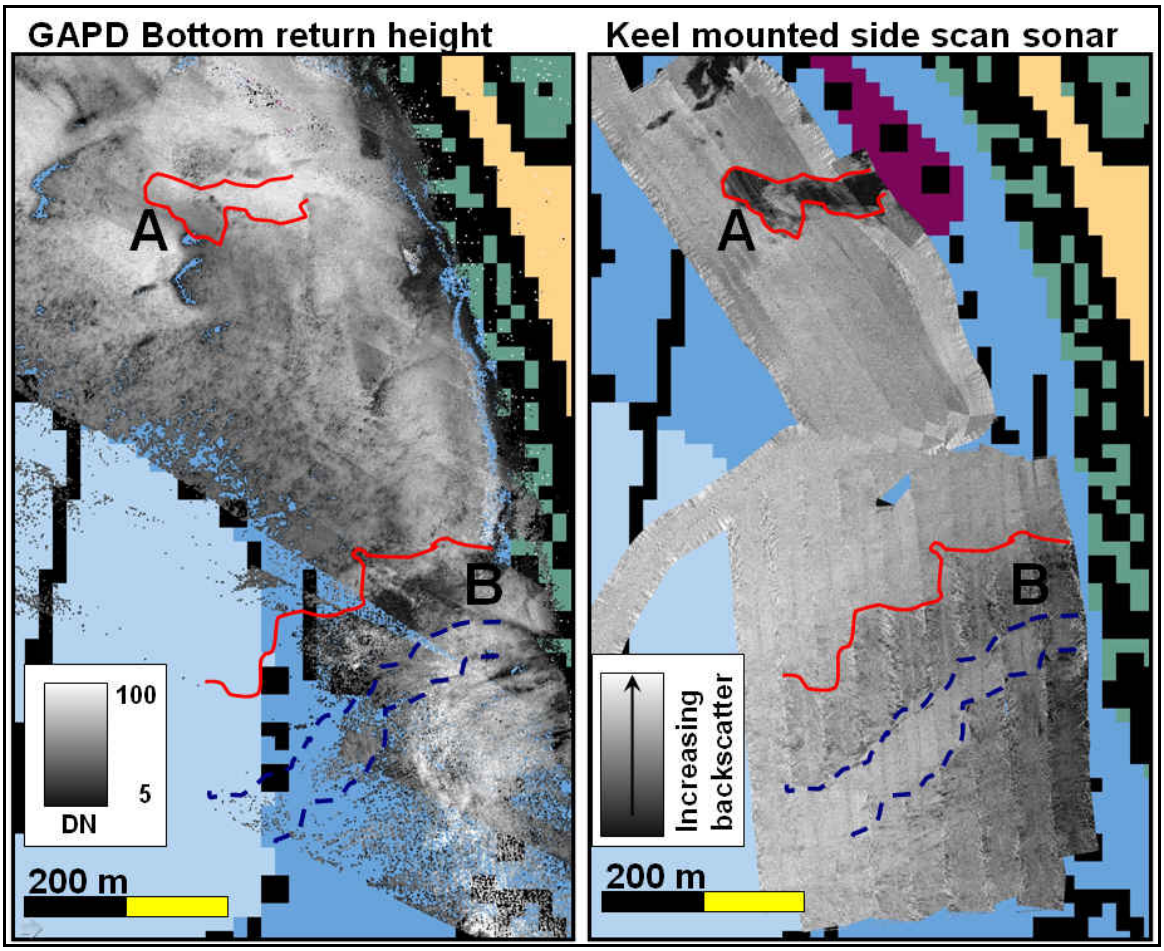

Figure 5.26 GAPD bottom return height map and keel mounted side scan sonar backscatter. Red contour bound weak acoustical backscatter, Blue (dashed) contour bounds and corridor with strong acoustical backscatter. Comparison of the waveform data within the contours show that acoustical backscatter and bottom return height do not always correlate with each other.

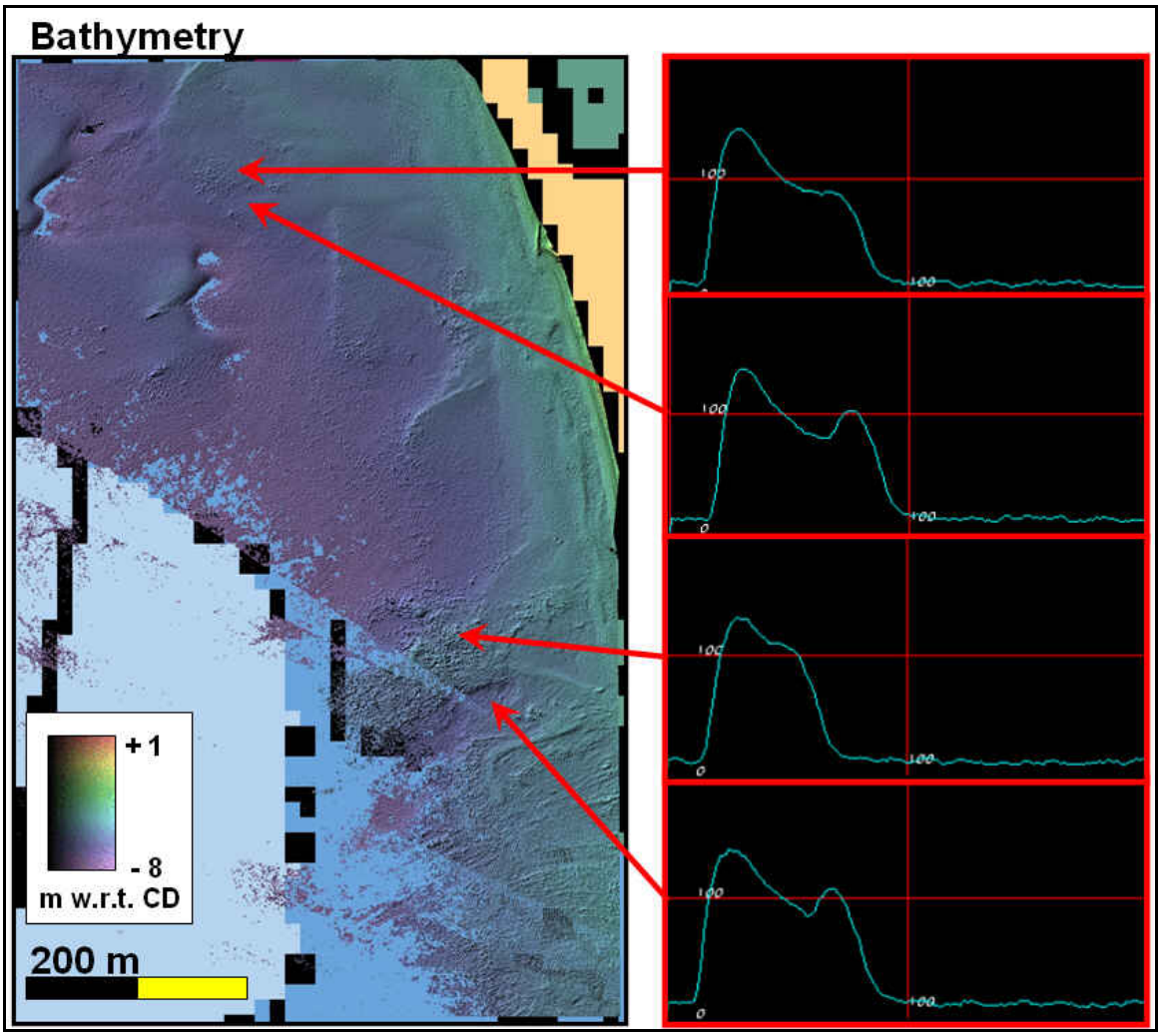

Figure 5.27 Bathymetry. Waveforms with low bottom return heights are present at noisy features in the DTM.

5.3.2 Height comparison

The previous section demonstrated low bottom return height values corresponding with aquatic vegetation presence. This section will explore the absolute and relative differences between vegetation dominant areas and areas with an unvegetated seabed in order to segregate the presence of vegetation from the surrounding seabed with the bottom return height. When we can establish typical bottom return height values (for our

dataset), those values may act as a threshold to isolate regions of dense seabed biological growth. In addition, a small set of sediment grabs is used to investigate a correlation with bottom return height values, specifically to investigate the presence of sediments with a reflectance similar to vegetation.

Tables 5.3 to 5.5 lists statistics of the bottom return height and k_s at seven areas with a vegetated seabed, and six areas with a unvegetated seabed (identified with ground truthing data and lidar bathymetry). The dataset names refer to the same datasets used in Section 4.4.3. Datasets C and D (Tables 5.3 and 5.4 respectively) overlap each other on successive days, so that we can examine day-to-day differences. As dataset B did not overlap with any of the isolated investigation areas, it is excluded from the analysis.

All datasets reveal a low bottom return height when the green laser beam strikes on vegetation although the values vary slightly among different datasets and waveform channels. Naturally, GAPD waveforms exhibit higher bottom return height and k_s values as a result of their FOV. As explained in Section 4.3, k_s-values are smaller at vegetated areas; a less strongly shaped bottom return of a vegetation hit influences the derivation of the volume return from which the k_s is extracted, leading to a slightly smaller k_s (less steep slope). Indeed, the slightly under estimated k_s will contribute to a lower bottom return height (derived from top of bottom return to the extrapolation of the k_s-line), but the waveform will inhibit a low bottom return in the first place due to lower reflectance of the green laser light from the vegetation (e.g. Lyzenga [1978]).

The mean bottom return height values of vegetated and unvegetated areas between different datasets vary; dataset D, for example, shows higher bottom return

height values compared to overlapping data from dataset C. In contrary, k_s-values from dataset D are higher as well, suggesting more turbid water. Without questioning this suggestion, higher k_s-values do not directly have to imply a reduced bottom return height resulting from more attenuation. Again, the mechanism behind the derivation of the bottom return height is the cause for this apparent contradiction. For that reason, the ratio of the mean bottom return height at vegetated and unvegetated seabeds ($\frac{\overline{height_{vegetated}}}{height_{unvegetated}}$) yields a useful term (Table 5.6).

This ratio reaches unity when mean bottom return height values of vegetated and unvegetated seabeds are the same. Interestingly, the ratios are consistent at all three datasets, at both GAPD and PMT waveforms. This consistency is reassuring, making it possible to approximate the bottom return height of vegetated or unvegetated seabeds once we have a mean value of one of them. With the ratios of varying datasets and waveform channels being fairly constant, it is assumed that the green laser beam will act coherently each time it strikes on vegetation. In addition, the consistency of the ratios between GAPD and PMT bottom return heights implies that both waveform channels are affected equally in areas of dense aquatic vegetation.

A final observation drawn from Tables 5.3 to 5.5 is the contribution of depth. Apparently an increase of depth, in addition to the presence of vegetation, contributes detrimentally to the bottom return height. Although depth effects to the waveforms were not noticed before (Section 4.4.5), an increase of depth in combination with vegetation presence indeed diminishes the bottom return. Section 5.1 and 5.3.1 demonstrated the success of a lidar return being influenced by vegetation presence and depth increase, as

well.

Table 5.3 Derived from dataset C: mean bottom return heights, k_s, and depth at 4 vegetated, and 3 unvegetated areas.

Dataset C					
	GAPD		**PMT**		**Depth CD (m)**
Area	$\overline{height}$ (DN)	$\overline{k_s}$ (DN/m)	$\overline{height}$ (DN)	$\overline{k_s}$ (DN/m)	
Vegetated 1	25	8.41	18	6.02	2.70
Vegetated 2	14	6.62	9	4.74	3.75
Vegetated 3	26	10.65	18	7.76	3.23
Vegetated 4	22	8.16	16	6.07	2.70
Mean	21.75	8.46	15.25	6.15	3.1
Stdev	5.44	1.67	4.27	1.24	0.5
Unvegetated 1	58	8.72	44	6.28	4.37
Unvegetated 2	54	6.05	42	4.61	3.30
Unvegetated 3	55	9.08	40	6.46	6.75
Mean	55.67	7.95	42	5.78	4.81
Stdev	2.08	1.67	2.00	1.02	1.77

Table 5.4 Derived from dataset D: mean bottom return heights, k_s, and depth at 4 vegetated, and 3 unvegetated areas.

Dataset D					
	GAPD		**PMT**		**Depth CD (m)**
Area	$\overline{height}$ (DN)	$\overline{k_s}$ (DN/m)	$\overline{height}$ (DN)	$\overline{k_s}$ (DN/m)	
Vegetated 1	35	17.96	27	13.32	2.70
Vegetated 2	24	11.84	18	9.86	3.75
Vegetated 3	32	14.47	23	11.34	3.23
Vegetated 4	24	15.73	16	11.85	2.70
Mean	28.53	15.00	21.08	11.59	3.1
Stdev	5.70	2.56	4.45	1.43	0.5
Unvegetated 1	61	17.07	50	13.36	4.37
Unvegetated 2	64	14.16	53	11.84	3.30
Unvegetated 3	58	10.59	44	8.79	6.75
Mean	61.18	13.94	48.76	11.33	4.81
Stdev	3.10	3.25	4.41	2.33	1.77

Table 5.5 Derived from dataset A: mean bottom return heights, k_s, and depth at 4 vegetated, and 3 unvegetated areas.

Dataset A

Area	GAPD $\overline{height}$ (DN)	GAPD $\overline{k_s}$ (DN/m)	PMT $\overline{height}$ (DN)	PMT $\overline{k_s}$ (DN/m)	Depth CD (m)
Vegetated 5	17	13.29	9	9.41	4.9
Vegetated 6	24	14.00	12	9.65	6.12
Vegetated 7	24	14.35	11	10.00	6.16
Mean	21.42	13.88	10.88	9.69	5.73
Stdev	3.85	0.54	1.22	0.30	0.72
Unvegetated 4	49	17.88	36	13.29	3.60
Unvegetated 5	57	17.53	38	12.12	4.35
Unvegetated 6	48	14.12	31	10.00	6.17
Mean	51.5	16.51	35.15	11.80	4.71
Stdev	4.68	2.08	3.37	1.67	1.32

Table 5.6 Ratio's of the mean bottom return height of the vegetated seabed, against the mean bottom return height of the un-vegetated seabed.

Ratio vegetated: unvegetated bottom return height		
Dataset	**GAPD**	**PMT**
A	0.42	0.31
C	0.39	0.36
D	0.47	0.43

One set of ground truthing data not documented so far is sediment grabs. As mentioned before, the value of sediment grabs is reduced without associated underwater photography. Associating underwater photography with the grabs not only allows us to conclude whether the green laser beam indeed reflected on the sediment, or the vegetation that grows on the sediment, but also allows us to see the color of the sediment (compared to the color of vegetation). We have to be aware that we will make a somewhat cumbersome comparison: we will compare the optical reflectance, influenced by color, with sediment size, while we are in fact comparing the optical reflectance with the color of the sediment or marine life that covers it.

A small selection of sediment grabs was collected around the Paspebiac sandspit (Figure 5.28). The grabs were mainly classified as “fine” or “very fine sand” covered by granules, (small) pebbles, or silt (Table 5.7). Sediment with color(s) close to the green spectrum (532 nm) may result in a bottom return similar to that of vegetation: marine life covered pebbles, for example.

The bottom return height values of GAPD and PMT waveforms corresponding to the grabs from overlapping datasets C and D are plotted against the local water depth in Figure 5.29. The horizontal dashed lines in the top and bottom portion of the graph depict the mean bottom return heights of the unvegetated, and vegetated seabed, respectively (derived from Tables 5.3 to 5.5). The labels are linked to grabs in Table 5.7 of Figure 5.28. A vertical dashed line presents the boundary after which PMT bottom return height values exceed those of the GAPD waveforms. Note that this boundary (at approximately 7 m CD) is the data quality boundary seen before in GAPD bottom return height maps (e.g. Figure 4.26 overleaf). We will focus on the sediment grabs in the left portion of the graph only, these represent reliable data from both GAPD and PMT waveforms. From this sub-selection, bottom return height values at sediment grab locations are well above the mean unvegetated seabed bottom return height, with the exception of grab 14. Grab 14, classified as “very fine sand with silt and pebbles,” is located in a region where the lidar frequently lost bottom track and waveforms inhibited low bottom return heights. Grab 14 is an example of low reflectance due to marine life, rather than sediment (color).

Despite the limited value of sediment grabs for this experiment, a low reflecting sediment was not found in the vicinity of the Paspebiac shore, allowing us to link low bottom return heights with vegetation presence. Now that we have established threshold

values, the following section will continue with these typical bottom return height values in order to recognize vegetated and unvegetated seabeds from lidar data.

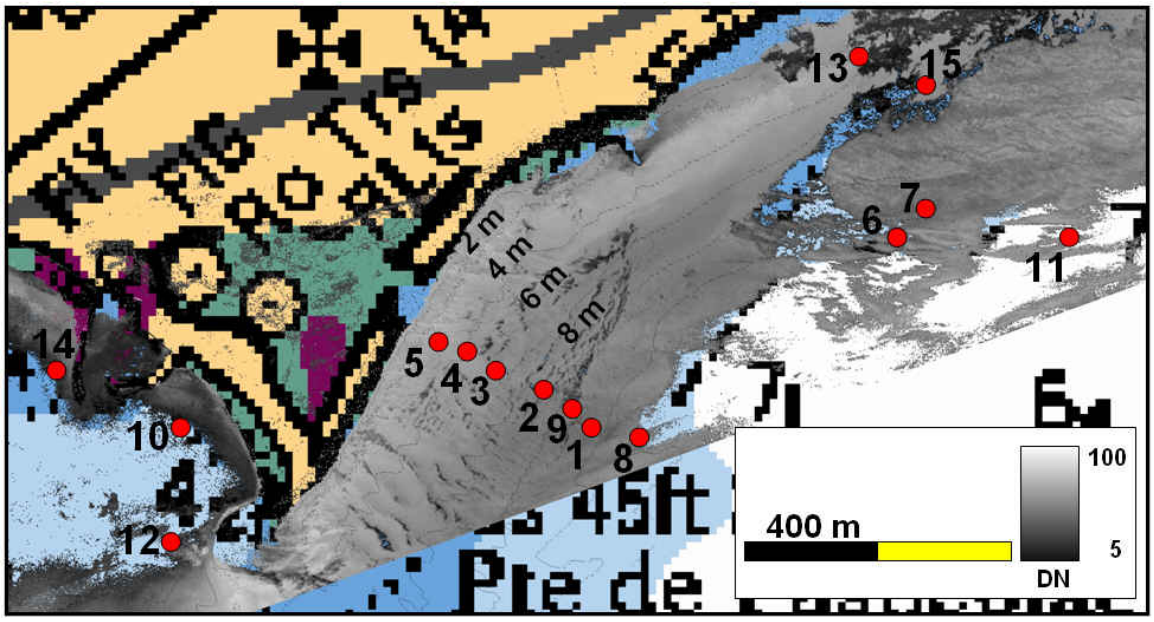

Figure 5.28 GAPD bottom return height with bathymetry contours at the Paspébiac sandspit. Numbered sediment grabs are listed in Table 5.7.

Table 5.7 Classification of the sediment grabs, located near the Paspébiac sandspit, Figure 5.29.

Grab	Classification
1	Fine sand with granules
2	Fine sand with granules
3	Fine sand with granules and pebbles
4	Fine sand with granules and pebbles
5	Fine sand with granules and pebbles
6	Fine sand with granules and pebbles
7	Fine sand with granules and pebbles
8	Fine sand with granules and small pebbles
9	Fine sand with pebbles
10	Silt with small pebbles
11	Very coarse sand with granules and pebbles
12	Very fine sand and silt
13	Very fine sand and silt with small pebbles
14	Very fine sand and silt with small pebbles
15	Very fine sand with granules

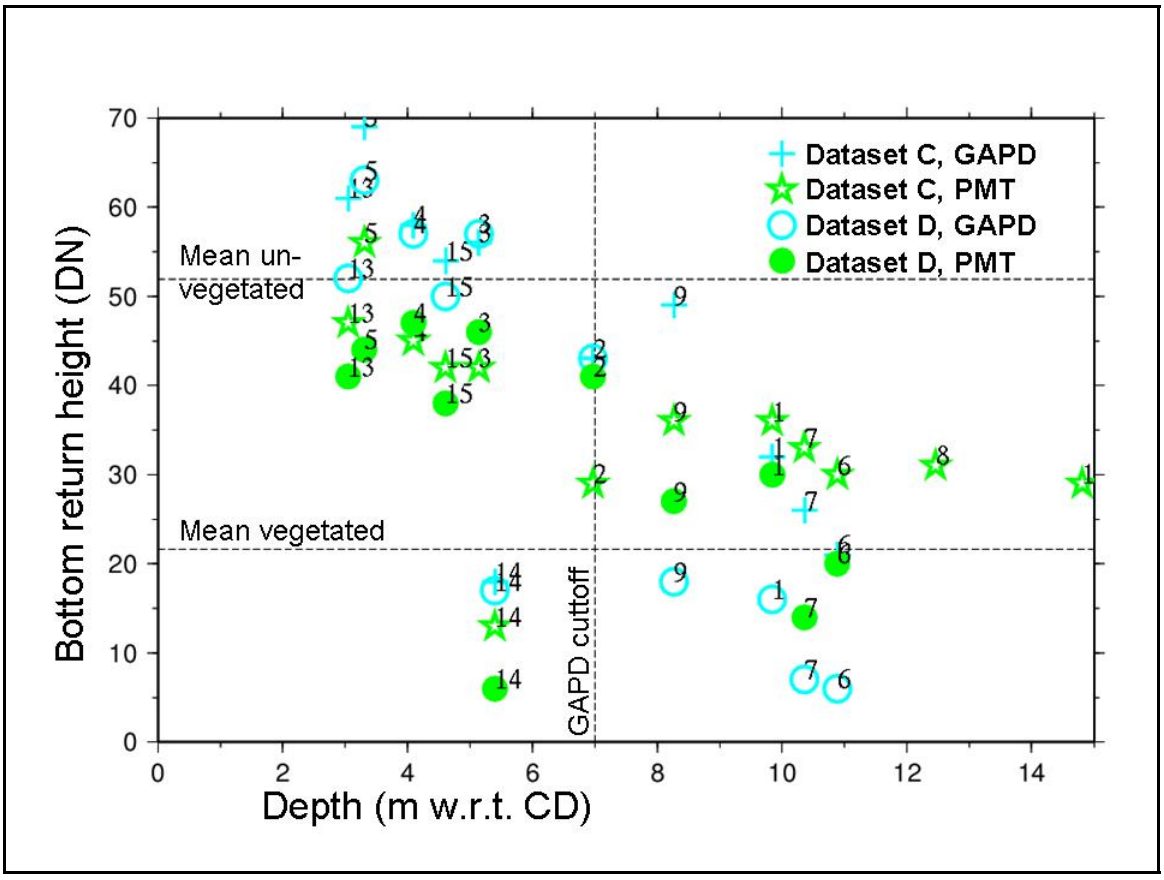

Figure 5.29 Sediment grabs associated with local bottom return heights. The graph includes four series: GAPD and PMT wavefroms from datasets C and D. The mean values for a vegetated and unvegetated seabed and the GAPD data quality cutoff depth is indicated are indicated with the dashed lines.

5.3.3 Sounding Validation

The possible presence of vegetation makes a bathymetric lidar dataset less trustworthy, but ground truthing data to validate the lidar soundings are seldom available. This section proposes a method to identify regions of biological growth, thus allowing the hydrographer to identify incorrect or doubtful soundings in terms of bottom tracking. The sections above demonstrated two important phenomena when the green laser beam strikes on vegetation: 1) low bottom return height, and 2) bottom mis-tracking. In

addition, acoustic backscatter can reveal potential habitats of vegetation. These phenomena were used in an automated logic to assess lidar datasets. The logic includes threshold (T) values of the lidar bathymetry slopes (between adjoining grid cells), bottom return heights, or acoustical backscatter (BS), and is based upon raster images of the slopes or acoustical backscatter against a raster image of the bottom return height. The logic compares overlapping grid cells (xy) against threshold values and then determines a classification. When lidar bathymetry slopes and bottom return heights are used, the following logic is invoked:

Table 5.8 Logic for validation based on lidar bathymetry slope and bottom return height.

Logic	Classification
$xy_{slope} > T_{slope}$ and $xy_{bottom\_return\_height} < T_{bottom\_return\_height}$	Tall growing vegetation, or marine life covered navigational hazard
$xy_{slope} < T_{slope}$ and $xy_{bottom\_return\_height} < T_{bottom\_return\_height}$	Low growing vegetation, or tracking vegetation canopy
$xy_{slope} > T_{slope}$ and $xy_{bottom\_return\_height} > T_{bottom\_return\_height}$	Valid sounding, but potential navigational hazard
$xy_{slope} < T_{slope}$ and $xy_{bottom\_return\_height} > T_{bottom\_return\_height}$	Valid sounding

When the green laser beam starts to track the vegetation, the slope of the DTM between adjoining grid cells will increase. The slope threshold for all the examples presented here is arbitrarily set to 6°, which corresponds to a depth change of 0.21 metres at 2x2 m grids. If the green laser beam tracks on top of the vegetation, the slope will change irregularly but may lie below the slope threshold. However, the returned waveform will have a decreased bottom return suggesting a vegetated seabed. Natural seabed topography passes the validation, while seabed objects (e.g. wreck, anchor) covered by marine life, would be classified as distrustful soundings. Vegetation classified

soundings should therefore always require the hydrographer's awareness. Unfortunately, the data used for this study did not include any (manmade) seabed objects to test the logic for this specific case.

A similar, logic was formulated for overlapping acoustical backscatter and bottom return height data (Table 5.9). Overlapping acoustical backscatter indicates vegetation habitats, from which it is possible to localize vegetation species. A natural next step is joining results from both logics to determine the substrate, vegetation presence, and topography of each overlapping grid cell. The remainder of this section will present results of the lidar sounding classifications.

Table 5.9 Logic to determine vegetation habitats.

Logic	Classification
$xy_{BS} > T_{BS}$ and $xy_{bottom\_return\_height} < T_{bottom\_return\_height}$	Pebble- or rock-based vegetation
$xy_{BS} < T_{BS}$ and $xy_{bottom\_return\_height} < T_{bottom\_return\_height}$	Sand-based vegetation
$xy_{BS} > T_{BS}$ and $xy_{bottom\_return\_height} > T_{bottom\_return\_height}$	Unvegetated pebbles or rocks
$xy_{BS} < T_{BS}$ and $xy_{bottom\_return\_height} > T_{bottom\_return\_height}$	Unvegetated sand

Figure 5.30 presents the same area as Figures 5.16 to 5.18 from the previous section, which revealed fields of vegetation in the aerial photo mosaic and bottom return height map. Those fields are now classified as tall or low growing vegetation once validated with the logic from Table 5.8, and should therefore be treated with suspicion by the hydrographer for safety of navigation purposes. In addition, validation of the soundings now also has an ecological value. The following two figures (Figures 5.31 and 5.32) depict the far right subset of the lidar data overlapped by acoustical backscatter data. This aiding dataset now tells us that the cluster of low growing vegetation seen in

the southern part was all pebble- or rock-based.

Aiding acoustical backscatter was also available at the Bonaventure coast in Figures 5.34 to 5.39. The validation of these datasets shows large clusters of soundings to be untrustworthy. These lidar datasets thus appear less efficient in terms of data coverage and safety of navigation purposes. For such densely vegetated areas, a lidar survey at a time before the vegetation grows or once it decayed would be preferred, although water clarity issues at that time of the year may constrain the efficiency of the survey. Multibeam water column data confirmed classification of alternating low and tall growing vegetation in the southern portion of Figure 5.35. An example of the water column data is depicted in Figure 5.36.

The final example of sounding validation discussed is the sandwave field near the Paspébiac sandspit, Figure 5.40. The sandwave troughs are classified as low growing pebble- or rock-based vegetation, a classification that is plausible since nearby underwater photography revealed marine life covered pebbles.

Although we can validate lidar bathymetry without aiding ground truthing data, some additional data may be necessary to determine threshold values. Based on the data available for this study, it is unclear exactly how much typical bottom return height values vary. The threshold value used for this study (30 DN) may therefore not suffice with other datasets. However, for the purpose of sounding validation, extreme slope or bottom return height values (derived, for example, with the vegetated: unvegetated ratio) can be applied to isolate suspicious lidar soundings.

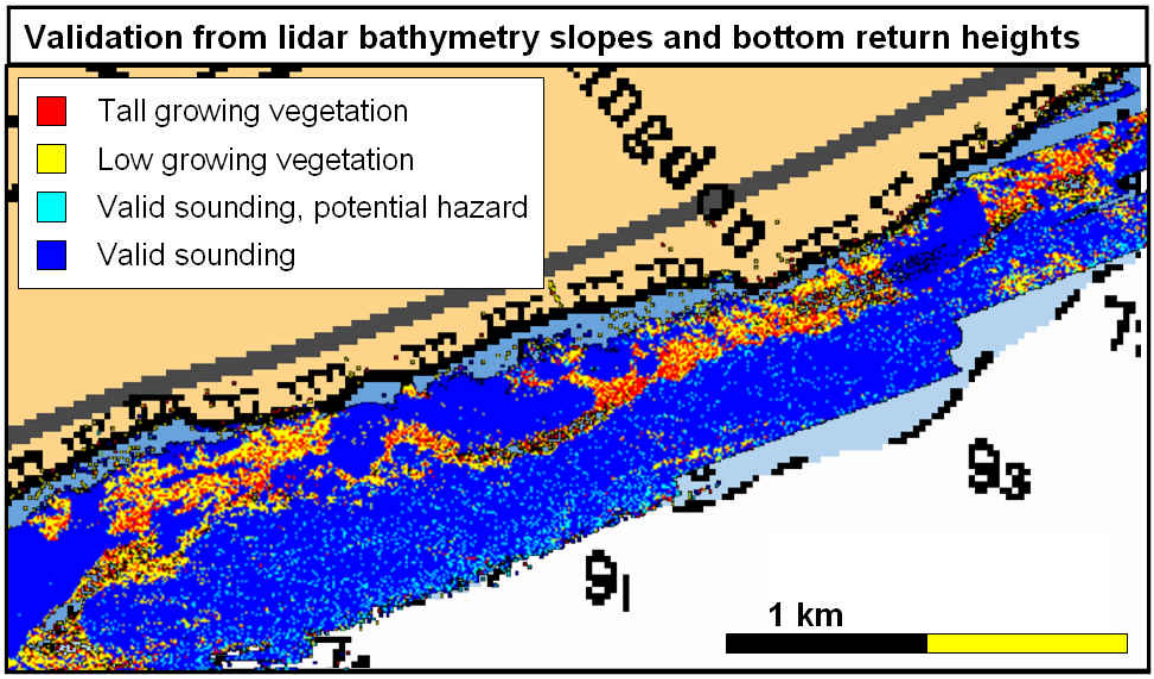

Figure 5.30 Validation of lidar soundings (displayed in Figure 5.32) from the bathymetry slopes and bottom return heights (displayed in Figure 5.17).

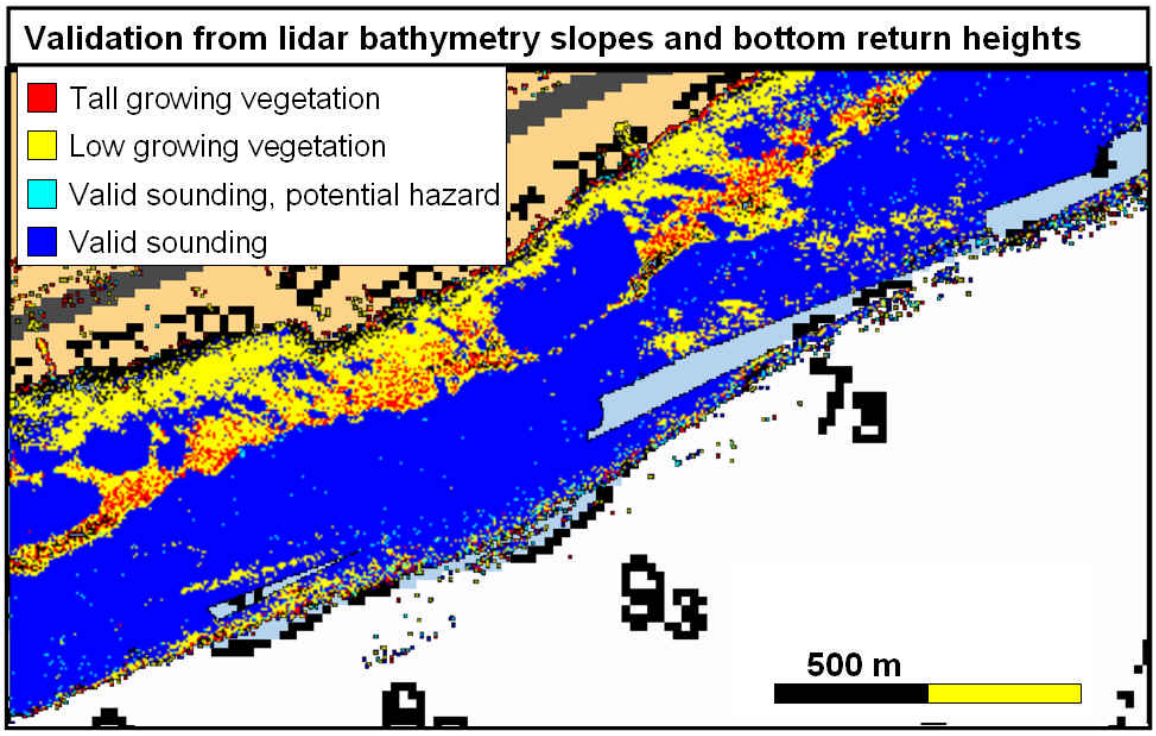

Figure 5.31 Validation of lidar soundings (displayed in Figure 5.32) from the bathymetry slopes and bottom return heights (displayed in Figure 5.17).

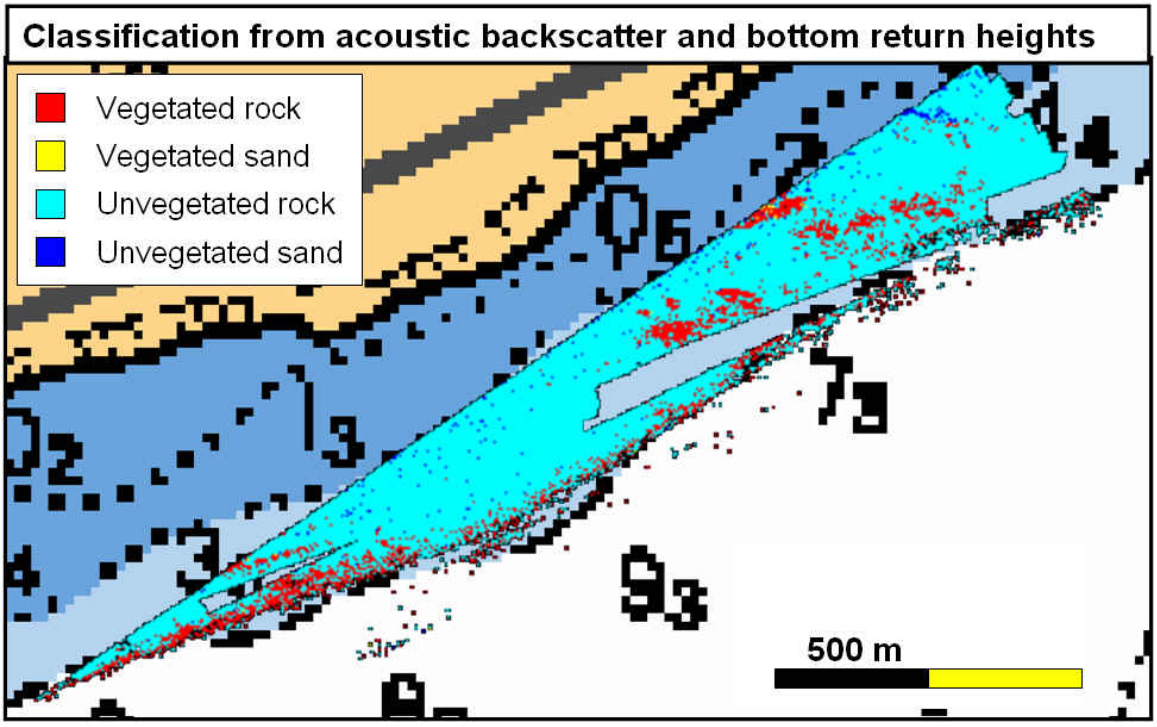

Figure 5.32 Classification of lidar data overlapping acoustical backscatter and bottom return heights (displayed in Figure 5.17).

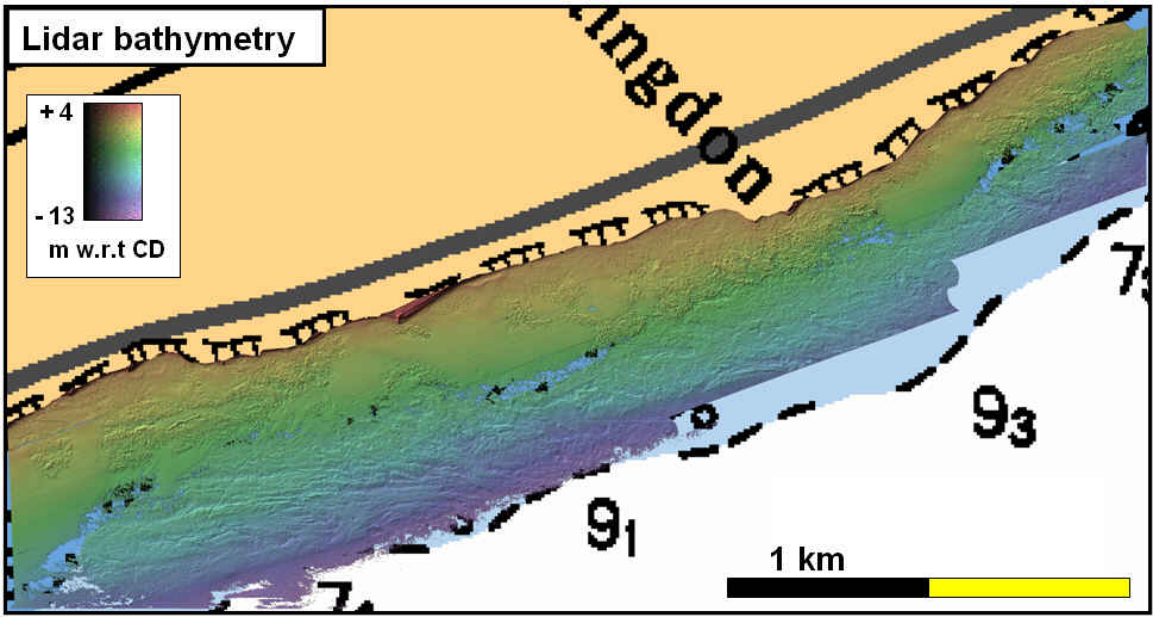

Figure 5.33 Matching lidar bathymetry of Figures 5.16 to 5.18 and 5.29.

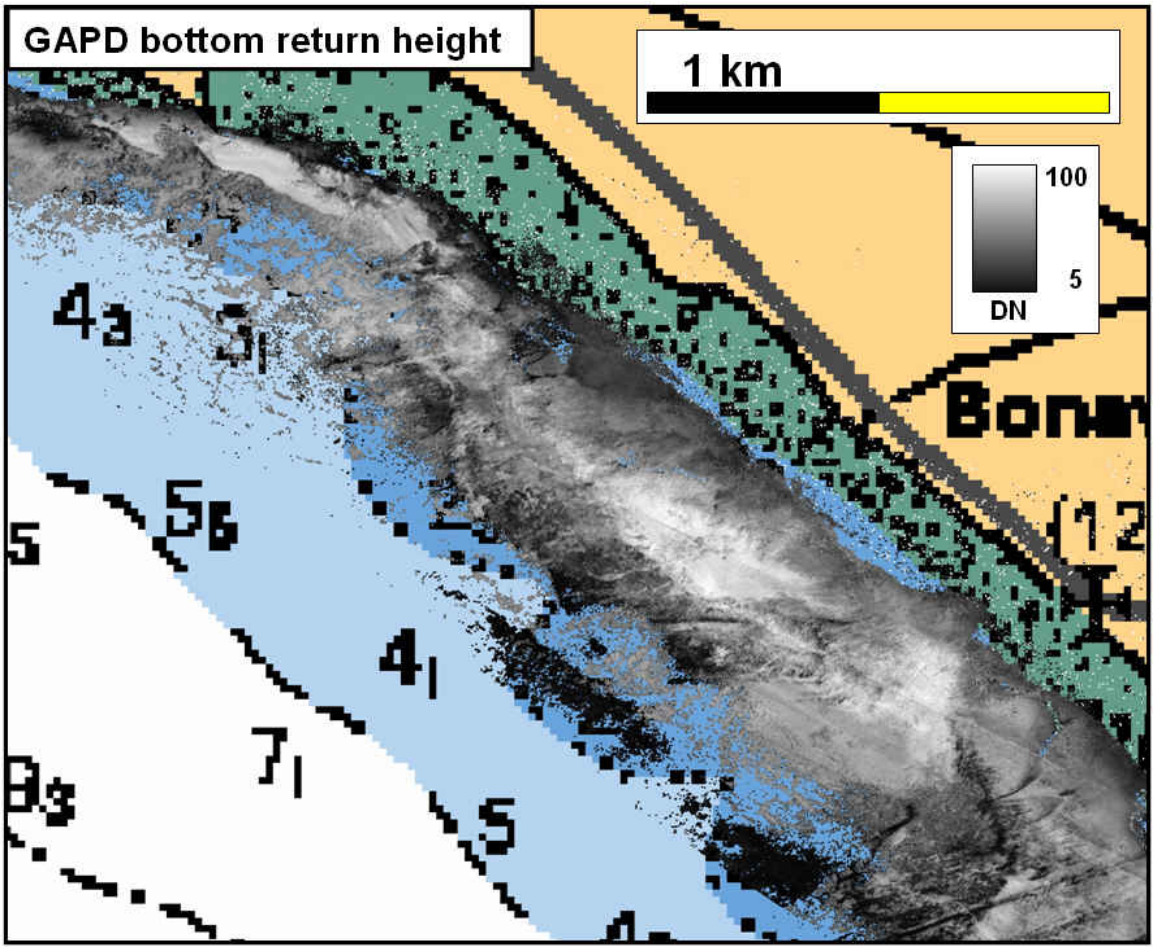

Figure 5.34 GAPD bottom return height near the Bonaventure coast.

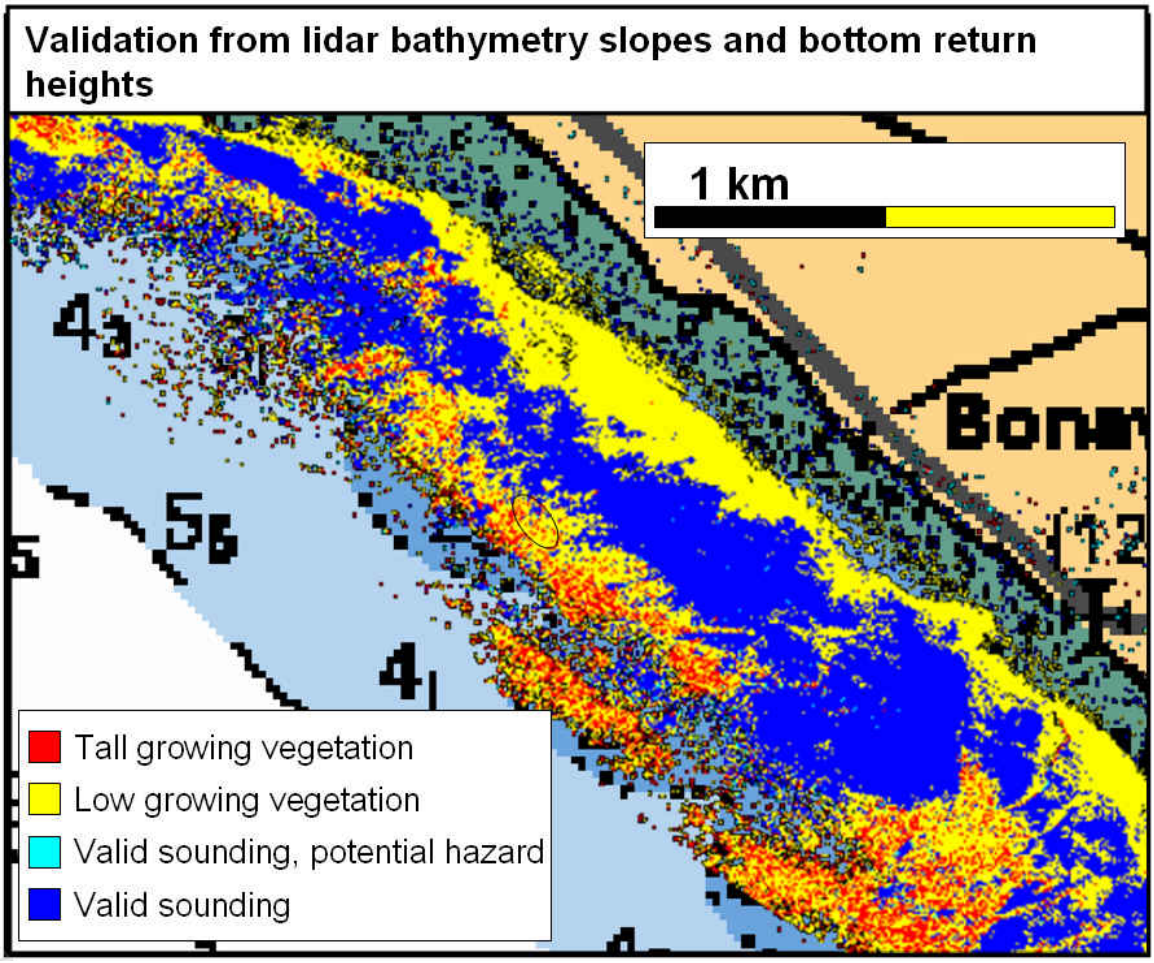

Figure 5.35 Validation of lidar soundings near the Bonaventure coast from the bathymetry slopes and GAPD bottom return heights. Multibeam watercolumn data in the ellipse (centre image) are plotted in Figure 5.35.

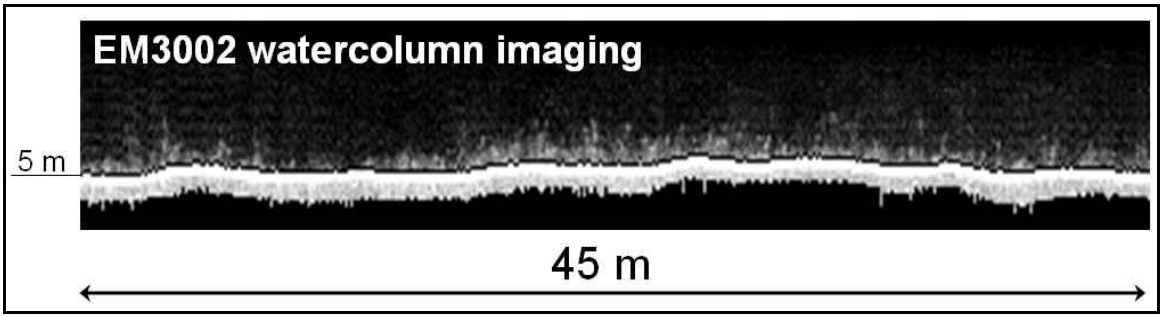

Figure 5.36 EM3002 multibeam watercolumn demonstrating irregular vegetation heights.

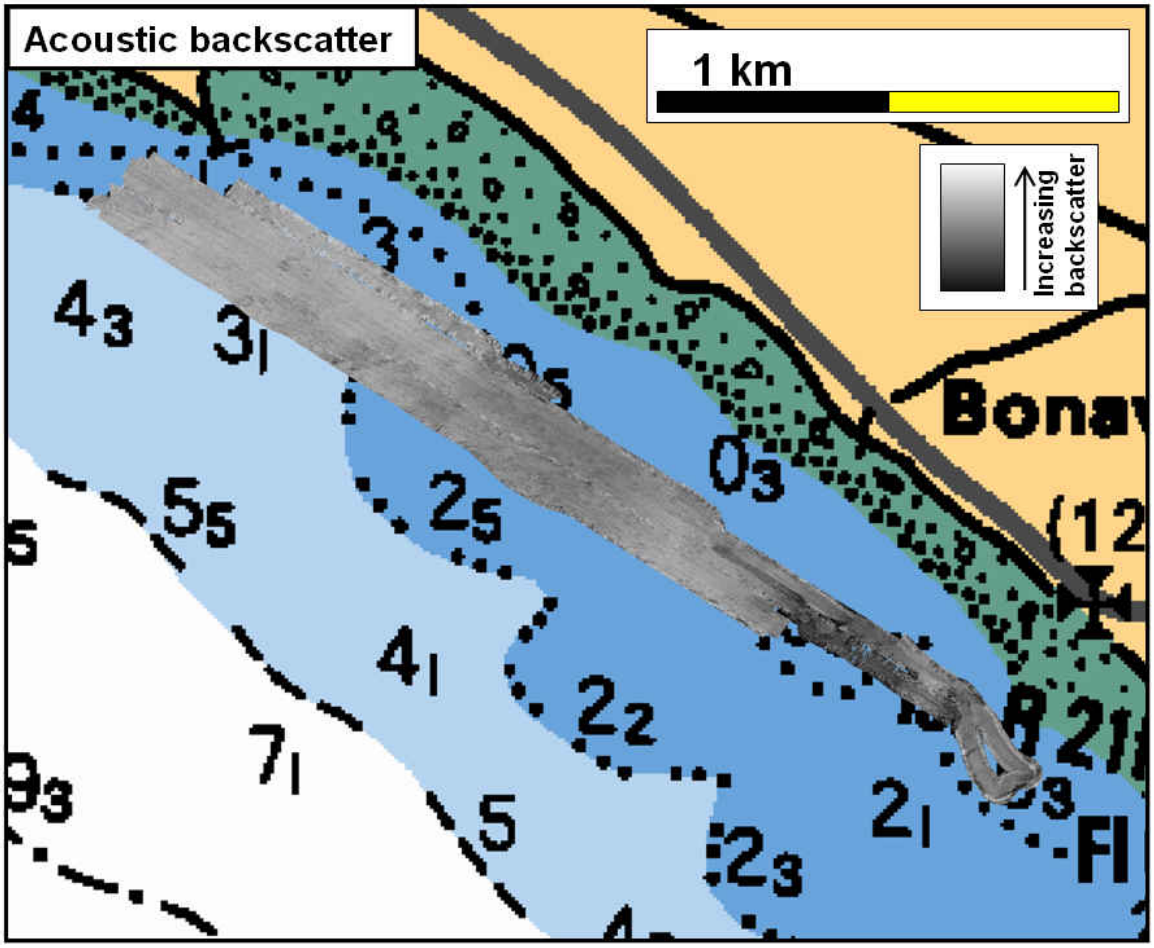

Figure 5.37 Keel mounted side scan sonar backscatter near the Bonaventure coast.

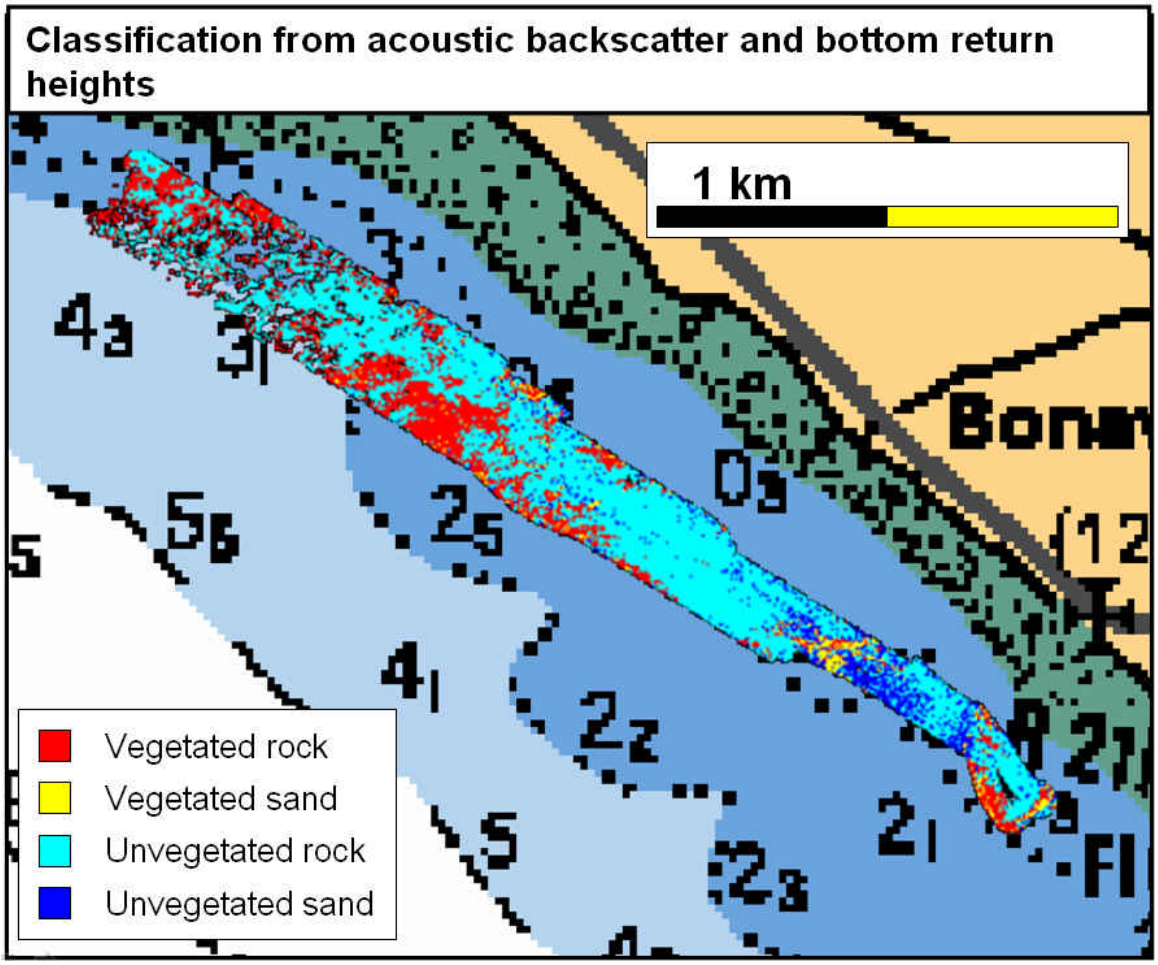

Figure 5.38 Classification of lidar data at the Bonaventure coast from overlapping acoustical backscatter and bottom return heights (displayed in Figure 5.33).

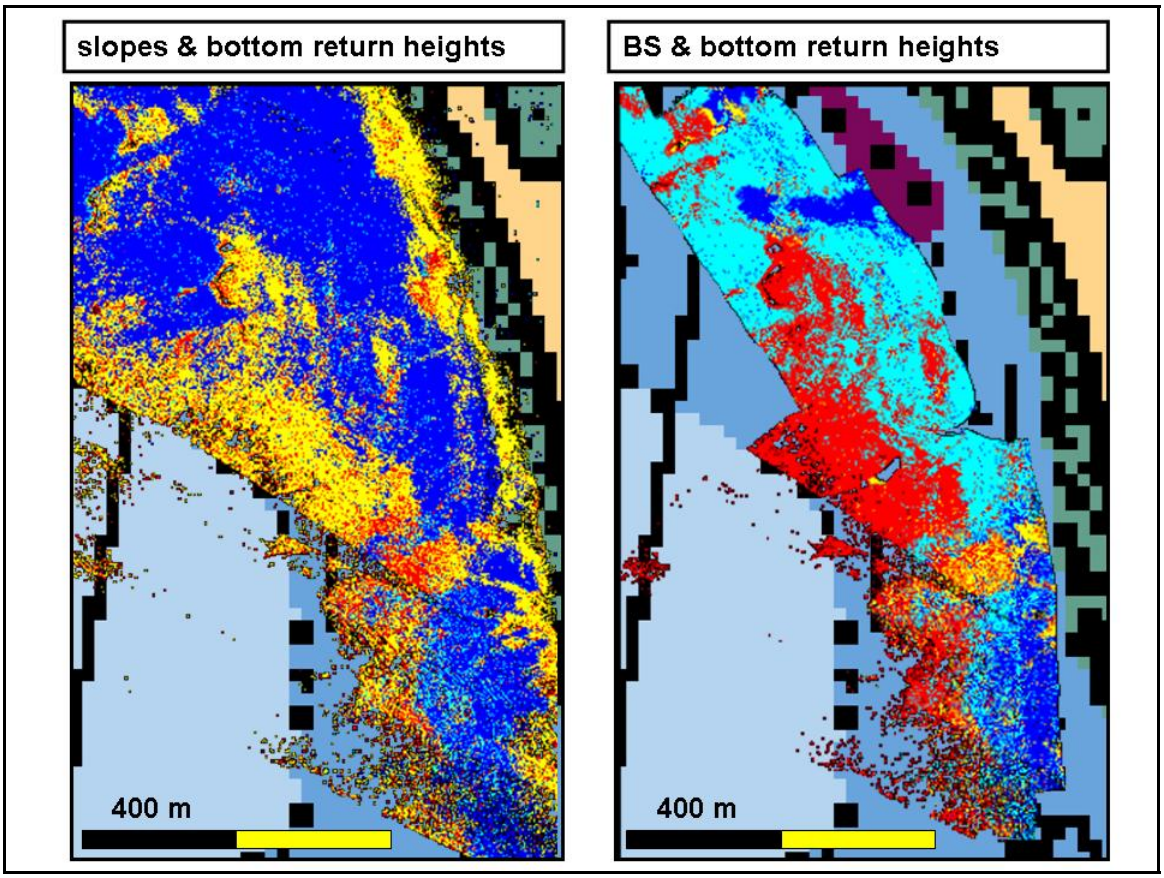

Figure 5.39 Lidar sounding validation (left) and classification (right) near the Bonaventure marina.

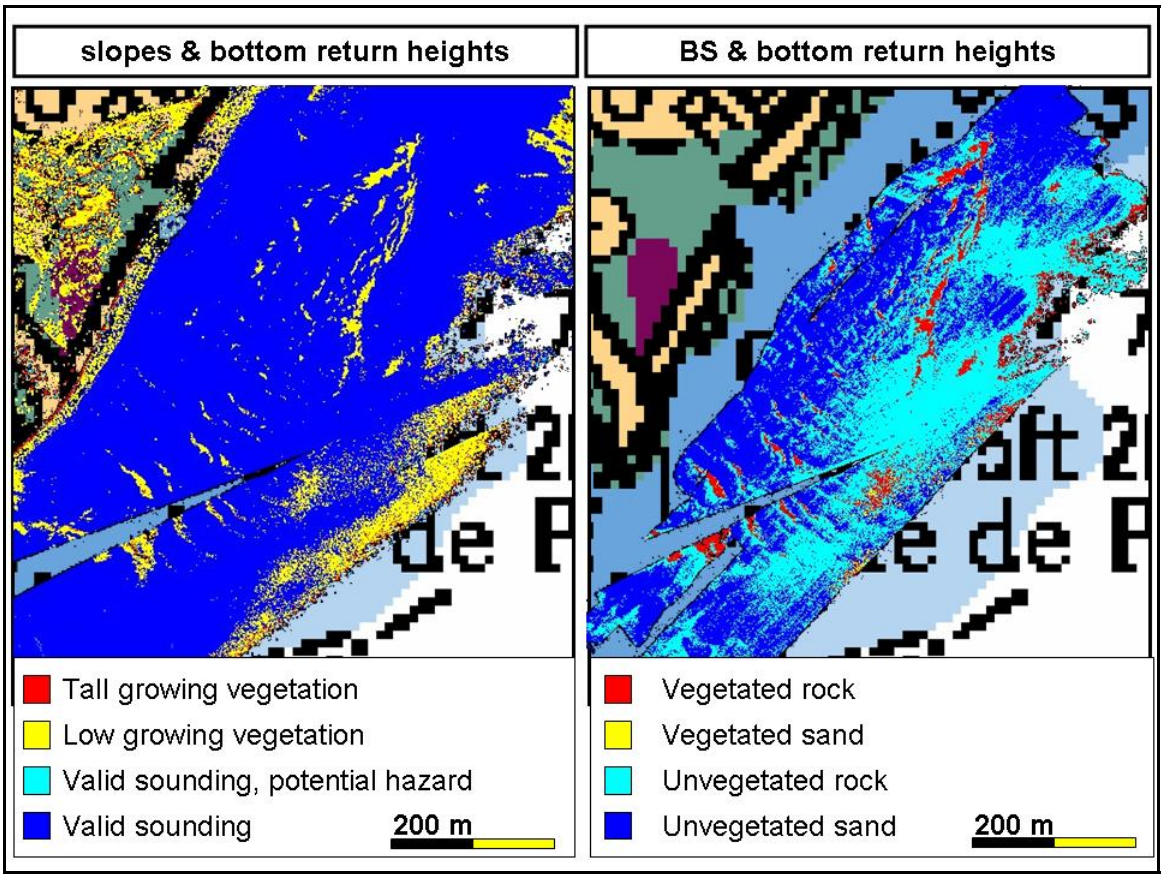

Figure 5.40 Validation and classification of the sandwave field east of the Paspébiac sandspit. Bathymetry, bottom return height, and acoustical backscatter maps are displayed in Figures 4.25, 4.26 and 4.27 respectively.

CHAPTER 6 Conclusions and Recommendations

6.1 Lidar Bottom Tracking

Although previous experience showed the multibeam can have difficulties in penetrating through particular dense layers of aquatic vegetation, multibeam data collected for this work were not contaminated by the vegetation. The varying bottom tracking performance of the multibeam is possibly due to different vegetation densities found in the survey areas. As the vegetation did not hinder the multibeam's bottom tracking, it acted as a reference against lidar data for its bottom tracking assessment. The watercolumn imaging functionality of the EM3002 and the Knudsen 200 kHz were appropriate tools to visualize the vegetation layers.

Acoustic and optical profiles demonstrated the difficulty the lidar had to penetrate through less dense vegetation layers and correctly determine the seabed. When vegetation was encountered, it was tracked by the green laser beam. As a result, the lidar returns too shallow depths, which, from a safety of navigation point of view, may seem acceptable, but the vegetation can also mask hazardous objects such as rock formations, anchors or wrecks covered by marine life. Above all, vegetation introduces an unacceptable depth bias (approximately as big as the vegetation is high), that degrades the reliability of the dataset, whether it is used for safety of navigation purposes, environmental studies, or hurricane assessments. In addition, if lidar surveys take place at different periods of the year, in vegetated areas which are part of cyclic operations, e.g. the eight year cycle of the US national coastal mapping program, recently developed or extinct vegetation fields will lead to misinterpretations of the geomorphologic changes.

The DTM analysis revealed a much larger (positive) systematic depth difference and variance between the lidar and multibeam datasets when these included biological growth. Standard deviations from vegetated areas greatly exceeded the measurement precision and IHO Order 1. Moreover, the lidar often did not track the seabed at all when vegetation was present. This behavior is most concerning, not only because the effective coverage, typically a great asset of bathymetric lidar, is reduced, but also because lidar datagaps do not necessarily result from depth and/or water clarity issues, but could represent marine life covered navigation hazards. Moreover, data from lidar systems that associate unsuccessful lidar soundings with a "no bottom at" statement, may do the hydrographers' judgment more harm than good. At the datagaps, associated lidar waveform data were unavailable to us, although this additional set would help in order to investigate non-tracking issues. In unvegetated areas the lidar showed the tendency to measure slightly shallower than the multibeam, which, in fact, is not surprising due to the much larger footprint of the lidar beams. The mean depth difference and standard deviation in unvegetated areas fell well within the manufacturer's accuracy specification and IHO Order 1.

In summary, a lidar dataset that includes vegetation populated areas introduces a false geomorphologic picture for habitat or engineering applications. Should some kind of approximation of vegetation presence be a desirable product, then lidar is a benefit to ecological mapping. In that case one would need an additional product (e.g. acoustical volume scattering, underwater or aerial photography, or (pseudo)-reflectance maps) to recognize aquatic vegetation fields. Green laser waveform data has a potential to identify aquatic vegetation and validate lidar soundings, Section 6.3.

6.2 Water Clarity Maps

An algorithm was developed that determines the slope of the volume return from each green laser waveform. The volume return slope describes the attenuation of light at 532 nm that falls within the receiver's FOV and is therefore referred to as the system attenuation coefficient. Although the system attenuation coefficient is in fact an intermediate product of the characterization process, necessary to determine the bottom return height, once mapped, the system attenuation coefficients yield a potential to identify water masses based on their water clarity. The system attenuation coefficients were seen to be biased by less distinct bottom return heights from vegetation soundings. Without a distinct bottom return, localizing the volume return is more challenging for the water clarity extraction algorithm. This challenge led, while accounted for as thoroughly as possible, to overestimated system attenuation coefficients, i.e. more clear water. Because the bottom return heights are relative to system attenuation coefficients, spatial patterns in water clarity maps were not overprinted on bottom return height maps. The logarithmic compression, utilized to account for the (linear) dynamic range of returned laser intensities, and the relative measurement of the return height, conveniently suppressed water clarity and depth related effects on the waveforms.

Water clarity values from PMT and GAPD derived waveforms vary in the absolute sense but spatially show the same variability (i.e., water clarity features and their prominence are seen in both water clarity data sets). The water clarity maps generated from the system attenuation coefficient showed the ability to discriminate different water masses, such as those that were separated from each other by a sand spit. The maps also

allowed for identification of day-to-day, and even line-to-line water clarity differences. The latter makes it possible to follow migrating water masses. These migrating water masses appeared to be less turbid than their surrounding water, and the patterns correlated strongly with infrared laser beam intensity maxima. It is hypothesized that, as the features were not present in aerial photography but were visible with the infrared waveforms (which can include a volume return), the migrating features seen in the water clarity maps are sub-surface. The inter-relations between system attenuation coefficient and infrared laser beam return intensity invites further investigation.

6.3 Characterization

Each green laser waveform was passed to an algorithm that characterized the waveform based on its bottom return height. To prevent land, shallow, or too deep returns corrupting the characterization process, these waveforms were filtered out with a separate process that assesses the quality of the characterization. Localizing and measuring the bottom return height (relative to the extrapolated system attenuation curve) is done with three different techniques: a derivative, maximal residual, and detrending approach. The combination of these three approaches was necessary to adapt to the less distinct bottom return heights of vegetation soundings.

Environmental effects on the green laser waveform, i.e. water clarity, flight altitude, seabed slope, and depth, were investigated, but none of these effects required accounting for, nor did they bias the interpretation of the characterization in any significant way. By deriving the logarithmic bottom return heights above the attenuation curve, effects of water clarity and depth were conveniently bypassed.

The bottom return heights were plotted spatially to map areas of varying seabed

reflectance. Clusters of low bottom return height values showed compelling agreement with densely populated areas of vegetation, identified from aerial photo mosaics, underwater photography, and single- and multibeam water column backscatter. In addition, keel mounted side scan sonar identified pebble- or rock formations, which are potential habitats for Laminaria sp. or related species, and these regions also matched with overlapping low bottom return height data. Low bottom return height clusters surrounded datagaps or regions of high acoustical backscatter, implying that the failure of a lidar sounding is frequently due to vegetation presence, rather than extinction depths.

A proposed method to validate lidar soundings in dense vegetated areas when ground truthing data are unavailable includes characterized waveforms. Image based thresholding of bottom return height and lidar bathymetry slopes data, were used to classify regions in terms of vegetation presence and seabed topography. Tall growing vegetation were identified when bottom return heights remained low (<30 DN) and bathymetry indicated unreasonable (>6°) topography. Similarly, low growing vegetation or the vegetation canopy was identified when the bathymetry revealed benign topography, while bottom return height values remained low. The results of these classifications showed good agreement with aerial photo mosaics and acoustic backscatter profiles. Overlapping side scan sonar backscatter, while not commonly available at most lidar surveys, aids with image classification by which potential habitats of the vegetation were identified. Furthermore, joining side scan sonar backscatter, lidar bathymetry slopes, and waveform characterization, has a potential to discriminate tall or low, and sand- or pebble-/ rock-based vegetation.

In order to set threshold values for validation, typical bottom return height values

of vegetated and unvegetated areas were determined for both PMT and GAPD waveforms. These values revealed survey-to-survey differences, but more importantly, the ratio between bottom return height values (in DN-log units) of vegetated and unvegetated areas is near constant (~0.4). Bottom return height values of sediment grabs were investigated to identify any low reflecting sediment, i.e. bottom return height similarly to that of vegetation. No such sediment was found, although only a small selection of sediment grabs was available, and without associating underwater photography it is uncertain whether the laser actually hit the sediment, or vegetation growing on the sediment. The stable ratio implies that bottom return height threshold values for vegetated seabeds can easily be determined. The ratio also implies that there is an unambiguous difference between waveform returns from vegetated and unvegetated seabeds, allowing us to discriminate vegetation easily from the surrounding seabed.

6.4 Recommendations

1) Missing waveforms

Unsuccessful SHOALS-3000 soundings were not associated with lidar waveforms. We could therefore only investigate the resulting datagaps if these were overlapped with ground truthing data. Analysis of the missing waveforms can aid in determining the reason behind a sounding failure. When a bottom is not detected due to extinction depths, the waveform will only consist of a volume return that joins the background noise at the extinction depth. In any other case, for example when vegetation does not produce a detectable bottom return, water clarity is not the constraining factor. An undetectable bottom return can be recognized by a sudden drop towards the background noise. A simple function can identify such a situation, from which the

observing hydrographer is warned that the extinction depth is definitely not reached. The desired function can additionally give an approximation of the depth at which the undetectable return was located, although this approximation can never be regarded as a least depth or "no bottom at" statement (Figure 6.1).

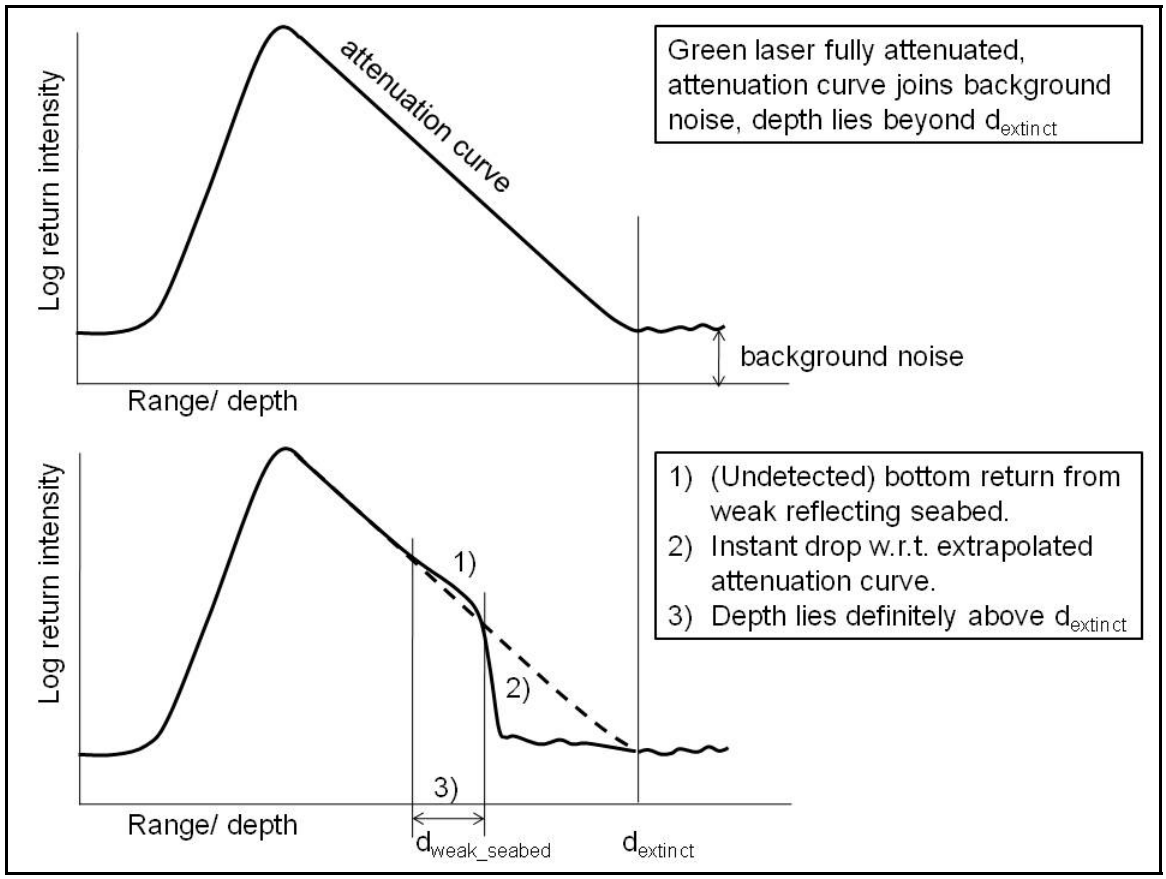

6.1 When the depth exceeds the extinction depth, the waveform only consists of a surface and volume return (top). An instant drop with respect to the extrapolated attenuation curve always occurs when the green laser signal reflects at a depth less than the extinction depth, regardless of the seabed reflectance (bottom). Given this phenomenon, the hydrographer can distinguish a waveform collected at depths exceeding the extinction depth, from a waveform with an undetectable bottom return.

2) Further investigation of the system attenuation curve

By simply determining the slope of the attenuation curve, bathymetric lidar data provide an interesting by-product. The system attenuation coefficient will improve if the

attenuation curve, on which the linear regression is performed, is longer and if waveforms are not contaminated by weak vegetation returns. It would therefore be favourable to have waveforms from deeper unvegetated seabeds. In addition, to examine the practicability of the derived system attenuation coefficient, a potential study area should include a turbidity source such as a river plume. The system attenuation coefficient presented in this work describes the water clarity over the complete water column, as the linear regression was performed between (sub-)surface and bottom. Should the regression be done at consecutive depth bins, then an actual water clarity profile could be constructed, from which water clarity maps at various depths could be compiled. From a selection of waveforms, it should then be possible to determine a three-dimensional water clarity model. To the author it is unknown on which (vertical) scale water clarity changes exist. However, the proposed method shows that a lidar waveform contains more information than is used for the range measurement.

3) Investigate correlations between water clarity and infrared laser beam

This work shows examples of a strong correlation between water clarity and infrared laser beam peak intensity patterns. Since the aerial photography did not reveal matching surface patterns, we believe that these features lie just below the water surface. Near real time oceanographic transects (including optical backscatter) would assist in the investigation.

4) Lidar survey planning

A large portion of this work relied on ship-based data that overlapped lidar

coverage. The net overlap was not entirely satisfying since the majority of lidar data were collected at depths un-navigable for our survey launch. The unanticipated limiting overlap is particularly frustrating since the lidar flight lines were changed last minute and Secchi disc measurements and laser performance predictions were made prior to the overflight but without communicating the results. A significant amount of ship-time could have been saved and focused on shallower areas that required denser line spacings. As a result, large portions of relatively deep were been mapped with ship-based acoustics but appeared somewhat superfluous. A future collaboration would require an improved communication of the lidar survey plan.

Bibliography

Banic, J., Sizgoric, S., O'Neil, R., (1986). "Scanning Lidar Bathymetry for Water Depth Measurement". *Proceedings of SPIE* – The International Society for Optical Engineering, Volume 633, pp. 187-195.

Brooks, M.W., Culpepper, E., Guenther, G.C., and LaRocque, P.E., (1998). "Advancements and applications of the SHOALS laser bathymetry system." *Proceedings ION GPS 98*, Institute of Navigation, Sept. 15-18, 1998, Nashville, TN, 8 pp.

Delpeche, N. (2006). Observations of Advection and Turbulent Interfacial Mixing in the *Saint John River Estuary, New Brunswick Canada.* M.Sc.E. thesis, Department of Geodesy and Geomatics Engineering, University of New Brunswick, Fredericton, N.B., Canada, 299 pp.

Dijkstra, S.J., Elston, G.R., (2004). "Bottom Segmentation and Classification Using Expectation-Maximization Clustering Methods on SHOALS Data". *Conference Proceedings: American Society for Photogrammetry and Remote Sensing,* Denver, CO, 23 - 28 May, 2004, 11 pp.

Duntley, S.Q., (1963). "Light in the Sea." *Journal of Optical Society America*, volume 53, pp. 214 – 232.

Elston, G.R., Dijkstra, S.J., (2004). "Robust Characterizatio of SHOALS Lidar signals for Bottom Segmentation and Classification: A Combinded Parameter-Estimation and Curve-Fitting Approach." *Conference Proceedings: American Society for Photogrammetry and Remote Sensing,* Denver, CO, 23 - 28 May, 2004.

Feygels, V.I., Kopilevich, Y.I., (1996). "Optimization of Laser Wavelength in Oceanographic Lidars." *SPIE* volume 2964, pp. 128 – 137, 1996

Feygels, V.I., Wright,W.C., Kopilevich, Y.I., Surkov,A., (2003). "Narrow Field of View Bathymetric Lidar: Theory and Field Test." *SPIE Ocean Remote Sensing and Imaging II*, volume 5155, 2003

Feygels, V.I., (2006). "Prediction of SHOALS-1000 Performance in Bay de Chaleur (Quebec) Region." Optech International Inc.

Geodetic Survey Division, NRCan, (2004). The GPS-H v2.01, http://www.geod.nrcan.gc.ca/software/gpsht_e.php

Gordon, H.R., (1982). "Interpretation of Airborne Oceanic Lidar: Effects of Multiple Scattering." *Applied Optics*, volume 21, number 16, pp. 2996-3001

Guenther, G.C., (1985), Airborne Laser Hydrography, *System Design and Performance Factors.* NOAA, Rockville, U.S.

Guenther, G.A., LaRocque, P.E., Lillycrop, W.J., (1994). "Multiple Surface Channels in SHOALS Airborne Lidar" Proceedings of SPIE, volume 2258, pp. 422-430.

Guenther, G.C., Eisler, T.J., Riley, J.L, Perze, S.W., (1996a). "Obstruction Detection and Data Decimation for Airborne Laser Hydrography." *Proceedings of the Canadian Hydrographic Conference*, Halifax, N.S., 15 pp.

Guenther, G.C., Thomas, R.W.L., LaRocque, P.E., (1996b). "Design Considerations for Achieving High Accuracy with the SHOALS Bathymetric Lidar System." *SPIE Laser Remote Sensing of Natural Waters from Theory to Practice*, volume 2964, pp 26–37.

Guenther, G.A., Cunningham, A.G., LaRocque, P.E., Reid, D.J., (2000). "Meeting the Accuracy Challenge in Airborne Lidar Bathymetry." *Proceedings of EARSeL – SIG – Workshop LIDAR, Dresden/FRG*, June 16 – 17, 27 pp.

Guenther, G.C., (2001), "The DEM Users Manual", Chapter 8 Airborne Lidar Bathymetry, pp 236-307.

Hare, R., (1994). "Calibrating LARSEN-500 Bathymetry in Dolphin and Union Strait using dense Acoustic Ground-Truth." *International Hydrographic Review*, Monaco, volume LXXI(1), March 1994. pp 91-108.

Hare, R., Godin, A., Mayer, L.A., (1995a). "Accuracy Estimation of Canadian Swath (Multibeam) and Sweep (Multitransducer) Sounding Systems." Canadian Hydrographic Service, Internal report 1995. 98 pp.

Hare, R. , (1995b). "Depth and Position Error Budgets for Multibeam Echosounding." *International Hydrographic Review*, Monaco volume LXXII (2), September 1995. pp 37-69.

Hughes Clarke, J.E., (2003). "A Reassessment of Vessel Coordinate Systems; What is it that we are Really Aligning." Proceedings of U.S. Hydrographic Conference, Rockville, Maryland, US, 12 pp.

Hughes Clarke, J.E., (2004a). "Seafloor Characterization Using Keel-Mounted Sidescan: Proper Compensation for Radiometric and Geometric Distortion." Proceedings of the Canadian Hydrographic Conference, Ottawa, CDROM, Rockville, 18 pp.

Hughes Clarke, J.E., (2004b). "Acoustic Backscatter Data Interpretation." Lecture 20 in the 36th UNB OMG / UNH CCOM Multibeam Sonar Training Course, Stavanger, Norway, 2004.

Hughes Clarke, J.E., (2004c). "Data Reduction for Chart Compilation Purposes." Lecture 29 in the 36th UNB OMG / UNH CCOM Multibeam Sonar Training Course,

Stavanger, Norway, 2004.

Hughes Clarke, J.E., (2006a). "Applications of Multibeam Water Column Imaging for Hydrographic Survey" *The Hydrographic Journal*, April Issues, 2006, 33 pp.

Hughes Clarke, J.E., Lamplugh, M., Czotter, K., (2006b). "Multibeam Water Column Imaging: Improved Wreck Least-Depth Determination" Proceedings, *Canadian Hydrographic Conference* 2006, CDROM, 10 pp.

IHO, (1998). "IHO Standards for Hydrographic Surveying." *IHO Special Publication no. 44*, 4th edition, 1998., 26 pp.

IHO, (2008). "IHO Standards for Hydrographic Surveying." *IHO Special Publication no. 44*, 5th edition, 2008., 36 pp

Jerlov, N.G., *Marine Optics*, Elsevier Scientific Pub., Amsterdam, 1976, 231 pp.

LaRocque, R.E., Banic, J.R., Cunningham, A.G., (2004). "Design description and field testing of the SHOALS-1000T airborne bathymeter." *Proceedings SPIE* volume 5412, *Laser Radar Technology and Applications IX*, pp162-184.

Lee, M., Tuell, G., (2003). "A Technique for Generating Bottom Reflectance Images from SHOALS Data." *Proceedings U.S. Hydrographic Conference*, Biloxi,

Mississippi, 2003, 13 pp.

Li, Z., Zhu, Q., Gold, C., (2005). Digital Terrain Modeling – Principles and Methodology. 305 pp.

Llewellyn, K. C., (2005). *Corrections for Beam Pattern Residuals in Backscatter Imagery from the Kongsberg-Simrad EM300 Multibeam Echosounder.* M.Eng report, Department of Geodesy and Geomatics Engineering, University of New Brunswick, Fredericton, N.B., Canada, 105 pp.

Lockhart, C., Arumugam, D., Millar, D., (2005). "Meeting Hydrographic Charting Specifications with the SHOALS-1000T Airborne Lidar Bathymetry." *U.S. Hydrographic Conference Proceedings*, San Diego, California, 2005, 8 pp.

Lyzenga, D.R., (1978). "Passive Remote Sensing Techniques for Mapping Water Depth and Bottom Features." *Applied Optics*, Vol. 17, No. 3 pp. 379-383.

Mobley, C.D., (1994). *Light and Water: Radiative Transfer in Neutral Waters*, New York, Academic, 2004, CDROM.

Moustier, de, C., (2004). "DTM Generation Methods and Pitfalls." Lecture 28 in the 36th UNB OMG / UNH CCOM Multibeam Sonar Training Course, Stavanger, Norway, 2004.

Oliveira Jr., A. M., (2007). *Maximizing the Coverage and Utility of Multibeam Backscatter for Seafloor Classification.* M.Sc.E. thesis, Department of Geodesy and Geomatics Engineering, University of New Brunswick, Fredericton, N.B., Canada, 112 pp.

Optech Incorporated (2004). Field Test Report for CHARTS, contract number: DACW42-01-C-0023, 82 pp.

Optech Incorporated, (2006). *SHOALS-3000 Specifications*, 2pp.

Pe'eri, S., Philpot, W., (2007). "Increasing the Existence of Very Shallow-Water LIDAR Measurements Using the Red-Channel Waveforms." *IEEE Transactions on Geoscience and Remote Sensing*, volume 45, number 5, May 2007, 7 pp.

Pope, R.W., Johnson, P., Lejdebrink, U., Lillycrop, J.W., (2002). "Airborne Lidar Hydrography: Vision for Tomorrow." *Sea Technology*, volume 43, number 6, pp. 27 – 34.

Riley, J.L., (1995). "Evaluating SHOALS Bathymetry using NOAA Hydrographic Survey Data." Proceedings, 24th Joint Meeting of UJNR Sea-Bottom Survey Panel.

Sabol, B.M., Graves, M.R., Preston, J.W. (2007). "Evaluation of Multibeam

Hydrographic System Performance in Dense Seagrass." *Proceedings U.S. Hydrographic Conference*, Norfolk, U.S., 2007, 12 pp.

Slootweg, P.A., (1978). "Computer Contouring with a Digital Filter", *Marine Geophysical Researches*, volume 3, pp.401-405.

Steinvall, O., Koppari, K., (1996). "Depth Sounding Lidar – An Overview of Swedish Activities and with Future Prospects." *SPIE Laser Remote Sensing of Natural Waters: From Theory to Practice: CIS Selected Papers*, volume 2964, pp. 2–25.

Thomas, R.W.L., Guenther, G.C., (1990). "Water Surface Detection Strategy for an Airborne Laser Bathymeter." *SPIE Ocean Optics*, volume 1302, pp. 597 – 609

Tuell, G., Park, J.Y., (2004). "Use of SHOALS Bottom Reflectance Images to Constrain the Inversion of a Hyperspectral Radiative Trasfer Model." *SPIE*, volume 5412, pp.185-193.

Tuell, G.H., Feygels, V., Kopilevich, Y., Weidemann, A.D., Cunningham, G.A., Mani, R., Podoba, V., Ramnath, V., Park, J.Y., Aitken, Y., (2005a) "Measurement of Ocean Water Optical Propeties and Seafloor Reflectance with Scanning Hydrographic Operational Airborne Lidar Survey (SHOALS): II. Practical Results and Comparison with Independent Data." *SPIE Remote Sensing of Coastal Oceanic Environment*, volume 5885, pp 1–13.

Tuell, G.H., Park, J.Y., Ramnath, V., Feygels, V., Guenther, G.C., (2005b). "SHOALS-enabled 3D Benthic Mapping." *SPIE Algorithms and Technologies for Multispectral, Hyperspectral, and Ultraspectral Imagery XI*, volume 5806, 11 pp.

Tulldahl, M., Andersson, M., Steinvall, O., (2000). "Airborne Laser Depth Sounding: Improvements in Position- and Depth Estimates by Local Corrections for Sea Surface Slope." *OCEANS 2000 MTS/IEEE Conference and Exhibition* , volume 2, pp.1421-1428.

Urick, R.J., (1983). *Principles of Underwater Sound*, 3rd edition, California, U.S., 423 pp.

Wang, C.K., Philpot, W.D., (2002), "Using SHOALS LIDAR System to Detect Bottom Material Change". *Geoscience and Remote Sensing Symposium, IGARSS'02, IEEE*, volume 5, pp.2690-2692.

Wang, C.K., (2005). "Ocean Bottom Characterization Using Airborne LIDAR: Monte Carlo Simulation and Investigation of Bottom Material Reflectance/Fluorescence." Ph.D dissertation, Cornell University, Ithaca, New York, 97 pp.

Wells, D.E., (1997). "MB7 – Lidar." TU Vienna Gastvorlesungen, 1997, 9 pp.

Yang, E., LaRocque, P., Gunether, G.C., Reid, D., Pan, W., Francis., K., (2007).

"Shallow Water Depth Extraxtion – Progress and Challenges." *Proceedings U.S. Hydrographic Conference*, Norfolk, U.S., 13 pp

Vita

Candidate's full name: Pim Phillip Dominique Marcel Kuus

Universities attended: Maritime Instituut Willem Barentz,
West-Terschelling, the Netherlands,
September 2001 – June 2005,
B.Sc. (Hydrography);

Workshop Presentations:

Kuus, P., Hughes Clarke, J., Brucker, S., (2007). "Characteristics of PMT/GAPD Laser Waveforms in Areas of Dense Seabed Algae", FUDOTeram Workshop, Toronto, March 2007

Kuus, P., Hughes Clarke, J., Brucker, S., (2007) "Assessment of Green Laser Bottom Tracking Ability in Algae-Contaminated Areas Including Waveform Characterization and Comparison with Acoustical Backscatter", JALBTCX Workshop, Seattle, May, 2007

Conference Presentations:

Kuus, P., Hughes Clarke, J., Brucker, S., "Assessment of Green Laser Bottom Tracking Ability in Algae-Contaminated Areas Including Waveform Characterization and Comparison with Acoustical Backscatter", (Poster) Geoide Annual Conference, Halifax, June, 2007

Submitted Conference Papers:

Kuus, P., Hughes Clarke, J., Brucker, S., "SHOALS-3000 Surveying Above Dense Fields of Aquatic Vegetation - Quantifying and Identifying Bottom Tracking Issues", *Canadian Hydrographic Conference 2008*, Victoria, B.C., May 5 – 8.